A *Col9a3* EXON 3 SKIPPING MOUSE AS A NOVEL MODEL FOR MULTIPLE EPIPHYSEAL DYSPLASIA

Silvia Lecci

Institute of Genetic Medicine

A thesis submitted for the degree of Doctor of Philosophy

November 2019

Declaration

I, Silvia Lecci, declare that no portion of the work compiled in this thesis has been submitted in support of another degree or qualification at this or any other University or Institute of Learning. This thesis includes nothing which is the work of others, nor the outcomes of work done in collaboration, except where otherwise stated.

……..

Silvia Lecci

Acknowledgments

I would like to thank my supervisor Professor David Young, for giving me this opportunity and for all his help, guidance, patience and encouragement throughout my PhD. He made me see the positive side of things and believe a bit more in myself.

I would like also to thank Professor Michael Briggs for his guidance, support and patience.

Thanks to the Functional Genomics Unit at Newcastle University for assisting with the animal care, and special thanks to Steve Smith for all his help and the nice chats.

Thanks to Professor David Young, Dr Colin Miles and Paul Cairns for the development and injection of CRIPSR/Cas9 system to generate the mutant mice.

Thanks to Professor Rob Vant 'T Hof for his help in generating the μCT data.

Thanks to Dr Kathleen Cheung for her help in the RNA-Seq data analysis.

Thanks to Dr Attila Aszódi and Bastian Hartmann for performing atomic force microscopy analysis.

Many thanks to Hua Lin for her help in the lab and her dedication to work.

Thanks to present and past members of SRG group for their help and for making my time in the lab so enjoyable.

The SYBIL consortium is gratefully acknowledged for the financial support during my PhD.

My deep and sincere gratitude to my family for their continuous and unconditional love, help and support. Thanks to Gerald for being so supportive and always next to me during the difficult time of the writing up, despite going himself through the same stressful time.

Finally, I would like to acknowledge the sacrifice of the many mice that were used in this study. Without them this thesis would have not been possible. I never enjoyed taking their life but I knew it was for a greater good.

Table of Contents

List of figures

List of tables

Abbreviations

AFM	Atomic force microscopy
BrdU	5-bromo-2'-deoxyuridine
BV	Bone volume
CILP	Cartilage intermediate-layer protein
Col9a3$^{\Delta ex3}$	Col9a3 $^{\Delta ex3/\Delta ex3}$ mutation
COL	Collagenous domain
COMP	Cartilage oligomeric matrix protein
Conn.Dn.	Connectivity density
Cort.Th.	Cortical thickness
CS	Chondroitin sulphate
DMM	Destabilization of medial meniscus
DSB	Double strand break
DTDST	Diastrophic dysplasia sulphate transporter
E.pm	Endocortical perimeter
ECM	Extracellular matrix
EGF	Epidermal growth factor
EJC	Exon junction complex
ER	Endoplasmic reticulum
FACIT	Fibril-associated collagens with interrupted triple helices
FGF	Fibroblast growth factor
FGFR	Fibroblast growth factor receptor
GAG	Glycosaminoglycan
GSEA	Gene set enrichment analysis

H&E	Haematoxylin and Eosin
HIF-1α	Hypoxia inducible factor-1α
hnRNPs	Heterogenous nuclear ribonucleoproteins
HR	Homologous recombination
HZ	Hypertrophic zone
ICD	Inter-canthal distance
IHC	Immunohistochemistry
ITM	Interterritorial matrix
IVT	*in vitro*-transcription
µCt	microcomputed-tomography
MED	Multiple epiphyseal dysplasia
MFC	Medial femoral condyle
MMI	Mean polar moment of inertia
MTP	Medial tibial plateau
NC	Non-collagenous domain
NHEJ	Non-homologous end joining
OA	Osteoarthritis
PAM	Protospacer-adjacent motif
PCA	Principal component analysis
PG	Proteoglycan
PHZ	Pre-hypertrophic zone
P.pm	Periosteal perimeter
PTC	Premature stop codon
PSACH	Pseudo-achondroplasia

PZ	Proliferative zone
rER	Rough endoplasmic reticulum
RRHO	Rank-Rank hypergeometric overlap
SMI	Structure model index
snRNPs	small nuclear ribonucleoproteins
T.Ar.	Tissue area
TALENs	transcription activator-like effector nucleases
Tb.N	Trabecular number
Tb.Pf.	Trabecular pattern factor
TSP	Thrombospondin
Tb.Sp	Trabecular separation
Tb.Th	Trabecular thickness
TEM	Transmission electron microscopy
TV	Tissue volume
UPR	Unfolded protein response
vWFA	von Willebrand Factor A
ZFNs	zinc-finger nucleases

Abstract

A *Col9a3* EXON 3 SKIPPING AS NOVEL MODEL FOR MULTIPLE EPIPHYSEAL DYSPLASIA.

Introduction: Multiple epiphyseal dysplasia (MED) is generally an autosomal dominant chondrodysplasia characterised by early-onset degenerative joint disease. Its genetic background is complex and heterogeneous and among the mutated genes are those encoding for the pro-α chains of the collagen type IX, *COL9A1*, *COL9A2* and *COL9A3,* where the majority of mutations lead to the skipping of a syngenic exon.

Aim: Reproduce in a mouse model the skip of exon 3 in the *COL9A3 g*ene to understand its pathogenic role in relation to MED.

Material and Methods: By CRISPR/Cas9 technology we generated two mouse lines, one carrying a deletion of *Col9a3* exon 3 (*Col9a3*$^{\Delta ex3/\Delta ex3}$*)*, reproducing the splicing events reported in a MED patients group and a *Col9a3*-null mouse (*Col9a3*$^{-/-}$*)*. On the mutant mice, we performed skeletal X-ray phenotyping and growth plate analysis, including immunohistochemistry and BrdU labelling to monitor proliferation. Ultrastructure of growth plate was visualised using Transmission electron microscopy (TEM). Sequential protein extraction and Atomic force microscopy (AFM) were used to evaluate growth plate cartilage stability, whereas articular cartilage integrity was assessed by destabilisation of the medial meniscus (DMM) surgery and during ageing. Bone density and ultrastructure was assessed by Microcomputed tomography (μCT). Mutant transcriptomes were obtained by RNAseq.

Results: The phenotyping of CRISPR/Cas9 generated offspring through DNA and cartilage RNA analysis had led to the establishment of two transgenic mouse lines, one splicing as predicted (*Col9a3*$^{\Delta ex3/\Delta ex3}$) and a second lacking the *Col9a3* transcript and collagen type IX protein (*Col9a3*$^{-/-}$). Both lines are viable, however only *Col9a3*$^{-/-}$ mice displayed detectable phenotypic abnormalities: mild short stature and hip dysplasia, abnormal tibial epiphysis morphology and delayed ossification of femoral head in 18-week old mice. A reduced level of growth plate chondrocyte proliferation was detected in both mutant mice compared to WT, along with softening of the proliferative zone shown by AFM indentation measurements on new-born and 6 weeks old animals. Interestingly, both mutant mice exhibited similar transcriptome profiles. Only in *Col9a3*$^{-/-}$ mice immunoblotting of sequentially extracted matrilin-3 and COMP proteins revealed different cartilage extractability from controls. Articular cartilage integrity seemed not to be affected by either mutation.

Discussion and conclusion: Analysis confirmed the production of a shorter transcript from cartilage of *Col9a3*$^{\Delta ex3/\Delta ex3}$mice. However, these mice still produced collagen type IX protein and had no overt phenotype apart from reduced chondrocytes proliferation and softer proliferative cartilage extracellular matrix. The *Col9a3*$^{-/-}$ mice had a mild skeletal phenotype and express no *Col9a3* transcript or protein, resulting in overall more unstable cartilage.

Both mutant mice will represent an important tool to gain insights on collagen type IX role into the matrix. In particular, the *Col9a3*$^{\Delta ex3/\Delta ex3}$ line, by recapitulating human Col9-MED, can add to our understanding of MED disease mechanism.

Chapter 1.

Introduction

1.1 Bone development

During embryogenesis bone tissue forms from the mesoderm layer. More specifically the axial skeleton derives from the somites, the appendicular skeleton from the lateral plate mesoderm, and the cranial neural crest gives rise to the branchial arch and craniofacial bones and cartilage. Bone formation, also called osteogenesis, is the transformation of the mesenchymal tissue into bone tissue and this can occur through mainly two mechanisms, intramembranous or endochondral ossification. Intramembranous ossification is the process through which flat bones such as those constituting the skull form. This mechanism involves the direct transformation of mesenchymal tissue into bone and starts when proliferating mesenchymal cells condense into compact nodules, which gives rise to osteoblasts. As bone precursor cells, the osteoblast produce an ECM able to incorporate calcium salt and therefore allow for pre-bone matrix calcification. During this process some osteoblasts remain engulfed in the calcified matrix they have secreted, becoming bone cells, osteocytes, and bony spicules start to radiate while the bone ossifies. A membrane of compact mesenchymal cells surrounding the calcified spicules, the periosteum, also deposits osteoid matrix and contributes to bone growth (Gilbert 2000).

Both ossification processes are regulated by various signalling pathways. These include members of the bone morphogenetic proteins (BMP), the fibroblast growth factor (FGF) groups and the Wnt signalling pathway (Shahi et al. 2017). Moreover, the activation of the transcription factor CBFA1, also known as Runx2, is responsible for mesenchymal cell transformation into osteoblasts and the activation of bone-specific extracellular matrix (ECM) protein genes (Komori 2010).

Endochondral ossification is the mechanism that allows long bones to develop and grow. The stepwise process involves the formation of a cartilage template from aggregated mesenchymal cells, which is then replaced by bone (Fig. 1.1). Endochondral ossification initiates when mesenchymal cells are induced by paracrine factors to express two transcription factors, Pax1 and Scleraxis, which are believed to be activators of cartilage-specific genes (Cserjesi et al. 1995, Sosic et al. 1997). Subsequently, the mesenchyme cells condense and differentiate into chondrocytes, which then proliferate and produce the ECM to form the cartilaginous template of the bone. Chondrocytes in the centre of the cartilaginous template become then hypertrophic, arrest proliferation and start secreting collagen type X into the matrix. Additionally, at this stage hypertrophic chondrocytes produce enzymes

promoting the generation of calcium and phosphate ions to permit the mineralisation of cartilaginous matrix. Finally, the majority of hypertrophic chondrocytes undergo apoptosis, facilitating blood vessel invasion and creating the space for the bone marrow. Blood vessels introduce osteoblasts, which produce bone matrix generating the primary ossification centre, which extends outwards in both directions to form the metaphysis of the newly formed bone. At the bone epiphysis secondary ossification centres form and only a cartilaginous area, called epiphyseal growth plate, remains between the primary and secondary ossification centres. This area is constituted by ordered chondrocytes organised into zones termed resting, proliferative, and hypertrophic and is responsible for longitudinal growth of the newly formed bone. In this area chondrocyte differentiation is tightly coordinated to allow longitudinal bone growth which continues as long as proliferation of growth plate chondrocytes occurs (Burdan et al. 2009). Within the resting or reserve zone, chondrocytes are small and uniform. They can be singular or in pairs, if they have divided, and are rich in lipid and cytoplasmic vacuoles. Resting chondrocytes proliferate at a low rate and have a reduced synthesis of proteoglycan and collagen type II. After the resting zone, the proliferative zone is present. Proliferative chondrocytes are flat and organised into longitudinal columns which with the immediate surrounding ECM, constitute the chondron. Mitotic activity is increased as well as the synthesis of collagen types II and XI. Below the proliferative zone is a layer known as the hypertrophic zone whose chondrocytes terminally differentiate and become larger. DNA synthesis is reduced and cellular division stops; conversely the synthesis of various components of the ECM is increased. Longitudinal growth of the skeleton is importantly affected by chondrocytes hypertrophy, as it has been reported that a great part of longitudinal growth depends on chondrocytes height, while the remaining on matrix synthesis and chondrocytes proliferation. Therefore, the differential growth of various bones seems to be related to differences in the size of hypertrophic chondrocytes (Ballock and O'Keefe 2003). Notably, the hypertrophic zone is the first zone that produces alkaline phosphatase, which by increasing phosphate ions, it allows the process of matrix calcification (Burdan et al. 2009).

While longitudinal growth occurs, a simultaneous bone resorption is carried out by osteoclasts forming the endosteum, the fibrovascular membrane that lines the medullary cavity of a long bone. This process has the double function of reducing the bone weight and creating the space for the bone marrow. At the same time the osteoblasts in the periosteum, the membrane that covers the outer surface of all bones, increase the diameter of the bone through intramembranous ossification. This process is called appositional growth, which

alongside bone resorption, is responsible for a constant bone remodelling which helps maintaining the structural integrity of the bone (Rauch 2005).
Longitudinal growth continues until adult age, after which the cartilage growth plate ossifies, fusion between epiphysis and metaphysis occurs and bone growth ceases completely. It is worth mentioning that a thin layer of cartilage is present on the surface of the bone epiphyses adjacent to the synovial cavity, and it is called articular cartilage. Its function is to facilitate joint movement, resist compressive forces and protect the underlying bone. As seen in the growth plate, also chondrocytes of articular cartilage follow a pattern of distinct layers according to their sub-population of cells and ECM organisation. The superficial zone, directly in contact with the joint space, produces a high level of lubricants and provides the ability to resist shear stress. This zone is formed by elongated cells, tightly packed and arranged parallel to the joint cavity and they represent a source of cartilage progenitors (Kozhemyakina et al. 2015). The middle or transitional zone forms approximately half of the total articular cartilage volume and consists of very large and round sparse chondrocytes, followed by the deep zone where mostly organized into column-like stacks perpendicular to the tissue synovial surface. This zone represents the 30% of the total cartilage and its mechanical properties are due to the production of the typical cartilage matrix molecules, such as collagen type II and aggrecan (Sophia Fox et al. 2009). Between the deep zone and the underlying subchondral bone, is found the last zone called calcified cartilage, which is separated from the not calcified tissue by a visible tidemark (Fig. 1.2). In this last zone, cells are even larger, entered an hypertrophic state, are active in matrix production and likely responsible for interactions with the underlying subchondral bone (Decker et al. 2015).
Disease- or ageing-driven degeneration of the articular cartilage surface leads to joint pain and dysfunction usually identified in osteoarthritis (OA).

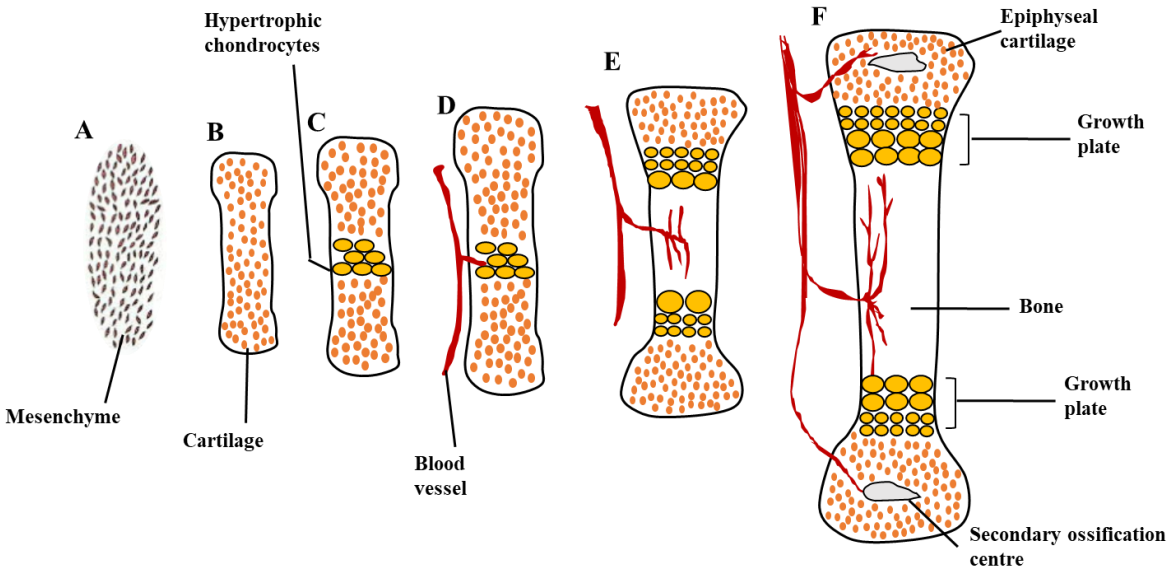

Fig. 1.1 | Endochondral ossification process. (A, B) Mesenchymal cells condense and differentiate into chondrocytes to form the cartilaginous model of the bone. (C) Primary centre of ossification forms when chondrocytes in the centre of the shaft undergo hypertrophy and apoptosis while they change and mineralize their ECM. Blood vessels can invade the empty spaces left by dead cells. (D, E) Blood vessels introduce osteoblasts, which bind to the degenerating cartilaginous matrix and deposit bone matrix. Secondary ossification centres also form as blood vessels enter near the tips of the bone. They are separated from the primary ossification centre by ordered zones of proliferating, hypertrophic, and mineralising chondrocytes (F).

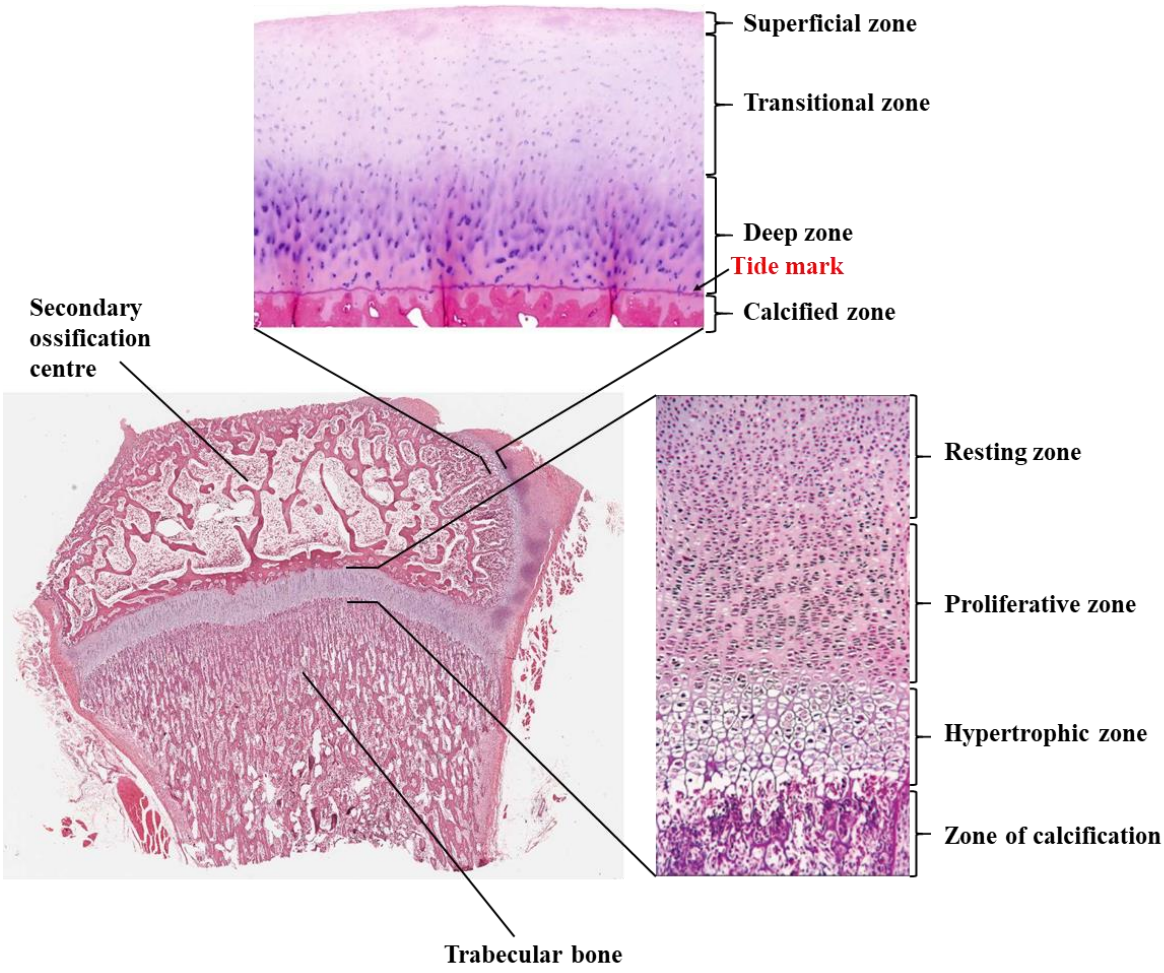

Fig. 1.2 | The epiphyseal growth plate. Magnified image of a 3-week old rat proximal tibial epiphysis section stained with H&E. Indicated is the epiphyseal growth plate, whose structure is divided in different zones, which is positioned between the secondary ossification centre and the trabecular bone. In addition, the magnified picture of the articular cartilage surrounding the tibial epiphysis showing its division in zones. (magnification x100). Adapted from (Burdan et al. 2009)

1.2 The cartilage extracellular matrix

In most multicellular complex organisms, cells and an intricate network of macromolecules, called the extracellular matrix (ECM), constitute the tissues. Different ECM composition is expressed in different multicellular systems, as a result of the independent evolution of multicellularity in distinct lineages. Despite this, the basic functions of ECM, such as cell adhesion, cell-to-cell communication and differentiation, remain common features (Abedin and King 2010). The ECM in cartilage comprises a variety of proteins and polysaccharides that are secreted locally by chondrocytes. Once in the extracellular space, they assemble into an organised meshwork in close association with the surface of the cell that has produced them.

Two main classes of extracellular macromolecules form the matrix: proteoglycans and fibrous proteins, such as collagen. In addition, glycoproteins, such fibronectin, laminin and elastin, have both structural and adhesive functions. Members of both classes come in a great variety of shapes and sizes. These molecules are mainly synthesised and secreted by stromal cells, such as fibroblasts, osteoblasts and chondrocytes. The proteoglycan molecules in cartilage form a highly hydrated, gel-like "ground substance" in which the fibrous proteins are embedded. This characteristic is given by the presence of several net negative charges that attracts positively charged sodium ions, which recruit water molecules via osmosis. This osmotic swelling gives to cartilage elastic properties, including the ability to resist compressive forces (Gentili and Cancedda 2009). This network enables the rapid diffusion of nutrients, metabolites, and hormones between the blood and the tissue cells. The collagen fibres are the main structural protein of the matrix, they contribute to the organisation of the matrix conferring it stability and specific mechanical properties according to the collagen content (Rozario and DeSimone 2010). Elastin fibres give it resilience. Finally, many matrix glycoproteins help cell binding in the appropriate locations, conferring typical structure and properties to cartilage. Moreover, cartilaginous ECM is remodelled continuously by a combination of synthesis and degradation by matrix metalloproteinases (MMPs) and 'a disintegrin and metalloproteinase with thrombospondin motifs' (ADAMTSs) proteinase family members (Takahashi et al. 2005).

Considering the possible different nature and composition, the ECM can have many functions, such as providing support or regulating intercellular communication and cell dynamic behaviour. In addition, it can be considered a depot for a wide range of cellular

growth factors, which can be released during altered physiological conditions, leading to the activation of a cascade of events affecting cellular functions.
In addition to the zonal stratification according to structure and composition mentioned for growth plate and articular cartilage matrix, within each zone different regions of the matrix can be distinguished according to proximity of chondrocytes, composition and collagen fibril organization. The pericellular matrix (PCM) immediately surrounds the cell membrane and it is a thin layer mainly containing sulphated proteoglycans, glycoproteins and very fine collagen fibres tightly packed, forming a dense woven enclosure around the chondrocyte (Poole 1997). The major components of PCM are collagen type IX, perlecan, hyaluronan, biglycan and other small aggregates. Remarkable is the presence of collagen type VI around the chondrocytes (Poole et al. 1992). It is believed that this matrix region may play a role in the initiation of signal transduction within cartilage (Eggli et al. 1985). Around the PCM, the territorial matrix (TM) is thicker region formed by cross-banded fine collagen fibrils organised in a basket-like network surrounding the PCM. This tight organization of fibrils confers to this region the ability to withstand mechanical stress, hence giving mechanical resistance to the chondrons. Finally, the interterritorial matrix (ITM), is situated between the chondrons. It is constituted by thick collagen fibrils, assembled in small groups alternated by lerger interfibrillar spaces. The differentiation of matrix in various compartments allows for differential distribution and diffusion of metabolites applying a tight zonal control of various cartilage pathways (Eggli et al. 1985).

1.3 Collagens

Collagen is the most abundant protein in mammals and in particular in humans account for one-third of the total protein content. Collagens represent the major component of connective tissues. Twenty-eight different types of collagen have been identified in vertebrates so far, constituted by at least 45 different polypeptide chains. Collagens provide both structural integrity and functional diversity within tissues and by interacting with specific receptors, provide signals (cellular adhesion, differentiation, growth and survival) to cells overlaying the collagen scaffold that can alter their behaviour (Mienaltowski and Birk 2014b). The generic collagen structure is formed by a triple helical assembly of α-chains. A different gene can encode each distinct α-chain and the α-chains of one collagen type are unique and differ from the α-chains of another collagen type. Collagens molecules can be homotrimeric, when their composition comprises three identical α- chains, or heterotrimeric,

comprising α-chains encoded by different genes of the same collagen type. The primary structure of α-chains contains a variable number of conserved Gly-X-Y repetitive motifs (where X and Y are often proline and 4-hydroxyproline, respectively), which permit the formation of hydrogen bonds between chains (Gordon and Hahn 2010). The formation of a triple helix is possible thanks to the presence of the glycine residue, the smallest amino acid residue, as it lacks a side chain, and allows sufficient space and flexibility to tightly pack three chains in the structure. According to their structural and functional properties, collagen molecules can be grouped into seven subfamilies:

- Fibrillar collagens are mainly present in connective tissues, they provide integrity and confer mechanical tensile strength. Collagen type I, II and III are the most abundant fibrillar collagens in vertebrates.

- Network-forming collagens, through the interruption in their triple helical structure, they are more flexible and they can associate with each other, forming networks. They can also interact with other ECM components giving rise to multi-molecular complexes. Collagen type IV is a network forming collagen present in the pericellular matrix of normal and osteoarthritic articular cartilage (Foldager et al. 2014). Another example is collagen type X, found exclusively in the hypertrophic zone of growth plate and basal calcified zone of articular cartilage (Gannon et al. 1991).

- Fibril-associated collagens with interrupted triple helices (FACIT) are characterised by the presence of non-collagenous domains that give flexibility to the molecule. FACIT closely interact with the surface of fibrillar collagens and link collagen fibres to each other and to other ECM molecules. They are also able to affect the surface properties of fibrils as well as fibril packing. Collagens type IX, XII, XIV and XX are FACIT collagens. Collagen type IX and type XII also possess covalently attached glycosaminoglycan side chains, and for this reason, they are also considered proteoglycans. Collagen type XII and XIV are expressed in musculoskeletal connective tissues, including tendons and ligaments at various times during development, and affect fibre supra-structures and tendon biomechanics (Ansorge et al. 2009b, Zhang et al. 2003). The general structure of FACIT collagens comprises short collagenous (COL) domains interrupted by non-collagenous (NC) domains with an N-terminal NC domain that protrudes from the fibril surface into the interfibrillar

space. The two C-terminal domains, NC1 and COL1, are considered to interact with other type of collagen fibrils (Mienaltowski and Birk 2014a).

- Anchoring fibrils are composed of collagen type VII that is a homotrimer flanked by a large and a small non-collagenous domains (NC1 and NC2). Collagen type VII molecules within the ECM usually dimerise in an antiparallel direction and are stabilised through disulphide bonds between the NC2 domains of the two molecules forming the dimer. Many dimers then aggregate to form the basement membranes in the stroma of ECM (Chung and Uitto 2010).
- Multiplexin collagens (types XV and XVIII), are characterised by the central triple helical collagen domain interrupted by several non-collagen regions and N- and C-terminal domains. Both are found in the basement membrane zones (Rehn and Pihlajaniemi 1994).
- Transmembrane collagens include types XIII, XVII, XXIII, and XXV. These are expressed in different cell types and act as cell surface receptors. They have a single transmembrane domain with an extracellular C-terminal domain composed by collagenous and non-collagenous parts and a cytoplasmic N-terminal domain (Mienaltowski and Birk 2014b). Of the transmembrane collagens, collagen type XIII is found in musculoskeletal tissues, particularly in myotendinous and neuromuscular junctions (Heikkinen et al. 2012, Latvanlehto et al. 2010).
- Collagen type XXVIII is expressed in peripheral nerves and has the triple helix flanked by a von Willebrand factor A (vWFA) structure at both N- and C- terminals (Gebauer et al. 2016).

1.4 Formation of Collagen Fibrils

After translation, collagen polypeptides have globular propeptide extensions at each end and a signal sequence at the N-terminal that is recognised by a signal recognition particle on the endoplasmic reticulum (ER) to target them from the ribosomes to the ER. At this level molecules are referred to as pre-procollagen (Hulmes 2008). Once in the ER, three post-translational modifications take place. First, the signal sequence is cleaved to form a propeptide. Then hydroxylases add hydroxyl groups to proline and lysine residues to allow the formation of cross-links among the α-peptides. The third modification is the attachment

of glucose or galactose to the hydroxyl groups of lysines. Then the hydroxylated and glycosylated propeptides twist and form a triple helix, now called procollagen (Khoshnoodi et al. 2006). Consequently, procollagen is delivered to the golgi apparatus for its glycosylation and then transported to the extracellular space by secretory vesicles. Once outside the cell, the two globular propeptide extensions at both ends of the collagen triple helix, are removed by specific N- and C- terminal collagen peptidases, triggering in this way fibril formation. Finally, an extracellular enzyme, named lysyl oxidase, transforms the several lysines and hydroxylysines amino groups into aldehydes that covalently crosslink each other, stabilising the collagen fibrils. The C-propeptide function is to direct the intracellular assembly of the procollagen molecule from its three constituent α-polypeptide chains. The general model proposed for fibril assembly that occurs in the extracellular space, is a concentric model that follows energy minimisation, whose result is a helicoidal organisation of collagen where molecules are leaning obliquely to the fibril surface (Hulmes et al. 1981). A tight control of fibril diameter and shape (along with heterotypic collagen interactions and interactions with other matrix components), is maintained in part by the N-propeptide, which is not immediately cleaved. Its presence functions to prevent incorporation into the centre of the fibril, thereby forcing all N-termini to the surface of the fibril, preventing further growth and limiting fibril diameter. This might provide a mechanism for diameter control for heterotypic collagen interactions such as types II/XI and IX in cartilage (Hulmes 2002). Fibrils are made by collagen molecules that are staggered with each other creating the typical repeating banding pattern. An overview or the main steps of collagen biosynthesis is shown in Fig.1.3.

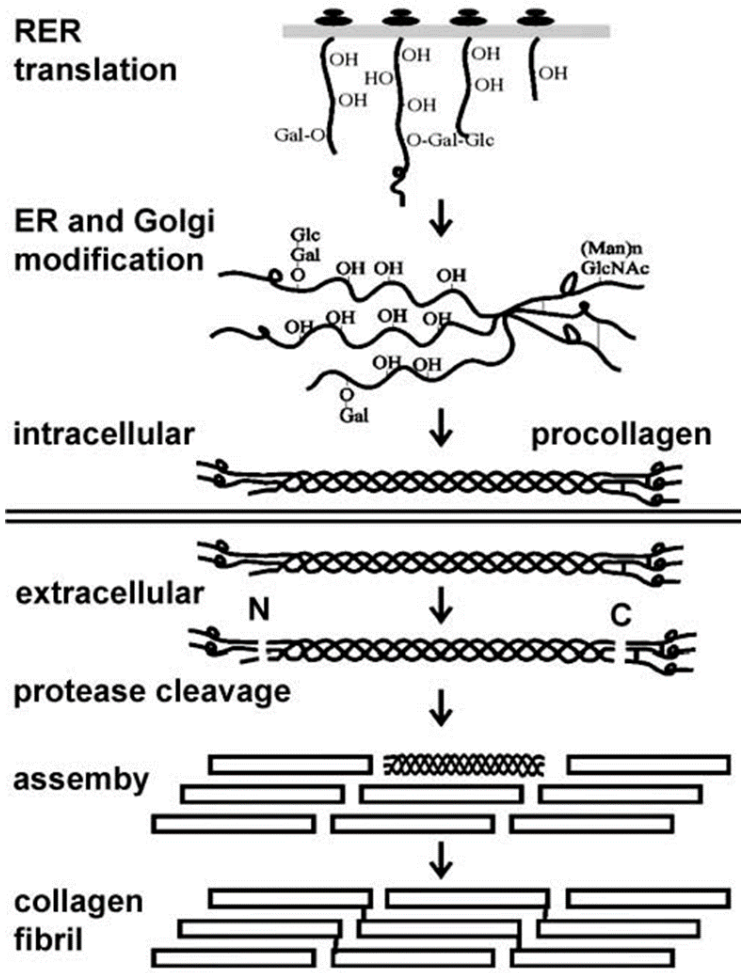

Fig. 1.3 | Overview of the steps involved in the production of collagen. After translation, procollagen chains undergo a large number of post-translational modifications (hydroxylation and glycosilation) that occur in the ER and the Golgi. At this level, the polypeptides are brought together by interactions between the C-propeptides and fold to form a rod-like triple-helical domain flanked by globular N-and C-propeptides. The removal of the N-and C-propeptides from fully folded procollagen only occurs after transport of procollagen from the Golgi stacks to the extracellur space, and results in collagen molecules that are then able to assemble into fibrils. Covalent crosslinks occur within and between triple-helical collagen molecules in fibrils. (Image source: cellbiology.med.unsw.edu.au/).

1.5 Cartilage collagens

Among the collagens specifically expressed within cartilage, we find types II, III, VI, IX, X, XI, XII and XIV. Cartilage fibrils are usually referred to as collagen type II which is the most abundant of the fibrillar framework, accounting for 90% of the total cartilage collagen. Collagen type II disorders comprise a diverse group of clinical phenotypes characterized by skeletal dysplasia, ocular manifestations, hearing impairment, and orofacial

features, whose severity ranges from perinatal severe lethal disorders to milder conditions appearing in adulthood (Gregersen and Savarirayan 1993-2019). Collagen type II provides tensile strength, is resistant to shearing forces and supports chondrocyte adhesion. However, the protein by itself is incapable of forming fibrils of the extensive lengths required in the tissues. It is instead always found as macromolecular composites, which include collagen type IX and XI (Mendler et al. 1989). Collagen type IX is a member of the FACIT family and it interacts with collagen type II and other components of cartilage ECM (for a fuller description see section 1.6 of this chapter). The biogenesis of the heterotypic collagen type II/IX/XI macromolecular structure and its functional complexity in cartilage fibrils is not fully understood. Overexpression of normal collagen type II in mice leads to a highly disorganised growth plate cartilage that contains abnormally wide fibrils with a strong banding pattern. This suggests the crucial importance of the correct molar proportions of cartilage collagens in fibrillogenesis (Garofalo et al. 1993). In addition, it is believed that collagen type XI is essential for the regulation of the lateral fibril growth (Blaschke et al. 2000). Direct evidence for this concept came from studies of *in vitro* fibrillogenesis by mixtures of soluble cartilage collagens (Eikenberry E. F. 1992). It was found that collagen type XI was essential in restricting lateral growth of collagen type II fibrils to a uniform width of about 20 nm, typical of cartilage fibrils (Blaschke et al. 2000). Collagen type II is known to interact with other ECM component to create a tight network between matrix and chondrocytes, aimed to facilitate and improve the stability of the tissue structure. Among its direct interactors there are the integrin receptor α10β1 (Camper et al. 1998), the proteoglycans fibromodulin and decorin (Hedbom and Heinegard 1993) as well as annexin V (Kim and Kirsch 2008), matrilin-1 (Winterbottom et al. 1992), matrilin-3 (Fresquet et al. 2007) and COMP (Rosenberg et al. 1998).

Collagen type III is a homotrimeric fibrillar molecule and is present in smaller amount compared to collagen type II in adult articular cartilage, where it localises onto the rest of the collagen fibril network. Its function seems to be reinforcing weakened collagen type II fibril networks in cartilage, as it is often present in sites of healing and repair (Wu et al. 2010).

Three distinct α–chains constitute the collagen type VI monomers. These monomers assemble in an antiparallel direction to form dimers, which then cross-link together to form the tetramers that make up collagen type VI microfibrils (Gelse et al. 2003). Moreover, its supramolecular assembly in antiparallel dimers and tetramers begins inside the cell. Tetramers stabilised by disulphide cross-linking then associate in the ECM to form the so

called beaded filaments. These microfibrils are localised predominantly to the pericellular matrix, bind to both decorin and biglycan (Wiberg et al. 2003) in vitro, and are proposed to integrate the cartilage fibrillar network that includes collagen type II (Budde et al. 2005). Collagen type VI disorders have a continuum spectrum of overlapping phenotypes encompassing Bethlem myopathy at the mild end and Ullrich congenital muscular dystrophy (CMD) at the severe end (Lampe et al. 1993-2020).

Collagen type X is present in the cartilage growth plate and localises in the hypertrophic zone. It is a short-chain homotrimeric $\alpha 1(X)_3$ collagen that is synthesised exclusively by hypertrophic chondrocytes during endochondral ossification. Collagen type X usually assembles into a hexagonal mesh-like network (Kwan et al. 1991), but it can also exist as a fibril-associated form in foetal cartilage (Schmid and Linsenmayer 1990). Collagen type X is a reliable marker for new bone formation in articular cartilage since it facilitates endochondral ossification through the regulation of matrix mineralisation and compartmentalisation of matrix components (Shen and Darendeliler 2005). Mutations in the *COL10A1* gene cause Schmid metaphyseal chondrodysplasia (MCDS) (OMIM # 156500). *COL10A1* pathogenic variants cause collagen type X protein misfolding which leads to aggregation within the ER of hypertrophic chondrocytes, triggering ER stress and activation of UPR, underlying the development of the MCDS (Rajpar et al. 2009).

Apart from Collagen type IX, other two members of the FACIT subfamily are expressed in cartilage, collagens type XII and XIV. Collagen type XII has been proposed to be involved in the regulation of cellular communication during bone formation (Izu et al. 2011). Conversely, collagen type XIV is known to regulate fibrillogenesis by regulating the entry of fibril intermediates into lateral fibril growth (Ansorge et al. 2009a). Finally, member of the collagen fibrillar family, collagen type XXVII localises throughout the growth plate and it is believed to play a role in the transition of cartilage into bone (Hjorten et al. 2007).

During cartilage development spatial and temporal changes occur in the expression of different types of collagens. For instance, Collagen types I and III are more abundant in the mesenchymal matrix of the developing limb bud. However, when chondrogenesis starts and mesenchymal cells condensation occurs, gene expression switches to the production of collagen types II, IX and XI (Kosher et al. 1986). In addition, as stated before, the expression of collagen type X is specific to hypertrophic chondrocytes of the growth plate. Furthermore, some types of collagens are slightly differentially expressed in different kinds of cartilage and

one example is the case of collagen type VI, which is more abundant in fibrillar cartilage, compared to elastic or hyaline cartilage (Eyre 2002). Finally, an important reduction of collagen synthesis occurs once skeletal growth is complete, and at this point production/remodelling of the fibril network is active only after injury events. Other factors that can alter the abundance and ratio of the components of the fibrillar network are the proteolytic and mechanical damages that occur during arthritis-like disorders (Bonnans et al. 2014).

1.6 Collagen type IX

Collagen type IX, a FACIT subfamily member, represents about 1% of the collagenous proteins in adult mammalian articular cartilage and 10% in foetal cartilage (Eyre 1991). Collagen type IX is found mostly in cartilage, but it also occurs in the eye (vitreum and avian cornea), ear (tectorial membrane), and intervertebral disc. It is a heterotrimeric collagen, whose structure comprises three α-helical polypeptide chains, α1(IX), α2(IX), α3(IX) encoded by three different genes, *COL9A1*, *COL9A2* and *COL9A3*, respectively. Each collagen type IX α chain comprises three collagenous domains (COL1-COL3) separated by three shorter non-collagenous domains (NC1-NC3), which add flexibility to the usually rigid collagen molecule (Olsen 1997) (Fig.1.4).

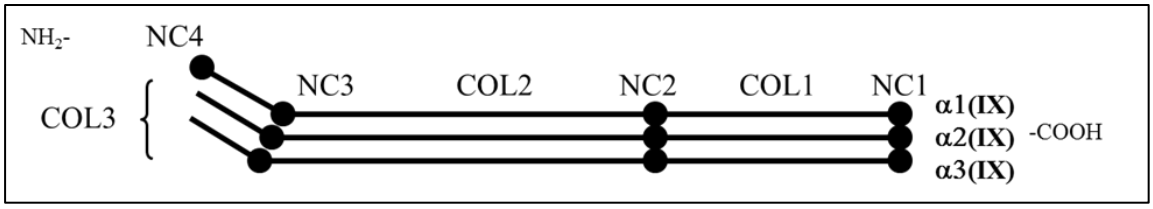

Fig. 1.4 | Schematic representation of collagen type IX structure. The molecule contains three collagenous domains, COL1, COL2 and COL3, and four non-collagenous domains, NC1-NC4 (Olsen 1997).

Two isoforms of collagen type IX are known, a short and a long form. This is due to the presence of two transcription start sites at a distance of 20 kilobases with each other in *COL9A1* which give rise to two α1(IX) variants. mRNA transcripts from the upstream site encode a large N-terminus globular NC4 domain of 266 amino acids, whereas the transcripts from the downstream site encode chains with an alternative shorter sequence, lacking the

NC4 domain. The long form is prevalently expressed in cartilage, whereas the shorter form of the mRNA transcript is mainly found in cornea and the vitreous of the eye. The incorporation of either form in the ECM is believed to contribute to the differences in the macromolecular organisation of the ECM in cartilage and cornea (Nishimura et al. 1989). It is hypothesised that the presence or absence of the amminoterminal region of the α1(IX) chain to act as discriminator for ligands, creating different ligands selection in different tissues. More specifically, it has been speculated that the amino-terminal globular domain of cartilage collagen type IX molecules interacts with the anionic glycosaminoglycan side chains of cartilage proteoglycans, providing a molecular link between collagen fibrils and proteoglycans. The absence of such a domain in the corneal form of the molecule is consistent with the absence of the large aggregating proteoglycans in cornea. The rate of transcription of each α1(IX) is not known, however it is believed that these rates depend on tissue specific transcription factors level or activity in corneal cells and chondrocytes. It is also believed that the ratio between the two transcript types may vary depending on specific physiological or pathological conditions. For example, in conditions characterized by cartilage degradation such as rheumatoid arthritis, it is possible that chondrocytes may contain higher levels of the short (corneal) form of α1(IX) collagen mRNA and that the synthesis of collagen IX molecules that lack the amino-terminal globular domain contributes to the pathological changes in the cartilage matrix (Nishimura et al. 1989). This hypothesis is supported by the observation of the presence of a sequence element in the downstream α1(IX) promoter, which is involved in regulation of the collagenase and stromelysin (a matrix metalloprotease) genes (Angel et al. 1987). Therefore, it could be speculated that the conditions that lead to an increased transcription of these genes also produce increased levels of the corneal form of α1(IX) mRNA.

As member of the FACIT subfamily, collagen type IX molecules are found periodically organised along the surface of collagen type II/ type XI fibrils, forming therefore a heterotypic structure, with the COL3 domain functioning as mobile hinge to allow the NC4 domain to project into the perifibrillar space (Eyre et al. 2004) (Fig. 1.5). The COL1 and COL2 domains are believed to maintain the correct linear distance between type II collagen molecules (Asamura et al. 2005). Additionally, a chondroitin sulphate (CS) glycosaminoglycan (GAG), is attached to a serine residue of α2(IX) NC3 domain (Huber et al. 1988). Covalent crosslinks connect collagen type IX with collagen type II molecules and studies suggested that its incorporation into the core of collagen type II/XI heterofibrils can

control the assembly, growth and diameter of the fibrils, a function fulfilled thanks to the unprocessed N-terminal non-collagenous domain of collagen type II (Gelse et al. 2003). Supporting this, chondrocytes deficient in collagen type IX exhibit fibrils with a larger diameter, indicating a role of the protein in controlling matrix assembly (Blumbach et al. 2009).

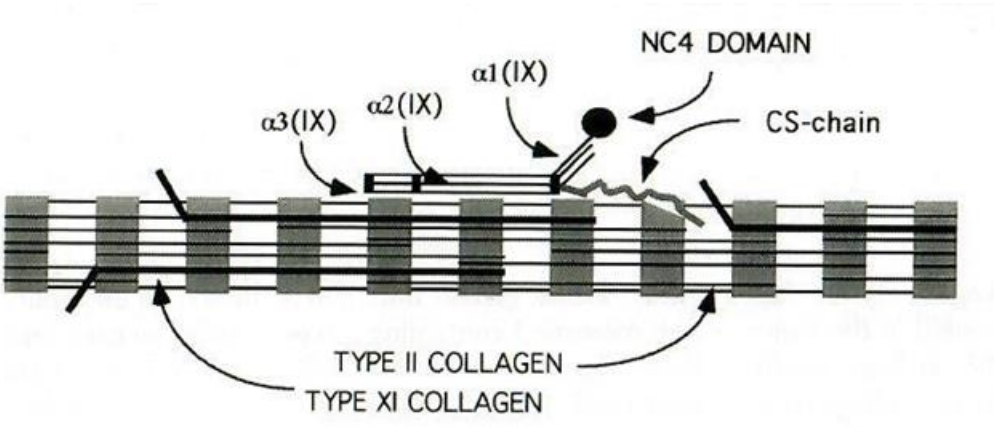

Fig. 1.5 | Supramolecular structure of collagen type IX alongside collagen type II. Collagen type IX associates via cross-links with the surface of the collagen type II and XI fibrils in an antiparallel direction. The globular NC4 domain and the triple-helical COL3 domain project out from the fibril surface whereas the CS-chain, covalently attached to a serine residue of α2-NC3 domain, faces down and inserts itself into the macromolecular structure (Muragaki et al. 1996).

Along with the collagen type II and XI interactions, studies showed that collagen type IX has the ability to bind to other non-collagenous components of the ECM such as matrilin-3 (Budde et al. 2005), COMP (Holden et al. 2001), fibronectin (Parsons et al. 2011), heparin (Pihlajamaa et al. 2004), fibromodulin (Tillgren et al. 2009), and various integrins (Sandya et al. 2007). These findings suggest collagen type IX to act as a macromolecular bridge between collagens fibrils and other matrix macromolecules (Shaw and Olsen 1991). Proteomic analysis on cartilage of collagen type IX null mice has given more insights about direct/indirect physical or genetic interaction of collagen type IX and other proteins. For example, along with higher expression of fibronectin detected in collagen type IX null mice, also the TGFβ-induced protein Tgfbi and collagen type XII were increased, while epiphycan, a small leucine-rich PG involved in fibril assembly, was reduced in abundance. These findings highlight the consequences of collagen type IX ablation which might disturb the

normal pattern of TGFβ signalling and fibril-assembly in the developing cartilage, as well as creating some sort of potential compensation through expression of another FACIT collagens (Brachvogel et al. 2013).

Mice lacking collagen type IX develop non-inflammatory degenerative joint disease with pathological changes comparable to some of those seen in human OA, suggesting the collagen type IX crucial role in maintaining the mechanical stability of articular cartilage (Fassler et al. 1994). Further details about mice carrying mutations in collagen type IX will be described in section 1.9.3 Collagen Type IX mice

1.7 Skeletal dysplasias

Skeletal dysplasias are an extremely heterogeneous and complex group of rare diseases that affect the development, organisation and homeostasis of the skeleton. Among the different mechanisms causing skeletal dysplasia, there are the alterations of ECM components or the establishment of an intracellular stress which lead as consequence to an abnormal change to chondrocyte proliferation and survival. These generalised heritable disorders of the bone and cartilage have an incidence of 1.3–3.2 per 10,000. The International Skeletal Dysplasia Society, in its latest nosology and classification of genetic skeletal disorders, identified a total number of 461 well-characterised phenotypes (Mortier et al. 2019). In this classification, these genetic disorders have been grouped according to clinical and radiological patterns along with the molecular ontology, giving rise to a total of 42 different groups caused by mutations in 437 genes identified in 425 listed disorders. Chondrodysplasias show a broad spectrum of phenotypic severity, varying from some disorders associated with mild disability, to others that are lethal at birth. Moreover, great variability is also found between chondrodysplasias belonging to the same group, and symptoms can sometimes differ between individuals carrying the same mutation. It is therefore extremely challenging to understand the causes underpinning the onset of each of these disorders and finding an adequate treatment. Moreover, the importance of studying skeletal dysplasias relies also on the fact that the knowledge gained by investigating these rare disorders can be applied to understanding more general mechanisms of cartilage degradation, such as that seen in OA. The focus of this Thesis is to further investigate multiple epiphyseal dysplasia (MED), a chondrodysplasia which shares one of the genetic

loci with pseudoachondroplasia (PSACH), and a continuum of phenotypic severity, hence belonging to the same bone dysplasia group (Table 1.1).

1.7.1 Multiple Epiphyseal Dysplasia and Pseudoachondroplasia group

Initially considered as two different entities, MED and PSACH are now classified together as a group of skeletal dysplasia comprising a continuum of clinical spectrum, from the more severe cases of PSACH to the mild forms of MED, without excluding a certain extent of phenotypic overlap between the two.

Pseudoachondroplasia is an autosomal dominant inherited condition characterised by a more severe phenotype than MED. Patients are usually diagnosed with PSACH early in life, when at the onset of walking they exhibit a waddling gait. Among the PSACH clinical findings are marked short stature and deformity of the legs, short fingers typical of brachydactyly, loose joints, ligamentous laxity and myopathy, but normal facial features, head size and intelligence (Briggs and Chapman 2002). Often the joint pain developed during childhood progresses into early onset osteoarthritis leading to joint replacement therapy early in life. Patients show small and irregular epiphyses, irregular metaphysis, and a delay in the ossification of annular epiphyses of the vertebrae upon radiographic analysis. A milder form of PSACH is recognised sharing clinical similarities with MED (Maroteaux et al. 1980).

Multiple epiphyseal dysplasia is a clinically heterogeneous ostechondrodysplasia whose incidence is about 1 in 10,000 people. The disorder is milder than PSACH, but its clinical features were initially classified into two kinds of MED, the milder Ribbing type and the more severe Fairbank type. The Ribbing type of MED comprises short stature, flat epiphyses, and consequently early-onset OA of the hips, whereas the Fairbank type is recognised because of the dwarfism, stubby fingers, and small epiphyses of several joints, including the hips (Fairbank 1947). Among the symptoms, MED patients suffer from pain and stiffness of multiple joints during childhood and adolescence and development of OA in late childhood to adulthood. In some patients only radiological evidence of MED or OA have been reported, in the absence of joints pain (Oehlmann et al. 1994) and in some forms of MED stature is not affected and patients are of normal height. However, MED associated phenotypes are extremely variable and sometimes families remain unclassified because their phenotype does not overlap with either the Ribbing or Fairbank clinical features.

Only mutations in the gene coding for the cartilage oligomeric matrix protein COMP have been reported to cause PSACH (Briggs et al. 1995). However, the genetics of MED is more complex. MED can be either dominant or recessive and is more genetically heterogeneous since mutations in several genes, the majority coding for ECM components, have been identified in patients. The autosomal dominant forms are caused by mutations in COMP (*COMP)* (EDM1; MIM# 132400), matrilin-3 (*MATN3)* (EDM5; MIM# 607078) and in the collagen type IX genes (*COL9A1* (EDM6; MIM# 120210), *COL9A2* (EDM2; MIM# 120260) and *COL9A3* (EDM3; MIM# 600969)). The recessive form of MED results from mutations in the diastrophic dysplasia sulphate transporter (*SLC26A2*) (EDM4; MIM# 226900) and rarely in mutations in *CANT1* (EDM7; MIM# 617719) coding for calcium-activated nucleotidase 1. However, an estimation of the incidence of the dominant and recessive forms is difficult, since both forms of this disorder may actually be more common and some people with mild symptoms may never be diagnosed. Nonetheless, it is estimated that mutations in *COMP* are responsible for at least half of the cases of MED, followed by *SLC26A2* mutations, which account for one-quarter depending on ethnicity. The remaining 25% of clinical cases, when classified, are due mainly to mutated *MATN3*, then to a lesser extent mutations in *COL9A1*, *COL9A2* or *COL9A3* genes (Unger et al. 2008). Nevertheless, for a great portion of MED cases, the underlying genetic cause remains still unknown.

Studies conducted on PSACH and the dominant forms of MED showed that in mice expressing the mutant forms of COMP or matrilin-3, ER stress which then affected as consequence chondrocyte proliferation and apoptosis, was detected in these mice. From these findings, arises the idea that the reduced proliferation and an increased and spatially dysregulated apoptosis, probably resulting in disrupted linear bone growth, could be considered the common disease mechanism for PSACH and dominant MED bone dysplasia family (Briggs et al. 2015). The disease mechanism of MED caused by collagen type IX mutations is still unknown and later in this thesis some of the most relevant findings leading to possible hypothesis will be discussed. When the recessive form of MED was investigated using a *Dtdst* knock-in mouse with a partial loss of function of the sulfate transporter, homozygous mutant mice were characterized by growth retardation, skeletal dysplasia and joint contractures. Along with the impaired sulfate uptake leading to a significant cartilage proteoglycan undersulfation, the reduced proliferation and/or lack of terminal chondrocyte differentiation was also hypothesised to contribute to the reduced bone growth (Forlino et al. 2005), as similarly considered for the dominant forms of MED. The mechanisms underlying the newly identified recessive form of MED caused by *CANT1* mutations is not clear.

CANT1 is localizes to the Golgi and is involved in the synthesis of glycosaminoglycans (GAG) and the posttranslational modification of proteoglycans. Nixon et al. demonstrated that fibroblasts with impaired CANT1 have reduced GAG synthesis due to the inability of CANT1 to transform UDP in UMP (Nizon et al. 2012). Based on this observation, it is hypothesised that *CANT1*-MED results from an indirect effect on normal ECM biosynthesis, due to the incorporation of many ECM proteins whose GAG posttranslational modifications may depend on wild-type CANT1 activity (Balasubramanian et al. 2017).

Table 1.1 | Multiple epiphyseal dysplasia and pseudoachondroplasia disease phenotype spectrum and related allelic disorders. Adapted from (Mortier et al. 2019). MIM No.: numerical assignment for inherited diseases, genes and functional segments of DNA, as listed in the comprehensive catalog Mendelian Inheritance in Man.

Multiple epiphyseal dysplasia and pseudoachondroplasia group				
Group/Name of Disorder	**Inheritance**	**MIM No.**	**Locus or Gene**	**Protein**
Pseudoachondroplasia (PSACH)	AD	177170	*COMP*	COMP
Multiple epiphyseal dysplasia (MED) type 1 (EDM1)	AD	132400	*COMP*	COMP
Multiple epiphyseal dysplasia (MED) type 2 (EDM2)	AD	600204	*COL9A2*	Collagen IX α-2 chain
Multiple epiphyseal dysplasia (MED) type 3 (EDM3)	AD	600969	*COL9A3*	Collagen IX α-3 chain
Multiple epiphyseal dysplasia (MED) type 5 (EDM5)	AD	607078	*MATN3*	Matrilin 3
Multiple epiphyseal dysplasia (MED) type 6 (EDM6)	AD	614135	*COL9A1*	Collagen IX α-1 chain
Stickler syndrome, recessive type	AR	614134	*COL9A1*	Collagen IX α-1 chain
Stickler syndrome, recessive type	AR	614284	*COL9A2*	Collagen IX α-2 chain
Stickler syndrome, recessive type	AR	120270	*COL9A3*	Collagen IX α-3 chain
Familial hip dysplasia (Beukes)	AD	142669	4q35	UFSP2
Multiple epiphyseal dysplasia with microcephaly and nystagmus (LowryWood)	AR	226960		
MED, autosomal recessive type 4 (rMED; EDM4)	AR	226900	*DTDST*	SLC26A2 sulfate transporter
Very rare form of MED, autosomal recessive type 7 (rMED; EDM7)	AR	617719	*CANT1*	Calcium-activated nucleotidase 1

1.7.2 Matrilin-3 in MED

Matrilin-3 is a protein encoded by *MATN3* and is a member of a family of oligomeric ECM proteins which share a similar domain structure (Deak et al. 1999). Matrilin-3 structure comprises a signal peptide, vWFA domain, four epidermal growth factor (EGF)-like domains and a coiled-coil oligomerisation domain (Belluoccio et al. 1998). Matrilin-3 is predominantly found as a homotetramer, but it can also oligomerise with matrilin-1 to form heterotetramers (Wu and Eyre 1998). While expression of matrilin-1 is exclusively cartilage specific, matrilin-3 is expressed in both cartilage and bone (Segat et al. 2000, Klatt et al. 2000), and more precisely in cartilage it is usually localised in the pericellular and interterritorial matrix of all growth plate zones (Klatt et al. 2002). Expressed during the early development of the skeleton, matrilin-3 has been proved able to interact with other important ECM components such as COMP, collagen type II and the collagenous domains of collagen type IX, sometimes in an ion dependent manner (Budde et al. 2005, Fresquet et al. 2007).

The vast majority of the mutations identified in *MATN3* and responsible for MED (EDM5) are missense variants localised in exon 2, which encodes for the vWFA domain of the protein. Only one mutation (p.Arg70His) has been identified in exon 1, which localises in the proximity of the vWFA domain and is believed to have a role in maintaining its structure and function (Maeda et al. 2005). Among those mutations of the vWFA domain, about 70% are variants affecting the β-sheet of the domain, while the remaining 30% have been identified in the α-helices of the same domain (Briggs et al. 1993-2019). *In vitro* and *in vivo* studies have suggested that these pathogenic variants are responsible for the misfolding of the vWFA domain which interferes with correct protein trafficking, eventually resulting in protein accumulation in the ER (Cotterill et al. 2005, Leighton et al. 2007, Nundlall et al. 2010, Otten et al. 2005).

Notably, a high intrafamilial MED phenotype variability results from *MATN3* mutations (Mortier et al. 2001), suggesting a contribution of other modulators to the phenotype of EDM5.

1.7.3 COMP in MED

COMP is a secreted pentameric glycoprotein of 524KDa (Hedbom et al. 1992) which is predominantly expressed in the ECM of cartilage, in tendon and skeletal muscle and bone (Di

Cesare et al. 1997, Fang et al. 2000, Maddox et al. 1997). In the epiphyseal growth plate COMP is localised in the territorial matrix of resting, proliferating and pre-hypertrophic zones. COMP is a modular protein that belongs to the thrombospondin (TSP) family and its structure is organised in a coiled-coil oligomerisation domain, four type II (EGF-like) repeats, eight type III (calmodulin-like) repeats and a large C-terminal globular domain (Newton et al. 1994). Within the ECM, COMP is able to bind to fibrillar and non fibrillar collagens and other proteins. Interactions with collagen type I, collagen type II, collagen type IX (Thur et al. 2001), fibronectin (Di Cesare et al. 2002), aggrecan (Chen et al. 2007), matrilins and integrins are reported (Fresquet et al. 2008, Mann et al. 2004, Chen et al. 2005). Moreover, Posey et al. proposed a role of COMP in regulation of collagen fibre diameter during their assembly (Posey et al. 2008a). Mutations in COMP cause PSACH and MED (EDM1). Around 85% of PSACH and MED mutations are localised in the T3 repeats, whereas the remaining 15% have been reported in the C-terminal domain of COMP (Suleman et al. 2012). PSACH-causing mutation are often missense, in-frame insertions/deletions mutations and have a dominant negative effect. Studies have shown that consequences of this dominant negative effect are identified into retention of mutant COMP into the rRER along with other ECM proteins (Hecht et al. 2005), leading to an ER overload response or alternatively into a partial secretion of mutant forms of COMP with potential ECM stability implications, while complete knock-out of COMP has no effect. The most common described is the in-frame deletion of an aspartic acid residue (p.D469del) from the seventh T3 repeat ($T3_7$), which accounts for approximately 30% of all PSACH (Suleman et al. 2012).
MED-causing mutations in COMP are responsible for the most severe and also most prevalent form of MED (Unger et al. 2008). Also for MED, COMP mutations are missense, insertions or deletions and they have been identified in exons coding for the T3 repeats and the C-terminal globular domain, despite the majority of deletions and insertions cause predominantly PSACH rather than MED.

There seem to be a correlation between the site of mutations and severity of the phenotype leading to MED or PSACH. It has been reported that missense mutations in the residues of $T3_4$ and $T3_5$ are more likely to result in MED, while mutations in $T3_6$–$T3_8$ will result in PSACH. In addition, it has been demonstrated that in position 473 of COMP, deletion or duplication of one or more aspartic acid residues result in either PSACH or MED (Briggs et al. 2014).

1.7.4 Collagen type IX in MED

Among the different types of MED, those caused by mutations in the collagen type IX genes (EDM2, EDM3, EDM6) are relatively benign. The typical features of COL9-MED patients are pain and stiffness mainly in the knee joints, symptoms which tend to appear late in patients' life. The phenotype consists of epiphyseal dysplasia mainly of the knee but also of other joints are reported in childhood, with osteochondritis dissecans and osteoarthritis of the knee joints in adulthood (Lohiniva et al. 2000). Stature is generally not affected. Notably, no effect on sight or hearing is reported in COL9-MED patients, differently from another disorder caused by collagen type IX mutations, Stickler syndrome, which will be described in section 1.8.

Surprisingly, all but one mutation reported thus far (Table 1.2) cause splicing defects consistently affecting the same region of the collagen type IX protein; the COL3 domain (Fig. 1.5). In *COL9A2* and *COL9A3* the COL3 domain is encoded by exons 2 to 10, and by exons 8 to 16 in *COL9A1*. The mutations reported in *COL9A2* and *COL9A3* affect only the splice acceptor sites in intron 2, splice donor sites in intron 3 and 5′ and 3′ regions of exon 3 (Bonnemann et al. 2000, Holden et al. 1999, Lohiniva et al. 2000, Muragaki et al. 1996, Nakashima et al. 2005, Paassilta et al. 1999, Spayde et al. 2000, van Mourik et al. 1998b). When assessed, these mutations cause the skipping of exon 3 during splicing, leading to an in-frame deletion of 12 amino acids residues within the COL3 domain. An insertion mutation has been reported in exon 8 of *COL9A1* gene in MED patients, leading to a complex splice pattern involving mainly exons 8 and 10 and causing the deletion of an equivalent region of the COL3 domain of collagen type IX. (Czarny-Ratajczak et al. 2001). Of all the MED forms described, the least is known about the disease mechanism in the collagen type IX variants. During collagen fibril formation, collagen α chains are associated through the C-terminal ends of the peptides, followed by triple helix formation that progresses towards the N-terminus (Engel and Prockop 1991). It is therefore questionable, considering the position of the COL3 domain in the whole protein, whether the 12 amino acid deletion is likely to prevent the synthesis or assembly of collagen type IX molecules, as suggested by evidence of enlargement of ER reported in some patients (Bonnemann et al. 2000). Alternatively, the mutations might interfere with the interactions between collagen type IX and other matrix collagens, such as collagen type II fibrils. However, in an electron microscopy examination of articular cartilage of MED patients with a *COL9A2* splicing mutation, no differences were observed in MED cartilage compared to control biopsies, presenting normal collagen fibril

appearance and a lack of inclusion bodies (van Mourik et al. 1998a, Muragaki et al. 1996). Despite this, the deletion is likely to affect the structure and the putative function of the COL3 and NC4 domain in mediating the interactions between the fibrils and other matrix components (Douglas et al. 1998, Nakata et al. 1993). Evidence of this was reported in a study concerning the characterisation of recombinant matrilin-3, a heterotrimeric protein important component of cartilage ECM. In the study, matrilin-3 A-domain was shown to bind to the COL3 domain of collagen type IX, but this binding was abolished by the in-frame deletion of the 12 amino acids from the COL3 domain of the α3(IX) chain (Fresquet et al. 2007). However, it is entirely possible that type IX collagen has a matrilin-3 binding site that involves all three α-chains, which could explain the reason why all collagen IX mutations characterised thus far result in an identical deletion in the COL3 domain, which is likely to play an important role in the pathogenesis of MED.

1.7.5 EDM3 Clinical cases

COL9A3 was proposed as a new and third locus for MED when in 1999, in a family diagnosed with a history of MED where no linkage was found with *COMP, COL9A1, or COL9A2*, the genes at the time known to be MED associated. The clinical spectrum presented by this family involved mainly knee joint problems with some individuals also presenting limited extension of the hip, but with an overall normal stature. When mutation analysis was performed, researchers found an A→T transversion in the acceptor splice site of intron 2 (A^{-2}IVS2→T) of *COL9A3*. As a consequence of this mutation exon 3 of *COL9A3* was skipped and an in-frame deletion of 12 amino acid residues in the COL3 domain of the α3 (IX) chain was proposed to be generated (Paassilta et al. 1999). This case was similar to the MED mutations reported previously in *COL9A2* (Muragaki et al. 1996, Spayde et al. 2000, van Mourik et al. 1998b).

The following year Bönnemann et al. described another family diagnosed with autosomal dominant MED, whose symptoms were predominantly localised at the knee joints along with a mild proximal myopathy. Genetic analysis indicated *COL9A3* as the locus where a splice acceptor mutation in intron 2 occurred due to a G →A transition (G^{-1}IVS2→A). Similarly to the previously reported case, this mutation resulted in an mRNA also lacking exon 3 and the corresponding encoded 12 amino acids. When studies were performed on patient epiphyseal cartilage biopsies, a dilated rER was observed, indicating abnormal processing of mutant

protein (Bonnemann et al. 2000). Interestingly, in an independent study, muscle weakness was also reported in the proband of a MED family with the same G^{-1}IVS2→A mutation (Lohiniva et al. 2000).

Nakashima et al. then identified a novel *COL9A3* mutation in 2005 in a family suffering from mild dysplasia of the hip, knee and ankle. The patients' stature was normal, and the OA phenotype of the knee was similar to idiopathic OA of age-matched individuals. Mutation analysis reported a G^{+5}IVS3→A mutation in the splice donor site of intron 3 of *COL9A3*. RNA analysis confirmed the in-frame deletion of exon 3 as result of this mutation, representing the first evidence of a splice donor mutation having the same effect of the previously reported acceptor site mutations (Nakashima et al. 2005).

It is intriguing how all these mutations cause the same molecular mechanism of skipping of exon 3, which then conveys a certain variability in the skeletal phenotype for the different patients, suggesting a more complex mechanism underlying the disease onset, and/or a role for genetic modifiers.

Interestingly, the only reported exception was a novel mutation in exon 2 of *COL9A3* that was detected in 2014 in a Korean family diagnosed with MED. The clinical findings involved epiphyseal changes predominantly affecting the knee joints, and only mildly other joints such as ankle, foot and wrist. Differing from the splicing mutations around exon 3, this mutation was a c.104G>A substitution in exon 2 of *COL9A3*. This missense mutation resulted in a substitution of Gly to Asp (p.Gly35Asp) in the "G-X-Y" consecutive sequence of the COL3 domain in the α3(IX) polypeptide. So, although this mutation was not involving aberrant splicing, the change in the amino acid sequence once again affected the COL3 domain. Researchers conducted molecular dynamic simulation to analyse the energy state and physical movement of the mutant α3(IX) polypeptide. They found that this amino acid substitution generated self-aggregation of the polypeptide strand which severely affected its interaction with the other strands in the formation of collagen type IX heterotrimer (Jeong et al. 2014).

Looking at the spectrum of COL9-MED mutations reported to date, a common characteristic is mutation affecting the COL3 domain, in α1(IX), α2(IX), α3(IX) (Fig. 1.6). Taken together these observations highlight the importance of COL3 domain in MED pathogenesis.

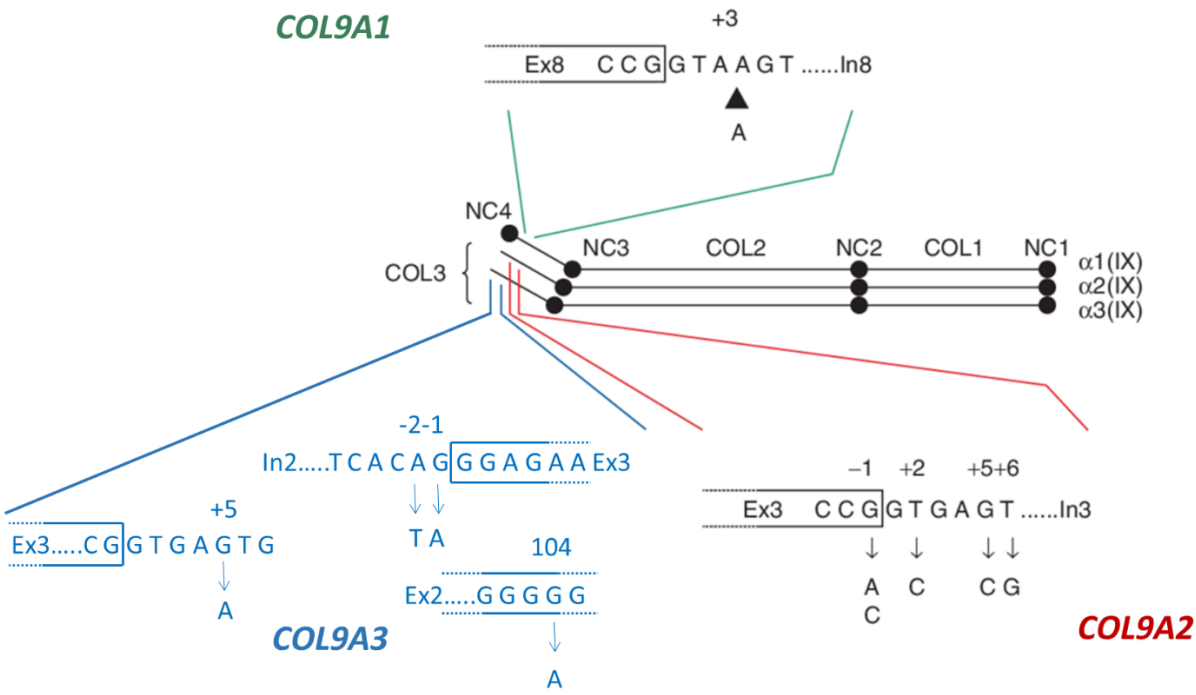

Fig. 1.6 | Collagen type IX MED mutations. Schematic representation of Collagen type IX molecule and the MED mutations reported to date in *COL9A1*, *COL9A2* and *COL9A3* genes. NC=non-collagenous domain; COL=collagenous domain; Ex=exon; In=intron. Adapted from (Briggs et al. 2017)

Table 1.2 | Collagen type IX gene mutations that result in phenotypes within the Multiple Epiphyseal Dysplasia disease spectrum. Integrated from (Briggs and Chapman 2002).

Gene location	Nucleotide change	Predicted protein change	Remarks	Reference
COL9A1 IVS8 as +3	ins A	Skipping of exons 8 or 10 or 8 and 10 and the in-frame deletion of either 25, 21 or 46 aa from the COL3 domain	Complex mRNA splicing pattern	(Czarny-Ratajczak et al. 2001)
COL9A2 IVS3 ds +2	T>C	Skipping of exon 3 and the in-frame deletion of 12 aa from COL3 domain	Normal appearance of rER	(Muragaki et al. 1996, van Mourik et al. 1998)
COL9A2 IVS3 ds +5	G>C	Skipping of exon 3 and the in-frame deletion of 12 aa from COL3 domain		(Holden et al. 1999)
COL9A2 IVS3 ds –1	G>A	Skipping of exon 3 and the in-frame deletion of 12 aa from COL3 domain	Decreased stability of mRNA from	(Holden et al. 1999)
COL9A2 IVS3 ds +6	T>G	Skipping of exon 3 and the in-frame deletion of 12 aa from COL3 domain	Decreased stability of mRNA from mutant allele	(Spayde et al. 2000)
COL9A3 IVS2 as –1	G>A	Skipping of exon 3 and the in-frame deletion of 12 aa from COL3 domain	Dilated rER	(Bonnemann et al. 2000, Lohiniva et al. 2000)
COL9A3 IVS2 as –2	A>T	Skipping of exon 3 and the in-frame deletion of 12 aa from COL3 domain		(Paassilta et al. 1999)
COL9A3 IVS3 +5	G>A	Potential skipping of exon 3 and the in-frame deletion of 12 aa from COL3 domain		(Nakashima et al. 2005)
COL9A3 104	G>A	p.Gly35Asp in the third position of the "Pro-Pro-Gly" consecutive sequence of the COL3 domain	self-aggregation of the α3 strand	(Jeong et al. 2014)

1.8 Other collagen type IX disorders

Mutation in collagen type IX have also been associated with other skeletal disorders such as Stickler syndrome recessive type, lumbar disc disease and progressive hearing loss.

1.8.1 Stickler syndrome recessive type

Stickler syndrome was first described in 1965 as a heterogeneous disorder affecting connective tissue (Stickler et al. 1965). Inter and intra familial variability is known in terms of clinical spectrum, hence requiring a combination of clinical and genetic analysis during diagnosis. Among the characteristic features are reported hearing losses, problems in the palate and facial development, and myopia with occasional retinal detachment. In addition, patients sometimes develop hypermobility of the joints and early-onset OA (Hanson-Kahn et al. 2018). Autosomal dominant and recessive forms of Stickler syndrome have been reported, in most cases caused by mutations in genes coding for cartilage expressed collagens. Heterozygous mutations in *COL2A1,* account for the 80–90% of dominant Stickler syndrome cases (Liberfarb et al. 2003). Other dominant cases are due to mutations in *COL11A1* (Majava et al. 2007) or *COL11A2,* causing a form of Stickler syndrome, which does not involve eye defects (Pihlajamaa et al. 1998). Fewer cases of the autosomal recessive form of Stickler syndrome have been described, and the vast majority involved homozygous variants in the collagen type IX genes *COL9A1, COL9A2,* and *COL9A3*. Ten families have been reported with homozygous loss-of-function variants in the collagen type IX genes either due to insertion of premature stop codons leading to nonsense-mediated decay or removal of the N-terminal regions of the collagen alpha chains necessary for chain association (Baker et al. 2011, Nikopoulos et al. 2011, Faletra et al. 2014, Hanson-Kahn et al. 2018, Van Camp et al. 2006, Nixon et al. 2019). The clinical spectrum does not seem to differ between variants in *COL9A1, COL9A2,* and *COL9A3* and mainly comprises high myopia and hypoplastic vitreous, whereas the facial flattening is not as pronounced and none of the cases presented with palate abnormalities. Joint dysplasia was also often reported, characterised by hypermobility, mild spondyloepiphyseal dysplasia and precocious osteoarthritis and was expected considering the importance of collagen type IX in articular cartilage. Although it is surprising how patients with homozygous variations in genes for collagen type IX did not show a more severe joint involvement compared to patients carrying other recessive or dominant variants in other Stickler syndrome associated genes. Such discrepancies could be due to the different modifications of collagen type IX in different tissues. As mention before,

the α1 chain of collagen type IX in cartilage has a large amino-terminal globular domain, whereas in vitreous the α1 chain is much shorter and the α2 chain has a very large chondroitin sulphate chain attached (Nixon et al. 2019). These differences may be the reason for the different penetrance of joint problems versus eye problems, possibly due to some sort of redundancy mechanism which takes place in cartilage but not in the vitreous. Compared to the dominant form of Stickler syndrome, sensorineural hearing loss was more consistent in collagen type IX mutation containing patients. This hearing loss appears to be congenital, suggesting that loss-of function mutations might have affected ear development.

Two other non-collagen genes have also been reported in association to a Stickler syndrome phenotype: *LRP2,* coding for the lipoprotein receptor-related protein-2 or megalin, an endocytic receptor which mediates the endocytic uptake of diverse circulating compounds, and when mutated causes many major malformations such as craniofacial features, developmental delay, intellectual disability, ocular findings, low molecular weight proteinuria, and sensorineural hearing loss (Schrauwen et al. 2014); and *LOXL3*, coding for the collagen type II cross-linker enzyme lysyl-oxidase-like 3, plays a role in the formation of crosslinks in collagens and elastin, and when deficient is expected to result in collagen defect (Chan et al. 2019).

1.8.2 Non syndromic hearing impairment

Mutation screening for *COL9A3* in non-syndromic sensorineural deafness patients and healthy controls has also been reported (Asamura et al. 2005). One identified mutation, which appeared recessive, was a homozygous inframe deletion of nine nucleotides at position 541–549 in exon 11, removing a Gly–Pro–Hypro triplet in the 5′-end of the collagen type IX COL2 domain. A second mutation appeared dominant and was a missense mutation, D617E (1851 C > A) in exon 31, which locates in the COL1 domain of the protein. Both mutations were considered good candidates for the pathogenesis of hearing loss since they were not detected in healthy patients or SNP databases and involve highly conserved amino acid residues. The hypothesis is that the mutated COL1 and COL2 domains affect the assembly and stability of the collagen type IX three-dimensional structure resulting in modifications of the integrity of collagen fibres in the tectorial membrane of the inner ear.

1.8.3 Intervertebral disc disease (DD)

Intervertebral disc disease (DD) (OMIM #603932) is the major cause of low back pain and it is defined as a degeneration of intervertebral discs with subsequent remodelling of the closely attached vertebrae which starts early in life. The degenerative phenotype is believed to be caused by the concurrence of genetic and environmental factors, rendering the disease a complex condition to treat (Feng et al. 2016). Recent epidemiological studies have highlighted genetic inheritance as driving factor for the development of this condition. It is still unknown whether the phenotype is due to the strong impact of a specific gene or multiple genes that contribute in a synergistic way to the pathogenesis, however it is more likely to be a polygene and multifactorial disease. The genes that have been associated to DD are *COL1A1* (Pluijm et al. 2004), *COL11A2* (Solovieva et al. 2006), *IL1B or A* (Solovieva et al. 2004), *ACAN* (Kawaguchi et al. 1999), *VDR* (vitamin D receptor) (Kawaguchi et al. 2002), *MMP3* (Takahashi et al. 2001), and *CILP* (cartilage intermediate-layer protein) (Seki et al. 2005). Polymorphisms in the collagen type IX genes, *COL9A2* and *COL9A3* have been identified as risk factors for lumbar DD. In a screen conducted in a Finnish population with intervertebral DD, a sequence variation, known as the Trp2 allele, in *COL9A2*, caused a glutamine to tryptophan substitution into the protein (Annunen et al. 1999). Subsequently, in another study performed on Finnish families, researchers found that the degree of vertebral disc degeneration was higher in those individuals carrying the Trp2 variant. A similar polymorphism in the *COL9A3* gene, causing a substitution of arginine to tryptophan (Trp3 allele) was described by Passilta et al. In their analysis, they found that in individuals carrying at least one Trp3 allele, the risk of lumbar disc degeneration was 3-fold increased (Paassilta et al. 2001). However such results were not confirmed in studies carried on other ethnic group populations (Seki et al. 2006, Kales et al. 2004), suggesting a variation of the genetic risk factors for DD according to ethnicity. Therefore, further investigation and in multiple ethnic groups are needed to understand the association of the Trp alleles with DD (Wu et al. 2018). Early changes during spine development have been reported in collagen type IX null mice. These alterations seemed to develop into disc degeneration defects later in these animal lives (Kamper et al. 2016).

1.9 Mouse models for the study of PSACH and MED

Mutation analysis performed on patients has shown that PSACH and the more severe cases of MED were caused by mutations in the same gene *COMP*. However, MED as mentioned before, is genetically heterogeneous, therefore also caused by dominant mutations in other genes coding for matrilin-3 and collagen type IX and recessive mutations in *SLC26A2* and *CANT1* genes.

Having identified the causative genes for these disorders, discovering the mechanism responsible for their pathogenesis turned out to be a more difficult challenge, especially when considering the low availability of patient tissue that could be studied. Though model systems that completely reproduce the human PSACH or MED phenotypes are not available, the generation of knock-in mice and some tissue culture models have provided important insights about these disease mechanisms. There are many limitations in using cell models for these diseases, such as the limited amount of patient chondrocyte materials usually available when the severe clinical phenotype requires joint replacement (Zhang et al. 2009). Moreover, the maintenance of a chondrocyte-like phenotype in monolayer cultures has been also an issue, as primary chondrocytes dedifferentiate in serial monolayer with respect to their morphological and biosynthetic phenotype, by changing from a round to a flattened fibroblast-like shape and secreting collagen type I instead of the cartilage-specific collagen type II (Zaucke et al. 2001). Even when 3D cultures are established, despite overcoming this problem, the matrix produced by chondrons does not completely mimic the ECM 3D organization usually found *in vivo*, but gradients and defects can occur in material properties, affecting proteins deposition and diffusion which will impact on chondrocytes behaviour (Tibbitt and Anseth 2009). In addition, there is also the fact that results obtained from cultured chondrocytes are cross-sectional, missing therefore information about how the disease progresses along human development (Posey et al. 2008b). Hence, the utility of mouse models to recapitulate human diseases have come into fruition. They represent a valuable source of material for different kinds of experiments and are a system that can be monitored and analysed throughout development. An important aspect to be taken into account when trying to reproduce this kind of skeletal disorders with mouse models is the correct correlation between human and mouse. Despite sharing similar bone biology, when comparing the human and mouse skeletal phenotype, some of the differences between the two systems might make extrapolation of meaning of results hazardous. We need to consider for example the different time frames in

which skeletal development occurs in the two systems. In most mouse strains, the peak bone mass is reached at the age of 4-6 months, so unlike humans, bone acquisition and longitudinal bone growth continue in mice after sexual maturity, which occurs at 6–8 weeks of age (Jilka 2013). Thus, from this derives our choice of specific time points when we evaluated the bone phenotype of our mutant mice, which will be described in detail into the results section of this thesis. Moreover, the difference of posture and patterns of mechanical loading constitutes another difference to be considered, with humans being bipedal, the impact on the skeletal elements will be different from mice. Both transgenic and knock-in approaches have been undertaken in the study of the PSACH-MED disease spectrum and some of them will be outlined in this thesis. The phenotype investigated through these mouse models has highlighted important aspects of the disease mechanism involving endoplasmic reticulum (ER) stress and chondrocyte proliferation, which contribute to the dysplastic skeletal phenotype.

1.9.1 Matrilin-3 mice

Transgenic knockout mice for matrilin-3 have been generated to better understand the role of the protein during skeletal development and in the pathogenesis of MED. When Ko et al. generated a knockout mouse line for matrilin-3, null mice were viable, of normal height, and without obvious abnormalities in the skeletal phenotype. Histology and ultrastructural analyses showed no defects in endochondral bone formation and intervertebral disc development. A compensatory effect of structurally and functionally related proteins was suspected to account for the absence of an obvious phenotype. However, expression analysis did not show compensatory upregulation of other members of the matrilin family. These findings suggested that the skeletal phenotype reported in MED disorders due to mutations in the *MATN3* gene, are more likely caused by the presence of a mutated protein rather than its absence (Ko et al. 2004). Likewise, a double knockout mouse for matrilin-1 and matrilin-3 (*Matn1/Matn3*) was found with similar normal features. The growth plate was of normal height and no change was noticed in any of its zones. The only variation noticed, was detected at the age of 7 days, when in double-deficient mice the collagen fibrils of the interterritorial matrix were larger in diameter and more densely packed, giving the matrix an overall increased density (Nicolae et al. 2007). To the contrary, in a *Matn3* null mouse independently generated by van der Weyden et al., researchers identified prenatal changes in the growth plate, with a larger hypertrophic zone and reduced chondrocyte proliferation, both

evidence of premature maturation of chondrocytes. These alterations recovered at the time of mouse birth and during postnatal development, thus confirming the lack of phenotype shown in the previous studies. Nonetheless, these mice were reported with increased bone mass density and to be more prone to develop OA (van der Weyden et al. 2006).

To generate a murine model of MED, Leighton et al. knocked-in the equivalent of an MED mutation into the mouse *Matn3* gene, substituting a valine with an aspartate (p.Val194Asp) mutation in the A-domain of matrilin-3. Homozygous mice reproduced the human phenotype, by developing progressive dysplasia and short-limbed dwarfism. The retention of the mutant protein in the ER was indicated by the observation of enlarged cisternae of ER within the chondrocytes, this triggered a cellular stress as indicated by upregulation of chaperones for the unfolded protein response (UPR). Moreover, the organisation of chondrocytes into chondrons was disrupted, along with reduced proliferation and spatially dysregulated apoptosis in the cartilage growth plate, all of which might have influenced linear bone growth and resulted in the short-limbed dwarfism phenotype presented by the mutant mice (Leighton et al. 2007).

1.9.2 COMP mice

Similarly to matrilin-3 deficient mice, knockout mice for COMP did not show skeletal abnormalities and did not reproduce any of the clinical features of PSACH and MED patients. The histological evaluation revealed a normal growth plate and no dwarfism or short limb phenotype, indicating endochondral ossification similar to WT animals. In addition, no evidence of OA was detected in COMP null mice up to the age of 14 months. Normal cell morphology and collagen fibrillary network in the ECM were confirmed by ultrastructural analysis of growth plate cartilage, articular cartilage, and Achilles tendons. The same hypothesis of possible compensation mechanisms expressed by functionally related proteins was not confirmed by expression analysis, with no variation in the protein levels of other components of the thrombospondin family (Svensson et al. 2002).

With the purpose to study the role of *COMP* mutations in the pathogenesis of PSACH, transgenic mouse models overexpressing mutated COMP were generated. This mutation was an in-frame deletion of 3 nucleotides which resulted in a deletion of a single aspartate at position 469 in the protein (D469del) and is known to cause a severe form of PSACH (Deere et al. 1998). The model generated by Schmitz et al. showed disease features similar to

PSACH patients, such as growth retardation in male mice, a disorganised growth plate with less densely packed fibrils and increased rate of cell apoptosis, and altered extracellular localisation of the mutant COMP in the growth plate. Evidence of enlarged ER cisternae suggested probable mutant protein retention. Other features not directly related to PSACH were observed, such as sternal malformations and the complete fusion of certain segments of the sternum (Schmitz et al. 2008). In the transgenic model for PSACH generated by Posey et al. expression of human mutant COMP with the same D469del mutation was induced, with the model reproducing the findings of human PSACH growth plate morphology, including a disruption of growth plate organisation, chondrocyte retention of mutant COMP as well as retention of matrilin -3 and collagen type IX. These have shown to be able to assemble with pro-collagen type II to form an intracellular matrix within the rER cisternae where they are retained, as previously reported for other PSACH causing COMP mutations (Merritt et al. 2007). Increased chondrocyte apoptosis in mutant growth plates was also shown by immunohistochemistry (Posey et al. 2009). The results obtained through these models demonstrated that the PSACH phenotype is caused by the generation, retention and partial secretion of the mutant COMP protein, rather than by its absence.

Using a knock-in approach, the D469del mutation was directly introduced into the mouse genome. COMP mutant mice did not display an obvious phenotype at birth, but in the post-natal period they developed short limb dwarfism. In this mouse model, disorganisation and reduced number of columns of chondrocytes in the growth plate and retention of the mutant COMP into the ER were confirmed. Chondrocyte proliferation was reduced, and cell death was increased and spatially dysregulated. Interestingly, no UPR response was found as the cause of the alterations described. Instead expression changes of genes involved in oxidative stress, cell cycle regulation, and apoptosis were observed, suggesting that a mechanism of chondrocyte stress might be at the base of the pathology induced by a mutant COMP (Suleman et al. 2012).

A model for a mild form of PSACH was generated by introducing p.Thr583Met mutation in the C-terminal globular domain (CTD) of COMP (Pirog-Garcia et al. 2007). In these mice mutant COMP was secreted into the ECM, and therefore no protein retention was occurring in the ER. However, a UPR was detected in combination with increased and spatially dysregulated apoptosis. Localisation of COMP, matrilin-3 and collagen type IX were also altered. At 9 weeks of age homozygous mice presented with shorter tibiae and hip dysplasia, and later in life developed articular cartilage degeneration, consistent with OA reported in

patients. Further phenotypic analysis pointed out that homozygous mice show mild myopathy equivalent to PSACH and MED patients. Finally, tendons of mutant mice were lax and weak with thicker fibrils, reproducing patients' joint laxity (Pirog et al. 2010).

1.9.3 Collagen Type IX mice

Several studies have investigated the role of collagen type IX in cartilage, and to do so transgenic mice harbouring different mutations have been generated. Fässler et al generated the first mutant mouse for a collagen type IX gene in 1994. To test the role of collagen type IX in the interaction with other fibrils and components of the ECM, using gene targeting in ES cells, they generated a mouse lacking both isoforms of α1 of collagen type IX (Fassler et al. 1994). Homozygous mice, despite lacking *Col9a1* RNA and protein, were viable and did not show an obvious skeletal phenotype or shorter stature at birth and early in life. Nonetheless, evidence of development of degenerative joint disease predominantly localised at the knee of 4-months old homozygous mice were reported to be similar to the human OA. A few years later was demonstrated that the lack of type IX collagen in Col9a1$^{-/-}$ mice results in age-dependent OA-like changes in the knee joints and temporomandibular joint (TMJ) (Hu et al. 2006). In 1997, Hagg et al. demonstrated that mice lacking the α1 chain, were a functional knockout of collagen type IX protein, although expression of the *Col9a2* and *Col9a3* genes, coding for the other two helices, was unaffected when rib cartilage was analysed (Hagg et al. 1997). The use of the *Col9a1*$^{-/-}$ mice allowed the investigation of stability and integration of other structural components within the ECM of cartilage when collagen type IX protein is missing, such as matrilin-3 and COMP proteins. Cartilage integrity was disrupted in collagen type IX deficient mice as shown by loss of matrilin-3 and COMP integration in the cartilage primordium of vertebral bodies and ribs of new-born *Col9a1*$^{-/-}$ mice . In fact matrilin-3 is known to interact directly with collagen type IX, or by means of COMP as adapter (Budde et al. 2005), and COMP has been shown to bind directly to Matrilin-3 and collagen type IX (Holden et al. 2001, Mann et al. 2004, Thur et al. 2001). In a study on adult *Col9a1* null mice, the absence of collagen type IX affected bone fracture healing as maturation of cartilage matrix was delayed and cartilage abundance reduced at the level of the healing callus (Opolka et al. 2007).

Collagen type IX has been also associated with the pathogenesis of osteoporosis. This derives from the observation of thoracic kyphosis and weight loss, resembling the clinical signs of

osteoporosis in aged *Col9a1*$^{+/-}$ mice. In addition, ageing leads to progressive loss of trabecular bone and bone deterioration in male and female heterozygous mice (Wang et al. 2008). In *Col9a1* null mice the growth of cartilage was profoundly affected. At birth, and in the early stages of post-natal development, mutant mice show broadened tibial condyles and shorter long bones. Large hypocellular central regions with consequently altered proteoglycan content were found in the tibia epiphysis (Blumbach et al. 2008, Dreier et al. 2008). Growth plate organisation was severely compromised: proliferative cells appeared rounded and lost their typical columnar distribution, whereas hypertrophic cells were enlarged, more loosely packed, and surrounded by more ECM. Moreover, the separation between proliferative and hypertrophic cells was no longer clear (Fig. 1.7). A reduction of proliferation rate was also reported. However, these alterations tended to ameliorate during adulthood. Remarkably, staining for collagen binding integrin, showed that β1-integrin levels in *Col9a1*$^{-/-}$ proliferative zones were strongly reduced, in particular in the proximity to the described hypocellular region. Whether the reduction in β1-integrin is a direct consequence of collagen type IX absence or due to other compromised cell vitality mechanisms remains unresolved. (Dreier et al. 2008). It is worth noting that *Col9a1*$^{-/-}$ mice develop progressive hearing loss. This finding is consistent with collagen type IX being expressed in the inner ear, hence its absence affects the structural integrity of the tectorial membrane in the cochlea (Asamura et al. 2005, Suzuki et al. 2005).

The absence of collagen type IX also severely affects the integrity of the cartilage of the intervertebral discs. At early stages of post-natal development, *Col9a1*$^{-/-}$ animals showed cellular disorganisation in the vertebral end plate, smaller nucleus pulposus and disturbed distribution of other matrix proteins. The change in matrix composition led to reduced tissue stiffness and a delay in the development of the vertebral body. (Kamper et al. 2016, Kimura et al. 1996)

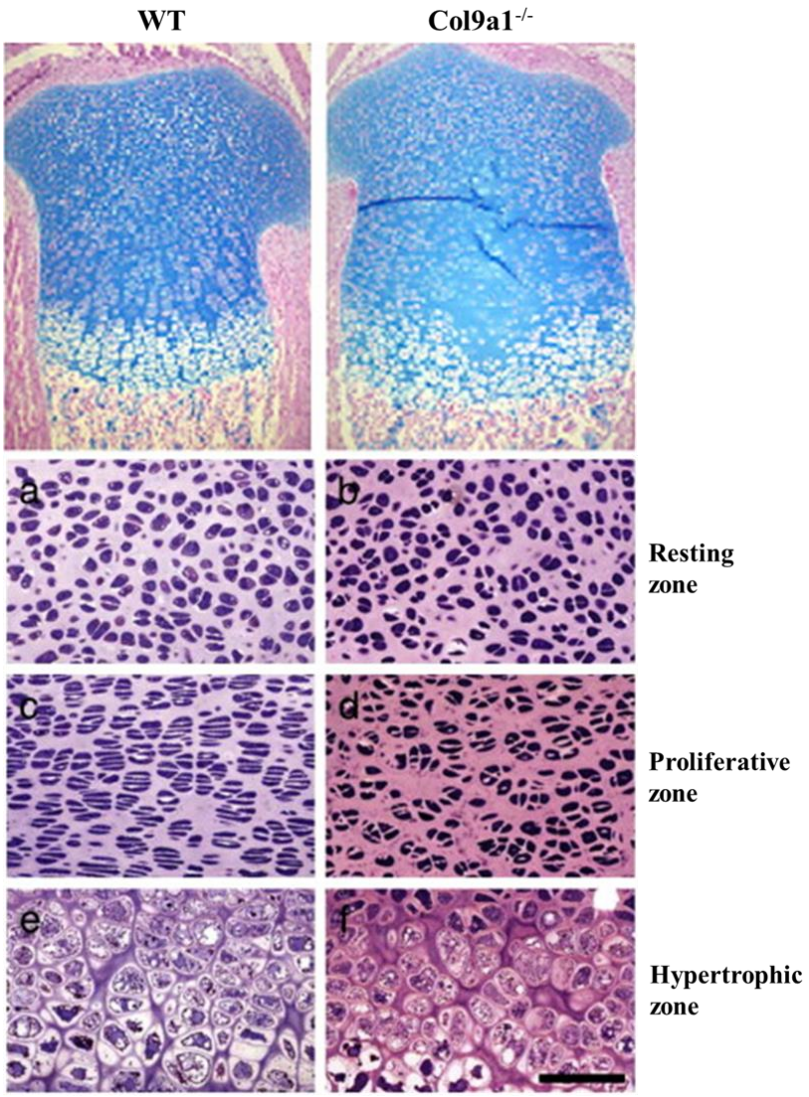

Fig. 1.7 | Cartilage growth plate defects in *Col9a1*$^{-/-}$ mice. Areas of hypocellularity and chondrocytes with altered morphology and spatial organization in *Col9a1*$^{-/-}$ mice. Adapted from (Blumbach et al. 2008, Dreier et al. 2008)

Transgenic mouse models have also been generated to better understand the role of collagen type IX in cartilage. A cDNA construct designed to create an in-frame deletion of parts of the COL2 and COL3 domains and the whole of the NC3 domain in the central part of cDNA encoding the αl (IX) chain, was injected into mice. Cartilage expression specificity was provided by collagen type II promoter and enhancer driving expression of the construct. The shorter α1 (IX) chain assembled with the endogenous α2 (IX) and α3 (IX) chains to generate mutant heterotrimeric collagen type IX. This transgenic mouse phenotype comprised OA like changes in the articular cartilage of knee joints, and mild chondrodysplastic features: mild dwarfism, cornea pathology, and spinal problems involving shrinkage of the nucleus

pulposus, the appearance of clefts in the annulus fibrosus, associated to herniation of disc material and slight osteophyte formation (Kimura et al. 1996, Nakata et al. 1993). Interestingly, growth plate abnormalities were detected only in null collagen type IX mice, but not in transgenic mice carrying a mutated protein.

The studies mentioned so far demonstrated the importance *in vivo* of the presence of the α1 polypeptide for the trimerisation with the other two polypeptide chains, since its absence impairs the formation of the whole collagen type IX heterotrimer. Interestingly, these findings were not confirmed by studies performed *in vitro,* when the mechanism of collagen type IX chains selection and assembly was tested using recombinant constructs expressing the three human α chains (Jaalinoja et al. 2008, Pihlajamaa et al. 1999). These studies showed the capability for α1 (IX) chains to form disulphide bonds with each other, therefore giving rise to an homotrimeric helical assembly $\alpha1(IX)_3$ which was also secreted *in vitro* and could function as an alternative collagen type IX molecule. However, in the case of co-expression of α1(IX), α2(IX) and α3(IX), the formation of the canonical heterotrimer containing all three chains remained the most favourable form of trimer assembly. Neither α2(IX) nor α3(IX) procollagen chains were able to generate homotrimers. These findings suggest the possibility that $\alpha1(IX)_3$ could compensate for the absence of α2(IX) or α3(IX). When examining *Col9a1*$^{-/-}$ mice, it was confirmed that a similar mechanism of compensation (i.e. the formation of a collagen type IX lacking α1 chains) was not possible.

The consequences of loss of the α2 (IX) were explored in a recent study where a knockout mouse for *Col9a2* was generated. Homozygous mice (*Col9a2*$^{-/-}$) lacked collagen type IX protein, indicating that α2(IX) chain is essential for the correct folding of the whole protein. *Col9a2*$^{-/-}$ mice showed defects in skeletal development, as evidence of short limbs, trunk, tail and retarded bone growth. Histological analysis showed growth plate defects similar to *Col9a1*$^{-/-}$ mice. Tibial epiphyseal cartilage was wider in knockout mice and a large hypocellular region was present in the centre of the proliferative zone. In addition, proliferative chondrocytes showed irregular morphology and disruption of columnar distribution was noticed in the proliferative and hypertrophic zones. The knockout mice exhibited significant reduced auditory function, reproducing the hearing defects reported by patients affected by Stickler syndrome. Finally, *Col9a2*$^{-/-}$ mice showed early onset degenerative joint changes, consistent with those observed in *Col9a1*$^{-/-}$ joints (Balasubramanian et al. 2019). Taken together, we can conclude that both α1(IX) and α2(IX) are essential for correct collagen type IX assembly, as their absence leads to a complete

knockout of the whole protein. From this we might hypothesise that a knockout of α3(IX) would give a similar outcome, however no transgenic mice carrying mutations in *Col9a3* have been described in the literature to date. This will be one of the aspects covered in this thesis.

1.9.4 Combined knockout mice

Some of the knockout mice for genes of various cartilage proteins did not exhibit an obvious skeletal phenotype. Functional redundancy between structurally related proteins was assumed to be the reason behind this lack of phenotype, but as stated before, in COMP deficient and matrilin-3 deficient mice no change in the expression of related proteins was detected (Ko et al. 2004, Svensson et al. 2002). In order to investigate the role of possible complementarity between different but related ECM components, combined knockout mice for multiple genes were generated. In collagen type IX/COMP double-deficient mice the phenotypic abnormalities were similar to the characteristics reported for the functional collagen type IX knockout. Increased thoracic spinal curve, shorter limbs and an alteration in the bone structure were some of the phenotypic abnormalities in mice deficient in both collagen IX and COMP. Remarkably, along with impaired columnar arrangement and a reduction in chondrocytes proliferation, a large uncalcified hypocellular region was found in the central region of the growth plate, again as reported for collagen type IX deficient mice. Similarly to *Col9a1*$^{-/-}$ mice, in the double knockout mice the disorganised appearance of the growth plate tended to improve with age (Blumbach et al. 2008). From these observations, it seems that the lack of collagen type IX is the predominant contributor to the phenotype of the double deficient mice, while the absence of COMP did not cause any specific morphological changes. Nonetheless, when matrix protein deposition was assessed, differences were noticed in the localisation of matrilin-3 in double deficient mice, indicating a role for COMP in matrix deposition.

To study the role of TSP1, TSP3, TSP5 (COMP), and collagen type IX in the growth plate, knockout mouse lines for each of the genes and combinatorial strains were generated. Again, from this study, collagen type IX appeared to have a more significant role in growth plate stability, although each combined knockout showed some growth plate alterations. The most disorganised growth plate was exhibited by TSP3/5/Collagen type IX knockout mice, which also showed a 20% reduction in limb length. Additionally, in the absence of both TSP5

(COMP) and collagen type IX, mice subjected to exercise develop cartilage degeneration (Posey et al. 2008a).

1.10 Genome editing: CRISPR/Cas9 and Non-homologous end joining repair

In recent years, the development of highly versatile genome-editing technologies has given researchers the ability to rapidly and economically introduce sequence-specific modifications into the genomes of a broad spectrum of cell types and organisms. The most commonly used genome editing technologies nowadays comprise zinc-finger nucleases (ZFNs), transcription activator-like effector nucleases (TALENs), homing endonucleases or meganucleases, and clustered regularly interspaced short palindromic repeats (CRISPR)-CRISPR-associated protein 9 (Cas9).

ZFNs are fusion proteins formed by an array of site-specific DNA-binding domains attached to the endonuclease domain of the bacterial FokI restriction enzyme. To cleave a specific site in the genome, ZFNs are designed as a pair that recognizes two sequences flanking the site, one on the forward strand and the other on the reverse strand. Upon binding of the ZFNs on either side of the site, the pair of FokI domains dimerize and cleave the DNA at the site, generating a double-strand break (DSB) with 5′ overhangs (Urnov et al. 2010). One potential disadvantages in the use of ZFNs is the difficult and extremely time consuming process of the assembling of optimized engineered ZFNs domains and the limitation of the target site selection (Gupta and Musunuru 2014).

TALE repeats comprise tandem arrays of 10 to 30 repeats (each repeat is 33 to 35 amino acids in length) that bind and recognize extended DNA sequences. TALE repeats have been used to create a new type of engineered site-specific nuclease that fuses a domain of TALE repeats to the FokI endonuclease domain, termed TAL effector nucleases (TALENs). Similarly to ZFNs, TALENs can generate DSBs at a desired target site in the genome (Bogdanove and Voytas 2011). TALENs are easier to design and have wider target site selection, however a clear disadvantage of TALENs is their significantly larger size compared to ZFNs.

Meganucleases are enzymes able to establish extensive sequence-specific contacts with their DNA substrate, showing great specificity (Stoddard 2011). However, unlike ZFNs and

TALENs, their binding and cleavage domains are not modular, so that the overlap in form and function make challenging their use for more routine applications of genome editing.

The recent discovery of bacterial adaptive immune systems known as clustered regularly interspaced short palindromic repeats (CRISPR) and CRISPR-associated (Cas) systems has led to the newest set of genome-editing tools. CRISPR-Cas systems use a combination of proteins and short RNAs to target specific DNA sequences for cleavage. The bacteria collect "protospacers" from invading DNA sequences (for example from bacteriophages), incorporate them into their genomes, and use them to express short guide RNAs, which can then be used by a CRISPR-Cas system to destroy any DNA sequences matching the protospacers during future invasions. The mode of action of this genome editing tool comprises two biological macromolecules, the Cas9 protein and a guide RNA, which interact to form a complex that can identify target sequences with high selectivity. The Cas9 protein is responsible for locating and cleaving target DNA. In its structure the Cas9 comprises six domains, REC I, REC II, Bridge Helix, protospacer-adjacent motif (PAM) Interacting, HNH and RuvC. The Rec I domain is the largest and is responsible for binding guide RNA. The role of the REC II domain is not yet well understood. The arginine-rich bridge helix is crucial for initiating cleavage activity upon binding of target DNA (Nishimasu et al. 2014). The PAM-Interacting domain confers PAM specificity and is therefore responsible for initiating binding to target. The HNH and RuvC domains are nuclease domains that cut single-stranded DNA (Nishimasu et al. 2014). In engineered CRISPR systems the guide RNA is a single strand of RNA that forms a T-shape comprised of one tetraloop and two or three stem loops, and it is engineered to have a 5′ end that is complementary to the target DNA sequence. When the artificial guide RNA binds to the Cas9 protein, it induces a conformational change converting the inactive protein into its active form. Once the Cas9 protein is activated, it stochastically searches for target DNA by binding with sequences that match its protospacer adjacent motif (PAM) sequence (Sternberg et al. 2014). A PAM is a two- or three-base sequence located within one nucleotide downstream of the region complementary to the guide RNA. PAMs have been identified in all CRISPR systems, and the specific nucleotides that define PAMs are specific to the particular category of CRISPR system (Mojica et al. 2009). The PAM sequence in Streptococcus pyogenes for example, the one mostly used in genome editing, is 5′-NGG-3′ (Jinek et al. 2012). When the Cas9 protein finds a potential target sequence with the appropriate PAM, the protein will melt the bases immediately upstream of the PAM and pair them with the complementary region on the guide RNA

(Sternberg et al. 2014). If the complementary region and the target region pair properly, the RuvC and HNH nuclease domains will cut the target DNA after the third nucleotide base upstream of the PAM (Anders et al. 2014). Previous studies demonstrated the efficiency of the system, as the expression of the Cas9 protein along with guide RNA(s) in mammalian cells, results in double strand breaks (DSBs) at target sites with a 20-bp sequence matching the protospacer of the guide RNA and an adjacent downstream PAM sequence (Cho et al. 2013).

Because target site recognition is mediated entirely by the gRNA, CRISPR-Cas9 has emerged as the most flexible and user-friendly platform for genome editing, eliminating the need for engineering new proteins to recognize each new target site. Its advantage compared to ZFNs and TALENs, which require recoding of proteins using large DNA segments for each new target site, is that CRISPR-Cas9 can be easily adapted to target any genomic sequence by changing the 20-bp protospacer of the guide RNA. This can be accomplished by subcloning this nucleotide sequence into the guide RNA plasmid backbone. The Cas9 protein component remains unchanged. This ease of use for CRISPR-Cas9 is a significant advantage over ZFNs and TALENs, especially in generating a large set of vectors to target numerous sites or even genome-wide libraries (Wang et al. 2014b) . The potential advantage of CRISPR-Cas9 is the ability to use multiple guide RNAs in parallel to target multiple sites simultaneously in the same cell (Cong et al. 2013). This makes it straightforward to mutate multiple genes at once or to engineer precise deletions in a genomic region. The main issue regarding CRISPR-Cas9 usage however, is the possibility of off-target effects mainly related to the guide RNA sequence specificity, demonstrating tolerance of single or multiple mismatches in the protospacer (Hsu et al. 2013). Off-target mutations have been reported at higher rate at sites where sequences are similar to the on-target sites sequences (Fu et al. 2013), however efforts to improve the specificity of CRISPR-Cas9 in mammalian cells are in progress.

The final goal of the use of such genome editing tools is the creation of DSBs in the genomic DNA of the organisms we are trying to modify. Cells repair DSBs using either the nonhomologous end joining (NHEJ) repair pathway, or the homology-directed repair (HDR). NHEJ repair can occur during any phase of the cell cycle, but occasionally results in erroneous repair. On the contrary, the HDR typically occurs during late S phase or G2 phase when a sister chromatid is available to serve as a repair template. Importantly, NHEJ is an error-prone repair pathway, since the process does not use a complementary template, thus the fusion of the blunt-ended DNA duplexes may result in deletion or insertion of base pairs.

The NHEJ repair process requires a nuclease to excise the damaged DNA, polymerases to fill-in new DNA, and a ligase to restore integrity to the DNA strands. The precise mechanism of NHEJ repair is still under investigation, however the model involves the Ku protein which is thought to bind to DNA end and to form a Ku-DNA complex at each end for preparation of ligation and recruiting of nuclease, polymerase and ligase activities in any order (Lieber 2008). The Ku heterodimer has been shown to recruit either directly or indirectly the main NHEJ factors, including DNA-PKcs, X-ray cross complementing protein 4 (XRCC4), DNA Ligase IV, XRCC4-like factor (XLF), and Aprataxin-and-PNK-like factor (APLF) to DSBs. These core NHEJ factors interact with each other to form a stable complex at the DSB (Davis and Chen 2013). The DSB ends undergo a step of DNA processing to make them compatible for ligation for the terminal step of the NHEJ pathway. The XRCC4 and Ku proteins conjugate to recruit specific processing enzymes. After processing, the stabilisation of the DNA ends is achieved by the interplay of XRCC4 and XLF with DNA-PKcs and Ku which produce a filament able to bridge, protect and stabilise the two regions of broken DNA ends. The final ligation and detachment of the NHEJ complex occurs when the DNA ends are ligated by the DNA-Ligase IV. XRCC4, XLF, and likely APLF contribute to the process while DNA-PKcs gets released after a conformational change, leaving the DSB finally repaired (Davis and Chen 2013) .

1.10.1 Transgenic animal models

Traditionally, homologous recombination has been used in mouse embryonic stem cells to create mouse lines with genetic alterations, such as gene knockouts or knockin. (Smithies et al. 1985, Thomas and Capecchi 1987). The main downside of this method has been the issue related to the time required for the generation of transgenic animal lines. The most eloquent example is in mice, as it takes more than a year to generate a genetically modified mouse using homologous recombination. In addition, when the same approach was used to modify human cells, the result was not as efficient, and alternative approaches (i.e. antisense oligonucleotide and short interfering RNAs) have been used. These techniques have only a transient effect and can sometimes have effects also on non-targeted genes (Qiu et al. 2005, Wang et al. 2014a). These limitations required more effective methods of gene modification to achieve transgenesis in multiple organisms. In recent years, novel genome-editing tools for the generation of genetically modified mice have been developed. These tools comprise the methods mentioned before, ZNFs, TALENs, meganucleases and CRISPR/Cas9 technology.

All three engineered nucleases outlined above have proven effective at producing targeted mutations in mouse embryos (Carbery et al. 2010, Cui et al. 2011, Wang et al. 2013, Wefers et al. 2013). The efficiency of each system was strongly depending on the nuclease, target site in the genome, and amount of RNA injected. However, the highest transgenesis efficiency has been demonstrated in experiments where CRISPR/Cas9 was used (Wang et al. 2013). Nowadays, CRISPR/Cas9 has become the preferred and elected approach for the generation of transgenic animal models, thanks to its incomparable ease of use. A particular advantage is that it is possible to obtain knockout animals in the first generation (assuming that the targeted gene is not embryonic lethal), dramatically speeding up the time needed to do genetic studies in animals. The Cas9 protein and transcribed sgRNA can be directly injected into fertilized zygotes to achieve heritable gene modification at one or multiple alleles in animal models such as rodents and monkeys (Li et al. 2013, Niu et al. 2014, Wang et al. 2013) . By bypassing the typical ES cell targeting stage in generating transgenic lines, the generation time for mutant mice and rats can be reduced from more than a year to only several weeks. Such advance, combined with highly specific editing, has paved the way for cost-effective and large-scale in vivo mutagenesis studies in rodent (Fu et al. 2013, Ran et al. 2013a). Another advantage of this approach is that embryos from any of a variety of animal strains can be used; in the case of mice, embryos from an inbred strain can be used to directly generate the knockout mice. Similarly, embryos from a strain that already carries genetic alterations can be used, relieving the need for many generations of interbreeding to obtain mice with multiple genetic alterations. The ability to perform multiplex gene targeting with CRISPR-Cas9 is also helpful in this regard.

Conversely, one outstanding challenge with transgenic animal models generated via zygotic injection of CRISPR reagents is genetic mosaicism, partly due to a slow rate of nuclease-induced mutagenesis. Studies to date have typically relied on the injection of Cas9 mRNA into zygotes (fertilized embryos at the single-cell stage). However, because transcription and translation activity are suppressed in the mouse zygote, Cas9 mRNA translation into active enzymatic form is likely delayed until after the first cell division (Oh et al. 2000) . Because NHEJ-mediated repair is thought to introduce indels of random length, this translation delay likely plays a major role in contributing to genetic mosaicism in CRISPR-modified mice. To overcome this limitation, Cas9 protein and sgRNA could be directly injected into single-cell fertilized embryos. The high rate of mutagenic repair by the NHEJ process may additionally contribute to undesired mosaicism, due to the risk of introducing indels that mutate the Cas9 recognition site and this event would then have to compete with zygotic division rates. To

increase the mutagenic activity of NHEJ, a pair of sgRNAs flanking a small fragment of the target gene may be used to increase the probability of gene disruption. A similar strategy has been adopted for the generation of mutant mice in our project and it will be explained in detail in future sections of this thesis work.

1.11 Splicing mechanism

Pre-mRNA splicing is the mechanism by which introns are removed from the pre-mRNA whilst exons are simultaneously joined together, forming a continuous protein-coding region (open reading frame, ORF) within the RNA sequence (Matlin et al. 2005). Splicing is a highly regulated process performed by a macromolecular complex called the spliceosome. This complex is constituted of between 150 and 300 individual proteins (Rappsilber et al. 2002), together with a group of small nuclear ribonucleoproteins (snRNPs) which consist of proteins bound to an RNA component (snRNA), which are crucial in the recognition of the splicing sites and the catalysis of the splicing reaction. The core elements of the spliceosome are able to recognise specific regions at both 5' and 3' ends of the intron called splice sites and this recognition mediates the splicing event. The sequence of the 5' splice site, also called donor splice site, comprises a nearly invariant "GU" dinucleotide sequence along with less conserved residues downstream. The 3' end, or acceptor splice site, is characterised by a conserved "AG" dinucleotide. Along the sequences at the two sites, the presence of an intron is also indicated by a further element, the branch site. This sequence is located 20-50 nucleotides upstream of the acceptor site and consists of a conserved adenosine typically followed by a track of 15–20 polypyrimidine residues.

The splicing mechanisms is a complex two-step trans-esterification reaction carried out by the spliceosome. In the first step, a lariat forms thanks to a nucleophilic attack of the 5' splice site phosphate group by the 3' hydroxyl group of the branch point adenosine. In the second step the free hydroxyl of the detached exon attacks the 3' splice site, creating two fused exons and a lariat intron (Montes et al. 2019).

1.11.1 Alternative splicing and nonsense-mediated decay.

While some exons are constitutively spliced into mRNA transcript, others are sometimes included and other times skipped, therefore alternatively spliced. Alternative splicing is one of the major sources of proteomic diversity, since many different mRNA

messages can be transcribed from one gene, which then can translate into several proteins with different sizes and/or functions. The importance of alternative splicing resides also in its capability of regulating gene expression by affecting mRNA stability, altering the untranslated regions (UTR) or the open reading frame (ORF) of a transcript (Matlin et al. 2005). Splice variants can thus arise from mechanisms including alternative promoters, preferential usage of exons or splice sites, scrambling of exon order and alternative polyadenylation. Splice site selection is influenced by the combinatorial effect of cis-acting elements (within the RNA sequence) and trans-acting factors. The splice site strength is a cis-acting element and is influenced by the sequence complementarity between the 5' and 3'splice sites with the snRNA component of the spliceosome snRNP. Along with the splice site strength, splice site selection is determined by other cis-acting elements, such as splicing enhancer and silencer sequences. These sequences can be found in intronic and exonic regions and are recognised by many auxiliary RNA-binding proteins (RBPs) which compete to either enhance or repress splice site recognition of both constitutive and alternative exons (Matlin et al. 2005). Trans-acting factors affecting splicing comprise the relative concentration, localisation and activity of RNA-binding proteins, such as members of the SR-protein family and the heterogenous nuclear ribonucleoproteins (hnRNPs). SR-proteins are generally considered enhancers of splicing, whilst hnRNPs are often considered splicing repressors. However, the activating or repressive activity of SR-proteins and hnRNPs is largely position-dependent (Erkelenz et al. 2013).

One third of alternative splicing events result in alteration to the open reading frame (ORF) of a gene, potentially leading to the generation of premature stop codons (PTCs) within the RNA sequence and subsequently targeting the transcript for nonsense-mediated decay (NMD) (Lewis et al. 2003). Accurate splicing of the pre-mRNA constitutes a key aspect in maintaining normal cellular physiology, and it is estimated that between 15% and 50% of human genetic diseases may arise from mutations to splice sites or splicing regulatory sequences (Cartegni et al. 2002, Faustino and Cooper 2003). As mentioned, nonsense-mediated mRNA decay (NMD) is a translation-coupled mechanism that eliminates mRNAs containing premature translation-termination codons which have been acquired as consequence of mutations or errors during transcription or RNA processing (Brogna and Wen 2009). Despite its physiological importance is not yet completely understood, NMD is thought to serve as an mRNA-surveillance mechanism to prevent the synthesis of truncated proteins that would potentially have toxic effects for the cell, such as dominant negative

interactions. In addition, studies involving the inactivation in different species of central components of the NMD machinery have highlighted its function in regulation of physiological gene expression. These studies led to the suggestion that some alternative splicing events had evolved to exploit NMD to achieve quantitative post-transcriptional regulation (AS-NMD) (McGlincy and Smith 2008). Two critical steps are recognised in the NMD pathway: the PTC recognition and discrimination from natural occurring stops and the mechanism by which PTC-containing mRNAs are targeted for fast degradation. Despite conservation of the NMD pathway, the nature of the signals and the decay pathway of targeted mRNAs vary across species. In mammals the PTC is recognised thanks to the crosstalk between the terminating ribosomes and a downstream exon junction complex (EJC), a multimeric protein complex deposited by the spliceosome ∼20–24 nucleotides upstream of exon–exon junctions. More specifically a stop codon is recognised premature if it is found spatially located more than 50-55 nucleotides upstream an EJC (McGlincy and Smith 2008). During translation, the ribosome proceeds along the mRNA displacing EJCs, until it reaches the stop codon where then a termination complex forms and the mRNA then goes on to direct protein synthesis. When an mRNA contains a PTC, it is still recognised by the ribosome as a stop codon, but the presence of an exon-exon junction downstream sets the conditions for the interaction between the termination complex and the EJC, which activates the NMD pathway. The UPF1, UPF2 and UPF3 proteins are core components of the surveillance complex whose basic function is conserved in eukaryotes (Conti and Izaurralde 2005), and their deletion or silencing results in the stabilization of PTC-containing mRNAs, highlighting their important role in the NMD pathway. The model proposed comprises the recruitment of UPF1 by translation release factors, and its interaction with the UPF2 and UPF3 proteins bound to the downstream EJC. This event facilitates the assembly of an active surveillance complex consisting of UPF1, UPF2 and UPF3 and possibly other proteins (Baker and Parker 2004). Once an RNA transcript is recognised as aberrant, the enzymes responsible for its degradation through NMD are those involved in general mRNA decay. One decay pathway for NMD substrates involves removal of the cap structure by the decapping enzymes, which expose the body of the transcript to 5′-to-3′ degradation by XRN1 (Muhlrad and Parker 1994). An alternative pathway, which also contributes to the decay of PTC-containing mRNAs, relies on the accelerated deadenylation and 3′-to-5′ degradation by the exosome and the Ski complex (Lejeune et al. 2003).

The human and mouse genomes have similar sequence organization and have most of their genes being homologous. Considering the important role of alternative splicing in gene regulation, researchers have wondered the conservation of such mechanism between human and mouse. From examination of human splice junctions, from a data set containing human transcripts from constitutively and alternatively spliced introns and exons, for comparison with mouse transcript data sets, researchers obtained a transcript coverage model indicating that 74% of constitutive human splice junctions and 61% of alternative human splice junctions are conserved in mouse. Therefore it was concluded that many, and probably most, alternative splicing events are conserved between human and mouse (Thanaraj et al. 2003).

1.12 Project aims

Multiple epiphyseal dysplasia (MED) is an autosomal chondrodysplasia characterised by early-onset degenerative joint disease. Among the mutated genes identified in MED patients are those encoding for the pro-α chains of the collagen type IX, where the majority of mutations are splice site mutations (affecting the syntenous exon 3). Interestingly, all splice site mutations reported in *COL9A2* and *COL9A3* genes, lead to the skipping of exon 3 and therefore to the in-frame deletion of 12 amino acids from the COL3 domain of the α-helix. The consistency of the splice site mutations reported so far is remarkable and emphasises the importance of the COL3 domain in the pathogenesis of MED. The hypothesis is that COL3 domain might have an important functional role for the protein in the matrix, but what that function is and why in the mutated form it causes EDM3 along with the other MEDs, is not clear.

The aim of this project was to address these unresolved questions. The strategy applied was to reproduce the skipping of exon 3 of *Col9a3* in a C57Bl/6 mouse line, in order to assess the molecular consequences of the phenomenon and to obtain a mouse model of EDM3. Using CRISPR/Cas9 genome editing technology, we have induced the deletion of exon 3, but our strategy led to the generation of two mutant mouse lines, $Col9a3^{\Delta ex3/\Delta ex3}$ and $Col9a3^{-/-}$. Therefore, the purpose of this thesis project was expanded to address additional related questions:

***Col9a3*$^{\Delta ex3}$**

Is the $Col9a3^{\Delta ex3}$ mouse a model of EDM3?
What is the role of the COL3 domain in the collagen type IX molecule and how, when mutated, does this contribute to the pathogenesis of EDM3?

***Col9a3*$^{-/-}$**

Is the $Col9a3^{-/-}$mouse a functional knockout of collagen type IX as previously demonstrated in $Col9a1^{-/-}$ and $Col9a2^{-/-}$ mice?
What are the differences and similarities with the previous described knockouts?
Like deletion of *Col9a1* or *Col9a2*, does the $Col9a3^{-/-}$ recapitulate aspects of Stickler syndrome?
Can we deduce from $Col9a3^{-/-}$ mice further information about the role of collagen type IX within the ECM?

Chapter 2.

Materials and Methods

2.1 Materials

2.1.1 Commercially available kits

Commercially available kits used in this study were: Quick Ligation™ Kit (M2200S, New England BioLabs, NEB); PureYield™ Plasmid Miniprep System (Promega, Southampton, UK); E.Z.N.A.® Tissue DNA Kit (D3396, OMEGA BIO-TEK); ReliaPrep™ RNA Tissue Miniprep System (Promega, Southampton, UK); mirVana™ miRNA Isolation Kit, with phenol (AM1560, Thermo Fisher Scientific); PHIRE Animal Tissue Direct PCR Mastermix Thermo (F170L, Fisher Scientific) DNA-free™ DNA Removal Kit (AM1906, Thermo Fisher Scientific); NucleoSpin® Gel And PCR clean-up (740609, Macherey-Nagel); MEGAshortscript™ T7 Transcription Kit (AM1354, Thermo Fisher Scientific); MEGAclear™ Kit Purification for Large Scale Transcription Reactions (AM1908, Ambion–Life Technologies Ltd.).

2.1.2 Cell culture reagents

DMEM/F-12 (High glucose, 21331020) and DMEM culture media were both purchased from Gibco, Life Technologies Ltd. (Paisley, UK). Foetal bovine serum (FBS), Dulbecco's phosphate buffered saline (PBS), trypsin-EDTA (derived from porcine pancreas), L-glutamine, penicillin-streptomycin, and dimethyl sulphoxide (DMSO), were purchased from Sigma-Aldrich (Poole, UK).

2.1.3 Cell lines

2.1.3.1 HEK 293T

HEK 293T cells were purchased from the ATCC (293T (ATCC® CRL-3216™)) and cultured in DMEM culture media containing 2mM L-glutamine, 100U/ml penicillin, 100µg/ml streptomycin and 10% (v/v) FBS (DMEM complete). This cell line, originated from a foetus, is a highly transfectable derivative of human embryonic kidney 293 cells and contains the SV40 T- antigen. Further details or datasheet available on ATCC website (www.atcc.org/).

2.1.3.2 NIH/3T3

NIH/3T3 cells were purchased from the ATCC (NIH/3T3 (ATCC® CRL-1658™) and cultured in DMEM culture media containing 2mM L-glutamine, 100U/ml penicillin, 100µg/ml streptomycin and 10% (v/v) FBS. This cell line is a derivative of a mouse embryonic fibroblast NIH/Swiss and has proven useful in DNA transfection studies. Further details or datasheet available on ATCC website (www.atcc.org/).

2.2 Methods: Generation and maintenance of mouse model

2.2.1 CRISPR/Cas9 gRNAs design

The first step for CRISPR/Cas9 genome editing is the design of the gRNAs, for which we used the online tool CHOP**CHOP** (http://chopchop.cbu.uib.no/) (Montague et al. 2014) selecting for *mus musculus* genome assembly and pasting the region of interest spanning the intronic region surrounding the exon 3 boundaries of Col9a3 gene (GRCm38/mm10, Pos.: >chr2:180599587-180600578). gRNAs hybridization with the two flanking regions of exon 3 will trigger double-strand breaks with subsequent deletion of the exon 3. Four gRNAs (Table 2.1) were chosen from the output list and no potential off-targets were found by searching for matches in the mouse genome.

Table 2.1. | Sequences of the chosen gRNAs obtained using CHOP**CHOP.** PAM sequences are shown in bold.

gRNA #	Target sequence	Genomic location	Strand	GC content (%)
#7	GATTCTCTCATCTATACCTG**GGG**	sequence:320	-	48
#8	GGGCCTGTGGAGACATTGTG**GGG**	sequence:349	-	65
#10	GGCCTGTGTTGCCCTAGGAG**AGG**	sequence:548	+	65
#11	GTTGCCCTAGGAGAGGCCTG**AGG**	sequence:555	+	65

2.2.2 In-vitro transcribed gRNAs cloning into viral vector

2.2.2.1 Lentiviral vector digestion

5 µg of pLKO.1-puro U6 sgRNA BfuAI large stuffer plasmid (a gift from Scot Wolfe; Addgene plasmid # 52628) was digested with 15U of FastDigest *Bfu*AI (NEB) and 3U of Fast AP (Fermentas) in 1X FastDigest Buffer containing 1mM DTT. Reaction volume was 60 µl in total. The digestion was incubated at 37°C for 30 minutes. Inactivation of the enzyme was then performed at 65°C for 10 minutes.

2.2.2.2 gRNAs oligo annealing

Oligonucleotide annealing was performed using 0.1nM of each oligo per pair (Table 2.2) in 1X T4 Ligation Buffer (NEB) in a total reaction volume of 10µl. This was incubated at 95°C for 5 minutes and then ramped down to 4°C at a speed of 0.1°C /sec.

Table 2.2. | Forward and reverse sequence of gRNAs oligonucleotides. Oligonucleotide sequence in uppercase plus additional sequence for cloning in lowercase.

Oligo name	Sequence
mCol9a3 g#7 F	accgGATTCTCTCATCTATACCTG
mCol9a3 g#7 R	aaacCAGGTATAGATGAGAGAATC
mCol9a3 g#8 F	accgGGGCCTGTGGAGACATTGTG
mCol9a3 g#8 R	aaacCACAATGTCTCCACAGGCCC
mCol9a3 g#10 F	accgGGCCTGTGTTGCCCTAGGAG
mCol9a3 g#10 R	aaacCTCCTAGGGCAACACAGGCC
mCol9a3 g#11 F	accgGTTGCCCTAGGAGAGGCCTG
mCol9a3 g#11 R	aaacCAGGCCTCTCCTAGGGCAAC

2.2.2.3 gRNA cloning and bacteria transformation

The Quick Ligation kit was used for the ligation reaction. Ligation was conducted using 50ng of pLKO digested plasmid with 1µl of undiluted oligo duplex obtained after gRNAs oligo annealing reaction. 1X Quick Ligase buffer (NEB) and nuclease-free water were added to a total volume of 9µl. 1µl of Quick Ligase enzyme (NEB) was finally added before gently mixing the reaction by pipetting up and down and centrifuging briefly prior to incubation at room temperature (25°C) for 5 minutes.

2µl of the ligation reaction was gently mixed to 50µl (one vial) of One Shot® Stbl3™ Chemically Competent *E. coli* (Invitrogen C737303) and incubated on ice for 30 minutes. Competent cells were then heat-shocked at 42°C for 45 seconds before being placed on ice for 2 minutes. 250µl of pre-warmed Super Optimal Broth (S.O.C.) medium (Invitrogen 15544034) were added to each vial of cells and incubated at 37°C horizontally for 1 hour at 225rpm in a shaking incubator. Subsequently, the transformation mixture was spread onto LB-agar plates containing ampicillin (100µg/ml) and incubated inverted at 37°C overnight. The following day individual colonies were selected and incubated in 5ml of LB supplemented with 100µg/ml ampicillin (Sigma-Aldrich) at 37°C in an orbital shaker at 225rpm for 16 hours prior to plasmid purification.

2.2.2.4 Minipreparation of plasmid DNA

Plasmid DNA minipreparations were performed using the PureYield™ Plasmid Miniprep System according to the kit manufacturer's recommendation. Plasmid DNA was eluted in 30µl nuclease-free water and DNA concentration was determined using a NanoDrop ND-1000 spectrophotometer. gRNA cloning was confirmed by Sanger sequencing (Source Biosciences, Nottingham, UK).

2.2.3 Virus production in HEK 293T cells

Viral particles were produced in HEK 293T packaging cells which were seeded at 3.8×10^6 cells per plate in 10ml DMEM complete in 10cm tissue culture plates and left at 37 ℃, 5% (v/v) CO_2 overnight. The following day a mixture of 3 transfection plasmids was prepared with 3.15µg of vector, 2.5µg of Packaging vector pPAX2 (Addgene plasmid # 12260) and 0.63 µg of Envelope vector pCMV-VSV-G (Addgene plasmid # 8454) per dish. 220 µl of DMEM and 19µl of FuGENE® HD Transfection Reagent (Promega E2311) were

finally added to the mixture before incubating for 15 minutes at room temperature and then adding dropwise to each dish. The third day the media from each dish was replaced with 10ml of fresh DMEM (plus supplements) with heat inactivated FBS. The viral supernatant was harvested at 48, 72, and 96 hours post transfection, centrifuged at ~500*g* for 10 minutes to pellet any cellular material, filtered through a 0.45 μm PES filter, and finally aliquotted and stored at -80 ℃ as soon as possible to avoid loss of titre. Cas9 containing viral particles were produced by exchanging the pLKO vector for LentiCRISPRv2 (Addgene plasmid # 52961). Similarly, Green fluorescent protein (GFP) viral particles were also produced by exchanging the pLKO vector for pLJM1-EGFP (Addgene plasmid # 19319), as a positive control for viral production and transduction (data not shown).

2.2.3.1 NIH/3T3 cells viral transduction

NIH/3T3 cells (2×10^5 per well) were seeded overnight in 3ml of medium in a 6 well-plate. The following day 500μl of medium was replaced with 500μl of medium containing pooled virus (pairs of gRNA virus and LentiCRISPRv2 virus (~165 μl of each)) and polybrene (Sigma Aldrich TR-1003) to give a final concentration of 8 μg/ml. The next day antibiotic selection for transduced cells was carried on by adding 2μg/ml puromycin (Sigma-Aldrich) per well and cells were incubated for 2-3 days. Cells transduced with GFP viral particles were assessed via fluorescent microscopy.

2.2.3.2 DNA extraction from transduced NIH/3T3 cells

Genomic DNA was purified from gRNA-transduced NIH/3T3 cells using E.Z.N.A. ® Tissue DNA Kit following manufacturer's protocol. Briefly, cells were harvested after trypsin treatment before adding 25 μL OB Protease Solution and 220 μL BL Buffer followed by incubation at 70°C for 10 minutes. 220 μL 100% (v/v) ethanol was added and the entire sample was then transferred into a HiBind® DNA Mini Column and centrifuged at maximum speed (≥10,000*g*) for 1 minute. Next, 500 μL HBC Buffer were added to the column and centrifugation at maximum speed was performed for 30 seconds. The column was placed into a new 2 ml collection tube and 700 μl DNA Wash Buffer added before centrifugation. This centrifugation was repeated to remove any trace of ethanol. The column was then centrifuged at maximum speed for 2 minutes to dry and finally DNA was eluted by centrifugation in 100μl of pre-heated (70°C) Elution Buffer after 2 minutes of incubation at room temperature.

2.2.3.3 Phire PCR

Polymerase chain reaction (PCR) on cell extracted DNA was carried out using Phire Hot Start II DNA. Each 20 µl PCR reaction mix contained 5X Phire Taq buffer, 0.2 mM dNTP mixture, 0.4 µl Phire Hot Start II Taq DNA Polymerase (Thermo scientific F-122L), and 0.5 µM of each primer (Table 2.3). An Applied Biosystems Veriti™ Thermal Cycler was used and PCR conditions are outlined in Appendix B.

Table 2.3. | Primer sequences used for mouse genomic DNA and cDNA amplification.
Primers were designed using Primer3.

Oligo name	Sequence
mCol9a3 F	GTGTCACTTGGAGGCTACTGTG
mCol9a3 R	CCCAGTAACAGACCACTGCATA
cDNA_Col9a3F	CCAGCCATGACCGGAGC
cDNA_Col9a3R	GTTCTCCAGGGGCACCTTTG

2.2.4 CRISPR/Cas9 genome editing

2.2.4.1 Production of gRNAs mRNA

The T7 promoter was added to the sgRNA templates using PCR amplification. The T7 promoter sequence, plus 6 bases at the 5' end as an extra 'landing platform' for the T7 polymerase, was added to the forward primer complementary to the gRNA cloned in the pLKO vector as shown in Fig 2.1. PCR amplification was performed using as reverse complement primer (AAAAGCACCGACTCGGTGCC) for the TRACR region within the vector. Using 2ng of DNA plasmid plus gRNA template, PCR was carried out using Q5 Hot Start High-Fidelity DNA polymerase (NEB #M0493). Each 100µl PCR reaction mix contained 5X Q5 Reaction buffer, 200 µM of dNTP mixture, 1µl of (0.02U/µl) Q5 Hot Start Polymerase, and 0.5 µM of each primer. An Applied Biosystems Veriti™ Thermal Cycler was used following thermocycling conditions outlined in Appendix B. Purification of template was then performed using a Macherey-Nagel NucleoSpin Gel and PCR clean-up kit according to manufacturer's instructions. Briefly, 2 volumes of Buffer NTI were added to 1

volume of sample to adjust DNA binding conditions prior to loading on a NucleoSpin® Gel and PCR Clean-up Column and centrifugation. Two washes with 700µl of Buffer NT3 were then performed before drying the column silica membrane for 1 minute. Elution of DNA in water was finally achieved by centrifugation at room temperature for 1 minute.

	Extra landing platform for T7 polymerase	T7 promoter sequence	gRNA coding sequence
3GT7 mCol9A3-7 F	5'-atgcat	TTAATACGACTCACTATAGG	GATTCTCTCATCTATAC-3'
3GT7 mCol9A3-11 F	5'-atgcat	TTAATACGACTCACTATAGG	GTTGCCCTAGGAGAGGC-3'

Fig 2.1. Schematic representation of the designed forward primers structure used for gRNAs production.

2.2.4.2 In vitro transcription (IVT) of *Col9a3* #7 and #11 gRNAs

The PCR amplified T7-sgRNA products (with gRNAs #7 and #11) were used as a template for in vitro transcription using the MEGAshortscript T7 kit. In a total volume of 20µl, 100nM of DNA template were incubated with 7.5 mM of each of the four ribonucleotides, 10X T7 reaction buffer and enzyme mix. The reaction was gently mixed before incubation at 37˚C for 2 hours. A TURBO DNase treatment at 37˚C for 15 minutes was finally performed.

2.2.4.3 Purification of sgRNA mRNA

Recovery of sgRNAs was performed using the MEGAclear 3 ™ Kit. The RNA sample was brought to 100 µL with Elution Solution and mixed gently. Subsequently, 350 µL of Binding Solution Concentrate were added to the sample and mixed before addition of 250 µL of 100% (v/v) ethanol. The RNA mixture was passed through a Filter Cartridge by centrifugation for 1 min at 10,000*g*. Two washes with 500 µL of Wash Solution were performed and centrifugation continued for 10–30 sec to remove the last traces of Wash Solution. The elution of RNA from the filter was obtained by applying 50 µL of RNase free water to the centre of the Filter Cartridge and incubation in a heat block set to 65–70°C for 5–10 minutes. The RNA was finally recovered by centrifuging for 1 min at room temperature (10,000–15,000*g*).

2.2.4.4 Zygote cytoplasm injection of gRNAs into foster mother

Zygote cytoplasm injection was performed by Dr Colin Miles and Paul Cairns to generate both transgenic mouse lines following the Ittner and Götz described procedure for pronuclear injection to obtain a transgenic mouse line (Ittner and Gotz 2007).

Briefly, 10–14 days before the first mating, anesthetised stud males were vasectomized and sterility was checked by breeding with females.

To produce zygotes for pronuclear injection, superovulation was induced in females through a first intraperitoneal injection of 5 IU pregnant mare's serum gonadotropin (PMSG) following by 5 IU of human chorionic gonadotropin (hCG), before mating with males. To obtain pseudo-pregnant females, females in oestrus (as indicated by a swollen, moist and pink vagina) were put together with vasectomised males until they were plugged. For zygote preparation, super ovulating females were sacrificed and zygotes harvested with follicular cumulus cells, after successive treatments with hyaluronidase (1-2 ul of 10 mg/ml hyaluronidase (H3884; Sigma)).
Preparation of DNA for injection was performed by Professor David Young.
Transgenic mice were generated by injecting a mix of recombinant Cas9 protein (TGEN_CP1, ToolGen, CamBioScience, UK) (final concentration of 40 µg/ul), with two IVT guide RNAs (each at 50µg/ul) in standard injection buffer (10mM Tris, 0.1mM EDTA pH 7.5) into the cytoplasm of fertilised eggs. Zygote injection was achieved thanks to the help of a holding capillary to stabilize one zygote in the centre of the plate and injection performed when position of the zygote was in the same plane of focus as the opening of the holder, ideally facing it with the polar body and the female and male pronuclei aligned horizontally. The swelling of the female pronucleus was considered as evidence of DNA injection. After injection, about 15-30 injected zygotes were reimplanted into foster mothers. Briefly, an anesthetised pseudopregnant female was incised parallel to the dorsal midline, and the ovary and attached oviduct and uterus gently pulled out from the fat pad in order to expose the infundibulum between the coiled oviduct and the ovary. The reimplantation capillary loaded with the injected zygotes arranged in a row was inserted into the infundibulum to slowly blow the zygotes inside, before pushing the ovary back into the abdomen and sewing up the incision. Reimplanted foster mothers were kept warm until fully recovered and hosted in cages until delivery of the first transgenic litter, referred to as Founder of transgenic line (F_0).

2.2.5 Maintenance

Mice were housed at the Functional Genomics Unit (FGU) at the Institute of Genetic Medicine at Newcastle University, in compliance with the Animals (Scientific Procedures) Act 1986 and its associated Codes of Practice. Up to 5 mice were housed together in independently ventilated cages (300cm^2, 12cm height) to allow enough space for physical activity/exercise. All animals had access to food and drinking water *ad libitum* and were subjected to a 12-hour light-dark cycle. When breedings were ended, re-introduction of the male breeders to already populated cages was avoided in order to avoid social incompatibility issues. The FGU technical staff performed the check and cleaning rota of the cages twice a week. Detailed records about each animal used in this study was recorded using the AniBio and Softmouse software systems and returns of procedures including severity limits and protocols performed annually to the Home Office. Every mouse procedure was performed under Project licences n° 60/4525-1 and n° P8A8B649A-1.

2.2.6 Genotyping

2.2.6.1 DNA extraction

Mice were ear-notched at postnatal day 21 and separated into male/female cages after the weaning period. DNA was extracted from ear biopsies using the PHIRE Animal Tissue Direct PCR Master mix (Thermo-Fisher) following manufacturer's instructions. Briefly, 20µl of Dilution Buffer plus 0.5µl of DNA Release Additive from the Kit were added to each sample, these were vortexed and centrifuged (13,000*g*) prior to subsequent incubations at room temperature for 2-5 minutes and at 98°C for 2 minutes. The DNA extracted was finally vortexed and centrifuged again before Phire PCR amplification or storage at -20 C until required. The PCR reaction consisted of 8 µL nuclease free water, 2X Phire green master mix, 0.5 µM forward and reverser primer (Table 2.3) and 1µL of extracted DNA mixture. PCR was performed in an Applied Biosystems® Veriti™ Thermal Cycler following the thermal cycle programme in Appendix B. PCR products were examined by agarose gel electrophoresis. PCR products in gel loading dye (NEB #B7025S) were loaded, onto a 1.5% (w/v) agarose gel in 1XTAE (Tris-Acetate-EDTA) buffer. In order to determine DNA band size, a DNA marker BIOLINE Hyperladder 100bp (BIO-33056) was loaded along with PCR products. The DNA was electrophoresed at 90 V for ~45 minutes and visualised under UV light using a UVP Geldoc-it imaging system.

2.3 Methods: Validation of mouse model

2.3.1 Bone measurements

3-week old mice were sacrificed by exposure to CO_2 and 9-week old mice were anesthetised using isoflurane. X-rays images were acquired as DICOM raw files using the Faxitron MX-20 cabinet X-ray system (Faxitron Bioptics) at 23 kV for 5 seconds. Raw files were then opened in the Fiji (ImageJ) software and bone measurements (tibia, femur, inner canthal distance (ICD), skull and hip angle) were performed using the measure tool (Fig 2.2). ICD was measured as a marker of intramembranous ossification, whereas length of the skulls, tibiae and femurs as indication of endochondral ossification. Hip development was assessed by measuring the angle formed by the tuberosity of the ischium protruding from the Ilium line. Average measurements of the right and left tibia, femurs and hip angles were calculated per mouse.

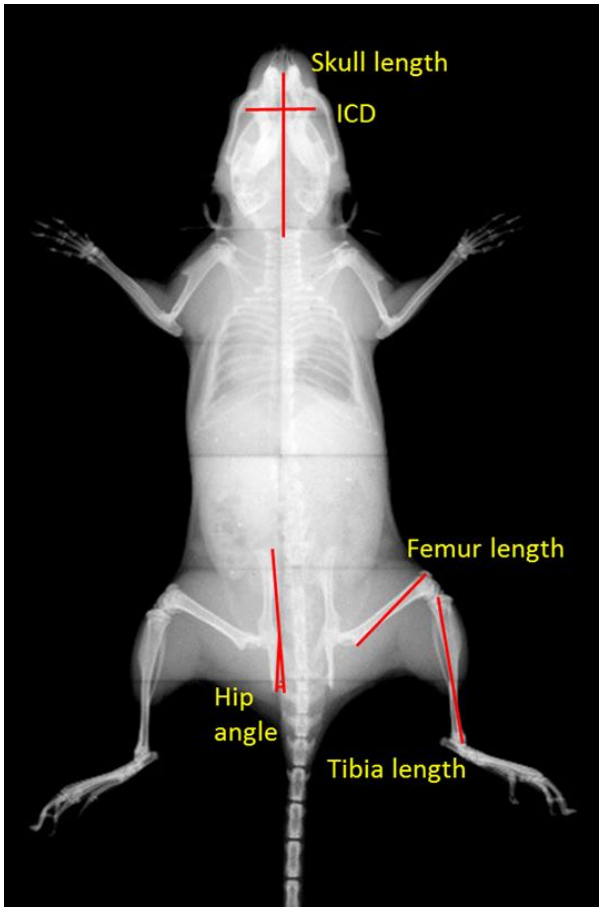

Fig. 2.2 | Radiographic analysis of skeletal mice morphology. Conventional scheme of mouse bone measurement used for x-ray analysis: the inner-canthal distance (ICD) measured as marker of intramembranous ossification whereas skull, femur and tibia length as markers of endochondral ossification. Hip angle assessed as a marker of general hip development.

2.3.2 Quantitative bone morphology by micro-computed tomography (µCT)

2.3.2.1 Dissection and fixation of bones for µCT

18-week old male mice were sacrificed by exposure to CO_2, subsequently the skin was removed from their right legs up to the hip and the head of the femur was dislocated from the hip socket in order to remove the limb from the mouse. The foot was cut from the ankle joint and the soft tissue removed carefully so as not to disturb knee joint. Legs were then fixed in 10 % (v/v) neutral buffered formalin (containing 4% (w/v) formaldehyde) overnight before being washed twice in PBS and being stored in 70% (v/v) ethanol and water for long-term storage, until analysis by µCT.

2.3.2.2 X-Ray micro-computed tomography (µCT)

Femurs and tibiae from 18-week old mice were subjected to bone density analysis to check their cortical and trabecular bone. All µCT scans were performed using the SkyScan 1272v2 µCT analysis instrument in the laboratory of by Professor Rob van‘t Hof at the Institute of Ageing and Chronic Disease, University of Liverpool (UK). Bone specimens were placed in 5ml sample vials filled with 70% (v/v) ethanol and then anchored to the rotating stage of the µCT X-ray chamber. For cortical bone density multiple 2D image projections of the full height knee were obtained with the following settings: a rotation step of 0.4°, an energy filter of 0.50 Aluminium, image format of 2016 x 1344 at a vertical position of 33 mm, oversized scan of 57 and a spatial resolution of 9 µm. X-rays were obtained at 50 kV and 800 mA. For Trabecular Bone density multiple 2D image projections of knees were obtained with a rotation step of 0.3°, an energy filter of 0.50 Aluminium, image format of 4032 x 2688 at a vertical position of 46 mm, not applying oversize scanning, and with a spatial resolution of 4.5 µm. The scanning protocol was set for each sample stage on the machine. To generate a reconstructed 3D bone image, 2D images for each bone were stacked and reconstructed using the NRecon (v1.6.4.1, Bruker) programme selecting the region of interest to be reconstructed. Reconstruction was performed with the smoothing function on, selecting a ring artefact of 5 and a beam hardening of 38% and with a Gaussian smoothing kernel in the advanced options. A dynamic range between 0 and 0.11 was then set before starting the process. 3D µCT reconstructions for trabecular bone was performed on the region which was 50 slides (225 µm) away from the femoral growth plate in femurs or tibial growth plate in tibiae. 3D µCT reconstructions for cortical bone was performed on the region

which was 50 slides (450 μm) away from the femoral great trochanter in femurs or the fibular notch in tibiae. The images shown in the results section are cross-sectional images of 3D μCT reconstructions obtained using the software CtVox for trabecular bone and Dataviewer for cortical bone from the median animals of each genotype at similar distance from the reference points mentioned. Worth mentioning that our standardised method of analysis and imaging did not take into account that one of the genotypes presented shorter long bones.

2.3.2.3 Bone architecture analysis from 3D μCT images

Reconstructed 3D bone images were used to analyse bone architecture using the CTAn (v.1.16) programme. The volume of interest (VOI) to be analysed was set using the Dataviewer programme. In order to analyse trabecular bone, the VOI was set to a depth of 900 μm, 225 μm from the bottom of the tibial or femoral growth plate. In order to analyse the cortical bone of the tibial and femoral shaft, the VOI was set to a depth of 450 μm, from the top of the fibular notch of the tibia or from the bottom the greater trochanter crest of the femur. Femoral and tibial trabecular and cortical VOIs were then opened in CTan and were used as the input with different software macros for cortical and trabecular analysis. The macros were written and kindly provided by Professor van't Hof. Reconstruction parameters and the selected VOI were kept consistent between all samples. The higher and lower grey threshold values corresponding to bone in the macro were set at 70 and 255 for cortical bone and at 60 and 255 for trabecular bone respectively. Statistical analysis on the results was carried out using the Student's unpaired *t*-test comparing the bone structural parameters between control and mutant mice.

2.3.3 Tissue preparation for histological and immunological analysis.

The mice were sacrificed and dissected removing the skin and part of the muscle, before knee joints were collected and fixed. Fixation was performed for 24 hours at room temperature or for 48 hours at 4°C in 4% (v/v) formaldehyde (for histological protocols) or in a solution of 95% (v/v) ethanol / 5% acetic acid (for immunohistochemical (IHC) protocols). After fixation the bones were decalcified in 20 % (w/v) EDTA pH 7.4 (Appendix A) for 1 week (for mice up to 2 weeks of age) or 2-3 weeks (for mice 3-9 weeks of age), with gentle agitation at room temperature.

Following decalcification, knee joints were washed with running tap water for 1 hour and then transferred in 70% (v/v) ethanol prior to overnight processing in a Thermo Scientific™ STP 120 Spin Tissue Processor (Appendix D). Tissue samples were then embedded in paraffin blocks in a flat orientation or patella down orientation (for destabilisation of medial meniscus (DMM) experiment) and left to set overnight.

Wax blocks were placed at -20°C prior to sectioning. Legs were sectioned using a Thermo Scientific™ HM 355S automatic microtome to 6μm sections (histology and immunohistochemistry) or 4 μm (DMM sectioning). Wax sections were fixed onto Superfrost® Plus slides (CellPath MBB-0102-54A) at 60 °C on a hot plate for 1 minute and left to air dry overnight. During sectioning, sister tissue sections were collected starting from the beginning of the appearance of the growth plate and finishing when the growth plate started to disappear, to be sure to cover the entire depth of the tissue. An average of 25-30 slides were collected per sample and they were numbered to be able to recognise the tissue depth at which sections were collected. Matching of the slides was carried out by choosing those slides with the same or close number for each genotype, representative of each region (initial, middle and end region) of the tissue. Matched numbered slides of different samples and biological replicates were then processed for staining and imaging showed in this thesis work.

2.3.4 Haematoxylin and eosin (H&E) staining

Sectioned formaldehyde-fixed joints were dewaxed in xylene and were hydrated in a decreasing series (100%, 95%, 75%, 50%) of ethanol and then washed with tap water for 1 minute. Slides were next submerged in filtered Harris modified haematoxylin for 1.5 minutes before being rinsed in tap water for 1 minute. Slides were dipped in 0.5% acid alcohol (Appendix A) followed by a water rinse, where needed, to remove excess stain, before a 30 seconds incubation in Scott's tap water to enhance nuclear staining. Subsequently, slides were stained in filtered alcoholic eosin Y for 30 seconds, and rinsed in water for the same time. Afterwards, stained slides went through dehydration in increasing concentrations of ethanol (50%, 75%, 95%, 100%) and placed in xylene before being mounted using DPX Phthalate-free mounting media (CellPath). Once dry, images were acquired using a DM5500 B bright field microscope (Leica), connected to a Leica DFC310 FX camera. All

morphometric measurements were performed by LAS V4.5 (Leica) and Fiji (Image J) software.

2.3.5 Toluidine blue staining

Toluidine blue staining of the cartilage growth plate was used to analyse sulphated proteoglycans. Formaldehyde-fixed limb specimens were sectioned and dewaxed in xylene, then sections were rehydrated to water through a series of decreasing ethanol concentrations as described previously. Slides were then incubated in 0.04 % toluidine blue pH 3.75 (Appendix A) for 2 minutes. To remove excess stain, slides were rinsed twice in water before being incubated in a Nuclear Fast Red solution for 50 seconds to counterstain the nuclei. Sections were then rinsed twice in tap water and were dehydrated in 75 % and 100 % ethanol for 3 minutes for each incubation, and finally placed in xylene before being mounted using DPX Phthalate-free mounting media (CellPath). Once dry, sections were imaged using a DM5500 B bright field microscope (Leica).

2.3.6 Safranin-O – Fast Green staining

This method is used for the detection of cartilage, mucin and mast cell granules on formalin- fixed paraffin-embedded tissue sections. The cartilage and mucin will be stained orange to red and the nuclei will be stained black in a green background corresponding to cytoplasm. The method is recommended as a semi-quantitative scoring system following DMM surgery. Two independent and blind scorers assessed cartilage damage eight-weeks post-DMM surgery (see 2.3.13 Surgical destabilization of the medial meniscus (DMM)). Briefly, slides were dewaxed and rehydrated as described in section 2.3.4. Slides were stained with Weigert's iron haematoxylin working solution (SIGMA-Aldrich, Poole, UK) for 10 minutes and then briefly washed under running distilled water. Slides were then quickly dipped in 0.5% acid alcohol to remove excess hematoxylin and then rinsed in running tap water to stop the reaction. Slides were then placed in 0.06% (w/v) Fast Green solution (SIGMA-Aldrich, Poole, UK) for 5 minutes and then quickly rinsed in 1% (v/v) acetic acid solution (SIGMA-Aldrich, Poole, UK) for no more than 10-15 seconds. Slides were then stained in 0.1% (w/v) Safranin O solution for 5 minutes before being transferred to 95% (v/v) ethanol for 1 minute and then subjected to two washes of 100% ethanol for 2 minutes each.

Finally, slides were placed twice in xylene for 10 minutes each, before mounting in DPX Phthalate-free mounting media and left overnight at room temperature to dry.

2.3.7 Picrosirius red staining

Picrosirius red staining was used to visualise collagen fibres (Appendix E.3). The reaction of the dye with collagen fibres is able to enhance their birefringence under polarised light, collagen fibrils then appear red, orange, yellow, or green depending on their thickness, going from red to green as thickness decreases. For picrosirius red staining paraffin sections were de-waxed and hydrated through a series of decreasing ethanol concentrations up to distilled water as previously described. Nuclei were then stained with Harris modified haematoxylin for 20 minutes and excess stain removed by washing in running tap water for 20 minutes. Picrosirius red stain was then applied to sections and incubated for 1 hour. Sections were then washed in two changes of 0.5 % (v/v) acidified water before dehydration through three changes of 100 % ethanol. Slides were finally immerged in xylene prior to mounting with DPX Phthalate-free mounting media. The staining was visualized at 20X magnification using transmitted polarised light with a Leica DM2700 P polarising microscope kindly available from Dr Cees van der Land at the School of Natural and Environmental Sciences, Geosciences Institute.

2.3.8 Immunohistochemistry

Three-week-old mice were sacrificed and their right legs harvested, fixed, decalcified, embedded and sectioned as described in section 2.3.3 Tissue preparation for histological and immunological analysis.. Sections were dewaxed in xylene and dehydrated through a decreasing gradient of ethanol before two washes in water and re-equilibration in PBS. Sections were pre-treated with 0.2% (w/v) bovine hyaluronidase in PBS and incubated at 37°C in a humidified chamber for 45 minutes for epitope unmasking. They were then incubated in 0.5% (v/v) Triton™ X-100 (Sigma) for 5 minutes and with 5µg/ml proteinase K in PBS for 5 minutes at room temperature, washing with PBS in between each step. Blocking was conducted with a 0.6% (v/v) goat serum (Vector Laboratories Ltd., UK), 1% (w/v) bovine serum albumin (BSA, Fisher Scientific) solution in PBS for 1 hour at room temperature. Sections were then incubated overnight at 4 °C with primary antibodies diluted in PBS. The following day, slides were washed in 1% (w/v) BSA/PBS and then incubated at

room temperature with secondary antibodies diluted in 1% (w/v) BSA. Antibodies were then removed with a final wash in PBS before mounting in Fluoroshield Mounting Media with DAPI (ab104139 Abcam). Antibody dilutions are listed in Appendix C.

Slides were imaged on a Zeiss AxioImager with Apotome (IGM, system 3) microscope, at 20X and 40X magnification selecting the DAPI and corresponding AlexaFluor™ filter sets on the ZenPro microscope associated software. Exposure times were set on negative control sections for equivalent antibodies (Appendix C, Fig.C1).

2.3.9 Bromodeoxyuridine (BrdU) labelling assay

For the detection of proliferative cells a 5'-bromo-2'-deoxyuridine (BrdU) labelling assay was performed on 3-week-old mice tissue sections. Mice were intraperitoneally injected with 0.01mL/g BrdU (Amersham RPN201) labelling reagent. Two hours post-injection, mice were sacrificed by exposure to CO_2 and right limbs were fixed for immunohistochemistry, decalcified, processed, embedded and sectioned as previously described.

BrdU positive cells were detected by immunohistochemistry. 6µm sections were dewaxed in xylene and dehydrated through a decreasing gradient of ethanol. To unmask antigens, slides were incubated in 4M HCl for 15 minutes. Slides were then neutralised in 0.1M borate buffer pH8.5 (Appendix A) for 5 minutes and then washed in PBS before blocking with 4% (v/v) donkey serum (AbD Serotec) (diluted in PBS) for 20 minutes at room temperature or overnight at 4°C. Incubation with anti-BrdU primary and subsequently secondary antibodies (Appendix C) was performed following an immunohistochemistry protocol as described in section 2.3.8 Immunohistochemistry. Slides were mounted using the Fluoroshield Mounting Media with DAPI and allowed to dry in a dark box overnight. Images of sections were acquired using a Zeiss AxioImager with Apotome (IGM, system 3) microscope at 20X magnification using the DAPI and AlexaFluor™488 filter sets using the tiles and stitching functions of the ZenPro software for higher imaging resolution. Exposure times were set on negative controls which were sections not probed with anti-BrdU antibody.

Raw images were viewed in Fiji (ImageJ), colour channels were split and images were converted to grey-scale. BrdU positive cells were counted using the Watershed Segmentation algorithm on the Fiji program and expressed as a percentage of total cells within the proliferative zone. Nine matched slides per mouse, from 3 mice per genotype, were counted

and analysed using a Student's unpaired *t*-test carried and statistical significance was given as $p < 0.05$.

2.3.10 Analysis of gene expression

2.3.10.1 RNA extraction from mouse tissue

Femoral head caps and xiphoids were dissected from 3-week old mice and snap frozen in liquid nitrogen and stored at -80 °C until further use. Total RNA was extracted by disrupting the frozen tissue using a Satoris Mikrodismembrator S, shaking for 1 minute at 2000 rpm. Briefly, the frozen tissue was placed in a cooled stainless steel vial containing a cooled stainless steel ball and frozen BL + TG buffer according to sample weight, supplied by the ReliaPrep™ RNA Tissue Miniprep System (Promega). RNA was then extracted from the powder obtained after tissue disruption using the ReliaPrep™ RNA Tissue Miniprep System according to manufacturer's instructions. Resulting RNA was eluted in 15µl RNase-free water and its concentration assessed using the NanoDrop ND-1000 spectrophotometer.

2.3.10.2 Reverse Transcription and cDNA amplification

For reverse transcription to 1µg of tissue extracted RNA, nuclease-free water was added to 9µl final volume and 0.1µg/µl random hexamers $pd(N)_6$ (Integrated DNA Technologies, IDT) were added and heated to 70°C for 5 minutes. The samples were then placed on ice. To the cooled samples a mixture of 0.25mM dNTPs (Bioline), 4µl of 5X First Strand Buffer, 10mM DTT, 1 µl (200 U) Moloney Murine Leukaemia Virus (M-MLV) reverse transcriptase (all ThermoFisher Scientific) and water was prepared for a total reaction volume of 20µl. Reverse transcription was performed at 42°C for 1 hour. The cDNA obtained was immediately used for PCR amplification following the protocol in section 2.2.3.3 Phire PCR and PCR cycling programme in Appendix B, or stored at -20°C for future use.

2.3.10.3 Isolation of rib primary chondrocytes

Mice at the age of 1 week were sacrificed by cervical dislocation, skinned and the chest internal organs removed in order to separate their thoracic cages. Once the sternum was removed, ribcages were cut and opened along the spine, cleaned from the bone marrow, and placed in warm PBS to keep moist, until all dissections were completed. Each ribcage was then digested with 2 mg/ml collagenase type II (Invitrogen) in Dulbecco's modified Eagle's

medium (DMEM) (Sigma-Aldrich) at 37°C for 75 minutes, vortexing every 15 minutes. Then in a Petri dish under the microscope, single ribs were separated and cleaned from muscle and fibrous tissue, cartilage harvested and digested with 2 mg/ml collagenase type II at 37°C for 3 hours, vortexing every 30 minutes. After incubation, cartilage was mechanically disaggregated by pipetting and released chondrocytes filtered, washed in PBS, and pelleted.

2.3.10.4 RNA isolation from primary chondrocytes

RNA was isolated from ribs primary chondrocytes using mirVana™ miRNA Isolation Kit according to manufacturer's protocol. Briefly, about 400µl of Lysis/Binding Buffer solution were added to each cell pellet according to estimated cell number and vortexed vigorously to obtain a homogenous lysate. Afterwards, organic extraction was carried out by adding 1/10 volume of 'miRNA Homogenate Additive' to the cells, mixing by inverting the tubes several times, and incubation on ice for 10 minutes. A volume of Acid-Phenol:Chloroform, pH 4.5, (#AM9720, Thermo Fisher Scientific) equal to the initial lysate volume was added, vortexed and samples centrifuged for 5 minutes at 10,000*g* at room temperature to separate the aqueous and the organic phases. The aqueous phase was recovered to a fresh tube. For final total RNA isolation, 1.25 volumes 100% ethanol were added to the aqueous phase, thoroughly mixed by vortexing, loaded onto a kit Filter Cartridge which was quickly centrifuged at 10,000*g*. The filter was then washed three times, first with miRNA wash solution 1, then miRNA wash solution 2 and finally wash solution 3, before and elution via centrifugation (10,000*g* for 30 seconds) into a fresh collection tube with 50 µl of pre-heated (95˚C) nuclease-free water. RNA was stored at -80 ˚C until further use.

2.3.10.5 RNA sequencing

RNA sequencing was carried out on RNA isolated from costal primary chondrocytes. The extracted RNA was initially subjected to a DNase treatment step using the DNA-free™ DNA Removal Kit (# AM1906, Thermo Fisher Scientific) in order to avoid genomic DNA contamination. RNA integrity was checked on an Agilent Technology Bioanalyzer and samples with a RNA integrity number (RIN) ≥ 8 (Appendix E.1) were considered for subsequent sequencing library preparation. Sequencing libraries were prepared from total RNA using the Illumina TruSeq Stranded mRNA library preparation kit following manufacturer's instructions. Briefly, the Poly-A containing mRNA molecules were purified using poly-T oligo attached magnetic beads. Following purification, the mRNA was

fragmented into small pieces using divalent cations under elevated temperature. Cleaved RNA fragments were copied into first strand cDNA using reverse transcriptase and random primers in the presence of Actinomycin D to prevent spurious DNA dependent synthesis. Second strand cDNA synthesis followed using DNA polymerase I and RNase H where the incorporation of dUTP in place of dTTP quenched the second strand during amplification. A further step of 3'-blunt end adenylation prevented the fragments from ligating to each other during the adapter ligation reaction. A corresponding single 'T' nucleotide on the 3' end of the adapter provided a complementary overhang for ligating the adapter to the fragment in order to prepare the double strand cDNA for hybridisation onto a flow cell. PCR enrichment of DNA fragments was conducted before final cDNA library preparation. Sequencing was performed on an Illumina NextSeq 500 platform (following manufactures instructions) yielding ~12 million 75 bp single reads per sample. Four samples were sequenced for each biological condition (n = 4). Read QC was performed using FastQC and summarised using MultiQC (Ewels et al. 2016). All samples passed QC. Transcripts were quantified using Salmon (Patro et al. 2017) in quasi-mapping mode to mouse genome build GRCm38/mm10 and summarised to gene level using the tximport package in R. Batch effects were estimated using the RUVs method from the RUVSeq package (Risso et al. 2014), the factors of unwanted variation were adjusted in the differential expression analysis model. Normalisation and differential expression analysis were performed using the DESeq2 package using default settings (Love et al. 2014). An FDR threshold of 0.05 was used to filter significant differentially expressed genes. Sequencing was performed by the Genomics Core Facility, Newcastle University, and bioinformatics by Dr Kat Cheung within the Bioinformatics Support Unit.

2.3.10.6 Sequential protein extraction

Three-week old mice were humanly sacrificed and their cartilage was dissected by dislocation of femoral head from the acetabulum of the hip joint and subsequent removal of cartilaginous femoral head cap. Five biological replicates per genotype were used, comprising both femoral heads from each mouse pooled together and immediately snap-frozen in liquid nitrogen and stored at -80°C until protein extraction step. In the first step of protein extraction, femoral heads were dissected into small pieces with a scalpel before being transferred into a pre-weighed clean Eppendorf and weighed. The first round of extraction was performed by incubation overnight at 4°C of with 10 volumes of cold Buffer I (0.15M

NaCl, 50mM Tris-HCl, pH 7.4) per weight in mg of tissue. The following day, samples were centrifuged for 5 minutes at 13,000*g* at 4°C and the supernatant collected in 100 µl aliquots, and stored at -80°C. Pellets from each sample were then resuspended in an appropriate volume of pre-chilled Buffer II (1M NaCl, 10mM EDTA, 50mM Tris-HCl, pH 7.4), vortexed vigorously, and incubated at 4°C on a rotating mixer overnight. The next day the same procedure as previously was performed, samples were centrifuged for 5 minutes at 13,000*g* at 4°C, the supernatant collected in 100 µl aliquots, and stored at -80°C. The pellet from this centrifugation was resuspended in cold Buffer III (4 M GuHCl, 10 mM EDTA, 50 mM Tris, pH 7.4), vortexed, and kept rotating overnight at 4°C. The following day samples were centrifuged at 13,000*g* at 4°C for 5 minutes and the supernatant removed in 100 µl aliquots and stored at -80°C. Ethanol precipitation of proteins was carried out adding 1.4ml of 96% (v/v) ethanol to each 100 µl aliquot and mixing gently before overnight incubation at 4°C. In the morning, samples were centrifuged at 4°C for 15 minutes at maximum speed and supernatant collected with help of a syringe. 1ml of wash solution made of 96% (v/v) ethanol with Tris-buffered saline (9:1 ratio) was added to pellets, vortexed to let them dissociate from wall of tube and incubated for 1 hour. Two more centrifugation cycles were carried out at max speed for 15 minutes (at 4°C) and the supernatant completely removed with a syringe to let the pellet air dry. Pellets were finally resuspended in 60µl of water and kept at -80°C until immunoblotting analysis.

2.3.10.7 SDS-polyacrylamide gel electrophoresis and immunoblotting

Sequential protein extracts were analysed by western blotting. Briefly, to 20µL ethanol precipitated proteins, 5X Laemmli sample buffer (all buffers are given in Appendix A) was added, this included 10% (v/v) β-mercaptoethanol when reducing conditions were applied. Samples were immediately loaded (if under non-reducing conditions) or denatured at 95°C for 5 minutes before being loaded into a 4-12 % NuPAGE® Bis-Tris precast gel (Invitrogen #NP0335BOX) alongside a Precision Plus Protein™ dual colour protein marker (Biorad #1610374). Electrophoresis was performed in NuPAGE MOPS SDS-PAGE running buffer (Invitrogen # NP0001) for 2 hours at 100 V. Electroblotting of proteins was carried out onto a Polyvinylidene difluoride membrane (PVDF) membrane in 1X Towbin transfer buffer overnight at 80mA at 4°C. Blocking for one hour in a 5% (w/v) solution of semi-skimmed powdered milk in PBS-T was carried out to prevent non-specific binding of antibody to the membrane. The membrane was then incubated overnight in the required concentration of

primary antibody in a 5% (w/v) BSA/TBS-T solution at 4°C. The following day the primary antibody solution was removed from the membrane and the membrane washed three times for 10 minutes in 1X TBS-T. The membrane was incubated at room temperature with a species appropriate horseradish peroxidase (HRP)-conjugated secondary antibody in a 5% (w/v) powdered milk/TBS-T solution for 1 hour. After secondary antibody incubation, the membrane was washed 3 times for 10 minutes in TBS-T to remove excess of antibody before being developed using Amersham ECL-advanced western blotting detection reagents (#RPN2106) and imaged using an Azure Imaging System. Primary and secondary Antibodies dilutions are outlined in Appendix C.

2.3.11 Atomic Force Microscopy (AFM)

Atomic Force Microscopy was performed on growth plate cartilage. Newborn and six-week old mice were euthanized and their hind limbs collected after peeling off their skin, embedded in optimal cutting temperature (OCT, CellPath) tissue freezing medium and snap-frozen in liquid nitrogen. The following steps of tissue processing, AFM measurements and analysis, were performed by Dr. Attila Aszodi and Bastian Hartmann at the Clinic for General, Trauma and Reconstructive Surgery Ludwig-Maximilians-University in Munich, Germany.

Cryo-sectioning: Samples were sectioned to 20 μm-thickness using a Leica Cryostat CM1950 (Leica Biosystems GmbH, Nussloch, Germany). In order to preserve the morphology of the undecalcified leg, before each cut, a transparent one-sided adhesive tape was placed on the sample and a transparent double-sided adhesive tape was placed on a microscope slide. After cutting the tape side of the section was attached to the chilled microscope slide via the double-sided adhesive tape. Samples were stored at -20°C until AFM measurements.

AFM measurements: Immediately before the measurement, the slide was taken out of the freezer and left at room temperature for 10 minutes. PBS was applied to the section and the tissue was given 5 minutes to equilibrate. AFM measurements were performed using a NanoWizard® I (JPK Instruments AG, Berlin, Germany). An overview force map on a square area of 30 × 30 μm containing 30 × 30 force-indentation curves was made to identify the location of the interterritorial matrix (ITM) and the cells. Three maps (3 × 3μm with 25 × 25 force-indentation curves) were made on the ITM. Parameters of the force curves were: a setpoint of 3V, Z-velocity of tip 15μm/s and a MLCT Cantilever E (Bruker AFM Probes,

Camarillo, CA, USA) with a nominal spring constant of 0.1N/m. Two slides per animal were measured and three animals for each genotype and age were examined.

Data processing: AFM curves were analysed using the JPK Data Processing software (JPK Instruments AG, Berlin, Germany). To obtain the stiffness value (Young's modulus), the Hertz-Sneddon-model for a pyramidal tip was fitted on each force-indentation curve. All Young's moduli of each genotype (three maps per slide; two slides per mouse; three mice per genotype) were merged to one distribution (histogram). Finally, a bimodal distribution was fitted on the histograms to obtain the peak values using Igor Pro software V. 6.3.7 (WaveMetrics Inc., Lake Oswego, OR, USA).

2.3.12 Transmission Electron Microscopy (TEM)

Transmission Electron Microscopy (TEM) was used to visualise cartilage ECM structure. Seven-day old pups were sacrificed by cervical dislocation and their tibia dissected by cutting the lateral and medial collateral ligaments and the two cruciate ligaments in order to detach the femur and leave the meniscus intact. As much soft tissue as possible was removed from the tibial epiphysis and metaphysis prior to fixation in 2% (w/v) glutaraldehyde in sodium cacodylate buffer at 4°C (provided by the EM unit) for a minimum of overnight, but up to two weeks incubation. Subsequent protocol steps were performed by staff at Newcastle University Electron Microscopy Research Services. A secondary fixation was performed with 1% (w/v) osmium tetroxide to preserve the lipid content and add contrast to the tissue. Tissue samples were then dehydrated through an increasing gradient of acetone before being impregnated in increasing concentration of resin in acetone prior to final embedding in 100% resin at 60°C for 24 hours. Semi-thin survey sections of 0.5µm were cut and stained with 1% toluidine blue in 1% borax to visualise the growth plate. Ultrathin sections of approximately 70nm were then cut using a diamond knife on either an RMC MT-XL or Leica EM UC7 ultra microtome. The sections were stretched with chloroform to remove compression and mounted in pioloform-filmed copper grids. The tissue sections were then stained with 2% aqueous uranyl acetate and lead citrate. The grids were examined at the Electron Microscopy Research Services Unit, using a Hitachi HT7800 transmission Electron Microscope and imaged with an Emsis Xarosa camera connected to Radius software.

2.3.13 Surgical destabilization of the medial meniscus (DMM)

DMM surgery and post-surgery mice checks were performed by Dr Dimitra Tsompani and Hua Lin in the Functional Genomic Unit (FGU) at the Institute of Genetic Medicine of Newcastle University.

In the pre-operation step, male mice at 10 weeks of age were used for the DMM surgery. Each mouse was anaesthetised separately using isoflurane (2.5-3.5%) 1L/min O_2 and then placed in a recumbent position applying the mask to their head. The left knee was shaved, and the area disinfected with chlorohexidine solution (ECOLAB, MN, USA). The animal was weighed and checked for any possible infection. Subcutaneous injection of buprenorphine (0.15ml, 3μg/ml solution) was then performed.

During operation, a small vertical incision in the skin just left of the knee joint was made using a scalpel, avoiding the patella ligament region. With curved scissors the incision was then enlarged and blood vessels were cauterised to avoid bleeding. The fat tissue was removed with a scalpel/scissors pealing back and avoiding blood vessels, which when necessary were cauterised. Once the medial collateral ligament and the patella ligament were recognised, a small vertical incision was made (large scalpel) down to the side of the patella ligament and extended to the left. The fat pad was cleared with two fine forceps to expose the medial meniscus with the white medial meniscotibial ligament (MMTL) lying horizontal extending towards and behind the patella region. Throughout the surgery, any veins were cauterised to avoid bleeding. Using a small scalpel blade an incision of the medial meniscus was made, then the skin flaps were held together with forceps and clipped. The clips were checked later that day and every day post-surgery up to removal seven days post-surgery.

In the post-operation, the animals were located in clean cages and the cages placed at 27°C until the animals regained consciousness. The following day a further dose of pain relief (buprenorphine, 0.15ml, 3μg/ml solution) was subcutaneously injected to all operated mice which were closely monitored thereafter to ensure successful recovery.

At the end of the experiment, eight weeks post-surgery, the animals were euthanised using CO_2 or by cervical dislocation and both knee joints harvested and fixed in formalin solution, overnight at room temperature with rotation, before decalcification in 20 % (w/v) EDTA pH 7.4, for 3 weeks at room temperature. After decalcification, legs were processed, wax-

embedded in patella down orientation and cut as described in section 2.3.3 Tissue preparation for histological and immunological analysis..

For each DMM joint, 100 serial 5µm-sections were collected on 25 slides, each slide with 4 'sister sections' in order to cover the whole interesting region. Then only 6 slides (Slide 1, 5, 10, 15, 20 and 25) were selected from each joint and Safranin-O staining, as described, was performed to visualise DMM damage. DMM damage scoring (Table 2.4) was carried out by different blind researchers, who scored the MFC and MTP throughout 6 slides (24 sections in total, each section presents a different level) for each DMM joint. The four maximal scores from each site for each scorer were chosen to calculate the mean of 4 maximal MFC or MTP. For MCF+MTP summed score, the two means together for each scorer were added and then combined different scorers' data to get a mean for each site or parameter (ie. MFC, MTP, and summed score MFC+MTP). The histological images shown in the DMM results represents the sections for each genotype which were associated with the highest score during analysis, therefore they do not represent matched sections in terms of tissue depth.

Table 2.4. | The recommended semi-quantitative scoring system for assessing cartilage damage on DMM mouse joints. Adapted from (Glasson et al. 2010)

Grade	Osteoarthritic damage
0	Normal
0.5	Loss of Safranin-O without structural changes
1	Small fibrillations without loss of cartilage
2	Vertical clefts down to the layer immediately below the superficial layer and some loss of surface lamina
3	Vertical clefts/erosion to the calcified cartilage extending to <25% of the articular surface
4	Vertical clefts/erosion to the calcified cartilage extending to 25- 50% of the articular surface
5	Vertical clefts/erosion to the calcified cartilage extending to 50- 75% of the articular surface
6	Vertical clefts/erosion to the calcified cartilage extending >75% of the articular surface

Chapter 3.

Generation of Col9a3$^{\Delta ex3}$ and Col9a3$^{-/-}$ mouse models using CRISPR/Cas9 genome editing.

3.1 Introduction: Genome editing strategy to generate the mutant mouse line.

As mentioned, Col9-MED patients whose mutations involve the *Col9a3* gene, have the recurrent skipping of exon 3 as result of aberrant splicing events. The reason for mutations being clustered around exon 3, in a 32-exon long gene, and how the loss of this exon is linked to the disease is unknown.

In our attempt to unravel this, we aimed to generate a mouse to model the disease mutations and ideally the disease phenotype reported for the patients. Here we will describe the strategy used to generate the genetically modified mouse, carrying the deletion of exon 3 in *Col9a3* gene as found in the Col9-MED subgroup of patients. CRISPR/Cas9 technology was applied in order to induce two-double strand cleavage with the concomitant excision of the genomic region encompassing *Col9a3* exon 3.

The procedure employed involved the following steps:

- Designing of gRNAs whose sequences were complementary to the intronic regions flanking the exon 3 boundaries of *Col9a3* mouse gene.
- In vitro verification of designed gRNAs in a mouse fibroblast cell line to select the efficient gRNA pair able to induce efficient deletion.
- Zygote cytoplasm injection of CRISPR/Cas9 machinery: *in vitro* transcribed functional gRNAs along with recombinant Cas9 protein.
- Genotyping of the first transgenic offspring (F_0) obtained after CRISPR/Cas9 injection.
- Screening of F_1 mutant mice to select the deletion mutation more representative of those reported in Col9-MED patients and establishment of the desired mutant mouse line for the following deep phenotyping study.

3.2 Designing of CRISPR/Cas9 genome editing system to target *Col9a3* exon 3 for deletion.

In order to use the CRISPR/Cas9 genome-editing tool to generate our transgenic mice, gRNAs were designed whose sequences were complementary to the intronic regions spanning the intron-exon boundaries of exon 3 of *Col9a3* gene. gRNAs targeting the exon 3 boundaries of mouse *Col9a3* were designed using the web tool CHOPCHOP ((Montague et al. 2014)) using the genomic region >chr2:180599587-180600578 (mm10 coordinates and centred around the 36 bp of exon 3) as input. A list of ranked (GC content and minimal off-targets) gRNAs were generated, with four gRNAs finally selected with the least number of off-targets (Fig. 3.1): #10 and #11 mapping precisely in position 548 and 555 on the sense strand of the genomic region, and gRNA #7 and #8 respectively in position 320 and 349 of the antisense strand.

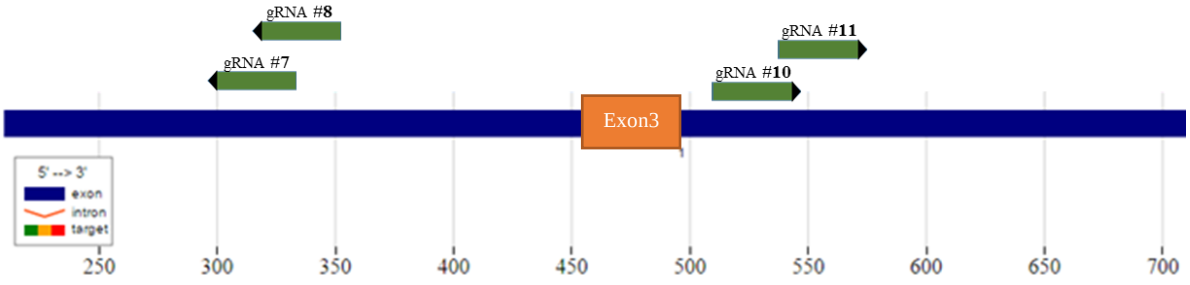

Fig. 3.1 | Position of the four gRNAs designed and chosen to be used for CRISPR/Cas9 genome editing. CHOPCHOP bioinformatic tool view of gRNAs #7, #8, #10 and #11 and their relative positions and orientation along a schematic representation of 5'- 3'*Col9a3* gene.

3.3 Functional testing of the *in silico*-designed gRNAs in a mouse fibroblast cell line.

The chosen *in silico*-designed gRNAs were subsequently tested for efficacy to select the pair that most likely was able to induce the desired deletion. Professor David Young kindly contributed to the design and the functional testing of the gRNAs. Each individual gRNA was cloned into pLKO.1 puroU6 viral vector and viral particles produced in HEK293T cells. A Lenti-Cas9-GFP vector provided the Cas9 protein complex. A mouse fibroblast cell-line (NIH 3T3) was transduced with various gRNA viral particle combinations (one up and downstream of exon 3) and the lenti-Cas9-GFP virus (Fig.3.2).

After transduction, extracted DNA from each cell line was used as template for PCR amplification to assess gRNAs efficiency, using PCR primers outside of the region to be deleted. Gel electrophoresis of the PCR amplicons coming from transduced fibroblasts confirmed gRNA pair #2 (highlighted by a yellow rectangle in Fig. 3.2) as the most efficient in generating the double strand cleavage and repair (presumably by non-homologous end joining repair (NHEJ)). The excision of the region encompassing exon 3, was indicated by the appearance of an amplicon smaller that the 'wild-type' region. All gRNA combinations produced low levels of the predicted cleavage size however, none appeared as efficient as gRNA pair #2. From this result gRNAs of pair #2 were selected to generate the desired deletion *in vivo*. The exact location of gRNA#7 and #11 with relative PAM sequence, exon 3 to be removed and PCR primers are presented in Fig. 3.3. Given the location of the gRNAs we predicted splicing between exon 2 and 4 should occur, as identified in patient samples.

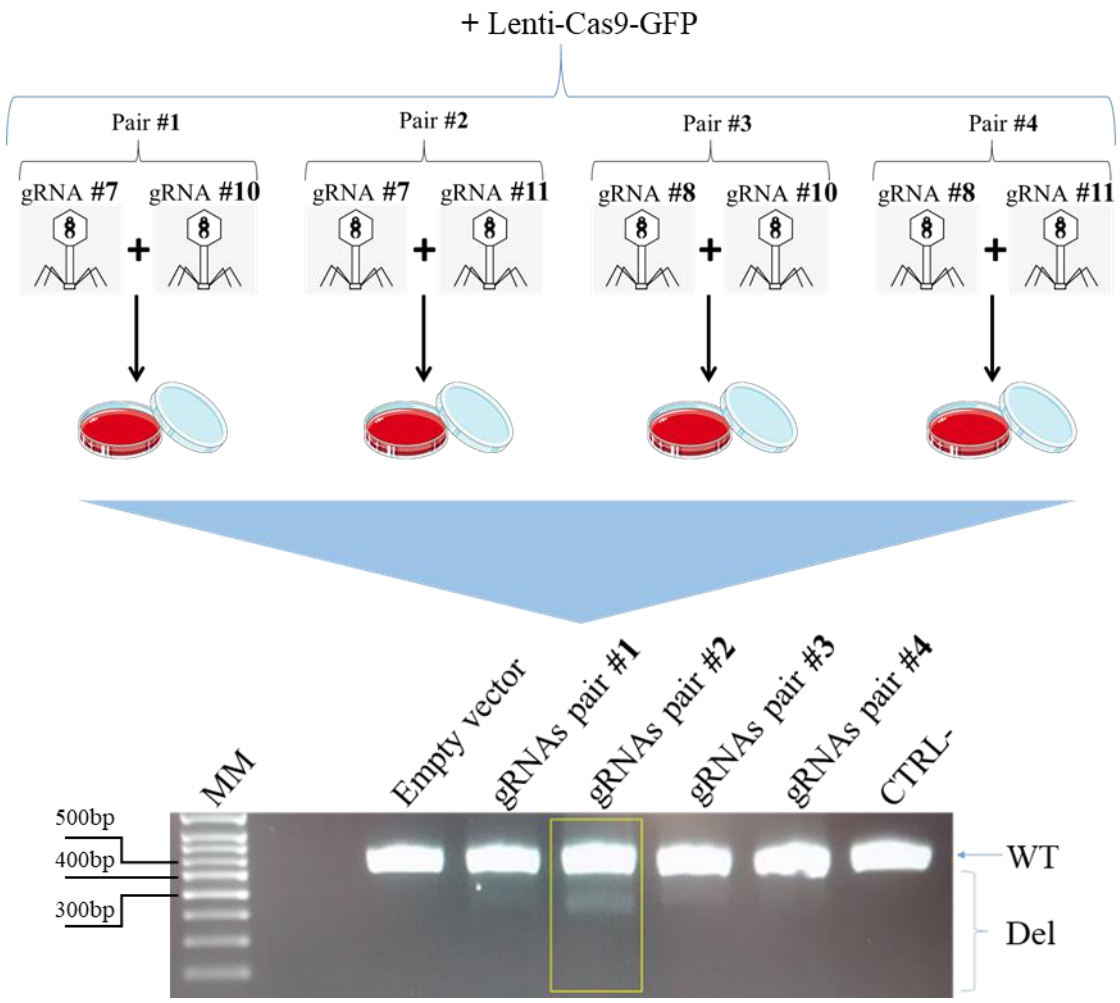

Fig. 3.2 | gRNA pair-viral transduction experimental plan and agarose gel electrophoresis of PCR products of mouse fibroblast DNA after transduction. The four gRNA pairs used to transduce mouse fibroblast prior to PCR amplification of extracted DNA. Highlighted in the yellow rectangle the gRNA pair showing relatively efficient deletion compared with the other pairs. Lane: MM, molecular marker; Empty vector, PCR product from cells transduced with empty pLKO virus (negative control); gRNAs pair #1, #2, #3, #4 corresponding respectively to pairs 1, 2, 3 and 4 of gRNAs (Table 3.1); lane :CTRL-, untransduced cells as a further negative control.

Col9a3

>chr2:180599587-180600578 (mm10)

5'-
TCTGCTGTAGCTGAGCACCCTGGCTCTGAGGCTCTTAAAGCTTCATATGAAAGTTTCACCCACCGGTAG
GTGTCCGTGGAGGGTACCGCTAATGGGCCTCCTTTCTGGAGAATGGGTGAGGAAGTGCTCACATGGAGT
CAAGAGGCTGCTCAGCTAGCCACAGCCACTCTATAAAGCTCTTAGGTCGGTGCAGAGGGACCATACGGA
GTGTCACTTGGAGGCTACTGTGCCGCTGTGTTCCTAGATGATCCCCAAATGCTGTGTGGCTGAGCTGAT
TTCTAGCTCACCCCATCCCTGGCTAGCTTGCAGAGGAGAGTTCCC**CAG▼GTATAGATGAGAGAATC**TGG
GGACCCCACAATGTCTCCACAGGCCCAGCTTTGAGGACTGGATTGGAGAATGGCCCAGCTCTAGGGTGG
GTTCCTGTTTTCAGGGCTTATATGTGCTCACTTTCATTTCCCCAGGGAGAAGCTGGCCCTCCAGGTCTG
CCTGGCCTTCCAGTAAGTGTCCCTGGTTGGAAAGGGGAGAGGTGGACCTGTCCTCACTGCTGAGGGCCT
GT**GTTGCCCTAGGAGAGGC▼CTG**AGGGCAGAGCCTGGAAGTGGGCAGGAGGGGAGCTCTTTGTGCCAGT
GTTCAGAGAAGCCAGAGAAGAGATAGTGGTGCTCTGTAGTGTCTCCCCACTGTGCCTGTGTGGGCCCCT
CACCTTGGCTGAAGATCCTCAGCCACTGATGTTCCTATGCAGTGGTCTGTTACTGGGGATGCTGTTTGG
TGAACATCCAGTTGATGGGACTGGGGCAGTCTTCTGGGGTTGCAGCAGAGTGGCAGGGTGAGCAGCCAT
CACCATGGCTGGCTGGTACCCAACATGGGGAGGACTTATGTTCCTTGATGGGGGCTAAAGCCTAGAGTC
TGATTCCTGTTGCATAACTCTGCCCTTTCCTCCCACCCAGGGACCCAAAGGGACCTCAGGGAAGCCAGG
GAAGCCGGGAGAGGCAGGACTGCCAGGA -**3'**

Fig. 3.3 | CRISPR gRNAs cleavage sites for exon3 deletion. Partial sequence of mouse chromosome 2 showing the sequence of the 2 gRNAs #7 and #11 (underlined) in the intronic regions flanking exon 3 (red). Predicted sites of cleavage by Cas9 protein (arrow heads), located between gRNA and the three nucleotides called PAM sequence (5'-NGG-3'; blue box). Exon 4 is depicted in green. Highlighted in yellow are the PCR primer locations used to verify effective deletion.

3.4 *In vitro* transcription and *in vitro* validation of gRNAs

From previous studies, a higher efficiency in gene targeting was reported when *in vitro* transcribed gRNAs were injected (Ran et al. 2013b). Therefore, we *in vitro*-transcribed the previously verified functional gRNAs #7 and #11 (2.2.4.2 In vitro transcription (IVT) of *Col9a3* #7 and #11 gRNAs). Briefly, the gRNA linked with TRACR was amplified by PCR from the corresponding pLKO vector. The 5' PCR primer used in the amplification included the T7 RNA polymerase binding sequence (TTAATACGACTCACTATA). The 3′ (reverse) primer was complementary to the 3′ region of the TRACR sequence. After purification the approximately 120 nt amplicon was used directly in the *in vitro* transcription (IVT) reaction. For the IVT, after optimisation we found that the addition of two extra guanosine nucleotides directly at the 5′ of the gRNA sequence improved transcription by T7 polymerase. Similarly, addition of several nucleotides upstream of the T7 sequence also increased the efficiency of RNA production, presumably aiding the binding of the polymerase to its target sequence. The synthesised gRNA/TRACR were also tested for their ability of cleave the *Col9a3* genomic

region, as amplified above, in an *in vitro* restriction digestion reaction with recombinant Cas9 (Fig 3.4).

Table 3.1 | List of Oligonucleotides. For the gRNA oligonucleotides the lower case bases are required for cloning into the restriction digested pLKO.1 vector. For the IVT oligonucleotides the sequences in red are the corresponding gRNA sequences.

Name	Sequence
gRNA	
mCol9a3 g#7 F	accgGATTCTCTCATCTATACCTG
mCol9a3 g#7 R	aaacCAGGTATAGATGAGAGAATC
mCol9a3 g#8 F	accgGGGCCTGTGGAGACATTGTG
mCol9a3 g#8 R	aaacCACAATGTCTCCACAGGCCC
mCol9a3 g#10 F	accgGGCCTGTGTTGCCCTAGGAG
mCol9a3 g#10 R	aaacCTCCTAGGGCAACACAGGCC
mCol9a3 g#11 F	accgGTTGCCCTAGGAGAGGCCTG
mCol9a3 g#11 R	aaacCAGGCCTCTCCTAGGGCAAC
Genomic PCR	
mCol9a3 PCR F	GTGTCACTTGGAGGCTACTGTG
mCol9a3 PCR R	CCCAGTAACAGACCACTGCATA
IVT	
3GT7 mCol9A3-7 F	atgcatTTAATACGACTCACTATAGGGATTCTCTCATCTATAC
3GT7 mCol9A3-11 F	atgcatTTAATACGACTCACTATAGGGTTGCCCTAGGAGAGGC
T7 TRACR R	AAAAGCACCGACTCGGTGCC

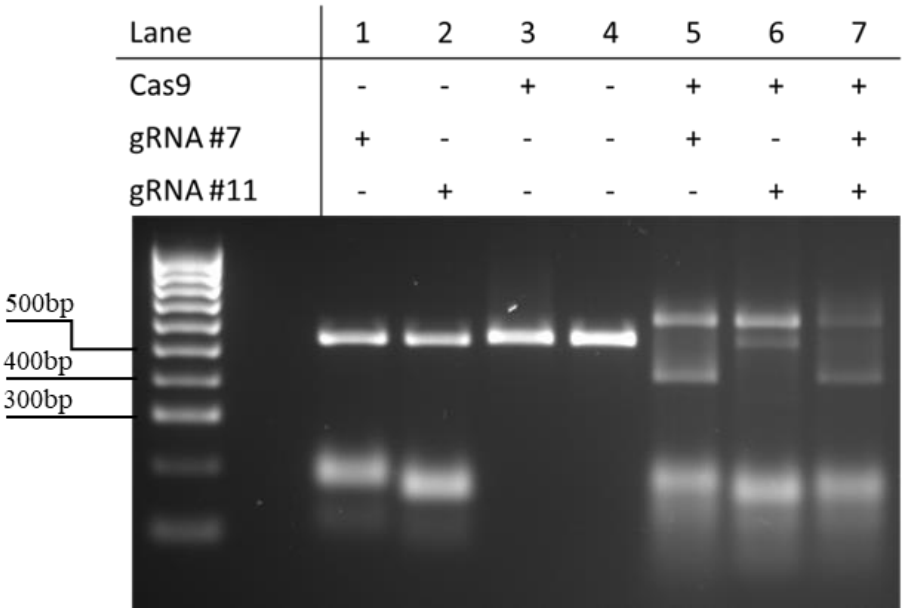

Fig. 3.4 | *In vitro* test restriction digestion using IVT gRNAs and recombinant Cas9. After PCR amplification, the purified *Col9a3* amplicon (115 ng) was incubated with recombinant Cas9 (500 ng; ToolGen) and the IVT gRNAs (350 ng) at 37°C for 1 hr, followed by agarose electrophoresis. In lane 1-4 the intact amplicon of 538bp is visible. gRNA #7 only cutting should result in a band of 117bp and gRNA #11 in a band of 364bp. A complex digestion pattern can only be observed in lanes 5-7 where all required components of the reaction are present.

3.5 Mouse zygote cytoplasm injection of *in vitro*-transcribed gRNAs

To generate the transgenic mice carrying the deletion of exon 3 of *Col9a3*, we adopted the direct zygote cytoplasm injection approach. In collaboration with Dr. Colin Miles and our animal colony manager Paul Cairns, the *in vitro*-transcribed gRNAs were injected into the cytoplasm of mouse donor zygotes along with recombinant Cas9 protein, following the Ittner and Götz stepwise procedure for pronuclear injection (Ittner and Gotz 2007). The zygotes used for injection were F_1 of a mixed C57BL/6 and CBA/ca strain background since F_1 zygotes have proved to have higher viability after injection (Ittner and Gotz 2007). The injected donor zygotes were then transferred into recipient foster mothers to obtain the first litters of transgenic mice, described as F_0.

3.6 First generation of transgenic mice (F_0) obtained after CRISPR/Cas9 zygote cytoplasm injection.

The F_0 mice obtained herein were the first CRISPR/Cas9-edited mice to be generated at Newcastle University therefore it was deemed important to fully evaluate the efficacy of pronuclear injection and whether our CRISPR/Cas9 system/strategy was effective. From the nineteen F_0 pups of first litter we extracted (ear-notch) DNA and performed PCR amplification using the same primers we previously used to assess the deletion efficiency of the different gRNA pairs. The PCR analysis showed eight out of nineteen pups were positive for a deletion (Fig. 3.5). Moreover, two of these positive mice, #8 and #17 (in yellow circle in Fig. 3.5) appeared near-homozygous for a deletion event, although each allele clearly contained a differing deletion. Thus, our zygote cytoplasm injection procedure and CRISPR/Cas9 system appeared highly effective at generation of transgenic deletion mice.

From Sanger sequence analysis of the purified deletion PCR products from each of the positive mice, we were able to confirm the efficacy and specificity of the gRNAs. No exon 3 was detected in any of the (putative deletion) amplicons purified, when their sequences were aligned with the *Col9a3* WT gene. Furthermore, Sanger sequence alignment of all the alleles containing the deletion, confirmed to some extent the heterogeneous repair (evident by the agarose gel electrophoresis; Fig. 3.5), due to the error-prone Non-Homologous End Joining (NHEJ) pathway to repair double-strand breaks. Thus, in total we generated over 10 differing *Col9a3*$^{\Delta ex3}$ alleles, with each mouse therefore representing a potential unique founder. In addition, Sanger sequences of these amplicons often gave poor results downstream of the first predicted CRISPR gRNA cleavage site, suggesting that each founder mouse was chimeric for *Col9a3*$^{\Delta ex3}$ deletion.

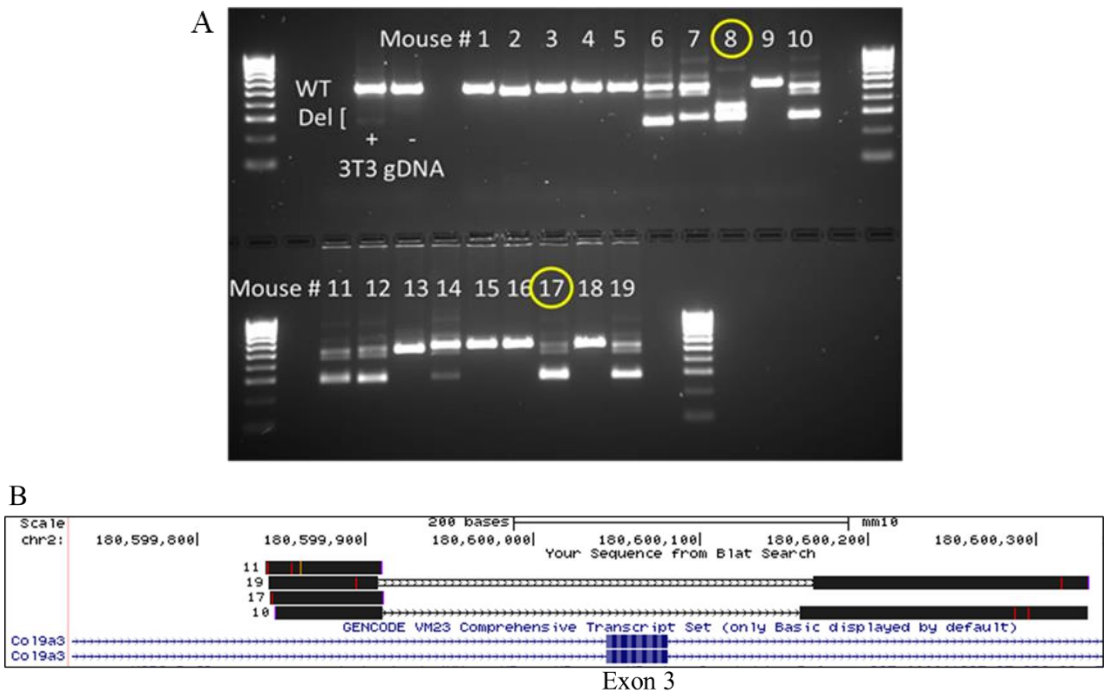

Fig. 3.5 | Genotype of the first transgenic mice (F_0). A. Gel electrophoresis showing the PCR product used to genotype the first litter of transgenic mice obtained after CRISPR/Cas9 injection. DNA extracted from mouse ear-notch at 3 weeks. From the PCR, eight mice resulted positive for the deletion, since a second smaller amplicon was visible. Two mice, #8 and #17 (yellow circle in the picture), appeared near-homozygous for a deletion. Transduced NIH/3T3 mouse fibroblast DNA and WT C57BL/6 DNA were used respectively as positive and negative control. MW, molecular weight ladder. B. BLAT alignment with UCSC Genome Browser of mouse deletion PCR products following Sanger sequencing. DNA from lower bands was sequenced using the mCol9a3 PCR F primer to test for deletion. Alignment of only those sequences with low level of chimerism is shown.

Since our Sanger sequencing had suggested some level of chimerism, we crossed all eight positive mice for the deletion with pure C57BL/6 mice to quantify and eventually select those where the mutation was also in the germline.

After crossing with pure WT, the different F_1 litters were genotyped. PCR amplification and Sanger sequencing from ear-notch DNA showed that mice number #6, #8, #10, #11, #12, #17 and #19 could be considered different founders of different *Col9a3*$^{\Delta ex3}$ lines (Fig. 3.6 A). Mouse founder #7 failed to produce any *Col9a3*$^{\Delta ex3}$ allele containing offspring. The two potentially homozygous founders #8 and #17 were bred with the same WT counterpart in the same cage and thus different deletion alleles appeared in their litter genotype. Founder line #19 could not be further analysed since the line failed to produce offspring.

Alignment of the Sanger sequenced deleted alleles confirmed the absence of exon 3 from all founders, with each founder generating differing alleles due to the error-prone NHEJ mechanism (Fig. 3.6 B; Fig. 3.7A and Fig.3.7B).

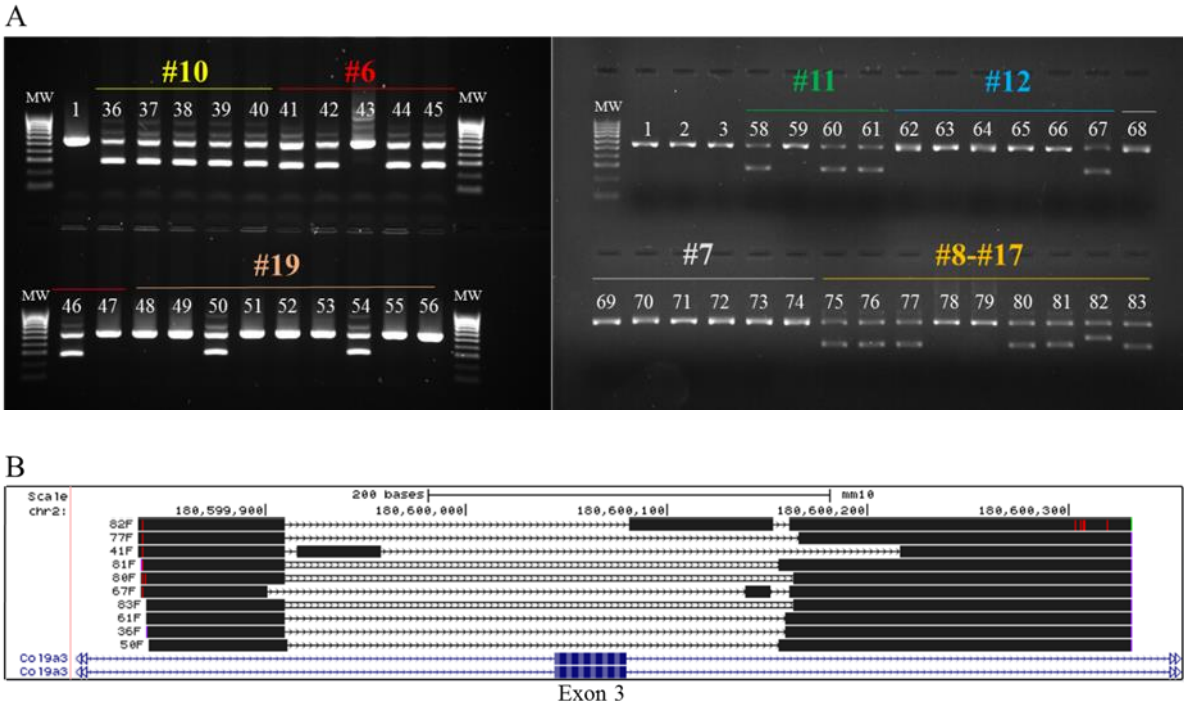

Fig. 3.6 | Genotype of F_1 of transgenic mice indicated which founder had a germline mutation. A. Gel electrophoresis of genotyping PCR products from mice born from initial founders crossed with WT (C57BL/6) animals (F_1). Offspring from different founders indicated by different colours. All founders expect #7 gave at list one litter member showing heterozygosity for the exon 3 deletion. Lane MW, molecular size marker; positive controls: lane 1= C57BL/6 DNA; lane 2= CBA/ca DNA; lane 3= NIH/3T3 DNA B. BLAT alignment with UCSC Genome Browser of mouse deletion PCR products following Sanger sequencing. A representative mouse from each founder was sequenced using the mCol9a3 PCR F primer: 36F for founder #10; 41F for founder #6; 50F for founder # 19; 61F for founder #11; 67F for founder #12; 77F, 80F, 81F, 82F, 83F for founders #8-#17.

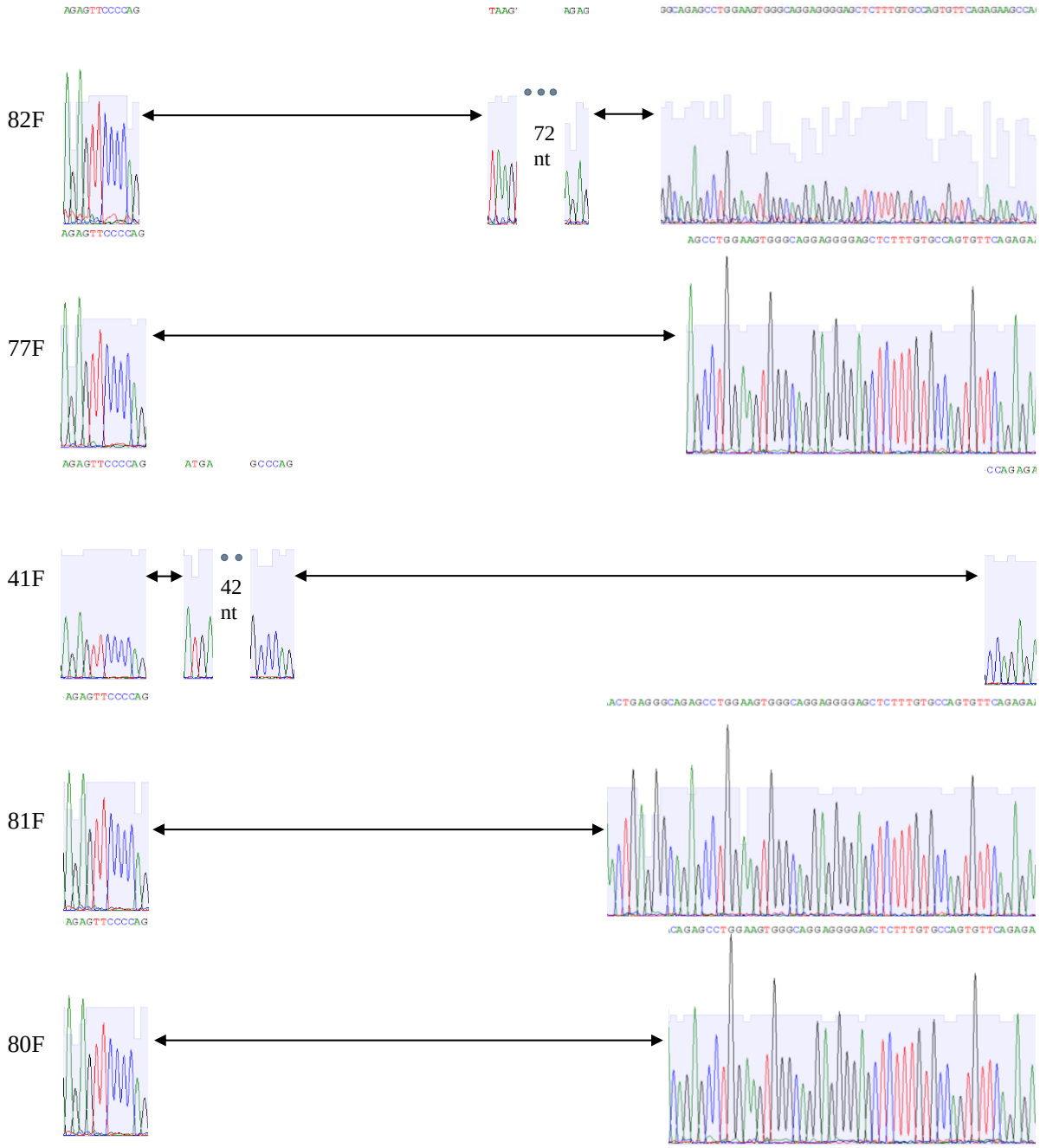

Fig. 3.7A | Sanger sequences of F_1 mice shows the heterogenous DNA repair after deletion by CRISPR/Cas9. Chromatograms of Sanger sequences of Fig. 3.6B showing the region in the deletion proximity Arrows indicate the deleted region after CRISPR/Cas9 cutting. Dots indicate the extension of the inserted regions as consequence of cell DNA repair after deletion.

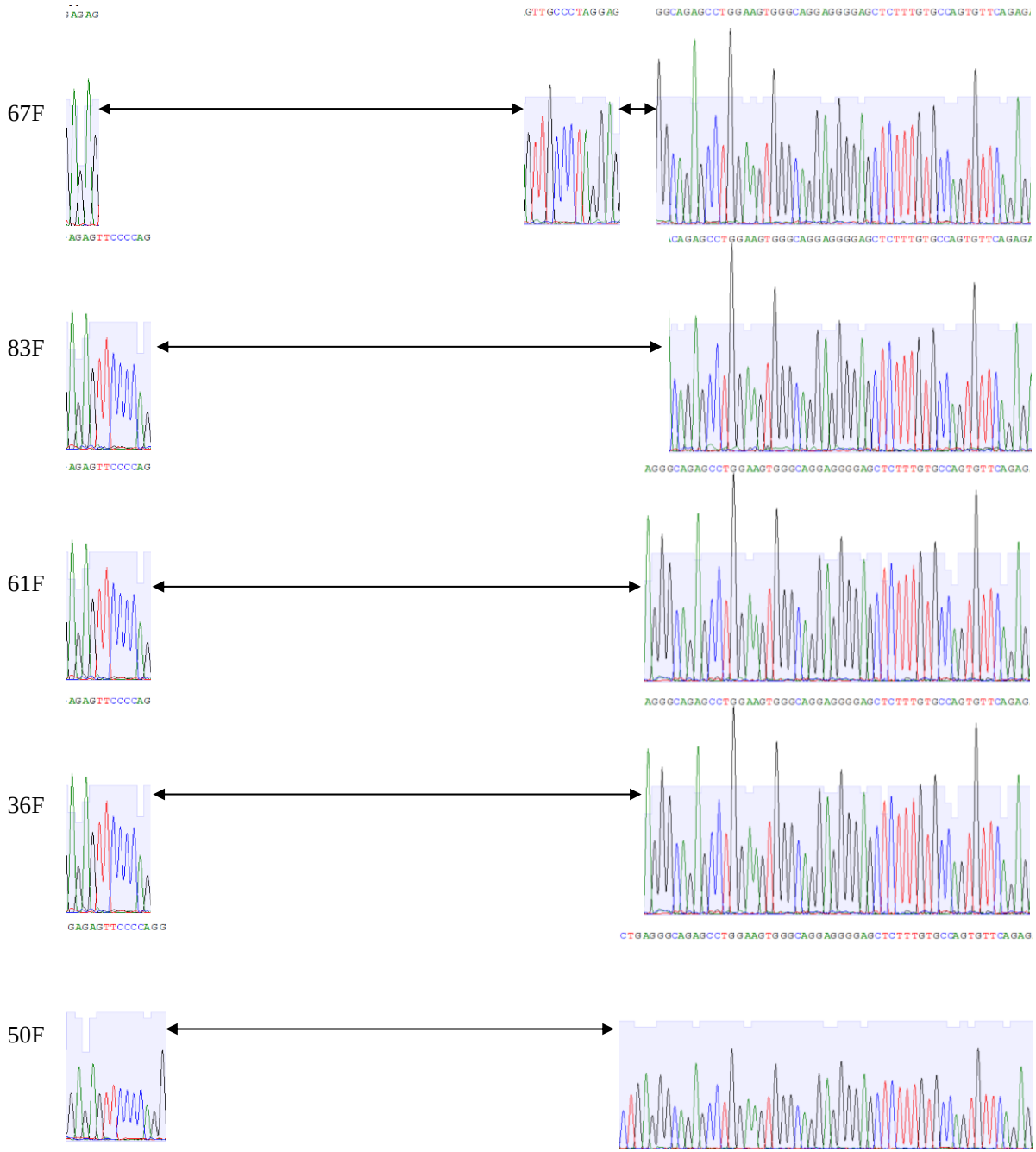

Fig. 3.7B | Sanger sequences of F_1 mice shows the heterogenous DNA repair after deletion by CRISPR/Cas9. Chromatograms of Sanger sequences of Fig. 3.6B showing the region in the deletion proximity Arrows indicate the deleted region after CRISPR/Cas9 cutting. Dots indicate the extension of the inserted regions as consequence of cell DNA repair after deletion.

3.7 cDNA and protein analysis confirmed the generation of *Col9a3*$^{\Delta ex3/\Delta ex3}$ and *Col9a3*$^{-/-}$ mutant mouse lines.

Having identified genetically differing founders and confirmed that the mutations were germline and specific for deletion of exon 3 of *Col9a3,* we examined the molecular consequences of each independent mutation event, with the purpose of determining which founder line best recapitulated the splicing events resulting in exon 3 skipping detected in MED (EDM3) patients.

RNA analysis, initially of the two founders presumed to be homozygous for the deletion (F_0 #8 and #17), was performed to assess whether a transcript of *Col9a3* which lacked exon 3 would be produced. Mice were sacrificed and RNA extracted from xiphoidal cartilage, reverse transcribed to cDNA, and PCR amplification performed using forward and reverse primers present in exon 1 and 5 of *Col9a3*, respectively. Both presumed 'homozygous' deletion founder mice produced only one PCR product, shorter than the WT amplicon and which Sanger sequencing confirmed to be lacking the 36 nucleotides of exon 3 (Fig.3.9). We could detect exon 2 spliced directly to exon 4, as no exon 3 was available to form the transcript (red square in Fig. 3.8), implying therefore that a correct splicing occurred in both mutant mice.

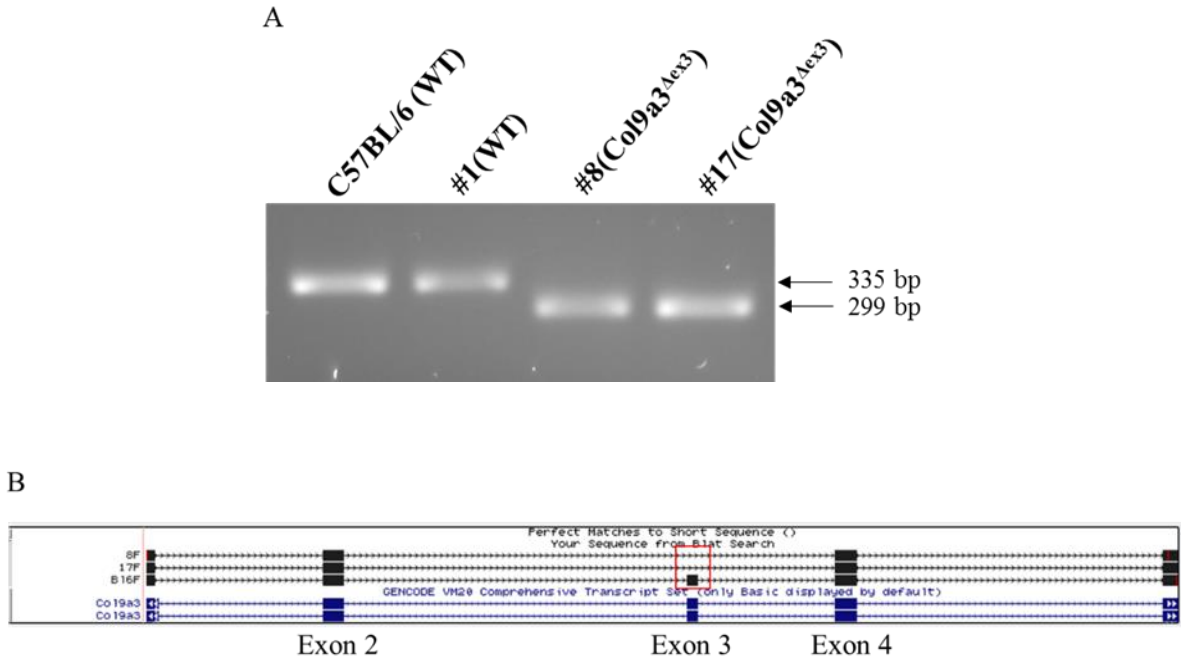

Fig. 3.8 | cDNA analysis of #8 and #17 founder mice revealed the expected splicing event. A. Gel electrophoresis following RT-PCR amplification of region spanning from exon 1 to 5 of Col9a3 transcript. #8 and #17 founders' cDNA bands are shorter than WT founder #1 and C57BL/6 cDNA. B. UCSC BLAT alignment of Sanger sequences obtained using a forward primer complementary to exon 1 of Col9a3 transcript. #8 (8F) and #17 (17F) showed identical sequence at exon 2 and 4 regions, but no exon3 when aligned with C57BL/6 (Bl6F) sequence (red square), proving that those 36 nucleotides of exon 3 are skipped as expected in both mutant mice.

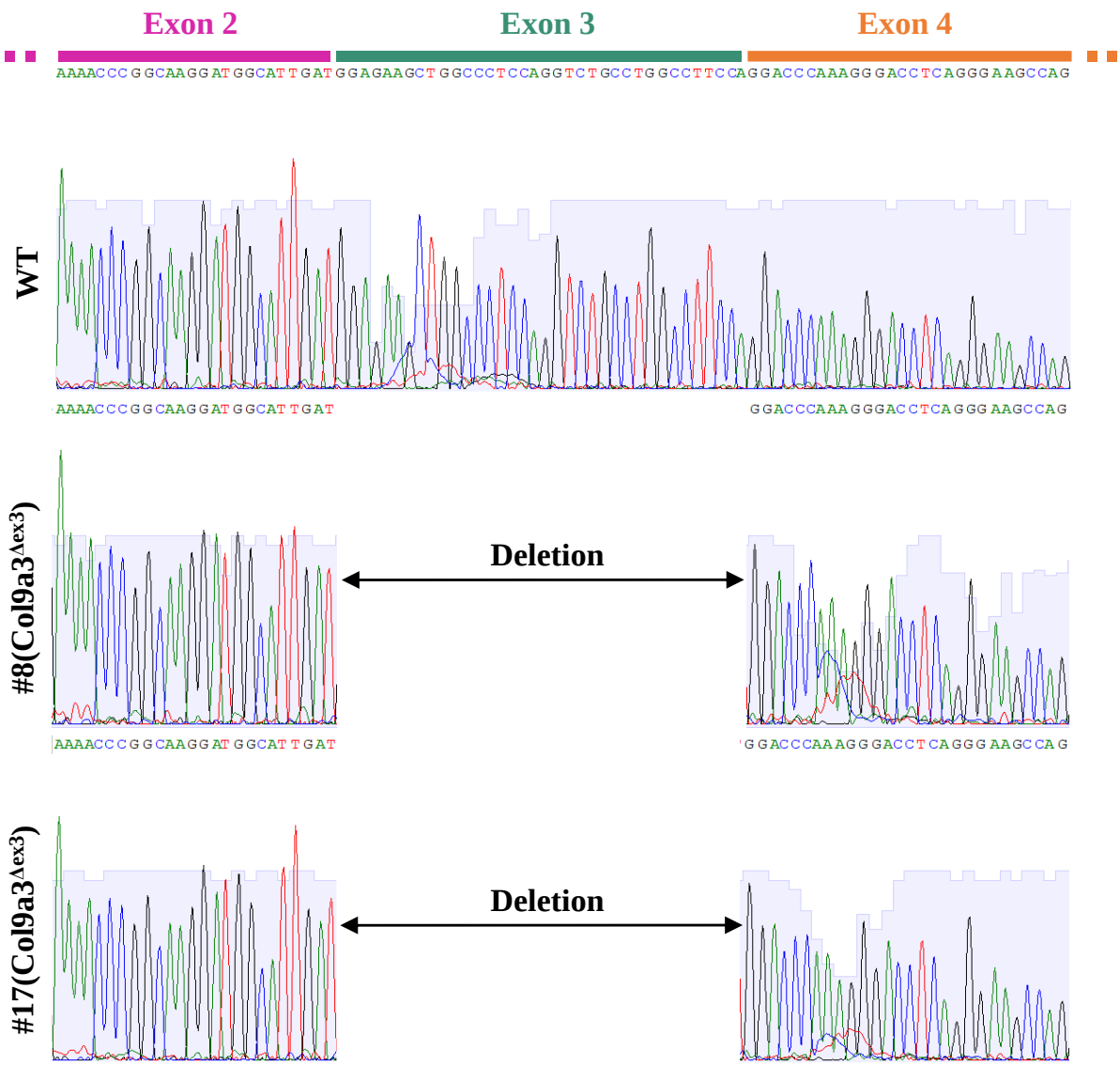

Fig. 3.9 | Sanger sequencing of #8 and #17 founder mice cDNA showed the precise deletion of exon 3. Sanger sequences obtained using a forward primer complementary to exon 1 of Col9a3 transcript. #8 and #17 showed identical sequence at exon 2 and 4 regions, but no exon3 when aligned with C57BL/6 (WT) sequence, proving that the 36 nucleotides of exon 3 are skipped in both mutant mice.

Along with the analysis of the two homozygous founders' mRNA, we examined offspring of each of the positive founder mice lines to determine if all the different mutations we had generated by CRISPR/Cas9 were producing the same exon 3 skipping spliced transcript, again using xiphoidal RNA. PCR amplification results showed that the heterozygous descendants from both founders #6 and #12 presented the expected exon skipping and WT transcript (note: additional and higher sized products were confirmed to be a PCR heteroduplex artefact, Fig 3.10 (Anglani et al. 1990). Interestingly, mice originating from

founders #10 but especially #11, surprisingly only produced one PCR band corresponding to the WT transcript (Fig. 3.10). From this, we inferred that no stable transcript was produced from founder #10 nor #11 mutated alleles.

Therefore, from the RNA screening of the different lines, we could summarise the generation of two groups of alleles which were germline: founders #6, #8, #12 and #17 whose deleted allele resulted in the predicted splicing event giving a shorter but still detectable *Col9a3* transcript lacking exon 3, that we called $Col9a3^{\Delta ex3}$; lines #10 and #11 where the mutated allele produced an unstable *Col9a3* transcript, thus null allele, denoted as $Col9a3^{-/+}$. Note that for convenience, we adopted the $Col9a3^{\Delta ex3}$ nomenclature throughout this thesis to indicate homozygous $Col9a3^{\Delta ex3/\Delta ex3}$ mutation. We decided then to proceed the analysis and breeding of founder #17 to establish the $Col9a3^{\Delta ex3}$ line and founder #11 for the $Col9a3^{-/-}$.

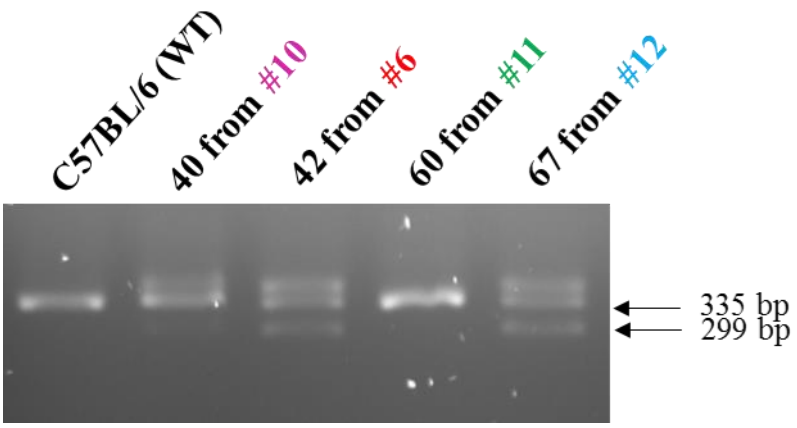

Fig. 3.10 | cDNA analysis performed on F_1 mice unravelled the consequences of allele variability generated by CRISPR/Cas9. Gel electrophoresis of cDNA amplification of region spanning from exon 1 to 5 of *Col9a3* transcript of F_1 heterozygous mice offspring from initial founders (indicated by colour). A smaller product compared to WT size amplicon, hence corresponding to a shorter transcript was detected from mice 42 and 67, descendants of founders #6 and #12, respectively. Only a WT sized amplicon was detected for heterozygous mice 40 and 60, offspring of breeding's of founders #10 and #11, respectively. WT and ΔEx3 amplicon sizes are indicated in base pairs (bp). The larger products, obvious from mouse 42 and 67 were determined to be a PCR heteroduplex artefact. This was confirmed by mixing equal amounts of cDNA from WT (C57BL/6) and $Col9a3^{\Delta Ex3/\Delta Ex3}$ Founder #17 and performing the PCR reaction (data not shown).

Subsequently, we examined the effect on protein expression of the change in transcript splicing. Protein was therefore extracted from femoral heads of a representative mouse with a shorter *Col9a3* transcript and one lacking the genetically altered *Col9a3* transcript, both compared to a WT mouse. No specific antibody recognising the collagen α3(IX) chain was available when this project started, therefore we used an antibody, kindly provided by Professor Frank Zaucke (Orthopedic University Hospital Friedrichsheim, Frankfurt, Germany) which recognises the NC4 domain of the collagen α1(IX) of collagen type IX heterotrimer. By Western blot analysis we were able to detect collagen α1(IX) protein, and therefore presumably collagen type IX heterotrimer, in WT and *Col9a3*$^{\Delta Ex3/\Delta Ex3}$ mice. However, we were unable to detect collagen α1(IX) in the protein extracted from the mouse lacking *Col9a3* transcript expression. This implies that the lack of *Col9a3* transcript and subsequent loss of collagen α3(IX) chain impairs the formation of all potential collagen type IX trimer.

We also analysed RNA-seq performed on both homozygous *Col9a3* mutant lines (*Col9a3*$^{\Delta ex3/\Delta ex3}$ and *Col9a3*$^{-/-}$) compared to WT mice (Chapter 5) to visualise the expression and splicing of *Col9a3*. These results were as anticipated by the RT-PCR findings. Essentially, for *Col9a3*$^{\Delta ex3/\Delta ex3}$ mice the expression level of *Col9a3* was almost identical to WT mice (average TPM 3063 ± 276 vs. 3090 ± 558, respectively). Further, for the *Col9a3*$^{\Delta ex3/\Delta ex3}$ mice, *Col9a3* exon 2 spliced directly to exon 4 using the GT/AG donor and acceptors as predicted. However, approximately 6% of transcripts also skipped exon 4, with exon 2 splicing directly to exon 5. Other than this, there was no evidence of aberrant donor/acceptor usage. However, for the *Col9a3*$^{-/-}$ mice, very low read numbers for *Col9a3* were detected and aligned, especially for exon 1 and 2 (with <0.4% of WT reads), which was maximally approximately 1.1% of the WT level. An aberrant novel exon was also detected for these mice, located between WT exon 4 and 5, which may represent an alternative first exon. Approximately 30% of the *Col9a3* transcripts would be predicted to start or contain this novel exon (gold line – Alt. exon – Fig. 3.11). These data, in line with the already described cDNA and protein analysis, were further evidence for the generation of a novel knockout mouse for *Col9a3.*

We could therefore conclude that our attempt at a creation of a Col9-MED mouse line was successful at the genomic level. We generated a mouse line exhibiting the deletion of exon 3 and a shorter *Col9a3* transcript, however we were unable to observe any effect on the α3(IX) protein. The stochastic creation of a second line, lacking *Col9a3* transcript and α1(IX)

protein, putatively a knockout for collagen type IX was considered an opportunity to deepen our phenotypic analysis, by comparing WT, Col9-MED and Col9-null mice. Furthermore, by assessing the consequences of *Col9a3*$^{-/-}$ mutation, we questioned whether possible overlapping phenotypic features or findings could be unraveled when comparing our mice to previously reported *Col9a1*$^{-/-}$ and *Col9a2*$^{-/-}$ mice.

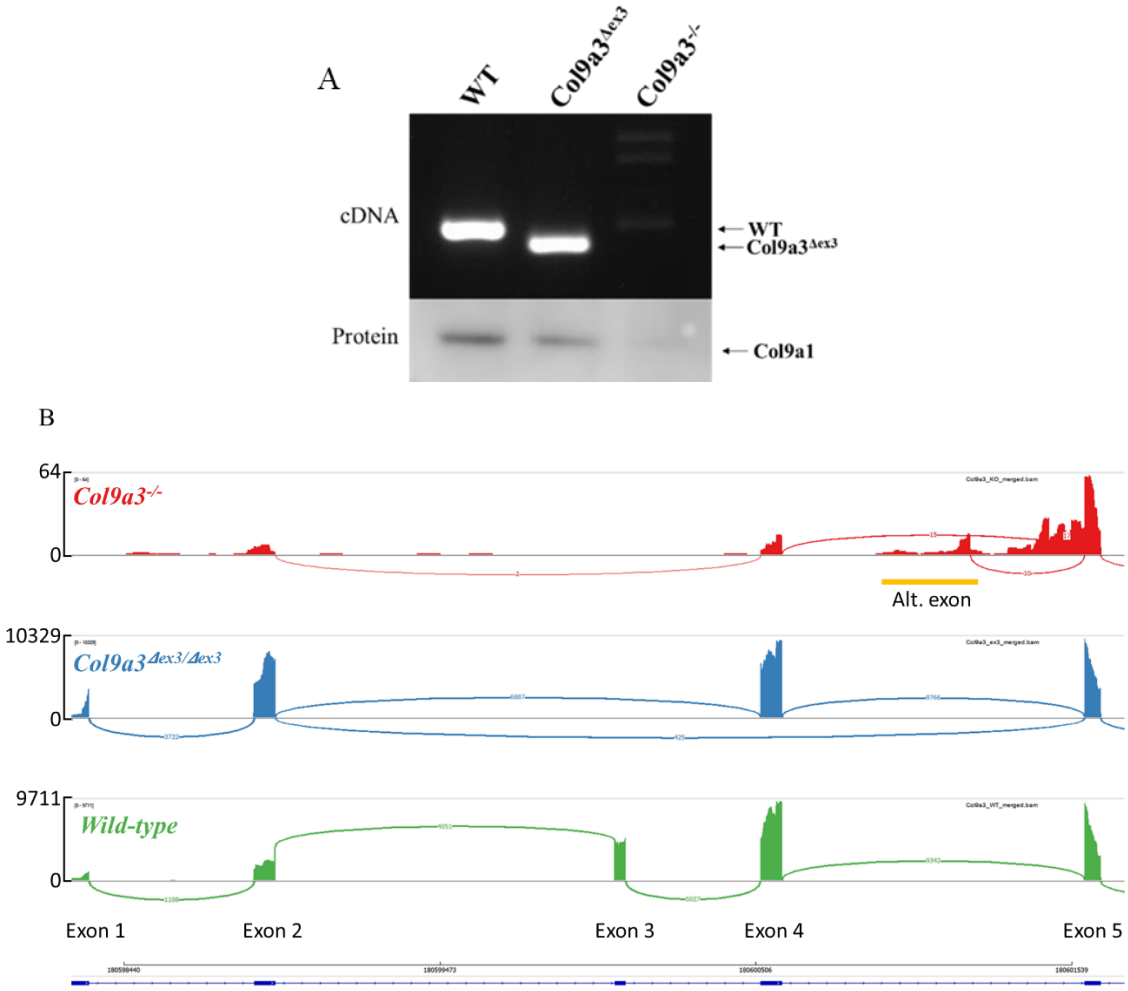

Fig. 3.11 | RNA and western blotting analysis confirmed the generation of two *Col9a3* transgenic mouse lines: *Col9a3*$^{\Delta ex3/\Delta ex3}$ *and Col9a3*$^{-/-}$. A. RNA and protein were extracted from of 3-week old femoral heads of homozygous mutant and WT mice. Gel electrophoresis of cDNA and Western blot of protein probed with antibody against α1 (IX), showed that *Col9a3*$^{\Delta ex3}$ mice produced a *Col9a3* transcript lacking exon 3, but normal collagen type IX protein. On the contrary, *Col9a3*$^{-/-}$ mice were almost completely lacking the transcript and α1 (IX) polipeptide. (Image of full blot in Appendix E, Fig. E4.B). Sashimi plot from RNA-seq data showing the number of reads covering the col9a3 exon 1 to exon 5 region confirmed the expected splicing event and the consequences of loss of exon3 in *Col9a3*$^{\Delta ex3}$ mice (blue plot). Aberrant splicing between exon 2 and 5 was apparent for approximately 6% of transcripts. *Col9a3*$^{-/-}$ mice were almost entirely lacking the transcript especially for the initial exons. Interestingly, an alternative cryptic exon (Alt. exon; gold line) was apparent, representing approximately ⅓ of the remaining transcript.

3.8 Mutation analysis of *Col9a3*$^{\Delta ex3/\Delta ex3}$ and *Col9a3*$^{-/-}$ sequences as result of CRISPR/Cas9 activity.

Having achieved our aim in obtaining the transgenic line that replicates the genomic result of selected human MED mutations, we questioned the mechanism underlying the generation of two different lines of mice when using the same genome editing system to mutate the *Col9a3* gene. Our genome-editing strategy clearly generated a wide-range of mutated alleles in the F_0 offspring even when utilising the same Cas9 and pair of gRNAs, though all induced mutations did result in the deletion of exon 3 of *Col9a3.* However, the cellular response to the various alleles clearly gave differing outcomes, evident when analysing extracted RNA and protein. Comparison of the DNA sequences encompassing the CRISPR/Cas9 deleted regions of the two alleles therefore was conducted in order to further elucidate the two different mutant lines chosen to be further phenotyped. (Fig. 3.12). We could identify the region corresponding to the Cas9 mediated double-strand break sites in-between the gRNAs and their PAM sequence. When comparing the sequence from the *Col9a3*$^{-/-}$ and *Col9a3*$^{\Delta ex3}$ mice the latter contained an additional 5 bases (AACTG) around the cleavage/repair site for gRNA#11, for which the AA was non-templated and therefore presumably added during the error-prone NHEJ repair mechanism. Since these five nucleotides are the only detected difference in the alleles between the two transgenic mice, we must assume that these are sufficient to stabilise the transcript in the *Col9a3*$^{\Delta ex3}$ animals. On the contrary, we hypothesized that in Col9a3$^{-/-}$ animals those missing five nucleotides might have created a new cryptic splice site leading to a potential unstable *Col9a3* transcript. We therefore performed *in silico* analysis of the region around the deletion in both mutant sequences, using the Human Splice Finder bioinformatics tool (HSF 3.1), able to recognise consensus sequences for potential splice sites (Desmet et al. 2009). The analysis result showed that the potential splice sites for that region were only partially the same between the two regions. According to HSF analysis, the *Col9a3*$^{-/-}$ sequence showed an additional potential acceptor splice site which instead was not present in the *Col9a3*$^{\Delta ex3}$ sequence (Fig. 3.13). This observation further supported our hypothesis of the formation of an unexpected splice site probably leading to an aberrant splicing and possibly nonsense-mediated decay of the remaining transcript.

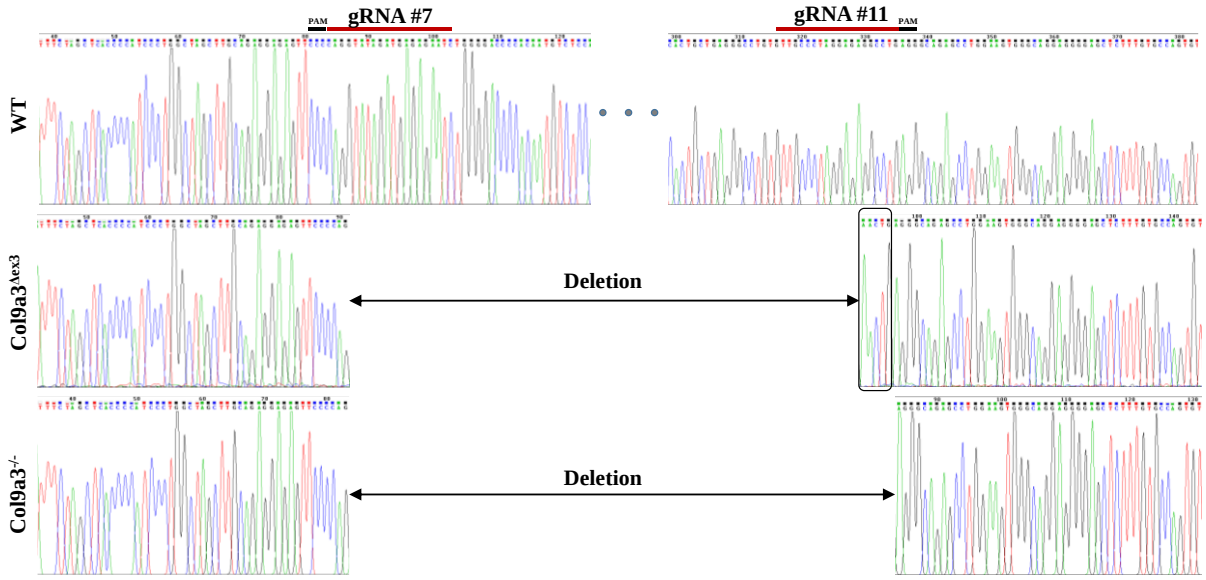

Fig. 3.12 | Differing deletion in the genomic sequence of *Col9a3*$^{\Delta ex3/\Delta ex3}$ *and Col9a3*$^{-/-}$ mice following CRISPR/Cas9 mediated cleavage and NHEJ-mediated repair. Alignment of Sanger sequence chromatograms obtained using a primer complementary to the upstream intronic region flanking the exon 3 of *col9a3* gene. Location of gRNAs (red lines) with their PAM sequences (NGG; black lines) are indicated. *Col9a3*$^{\Delta ex3/\Delta ex3}$ and *Col9a3*$^{-/-}$ differed in their deletion of exon 3 with the former having an additional 5 nucleotides, AACTG (black rectangle), of which the AA were non-templated.

Fig. 3.13 | Potential additional acceptor splice site in *Col9a3*$^{-/-}$ sequence. Human Splice Finder sequence analysis graph showing the potential acceptor and donor splice site in *Col9a3*$^{\Delta ex3}$ and *Col9a3*$^{-/-}$ genomic sequences. The presence of a potential further acceptor splice site in position 23 is shown in *Col9a3*$^{-/-}$ sequence (red square), but it is not reported in the same position in *Col9a3*$^{\Delta ex3}$sequence.

3.9 Discussion

In this first chapter, we described the strategy and procedure used to generate our mutant mice. One mutant was able to produce the *Col9a3* transcript, but lacked exon 3 (*Col9a3*$^{\Delta ex3/\Delta ex3}$ or *Col9a3*$^{\Delta ex3}$ in this thesis) and a second mouse which was almost null for the *Col9a3* transcript and also lacked collagen type IX protein (precisely α1(IX)), which we termed *Col9a3*$^{-/-}$. We created our mutant mice using the CRISPR/Cas9 genome editing system. Our choice was driven by the speed, efficacy and simplicity of this recent genome-engineering technology. We chose to use 'wild-type' Cas9, which uses HNH and RuvC nucleases to cleave both strands of the DNA. When a double strand break is induced, the cell double strand break machinery is activated and cells will go through the non-homologous end joining repair pathway, which will result in insertions or deletions disrupting the targeted locus. Cas9 can also be engineered with an inactive nuclease domain to create a 'nickase' version of the enzyme which introduces single-strand cleavages. The use of such nickases, either singularly, or in pairs, can reduce off-target effects (Ran et al. 2013a) and when combined with a repair template, prove more versatile in inserting specific mutations or specific DNA sequences. However, such 'homology-directed repair' occurs with low efficiency compared to the NHEJ methods of repair.

To generate a mouse recapitulating the splice sites mutations of Col9-MED patients, which result in exon3 skipping, the simplest approach was deemed to induce two double strand breaks in the intronic regions flanking exon 3. We therefore designed gRNAs complementary to the intronic regions flanking exon3 of *Col9a3* gene, which were initially tested for cleavage efficiency in a mouse fibroblast cell line. Subsequently, the *in vitro* verified functional gRNAs, were *in vitro* transcribed and in collaboration with Dr. Colin Miles and Paul Cairns, they were injected into the cytoplasm of mouse donor zygotes along with recombinant Cas9 protein, following a published protocol (Ittner and Gotz 2007). The genotyping result of F_0 showed a remarkable eight out of a total litter of nineteen pups to be positive for the deletion, with a suggestion that several were potentially homozygous. This result was considered positive not only because it demonstrated that the CRISPR/Cas9 system designed was efficient in mice, but also that the cytoplasm injection procedure performed in our lab had a good success rate. Our data and experience confirmed previous reports surrounding the efficacy and efficiency of generating genetically modified mice using the CRISPR/Cas9 system (Wang et al. 2013). Mutant mice were conventionally generated by

insertional mutagenesis (Kool and Berns 2009) or by gene-targeting methods (Capecchi 2005), both of which were costly, time-consuming and prone to failure. A series of studies then demonstrated that the induction of double strand breaks (DSB) in DNA can trigger genome editing by HR-mediated recombination. Moreover, it was shown that insertions or deletion mutations (indels) via the error-prone NHEJ repair pathway were obtained when a homologous repair template was not provided during induced double-strand breaks (DSBs). Therefore, alternative methods based on nucleases were developed to achieve genome editing through DSBs. Among these, meganucleases (Smith et al. 2006) zinc finger nucleases (ZNFs) (Urnov et al. 2005) or transcription activator-like effector nucleases (TALENs) (Christian et al. 2010), have been used to generate mutant mice, but such systems are complex and generally have low efficiency (Hsu et al. 2014). The type II RNA-guided endonuclease Cas9 instead, has the advantage in that its specificity is provided by a simple gRNA complementary to the region to be mutated, without the need to modify proteins. The method is therefore easy to use, more efficient and specific. In addition, to generate transgenic animals, Cas9 protein and transcribed sgRNA can be directly injected into the fertilized zygotes, without going through the typical step of ES cells targeting. This decreases considerably the time needed for generation of the mice and with it the associated costs, another reason why we opted for CRISPR/Cas9 editing as our mutagenesis strategy to generate our mice.

Sanger sequencing of all the alleles positive for the deletion on gel electrophoresis, confirmed that the shorter amplicons were missing exon 3 and the proximal intronic regions, confirming CRISPR/Cas9 efficiency and specificity, but also the variability of the sequences carrying the mutation. This variability is almost certainly due to the stochastic pattern of NHEJ repair that occurs after a double-strand break. Since these were the first CRISPR/Cas9 mutant mice generated in our facility, we deemed it important to determine the true efficiency of our mutation. Therefore, we bred the mutant animals with pure C57BL/6 mice to ensure that even if the mutant F_0 were chimeric, the deleted allele was present in the germline. From these matings, each of the six mice whose unique mutation/allele was inherited was considered at this point a founder of a new mouse line. To identify a mutant line carrying the deletion which recapitulates the human MED situation, we analysed the cartilage (xiphoid) mRNA of these lines. Interestingly, RT-PCR of the *Col9a3* region spanning exon 3 showed that some lines produced the anticipated spliced transcript (Founder #6, #8, #12 and #17) whilst no mutant transcript was detectable in others (#10 and #11). These data suggested that the

heterogeneous repair that occurred after Cas9 cleavage had also fortuitously generated a *Col9a3* null mutation. We therefore proceeded to screen the mutant lines for the expression of collagen type IX protein. No specific α3(IX) antibody was available for our study, but a specific antibody recognising the NC4 domain, in essence the α1(IX) of collagen type IX, was able to detect 'normal' levels of the protein in mice homozygous for the deletion allele Δex3. However, mice lacking *Col9a3* transcript showed no α3(IX) protein. Such observation confirmed the generation of a knockout line for *Col9a3* gene, but also that this deletion might have affected overall collagen type IX stability.

In the attempt to understand the genetic rationale for the two differing consequences of the mutations generated, we examined the region of *Col9a3* that was directly targeted and edited by CRISPR/Cas9. From sequencing of the various alleles it was apparent that the deletion in *Col9a3*$^{\Delta ex3}$ allele terminates five nucleotides upstream than for the *Col9a3*$^{-/-}$ allele. A short sequence of AACTG, different from the canonical GCCTG, was indeed found in the intronic region surrounding the deletion in *Col9a3*$^{\Delta ex3}$ mice, but not in *Col9a3*$^{-/-}$ animals. The non-templated AA were a probable result of the NHEJ repair mechanism. We might predict those five base pairs to be relevant in discerning the two mutant lines, however the link between the sequence mismatch described and the actual detection of either a shorter or absent *Col9a3* transcript remains unclear.

We could speculate that the five base pair deletion difference contributed in *Col9a3*$^{-/-}$ genomic sequence to the formation of a possible new cryptic splice site leading to an unstable transcript. This in turn would trigger the non-sense mediated decay pathway (NMD), a cellular monitoring mechanism targeting mutant mRNAs for degradation (Hug et al. 2016). However surprisingly, as it will be described in Chapter 5, the genes involved in the NMD pathway resulted downregulated in both mutant mice in costal chondrocytes RNA. When we compared the two mutant genomic regions for potential splice sites, our *in silico* analysis indeed predicted the presence of an additional splice site only present in the *Col9a3*$^{-/-}$ deletion region. Nonetheless, our hypothesis remained theoretical and taking into account that no full gene sequencing was performed, we could not exclude the possible presence of other mutations generated by possible unspecific gRNAs pairing in regions outside of those targeted.

In conclusion we successfully used the CRISPR/Cas9 genome editing system to generate a *Col9a3*$^{\Delta ex3}$ mutant mouse line which reproduces Col9-MED patients genetic defect. We also generated a second mouse line, *Col9a3*$^{-/-}$, which lacked the *Col9a3* transcript and collagen

type IX protein. The deep phenotyping performed on both mutant mouse lines will be described in detail in the next chapters of this thesis.

Summary highlights

- Our designed CRISPR/Cas9 genome editing system was efficient and specific both *in vitro* and *in vivo*
- Two mouse lines were generated as a result of the heterogeneous NEHJ repair mechanism after Cas9 cleavage.
- A *Col9a3*$^{\Delta ex3}$ mouse, mimicking the MED situation and able to produce a transcript lacking exon 3, but presumably not affecting collagen type IX protein assembly, was successfully generated.
- A *Col9a3*$^{-/-}$ mouse, null for *Col9a3* transcript and collagen type IX protein was fortuitously generated and was maintained to complement the *Col9a3*$^{\Delta ex3}$ mouse phenotypic analysis.

Chapter 4.

Bone phenotypic analysis of mice with altered or absent Collagen Type IX

4.1 Introduction

Patients diagnosed with MED due to exon 3 skipping mutations in the gene encoding the α3 polypeptide of collagen type IX molecule (OMIM#600969), present a relatively mild phenotype when compared to those diagnosed with other MED-causing mutations (eg. *COMP* and *MATN3*). Orthopaedic and radiologic evaluation of EDM3 patients have shown abnormalities involving mainly the pelvic girdle and the lower limbs. Previous studies showed evidence of flat and mildly dysplastic hips, flat and irregular knees and ankles, but overall normal stature (Bonnemann et al. 2000, Jeong et al. 2014, Nakashima et al. 2005, Paassilta et al. 1999, Lohiniva et al. 2000). It is still unknown how collagen type IX splice site mutations, and consequently the skipping of exon 3, can result in such clinical findings. Long bone formation relies on endochondral ossification, where an initial cartilaginous scaffold is replaced by bone, leaving a layer of cartilage, named epiphyseal growth plate, through which post-natal longitudinal bone growth occurs. Considering this mechanism and taking into account the EDM3 clinical findings, our hypothesis was that collagen type IX, an important component of the cartilage ECM, may have a direct or indirect role in bone formation, development and/or homeostasis.

We therefore assessed the *Col9a3*$^{\Delta ex3}$ mice for their potential use as a model for Col9-MED, starting with an evaluation of their skeletal phenotype. The *Col9a3*$^{-/-}$ mouse was used as constant comparator in all the phenotypic analysis.

In this chapter the bone phenotype of our mutant mice was explored exploiting two main techniques: x-ray morphometric analysis and micro-computed tomography (μCT). The main purpose was to test for similarities between the skeletal features of *Col9a3*$^{\Delta ex3}$ mice and EDM3 patients. In addition, the comparison between our two mutant mice could help to unravel if an ECM containing a mutated collagen type IX would result in a similar or different bone phenotype compared to a matrix lacking collagen type IX. Together, these data would add to our understanding of the role of collagen type IX in bone development.

4.2 Radiographic analysis of *Col9a3$^{\Delta ex3}$* and *Col9a3$^{-/-}$* mice.

4.2.1 X-ray analysis of hind limbs and hips.

The skeletal morphology of *Col9a3$^{\Delta ex3}$* and *Col9a3$^{-/-}$* mice was assessed by analysis of whole-body x-ray images. Observations at birth did not indicate any obvious morphological or size difference in any of the mutant mice compared to WT. For this reason, we opted to evaluate later stages of post-natal bone development. Radiographic images were taken from animals at 3 weeks, corresponding to the weaning age, and at 9 weeks, the stage in which mice reach sexual maturity and their bone growth drastically slows (Jilka 2013). An initial evaluation of heterozygous *Col9a3$^{\Delta ex3/+}$* and *Col9a3$^{+/-}$* mice compared with their WT littermates identified no differences in size or bone morphology, hence from this stage, only homozygous mice were phenotyped further. Radiographic images of the dorsal view of 3- and 9-week old female and male animals showed that *Col9a3$^{\Delta ex3}$* and *Col9a3$^{-/-}$* skeletal phenotypes were not influenced by sex. Therefore for the full radiographic analysis only the gender whose highest number of mice was available at the moment of data collection was used, in order not to require more animals, in compliance with the 3Rs principle (Flecknell 2002).

From whole-body radiographs, at 3-weeks of age, the height of female homozygous *Col9a3$^{\Delta ex3}$* mice was the same size as their female WT littermates, whereas *Col9a3$^{-/-}$* mice were shorter in size overall (Fig. 4.1). The radiographic investigation applied, was based on the measurement of established skeletal parameters previously used in the assessment of mouse models of other skeletal dysplasias. The length of the femur and tibia were markers of endochondral ossification. The extent of the angle formed by the protrusion of the tuberosity of the ischium from the ilium was analysed as a marker of general hip development and potential dysplasia. At 3 weeks of age both mutant mice showed tibias on average significantly shorter compared to WT, which were respectively 96% for *Col9a3$^{\Delta ex3}$* and 89% for *Col9a3$^{-/-}$* (Fig. 4.2A). When we measured the femur length, only *Col9a3$^{-/-}$* mice presented a significant reduction at 3 weeks, as their femur was 91% of WT length. When mice reached skeletal maturity at 9 weeks of age, both *Col9a3$^{\Delta ex3}$* and *Col9a3$^{-/-}$* male animals had significantly shorter femurs at 95% and 85% the length of WT bones, respectively. Only male *Col9a3$^{-/-}$* mice displayed a reduction of the average tibia length (89% of WT) at 9-weeks (Fig.4.2B).

Upon examination of the hip angle of mutant mice, we detected a strongly wider average hip angle in *Col9a3*$^{-/-}$ mutant mice. Measurements showed a 2-fold increase in the angle of 3-week old female mice and 8-fold increase in 9-week old male *Col9a3*$^{-/-}$ mice angle compared to WT (Fig. 4.2A-B). This observation suggested the *Col9a3*$^{-/-}$ mice hip to be dysplastic, as morphologically evident in Fig 4.1. Although in *Col9a3*$^{\Delta ex3}$ mice we detected a slight increase in hip angle this was not statistically relevant compared to that of WT littermates at 3 weeks of age. Moreover, *Col9a3*$^{\Delta ex3}$ hip angle values were equal to WT in 9-week old mice. Interestingly, along with the dysplasia of the hip, in *Col9a3*$^{-/-}$ mice we observed a broadened tibial condyle and metaphysis (red circle in Fig. 4.1) which was consistent in 9-week animals of the same genotype. No such phenotype was observed at any age for the *Col9a3*$^{\Delta ex3}$ mice.

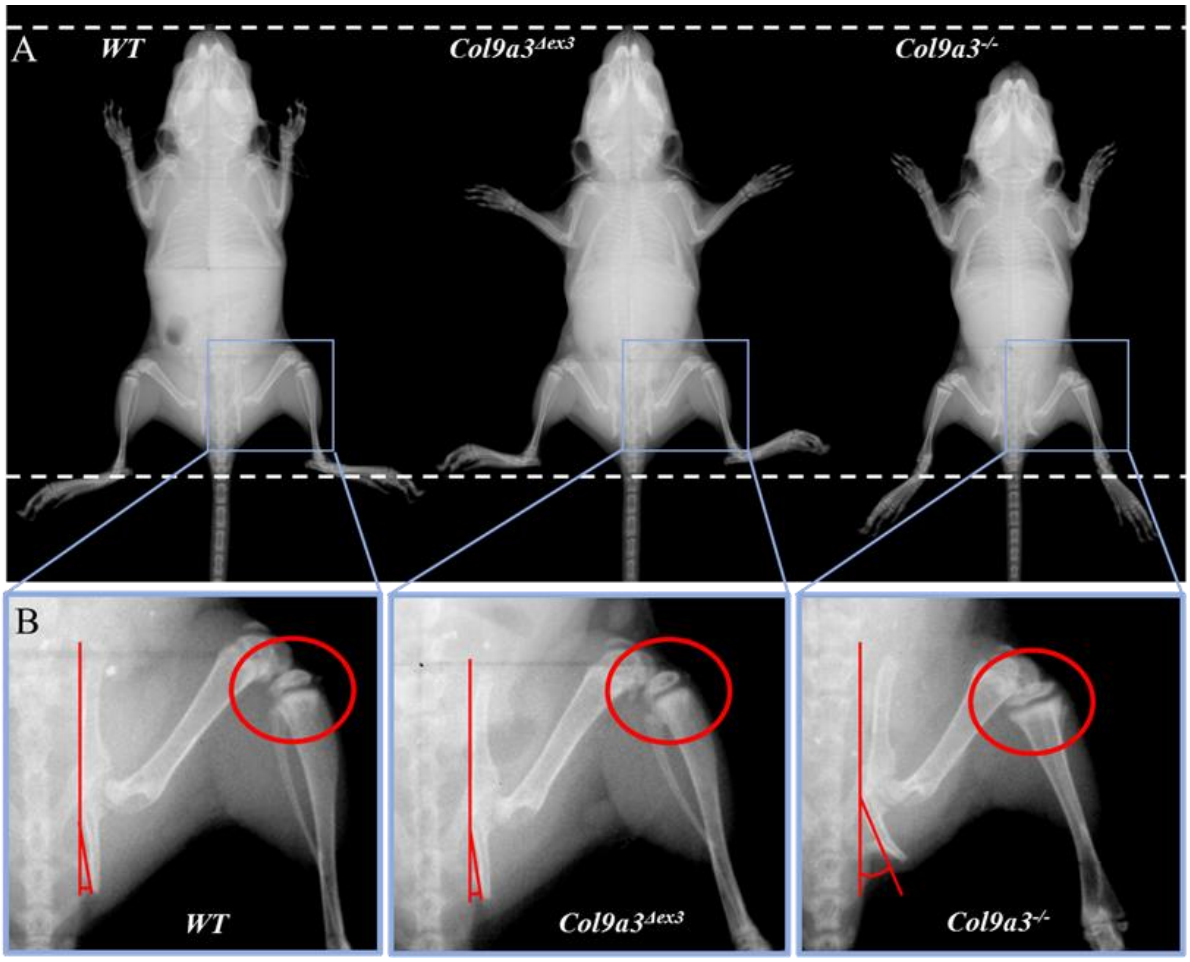

Fig. 4.1 | Radiographic images of WT, *Col9a3*$^{\Delta ex3}$ and *Col9a3*$^{-/-}$ skeletal phenotype.
A. Representative X-ray images of 3 week old female mice (dorsal view). B. close-up of 3-week old hips and right legs. The extent of alteration of the hip angle and the tibial condyle are indicated in red. *Col9a3*$^{-/-}$ mice displayed irregular and wider tibial epiphyses and hip dysplasia (assessed by hip angle) compared to *Col9a3*$^{\Delta ex3}$ or WT mice, which had a similar phenotype.

A

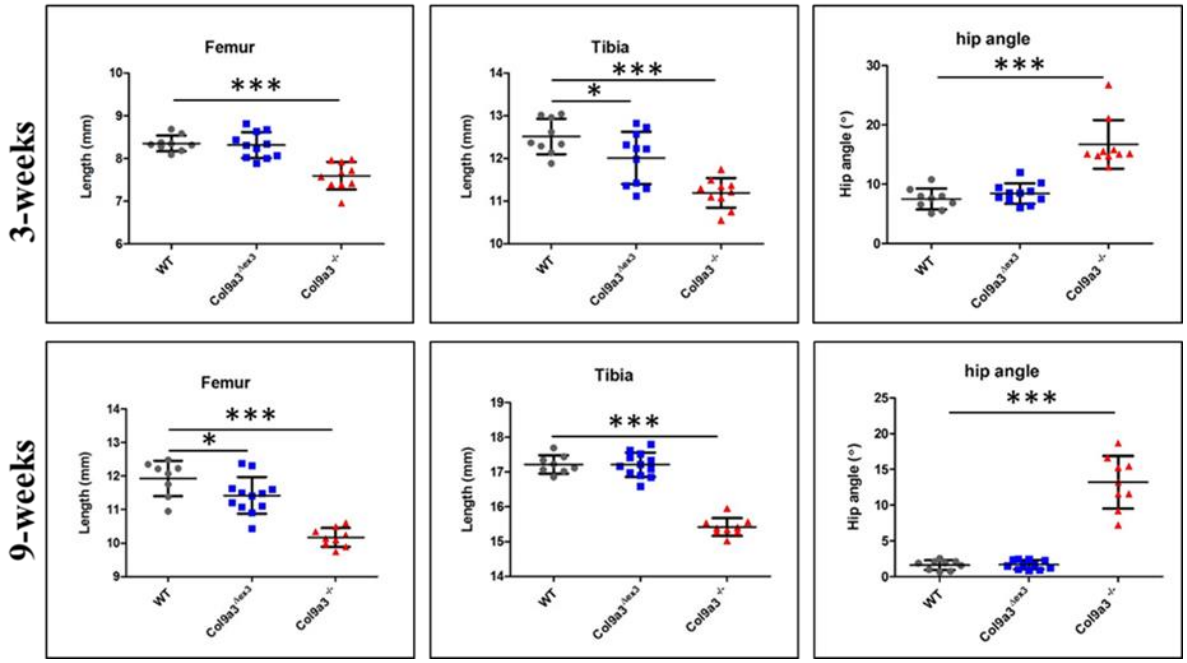

B

Age (Weeks)		WT	*Col9a3^{Δex3}*	*Col9a3$^{-/-}$*
Femur (mm) ± SD	3	8.35 ± 0.18	8.31± 0.30	**7.59 ± 0.32*** **
	9	11.97 ± 0.51	**11.34 ± 0.49 ***	**10.17 ± 0.27*** **
Tibia (mm) ± SD	3	12.51 ± 0.41	**12.01± 0.61***	**11.19± 0.34*** **
	9	17.27 ± 0.28	17.18 ± 0.34	**15.42 ± 0.25*** **
Hip angle (°) ± SD	3	7.50 ± 1.75	8.43 ±1.71	**16.71± 1.71*** **
	9	1.62 ± 0.66	1.67 ± 0.62	**13.21 ±3.67*** **

Fig. 4.2 | Morphometric analysis of femurs, tibia and hip angle in WT, *Col9a3^{Δex3}* and *Col9a3$^{-/-}$* mice. A. Tibia and femur bone lengths and hip angle were measured at 3 weeks of age in female mice (WT N=9; *Col9a3^{Δex3}* N=11; *Col9a3$^{-/-}$* N= 10) and 9 weeks of age in male mice (WT N=9; *Col9a3^{Δex3}* N=11; *Col9a3$^{-/-}$* N= 9) of all 3 genotypes. B. Table showing the average values and statistical significance of femur, tibia and hip angle measurements. SD = standard deviation; *p<0.05, ***p<0.001, two tailed t-test.

4.2.2 Morphometric analysis of the skull.

According to the literature, no cranio-facial abnormalities have been reported in EDM3 patients. However, loss of function recessive mutations in the *COL9A3* gene have also been associated with Stickler syndrome. Like MED, Stickler syndrome is a genetically heterogeneous disorder with a highly variable clinical spectrum. Among the clinical findings of Stickler syndrome caused by loss of function mutations in *COL9A3* gene are high myopia, hearing loss and mid-face hypoplasia (Faletra et al. 2014). We therefore, assessed the x-rays of the skull of mice of all three genotypes to identify any relevant morphological changes due to the *Col9a3* mutations carried by our mice. The morphology of *Col9a3*$^{\Delta ex3}$, *Col9a3*$^{-/-}$ and WT mice skulls was evaluated at 3 and 9 weeks on mice dorsal radiographs. The bones that form the skull originate from different processes according to their position. Endochondral ossification is the mechanisms through which the cranial base and caudal cranial vault are formed, whereas intramembranous ossification is at the base of the craniofacial and rostral cranial vault development (Percival and Richtsmeier 2013).

Following established guidelines for the assessment of mouse models for genetic skeletal diseases, two parameters were taken into account: the inner canthal distance (ICD) measured as a marker of intramembranous ossification; and skull length as indication of endochondral ossification in the skull (Fig.4.3). The ICD was similar for all genotypes at both ages examined. In contrast, the skull length was influenced by genotype, but only significantly in *Col9a3*$^{-/-}$ mice. The average skull length of *Col9a3*$^{-/-}$ female mice at 3 weeks of age and in male mice at 9-weeks was 92.8% and 89.4% of the average value measured in WT littermates, respectively (Fig. 4.4A-B). Although the *Col9a3*$^{\Delta ex3}$ mice showed a small decrease in skull length at both time points investigated, the differences were not statistically significant.

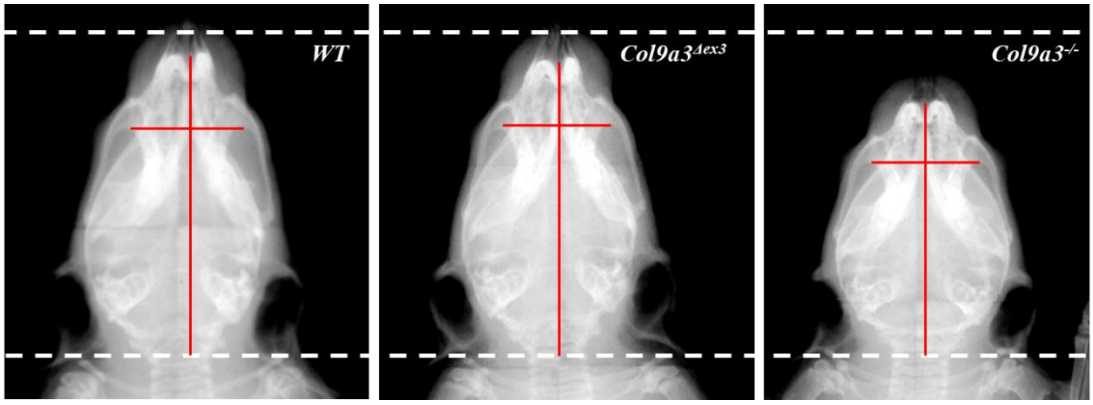

Fig. 4.3 | Radiographic images of skull parameter comparison in WT, *Col9a3*$^{\Delta ex3}$ and *Col9a3*$^{-/-}$ mice. Representative skull x-ray dorsal view images of 3-week old female mice. The horizontal and vertical red lines represent ICD and skull length respectively. White dashed lines are indicated as reference for the skull length.

A

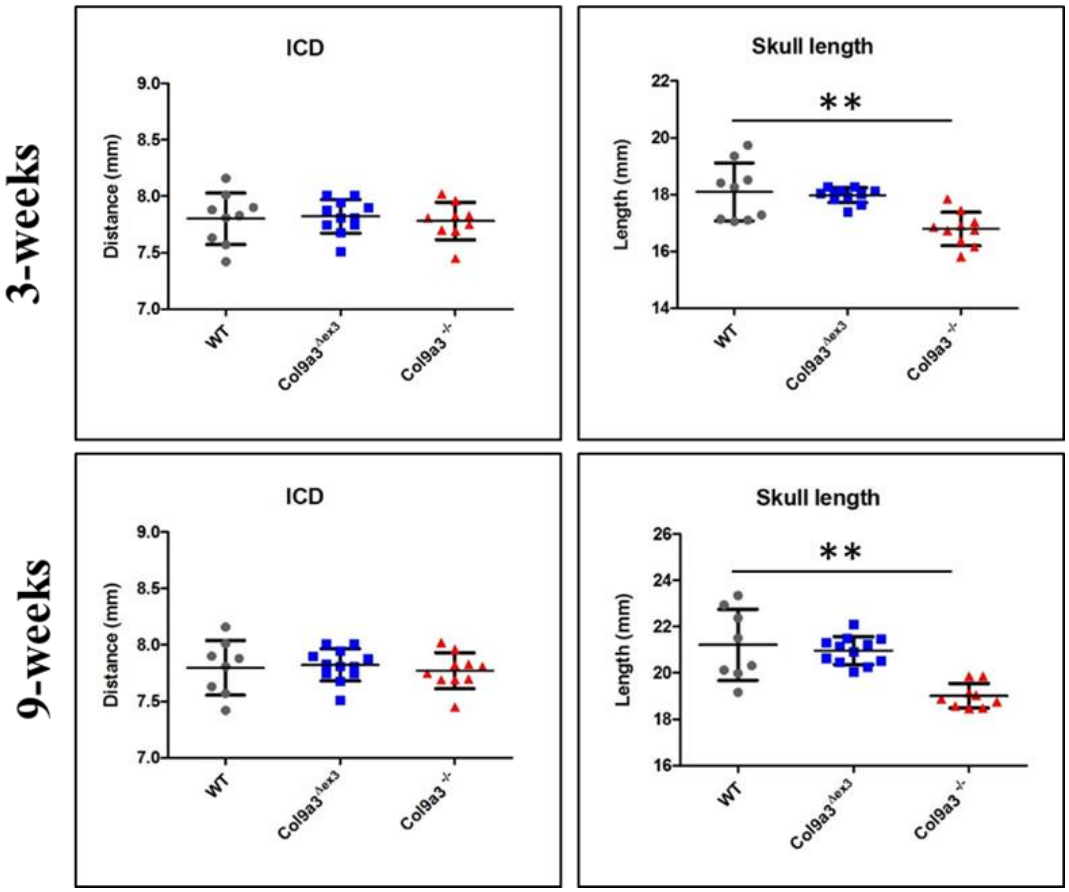

B

Age (Weeks)		WT	*Col9a3$^{\Delta ex3}$*	*Col9a3$^{-/-}$*
ICD (mm) ± SD	3	6.73 ± 0.26	6.78 ± 0.14	6.77 ± 0.15
	9	7.80 ± 0.23	7.82 ± 0.15	7.78 ± 0.16
Skull Length (mm) ± SD	3	18.09 ± 1.01	17.97 ± 0.26	**16.79 ± 0.58****
	9	21.25 ± 1.44	20.93 ± 0.60	**19.01 ± 0.53****

Fig. 4.4 | Morphometric analysis of the skull in WT, *Col9a3$^{\Delta ex3}$* and *Col9a3$^{-/-}$* mice.
ICD and skull lengths were measured at 3 weeks of age in female mice (WT N=9; *Col9a3$^{\Delta ex3}$*N=11; *Col9a3$^{-/-}$* N= 10) and 9 weeks of age in male mice (WT N=9; *Col9a3$^{\Delta ex3}$*N=11; *Col9a3$^{-/-}$* N= 9) of all 3 genotypes. A. The average ICD and Skull length of homozygous *Col9a3$^{\Delta ex3}$* and *Col9a3$^{-/-}$* mice is shown. B. Table showing the mean values and statistical significance of femur, tibia and hip angle measurements ±SD (standard deviation). Statistical analysis: **p<0.01, two tailed t-test.

4.3 *Col9a3$^{\Delta ex3}$* and *Col9a3$^{-/-}$* mice differ in their bone ultra-structure.

To investigate the effects on bone phenotype following deletion of exon 3 of *Col9a3* gene or the ablation of collagen type IX protein, we performed µCT analysis on mice of all three genotypes. We performed the analysis on adult long bones, using femurs and tibiae from 18-week old male mice. The two types of bone tissues are cortical and trabecular, which differ in structure and function. Cortical bone is compact and constitutes the outer part of bones where its function is to provide protection and support but also to be a calcium reservoir for the functioning of all body organs. The outer surface of cortical bone is called the periosteum, and its inner surface endosteum, which is the perimeter dividing cortical from trabecular bone. The trabecular, also called cancellous bone, is a spongy type of bone made by a porous network of thin columns of bone forming the trabeculae. It is primarily found at the end of long bones and in the interior vertebrae. It harbours blood vessels and bone marrow.

3D reconstruction of scanning images with a resolution of 4.5 µm allowed for visualisation of the trabecular structure of the distal femurs and the proximal tibiae. For cortical bones, we analysed the femur and tibia shafts, whose structure was 3D reconstructed from scanning images with a resolution of 9 µm.

4.3.1 Trabecular analysis of femurs in adult mice.

Trabecular analysis showed no difference in the total volume (TV) and bone volume (BV) of the region of interest in *Col9a3*$^{\Delta ex3}$ femurs, but these parameters were significantly increased (by 35% and 23%, respectively) in *Col9a3*$^{-/-}$ mice compared to WT controls (Fig 4.5 and Table 4.1). Interestingly, when the ratio of the segmented bone volume to the total volume (BV/TV) was evaluated, a significant 19% decrease in *Col9a3*$^{\Delta ex3}$, but no relevant change in *Col9a3*$^{-/-}$, was observed. The mean thickness of trabeculae (Tb.Th) was reduced only in *Col9a3*$^{-/-}$ femurs at 89% of WT femoral Tb.Th. The measure of the average number of trabeculae per unit length, called trabecular number (Tb.N), and the mean distance between trabeculae, trabecular separation (Tb.Sp.) were both significantly changed in *Col9a3*$^{\Delta ex3}$. While we measured a 16% increased trabecular separation in *Col9a3*$^{\Delta ex3}$ mice when compared to WT, their trabecular number was significantly reduced to 80% of WT mean values, suggesting a less compact trabecular bone (Fig. 4.5). No difference was observed in *Col9a3*$^{-/-}$ mice for these variables. The trabecular pattern factor (Tb.Pf.) as well as the structure model index (SMI), which defines the plate- versus rod-like characteristic of the trabecular bone structure, were not altered compared to the mean value of WT in both mutant mice. The final parameter analysed was an index that measures the degree of connectivity of trabeculae normalised by TV, the connectivity density (Conn. Dn.). *Col9a3*$^{\Delta ex3}$ trabecular connections were significantly less dense with mean values corresponding to 76% of mean control values. The findings, in relation to Tb.N and Tb.Sp. values, suggest a less structured trabecular bone in *Col9a3*$^{\Delta ex3}$ femurs.

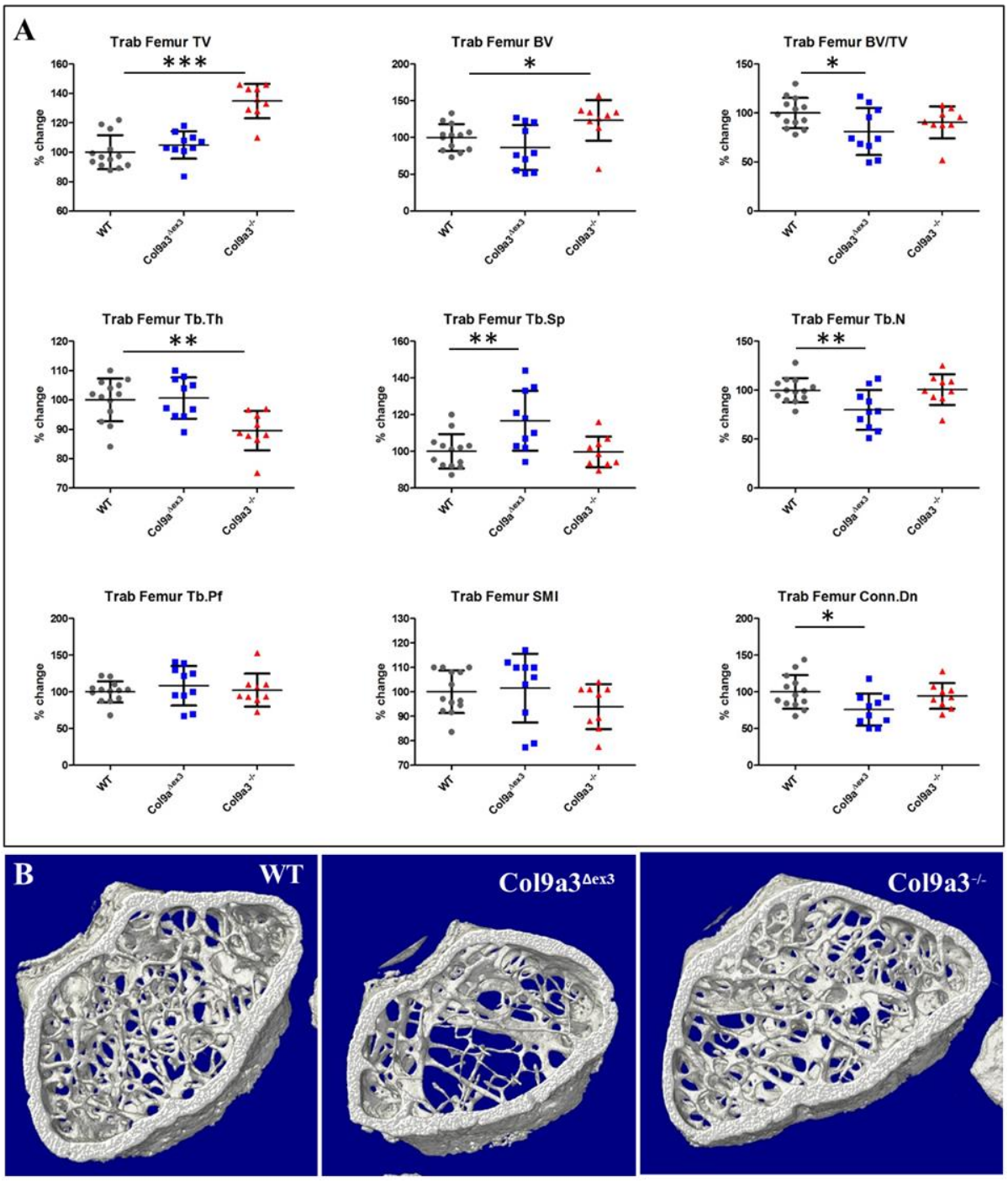

Fig. 4.5 | Trabecular morphometry of femurs of 18-week old mice. A. Morphometric analysis of trabecular bone from femurs of 18-week old male WT (N=13) *Col9a3*$^{\Delta ex3}$ (N=10) and *Col9a3* $^{-/-}$ (N=9) mice. Data of the graphs, relating to *Col9a3*$^{\Delta ex3}$ and *Col9a3* $^{-/-}$ mice are shown as percentage of change compared to WT measurements. Data are shown as means ±SD (standard deviation). Statistical analysis (*Col9a3*$^{\Delta ex3}$ or *Col9a3* $^{-/-}$ vs WT) : *p<0.05, **p<0.01, ***p<0.001, two tailed t-test. B. Cross-sectional images of 3D µCT reconstructions using CTVox software of femurs from the median animals of each genotype, taken 50 slides (225 µm) away from the femoral growth plate.

Trabecular analysis of the femur (18-weeks)			
	WT (n=13)	***Col9a3*$^{\Delta ex3}$ (n=10)**	***Col9a3*$^{-/-}$ (n=9)**
TV (mm^3)	2.27 ± 0.26	2.38±0.21	**3.07±0.27*** **
BV (mm^3)	0.45±0.08	0.39±0.14	**0.55±0.12***
BV/TV (%)	19.76 ± 3.05	**16.03 ± 4.77***	17.86 ± 3.19
Tb.Th (µm)	61.34±4.43	61.80±4.37	**54.95±4.11****
Tb.Sp (µm)	184.92±17.37	**215.68±30.46****	184.52±15.54
Tb.N (mm)	3.22±0.39	**2.57±0.65****	3.24±0.51
Tb.Pf (1/mm)	19.51±2.81	21.17±5.27	19.99±4.36
SMI	2.18±0.19	2.22±0.31	2.05±0.20
Conn.Dens. ($1/mm^3$)	392.78±90.05	**298.33±85.60***	370.49±68.96

Table 4.1. | µCT analysis of trabecular bone in femurs of WT, *Col9a3*$^{\Delta ex3}$ and *Col9a3*$^{-/-}$ male mice at 18 weeks of age. Data obtained from µCT trabecular parameters measurements in femurs and used to generate the graphs in Fig. 4.5. Data are shown as means ±SD (standard deviation). Statistical analysis (*Col9a3*$^{\Delta ex3}$ or *Col9a3* $^{-/-}$ vs WT): *p<0.05, **p<0.01, ***p<0.001, two tailed t-test.

4.3.2 Trabecular analysis of tibiae in adult mice.

The same analysis performed on mice femurs, was also performed on tibiae to assess their trabecular structure (Fig. 4.6 and Table 4.2). As reported for the femur, in *Col9a3*$^{-/-}$ tibiae we measured an increase in trabecular TV, which was 32% higher than WT.

The BV in *Col9a3*$^{\Delta ex3}$ tibiae was 68.5% of the WT and 18% higher, but not statistically significant, in *Col9a3*$^{-/-}$. Consistently with the trabecular femur results, in tibiae from *Col9a3*$^{\Delta ex3}$ the BV/TV was significantly decreased to 65.6% of the mean control BV/TV. Trabecular thickness (Tb.Th) was reduced in *Col9a3*$^{-/-}$ tibiae by 10% and unchanged in *Col9a3*$^{\Delta ex3}$ mice. The remainder of the trabecular variables were significantly changed only in *Col9a3*$^{\Delta ex3}$ compared to WT. We observed an increment of trabecular separation and pattern factor in *Col9a3*$^{\Delta ex3}$ tibiae, whose mean values were respectively 28.6% and 23.7% higher than WT mean Tb.Sp. and Tb.Pf. Moreover, the trabecular number and connectivity density were 66.5% and 65% of WT, respectively, and significantly decreased. As mentioned previously, the structure model index (SMI) defines the trabecular structure and was set to be 0 for perfect plates and 3 for perfect rods. In *Col9a3*$^{\Delta ex3}$ femurs, we measured a 14% increase in the SMI mean value, thus indicating a more “rod-like” structure than “plate-like” compared to controls.

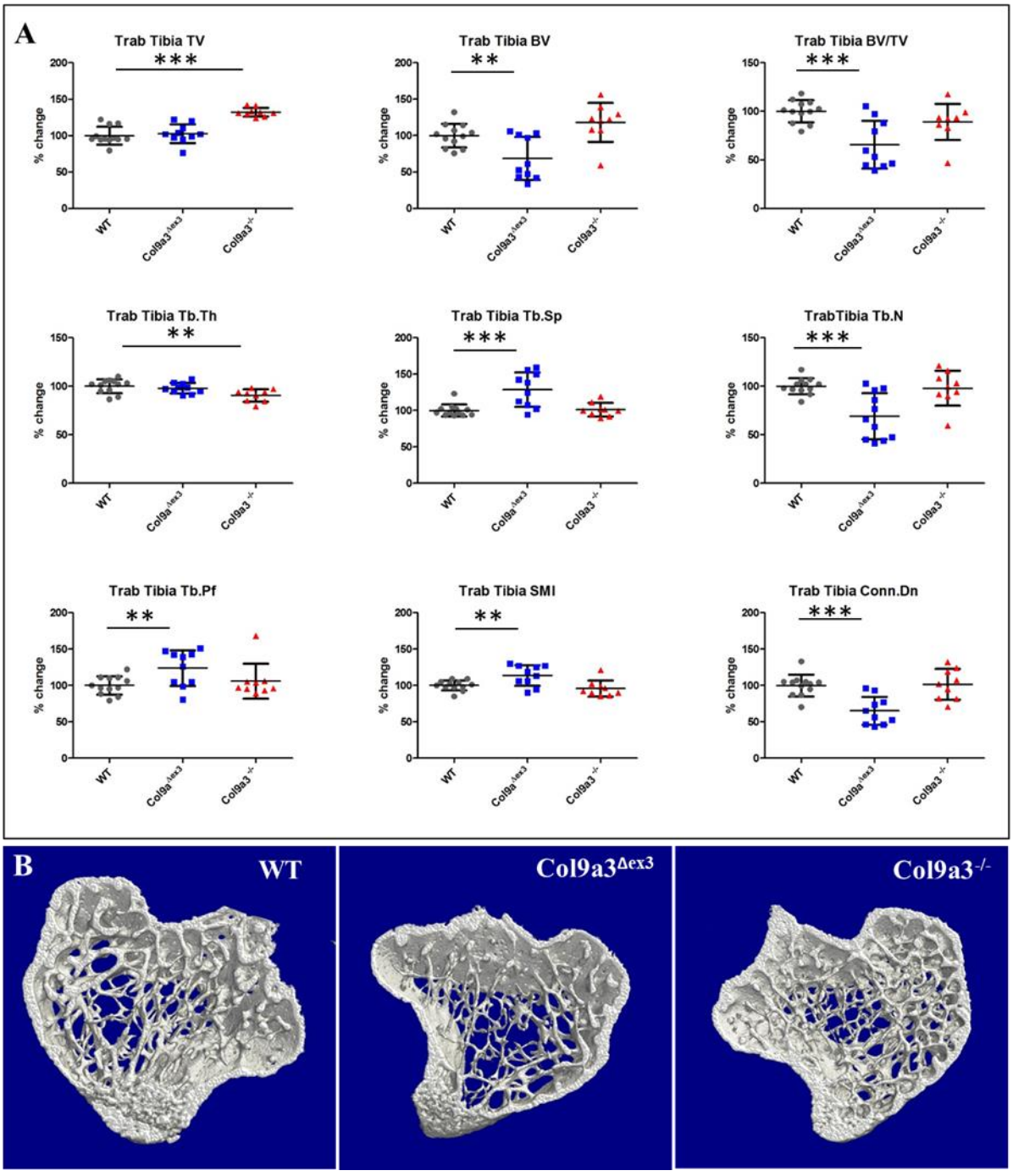

Fig. 4.6 | Trabecular morphometry of tibia of 18-week-old mice. Morphometric analysis of trabecular bone from tibiae of 18-week old male WT (N=13) *Col9a3*$^{\Delta ex3}$ (N=10) and *Col9a3* $^{-/-}$ (N=9) mice. A. Data of the graphs, relating to *Col9a3*$^{\Delta ex3}$ and *Col9a3* $^{-/-}$ mice are shown as percentage of change compared to WT measurements. Data are shown as means ±SD. Statistical analysis (*Col9a3*$^{\Delta ex3}$ or *Col9a3* $^{-/-}$ vs WT): *p<0.05, **p<0.01, ***p<0.001, two tailed t-test. B. Cross-sectional images of 3D µCT reconstructions using CTVox software of tibiae from the median animals of each genotype, taken 50 slides (225 µm) away from the tibial growth plate. Note the obvious altered trabecular bone architecture and low bone volume, connectivity, and the rod-like appearance in *Col9a3*$^{\Delta ex3}$ when compared to WT and *Col9a3* $^{-/-}$.

Trabecular analysis of the tibia (18-weeks)			
	WT (n=13)	***Col9a3$^{\Delta ex3}$*(n=10)**	***Col9a3$^{-/-}$*(n=9)**
TV (mm^3)	1.88 ± 0.22	1.93 ± 0.24	**2.48 ± 0.11*** **
BV (mm^3)	0.32 ± 0.05	**0.22 ± 0.09** **	0.38 ± 0.08
BV/TV (%)	17.13 ± 1.95	**11.24 ± 4.21*** **	16.17 ± 1.80
Tb.Th (µm)	55.84 ± 3.94	54.72 ± 3.01	**50.54 ± 3.58** **
Tb.Sp (µm)	182.94 ± 15.25	**235.41 ± 43.20*** **	184.69 ± 16.76
Tb.N (1/mm)	3.07 ± 0.25	**2.04 ± 0.71*** **	3.01 ± 0.55
Tb.Pf (1/mm)	22.53 ± 2.80	**27.87 ± 5.52** **	23.85 ± 5.39
SMI	2.02 ± 0.14	**2.29 ± 0.29** **	1.93 ± 0.22
Conn.Dens. ($1/mm^3$)	194.48 ± 29.37	**126.55 ± 37.66*** **	197.37 ± 41.15

Table 4.2. | µCT analysis of trabecular bone in tibiae of WT, *Col9a3$^{\Delta ex3}$* and *Col9a3$^{-/-}$* male mice at 18 weeks of age. Data obtained from µCT trabecular parameters measurements in tibiae and used to generate the graphs in Fig. 4.6. Data are shown as means ±SD. Statistical analysis (*Col9a3$^{\Delta ex3}$* or *Col9a3 $^{-/-}$* vs WT): *p<0.05, **p<0.01, ***p<0.001, two tailed t-test.

4.3.3 Cortical analysis of the femur in adult mice.

For cortical bone evaluation, 3D and 2D parameters were considered (Fig 4.7 and Table 4.3). From the 3D analysis, the ratio of the segmented bone volume (BV) to the total volume (TV) of the region of interest, BV/TV, was significantly reduced in cortical bone of *Col9a3*$^{-/-}$ femurs. No genotype specific difference in cortical thickness (Cort.Th) was observed in femurs. From the 2D analysis the following variables were extrapolated: the total cross-sectional area inside the periosteal envelope, tissue area (T.Ar.); the periosteal perimeter (P.Pm); the endocortical perimeter (E.Pm); and the mean polar moment of inertia (MMI), a parameter which describes the resistance of cortical bone to torsion, so an indication about cortical bone stiffness.

In *Col9a3*$^{\Delta ex3}$ femoral cortical bone, the only significant change was in the periosteal perimeter, which was increased by 5.5%. For all the other variables, mean values equivalent to WT controls were observed. In contrast, *Col9a3*$^{-/-}$ mice showed a relevant increase in tissue area, periosteal, and endosteal perimeters, of 18.1%, 11.1% and 18.7% as compared to WT, respectively, resulting in an overall wider bone. *Col9a3*$^{-/-}$ femurs were also determined to be stiffer compared to WT, with their MMI measuring 38% higher than the mean control value. An overall wider bone diameter was observed in the femurs of both mutant mice, but which was more pronounced in *Col9a3*$^{-/-}$.

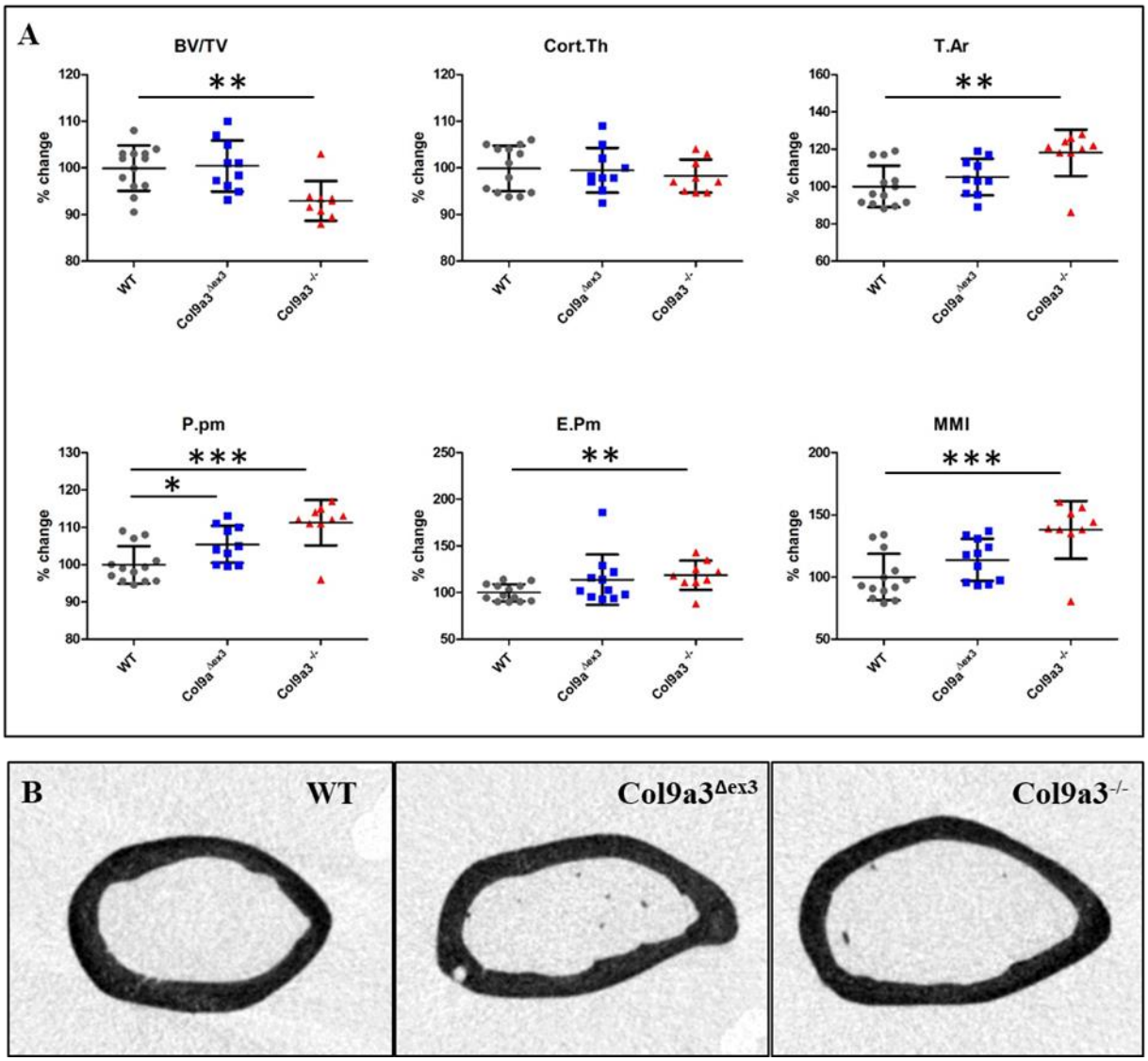

Fig. 4.7 | Cortical morphometry of femurs in 18-week old mice. A. Morphometric analysis of cortical bone from femurs of 18-week old male WT (N=13) *Col9a3$^{\Delta ex3}$* (N=10) and *Col9a3 $^{-/-}$* (N=9) mice. A. Data of the graphs, relating to *Col9a3$^{\Delta ex3}$* and *Col9a3 $^{-/-}$* mice, are shown as percentage of change compared to WT measurements. Data are shown as means ±SD. Statistical analysis (*Col9a3$^{\Delta ex3}$* or *Col9a3 $^{-/-}$* vs. WT): *p<0.05, **p<0.01, ***p<0.001, two-tailed t-test. B. Cross-sectional images of 3D µCT reconstructions obtained using the software Dataviewer of femurs from the median animals of each genotype, taken 50 slides (450 µm) away from the femoral great trochanter.

Cortical analysis of the femur (18-weeks)			
	WT (n=13)	***Col9a3*$^{\Delta ex3}$(n=10)**	***Col9a3*$^{-/-}$(n=9)**
TV (mm^3)	1.95±0.22	2.05±0.19	**2.39±0.07****
BV (mm^3)	0.90±0.07	0.94±0.06	**1.01±0.04***
BV/TV (%)	46.05±2.26	46.25±2.56	**42.21±0.98****
Cort. Th (µm)	222.77±11.05	221.60±10.68	219.50±7.69
T.Ar (mm)	2.17±2.17	2.28±0.21	**2.56±0.27****
P.Pm (mm)	5.73±0.29	**6.05±0.29***	**6.37±6.37*****
E.Pm (mm)	4.65±0.42	5.38±1.28	**5.52±0.73****
MMI (mm^4)	0.57±0.11	0.66±0.09	**0.78±0.13*****

Table 4.3. | µCT analysis of cortical bone in femurs of WT, *Col9a3*$^{\Delta ex3}$ and *Col9a3*$^{-/-}$ male mice at 18 weeks of age. Data obtained from µCT cortical parameters measurements in femurs and used to generate the graphs in Fig. 4.7. Data are shown as means ±SD. Statistical analysis (*Col9a3*$^{\Delta ex3}$ or *Col9a3* $^{-/-}$ vs WT): *p<0.05, **p<0.01, ***p<0.001, two tailed t-test.

4.3.4 Cortical analysis of tibiae in adult mice.

Interestingly, we observed different results from cortical bone analysis in adult tibiae. In contrast with the changes measured in femoral cortical bone, in the tibial cortical bone the genotype did not affect either 3D or 2D parameters, with the exception of cortical thickness in the *Col9a3*$^{-/-}$ mice (Fig. 4.8 and Table 4.4), which was significantly reduced (95.7% of the average WT value). Mean values equal to WT were exhibited for all other cortical parameters in *Col9a3*$^{\Delta ex3}$ and *Col9a3*$^{-/-}$ mice.

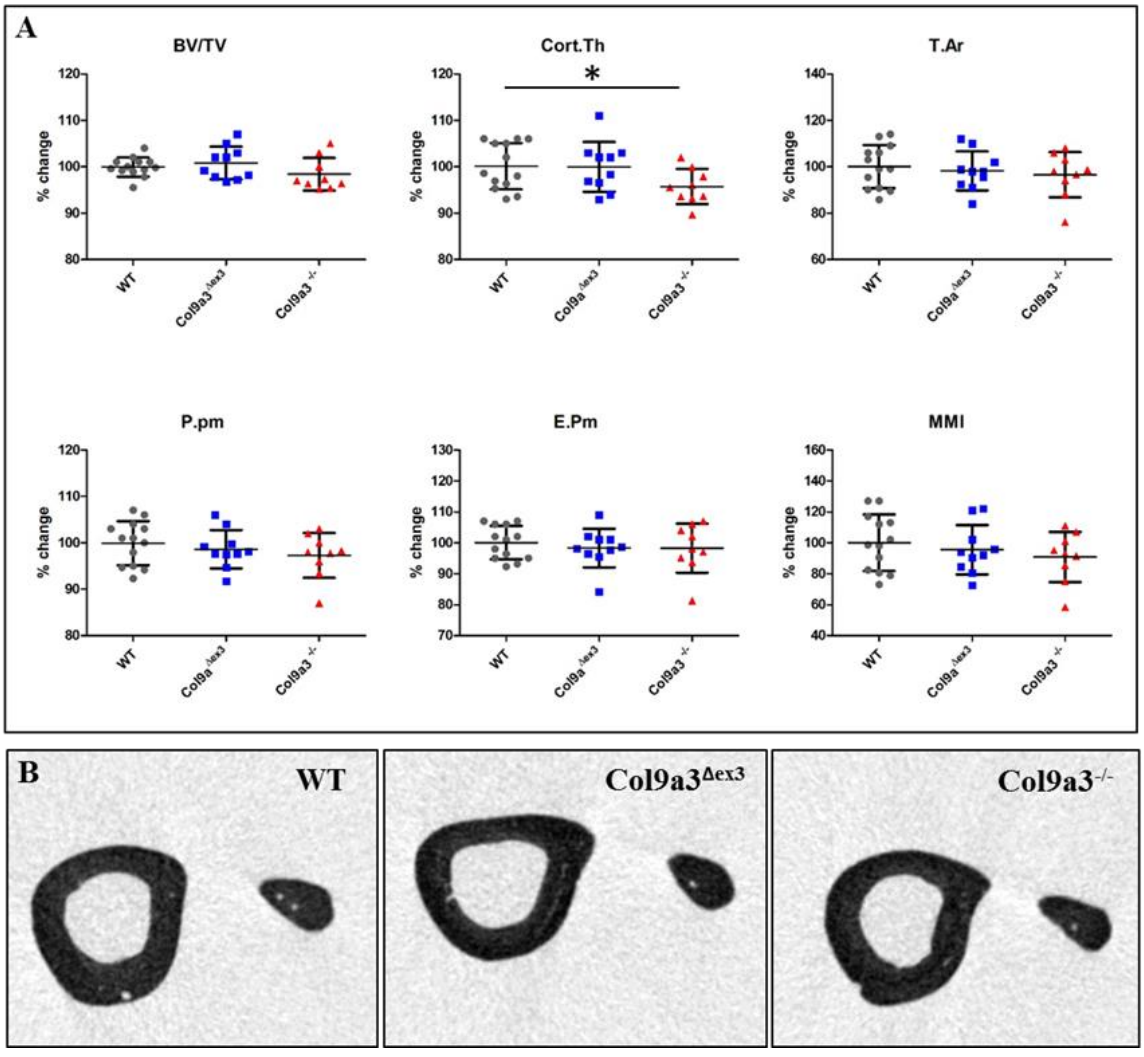

Fig. 4.8 | Cortical morphometry of tibiae in 18-week old mice. A. Morphometry analysis of cortical bone from tibiae of 18-week old male WT (N=13) *Col9a3*$^{\Delta ex3}$ (N=10) and *Col9a3* $^{-/-}$ (N=9) mice. Data of the graphs, relating to *Col9a3*$^{\Delta ex3}$ and *Col9a3* $^{-/-}$ mice, are shown as a percentage change compared to WT measurements. Data are shown as means ±SD. Statistical analysis (*Col9a3*$^{\Delta ex3}$ or *Col9a3* $^{-/-}$ vs. WT): *p<0.05, **p<0.01, ***p<0.001, two tailed t-test. B. Cross-sectional images of 3D µCT reconstructions obtained using Dataviewer software of femurs from the median animals of each genotype, taken 50 slices (450 µm) away from the fibular notch.

Cortical analysis of the tibia (18-weeks)			
	WT (n=13)	***Col9a3$^{\Delta ex3}$*(n=10)**	***Col9a3$^{-/-}$*(n=9)**
TV (mm^3)	1.02±0.09	1.00±0.08	0.98±0.10
BV (mm^3)	0.67±0.06	0.67±0.06	0.64±0.05
BV/TV (%)	66.12±1.42	66.60±2.29	65.11±2.39
Cort. Th (µm)	268.94±13.16	269.13±14.65	**257.56±10.28***
T.Ar (mm)	1.13±0.11	1.11±0.09	1.10±0.11
P.Pm (mm)	4.10±0.20	4.05±0.17	3.99±0.20
E.Pm (mm)	2.39±0.13	2.35±0.15	2.34±0.19
MMI (mm^4)	0.19±0.03	0.18±0.03	0.17±0.03

Table 4.4. | µCT analysis of cortical bone in tibiae of WT, *Col9a3$^{\Delta ex3}$* and *Col9a3$^{-/-}$* male mice at 18 weeks of age. Data obtained from µCT cortical parameters measurements in tibiae and used to generate the graphs in Fig. 4.8. Data are shown as means ±SD. Statistical analysis (*Col9a3$^{\Delta ex3}$* or *Col9a3 $^{-/-}$* vs WT): *p<0.05, **p<0.01, ***p<0.001, Two tailed T-test.

.

4.3.5 Bone phenotypic analysis of the femoral head and tibial subchondral bone.

During bone µCT analysis we also assessed other anatomical regions of the long bones under investigation, including the femoral head of the proximal femurs and the subchondral bone of tibiae in both mutant and WT mice.

From µCT reconstructed images of the proximal femoral epiphysis, we observed a variability in bone composition according to genotype. This finding was of interest when it was compared to our µCT observations on the distal femoral epiphysis described in the previous section. At 18 weeks, the proximal femoral epiphysis of *Col9a3*$^{\Delta ex3}$ male mice presented all the characteristics of a fully mature bone, comparable with WT animals. The proximal cancellous bone was fully calcified and fusion between epiphysis and metaphysis had occurred, in conjunction with complete physeal resorption (Fig. 4.9). In addition, the cancellous bone appeared similar to WT with no evidence of reduced trabeculae density or altered trabecular space, somewhat different from what we observed in the distal femur. Surprisingly, the *Col9a3*$^{-/-}$ proximal femoral epiphysis showed an important morphological change in its cancellous bone composition. *Col9a3*$^{-/-}$ epiphysis appeared still in a mineralised cartilaginous state, where a distinct layer of articular cartilage was not yet reduced in thickness. Formation of trabecular bone was not observed, but a clear separation of epiphysis from metaphysis was still present. These features are usually associated with a physeal senescence state during the postnatal development of the murine proximal femoral physis (Cole et al. 2013). Hence, *Col9a3*$^{-/-}$ mice were at an earlier stage in the proximal femur development process compared to *Col9a3*$^{\Delta ex3}$ and WT mice, whose proximal epiphysis were in the final stage of calcification denoting completed post-natal development.

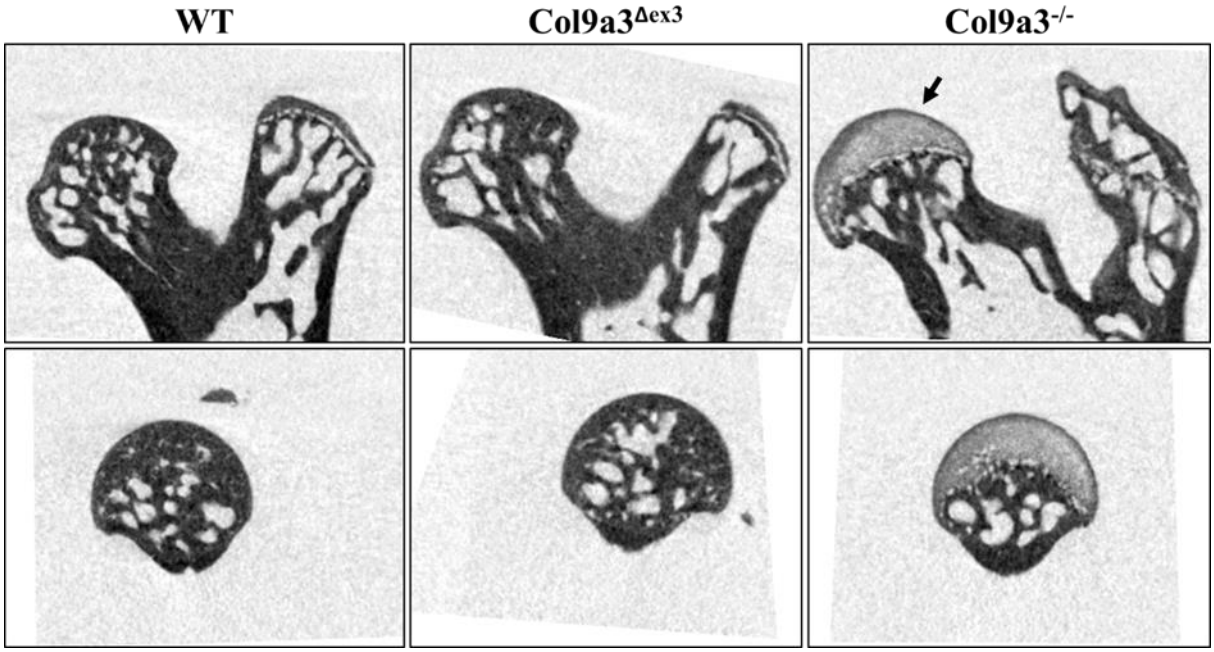

Fig. 4.9 | µCT analysis of proximal femoral epiphysis. Coronal (top) and trans-axial view (bottom) of µCT reconstructed images of proximal femoral epiphysis from 18-week old male WT, *Col9a3*$^{\Delta ex3}$, and *Col9a3*$^{-/-}$ mice. Difference in the developmental state of epiphysis indicated by black arrow.

The evaluation of tibial subchondral bone in 18-week old male mice highlighted another interesting morphological change in both mutant mice lines. In *Col9a3*$^{\Delta ex3}$ there was a lower level of trabecular bone, with reduced presence of trabeculae, which were also thinner than those forming the subchondral bone of WT mice (Fig. 4.10). This observation was in line with the data from the trabecular morphometry on tibial cancellous bone, findings confirmed by the coronal view of *Col9a3*$^{\Delta ex3}$ tibia, where an overall decrease of trabecular bone was observed in the region below the physis. *Col9a3*$^{-/-}$ subchondral bone resembled the structure of that of the WT mice, showing similar sclerotic regions in the lateral condyle, typical of C57Bl/6 background mice (personal communication from Professor Rob Van 'T Hof, University of Liverpool). More trabecular bone was visible in both metaphysis and epiphysis in *Col9a3*$^{-/-}$ tibia, as already stated. Moreover, looking more carefully at the subchondral plate of both *Col9a3*$^{\Delta ex3}$ and *Col9a3*$^{-/-}$ mice, we noted a thinner bone in the medial and lateral tibial plateau compared to WT in *Col9a3*$^{\Delta ex3}$ mice (black stars in Fig. 4.10), but not obvious change in the subchondral plate of *Col9a3*$^{-/-}$ mice. However, in both mutant mice, the tubercles of the intercondylar eminence were lost, giving an overall less defined subchondral plate when compared to WT.

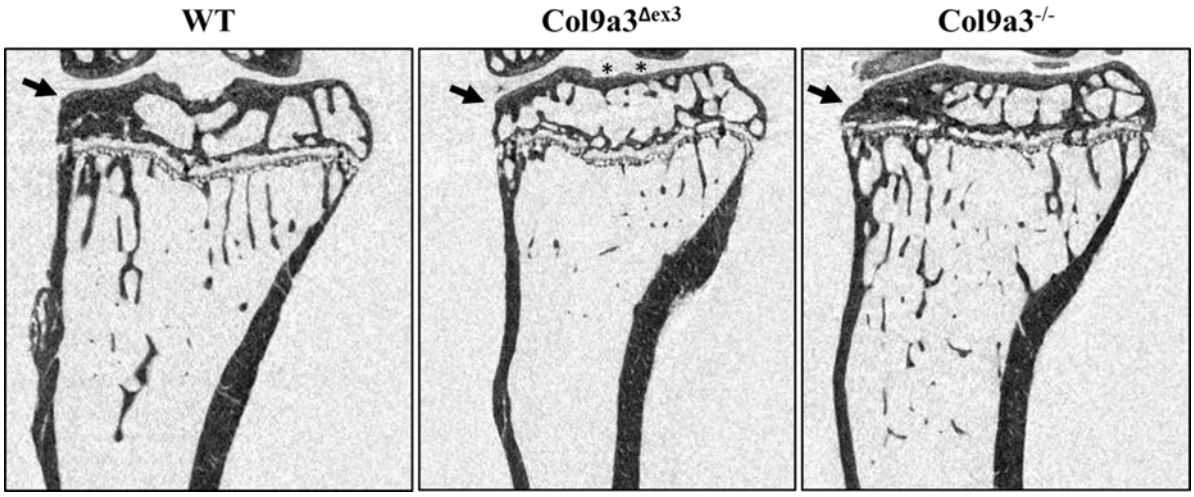

Fig 4.10 | µCT analysis of tibial subchondral bone. Coronal view of µCT reconstructed images of proximal tibial epiphysis and metaphysis from 18-week old male *Col9a3$^{\Delta ex3}$*, *Col9a3$^{-/-}$* and WT mice. Note the reduced subchondral cancellous bone in *Col9a3$^{\Delta ex3}$*, along with medial and lateral tibial plateau indicated by black stars. Sclerotic regions of the lateral condyle are indicated by black arrows.

4.4 Discussion

In this chapter we described the skeletal phenotype of our novel mutant *Col9a3*$^{-/-}$ and *Col9a3*$^{\Delta ex3}$ mice. The aims of this chapter were essentially two: to verify the presence of possible commonalities between the skeletal defects of *Col9a3*$^{\Delta ex3}$ mice with EDM3 cases caused by similar exon 3 skipping mutations in *COL9A3*; to compare the consequences at the bone level of the two *Col9a3* mutations generated, using other collagen type IX knockout mice as a point of reference. Radiographic evaluation was performed on homozygous mice at two different time points during post-natal development, at a young age (3 weeks), and at 9 weeks, corresponding to the age of skeletal maturity (Jilka 2013). Radiographic analysis showed that the majority of the skeletal abnormalities were detected in *Col9a3*$^{-/-}$ mice. The *Col9a3*$^{\Delta ex3}$ skeletal phenotype was characterised by normal stature, with no skull abnormality, and no overt morphological changes – with the exception being a shorter femur length measured in 9-week old animals. At 3 weeks of age these mice had a reduced tibia length however, this growth delay was recovered when skeletal growth was complete at 9 weeks. *Col9a3*$^{\Delta ex3}$ mice did not display a hip dysplasia often detected in mouse models of skeletal dysplasia disorders. Therefore, from radiographic analysis, we could not detect any striking skeletal abnormality, similarly to some EDM3 patients' clinical data. EDM3 patients are indeed classified in the mildest part of the spectrum of skeletal abnormalities associated with chondrodysplasias.

On the contrary, the *Col9a3*$^{-/-}$ phenotype was characterised by overall shorter stature, shorter tibiae and femurs (at both 3 and 9 weeks of age), and abnormal wider tibial epiphysis compared to WT animals. The hip angle was significantly larger at 3 weeks compared to WT, with the difference even more pronounced when mice reached skeletal maturity. Not surprisingly, many of the features described about the *Col9a3*$^{-/-}$ mice phenotype, are shared with the knockout mouse for *Col9a1* gene (*Col9a1*$^{-/-}$) and *Col9a2* (*Col9a2*$^{-/-}$), mutations leading in both mice to a functional knockout of collagen type IX. Dreier R. et al. described the *Col9a1*$^{-/-}$ mouse phenotype to be characterised morphologically by a reduction in length and increased width in all long bones analysed (including the tibia and femur), along with broadened tibial condyles (Dreier et al. 2008). These commonalities between *Col9a1*$^{-/-}$ and our *Col9a3*$^{-/-}$ mouse, further confirmed our mouse as a valuable *Col9a3* knockout, which could provide insights about the importance of each α helix which forms the collagen type IX molecule.

Moreover, the evidence of a shorter skull length, but unaltered intercanthal distance, detected in *Col9a3*$^{-/-}$ mice, suggests that ablation of collagen type IX could affect directly or indirectly endochondral ossification in the development of the skull.

Along with the assessment of bone morphology by radiography, we further investigated long bones microstructure of our mutant mice using µCT. The trabecular and cortical bone were analysed in the femur and tibia of adult male mice by µCT. In *Col9a3*$^{\Delta ex3}$ mice, the same trabecular pattern was observed in 18-week old femurs and tibiae when compared to their age-matched WT littermates. The reduced ratio of bone volume per tissue volume, trabecular number and connectivity density, along with increased space between trabeculae, detected in femurs and tibiae, indicated *Col9a3*$^{\Delta ex3}$ mice to be characterised by a low trabecular bone phenotype, relative to their WT littermates. In addition, their tibiae structure model index, suggested a "rod-like" structure of trabeculae. The conversion from plate elements to rod elements is frequently associated to age- or disease- related degeneration of cancellous bone that leads to a more fragile bone, as often seen in osteoporosis. What was immediately apparent for *Col9a3*$^{-/-}$ mice instead, was their higher total tissue volume, indicating their long bones to have a larger average diameter than the WT average. Interestingly, their trabecular thickness mean value was lower compared to WT in both femur and tibia. There are contradictory hypotheses in the literature about the correlation between bone volume and trabecular thickness, often reporting how thicker trabeculae are more likely to be associated to high volume fractions (Macdonald et al. 2011, Beresheim et al. 2018). However, Waarsing et al. showed in rats how this relation could be reversed due to ageing, as they demonstrated that trabecular thickness increases with decreasing volume fraction when a mechanism of bone degradation is triggered. Their hypothesis suggested that the variation noticed could be due to compensatory mechanisms aimed at maintaining bone strength despite microstructure changes (J.H. Waarsing 2004). The same hypothesis could be applied to our data. We might speculate that the decreased trabecular thickness could be a compensatory response for a larger bone, which with thicker trabeculae, would become overly compact and heavy.

Previously, from µCT analyses conducted on lumbar bones of females and males *Col9a1*$^{-/-}$ mice at 8-10 weeks of age, Wang et al. showed how homozygous females had a more pronounced trabecular bone phenotype caused by *Col9a1*$^{-/-}$ mutation than homozygous male littermates. In *Col9a1*$^{-/-}$ females the lumbar bone volume fraction, trabecular thickness and connectivity density were significantly decreased and trabecular spacing increased, showing a trabecular profile more similar to our *Col9a3*$^{\Delta ex3}$ male mice. Whereas, as reported from our

trabecular analysis performed on *Col9a3*$^{-/-}$ males, also in *Col9a1*$^{-/-}$ males, the genotype seemed not to have a relevant influence on trabecular bone, since only the connectivity density was significantly lower. However, with ageing, both female and male heterozygous (*Col9a1*$^{+/-}$) mice displayed a significant loss of trabecular bone (Wang et al. 2008). Conversely, in another study, similar findings to our *Col9a3*$^{-/-}$ mice were found in *Col9a1*$^{-/-}$ animals vertebral bodies. They showed higher TV and initially reduced BV/TV, which then returned to normal by the age of 10 months (Kamper et al. 2016).

Cortical analysis did not show overt changes in *Col9a3*$^{\Delta ex3}$ mice, apart from an increased periosteal perimeter in 18-week old femurs. In *Col9a3*$^{-/-}$ mice the pattern of cortical changes recorded in femur was completely consistent with a bone characterised by a wider diameter. In fact, a reduction in the bone volume to tissue volume ratio, along with the increased tissue area, periosteal and endosteal perimeters were measured in *Col9a3*$^{-/-}$ femurs. As a consequence of the increase in periosteal diameter, the mean polar moment of inertia was increased, indicating that the *Col9a3*$^{-/-}$ mice would be less prone to fragility fracture than WT. In *Col9a3*$^{-/-}$ tibiae only the cortical thickness was significantly lower, leaving all the other parameters equal to WT. Such a result could be explained inferring the same hypothesis suggested for trabecular bone. We could speculate that the bone, being larger, adapted its cortical thickness to be less heavy while at the same time maintaining its supportive function.

The evaluation of the tibial subchondral bone confirmed the low trabecular bone phenotype of *Col9a3*$^{\Delta ex3}$ mice and a commonly less defined subchondral plateau in both mutant mice. The analysis of the proximal femoral epiphysis by µCT revealed that while in WT and *Col9a3*$^{\Delta ex3}$ mice calcification, resorption of the physis, and epiphyseal fusion were complete (as expected in male mice at the age of 18 weeks), in *Col9a3*$^{-/-}$ mice maturation of proximal femurs was delayed. *Col9a3*$^{-/-}$ femoral head cartilage was still in the senescent state, calcification had been initiated, but the physis was still preventing epiphysis and metaphysis fusion. This observation was unexpected, considering that no indication of delayed ossification was noticed from µCT images of *Col9a3*$^{-/-}$ distal femur and tibia. Additionally, it is worth noticing that the proximal femur of the *Col9a3*$^{\Delta ex3}$ mice did not show evidence of a lower trabecular bone phenotype, unlike for their *Col9a3*$^{\Delta ex3}$ distal femur and proximal tibia. Therefore, we could observe different bone microstructure in distinct regions of the same bone. These findings confirm that bone morphology and microarchitecture are genetically determined on a site-specific basis according to the anatomical region (Judex et al. 2004).

In conclusion, our observations suggested that the potential presence in the ECM of a mutated collagen type IX affects long bone development or homeostasis differently when compared to its total absence from the ECM. However, the mechanism by which this differential outcome takes place is not clear.

In the next chapter we will analyse aspects of bone development by examining the tibial growth plate phenotype and the cartilage proteome of *Col9a3*$^{\Delta ex3}$ and *Col9a3*$^{-/-}$ mice, compared to WT, to identify possible mechanisms contributing to the bone phenotype observed.

Summary highlights:

- Radiological findings did not indicate remarkable skeletal abnormalities in *Col9a3*$^{\Delta ex3}$ mice, which recall some EDM3 patients' phenotype.

- *Col9a3*$^{-/-}$ reproduced (radiologically) the *Col9a1*$^{-/-}$ and *Col9a2*$^{-/-}$ mice phenotype.

- *Col9a3*$^{\Delta ex3}$ mice showed a reduced trabecular bone but normal cortical bone phenotype, whereas long bones in *Col9a3*$^{-/-}$ mice were characterised by a stiffer cortical bone with a wider diameter.

- The regulation of bone development and homeostasis differs in distinct bones and in their different anatomical sites, adding mechanistic complexity. From our data, we suggest that collagen type IX has a role in the complex mechanism of bone regulatory pathways; however, its specific function remains unknown.

Chapter 5.

Evaluation of Col9a3$^{\Delta ex3}$ and Col9a3$^{-/-}$ cartilage pathology

5.1 Introduction

In Chapter 4 we described the bone phenotype of *Col9a3*$^{\Delta ex3}$ and *Col9a3*$^{-/-}$ mice, with radiological analysis showing that morphological defects were more predominant in *Col9a3*$^{-/-}$ mice. Analysis of the bone micro-structure identified different changes between *Col9a3*$^{\Delta ex3}$ and *Col9a3*$^{-/-}$, suggesting that each mutation affected bone development, homeostasis, or both mechanisms differently. To further unravel this observation, we performed phenotypic analysis of cartilage tissue in the mutant mice, in order to identify tissue morphological changes that could help to explain the origin of the observed bone defects. In a previous study, cartilage biopsies from MED patients lacking exon 3 of *COL9A3* due to a G to A transition in the splice acceptor site of intron 2 in the gene, showed chondrocyte and cartilage matrix abnormalities. MED chondrocytes were found with intracytoplasmic inclusions, enlarged rough endoplasmic reticulum (rER), containing electron-dense and –lucent material, likely to be retention of abnormally processed matrix proteins. An accumulation of lipids was observed in the cytoplasm and rER for some epiphyseal cartilage biopsies (Bonnemann et al. 2000). Unfortunately, there is a small number of reported studies performed on tissue from MED patients with collagen type IX mutations and this is probably due to low availability of patients' biopsy samples. Nonetheless, previous works conducted on *Col9a1*$^{-/-}$ and *Col9a2*$^{-/-}$ mice described evidence of growth plate anomalies. These included, altered columnar distribution of chondrocytes, loss of clear distinction between different zones, reduced number of cells in the epiphyseal middle region at early stages of development, along with altered integration of other matrix proteins (Balasubramanian et al. 2019, Blumbach et al. 2008, Budde et al. 2005, Dreier et al. 2008).

Given the above, for our study a deep analysis of the epiphyseal growth plate was performed, at different stages of development and using a variety of different investigation methods. Light microscopy and transmission electron microscopy were used to visualise growth plate structure and chondrocytes morphology and ultrastructure. By immunohistochemistry (IHC), we assessed the presence and localisation of selected matrix proteins in addition to quantifying chondrocyte proliferation. Finally, in the attempt to explain the reasons underlying the bone and cartilage findings observed in the mutant mice, we performed RNA-sequencing on their chondrocytes mRNA with the purpose to identify possible gene expression variations contributing to their phenotypes.

5.2 Analysis of *Col9a3$^{\Delta ex3}$* and *Col9a3$^{-/-}$* murine growth plate

5.2.1 Histological analysis of growth plate structure

In order to analyse the epiphyseal growth plate architecture, tibiae from female mice at 3-weeks of age were collected and processed for histology. Tissue sections were subjected to Haematoxylin and Eosin (H&E) staining to visualise the general tissue structure. Haematoxylin specifically stains cell nuclei blue, and eosin stains the extracellular matrix (ECM) and cytoplasm pink. Using H&E we were able to visualise chondrocyte arrangement throughout the different zones constituting the growth plate, in both mutant mice and their WT littermates. Going from the epiphyseal to the diaphyseal side, in WT tibial sections, we could recognise a defined resting zone with its reservoir of small and circular chondrocytes, the proliferative zone whose flattened chondrocytes were arranged in regular columns parallel to the axis of the bone, and finally the mature and enlarged chondrocytes of the hypertrophic zone. From morphometric analysis, both mutant mice exhibited a total height of the growth plate comparable to WT controls. No visible difference was detected in the organisation of chondrocytes in *Col9a3$^{\Delta ex3}$* growth plate zones compared to WT (Fig. 5.1), although their relative height was changed, with the proliferative zone reduced by 15% and the hypertrophic zone 9% larger (when measured relative to the total growth plate height) (Fig. 5.2). In *Col9a3$^{-/-}$* mice, the spatial organisation of chondrocytes in the different growth plate zones was impaired. The separation between resting and proliferative zone was lost and proliferative chondrocytes were no longer flat and organised in columns, but were instead rounded and randomly clustered. In addition, the neat distinction between proliferative and hypertrophic zone was hard to determine, as some proliferative cell invasion within hypertrophic region was noted. For this reason, we measured a 15% higher proliferative zone and 20% narrower hypertrophic zone in homozygous mice for *Col9a3$^{-/-}$* mutation (Fig. 5.2); however, the lack of precise separation between the two regions made morphometric analysis difficult. *Col9a3$^{-/-}$* hypertrophic chondrocytes had no obvious anomaly in their shape, apart from some sporadic cell enlargement. Larger intercellular spaces surrounded hypertrophic chondrocytes at the boundary with proliferating cells (Fig. 5.1).

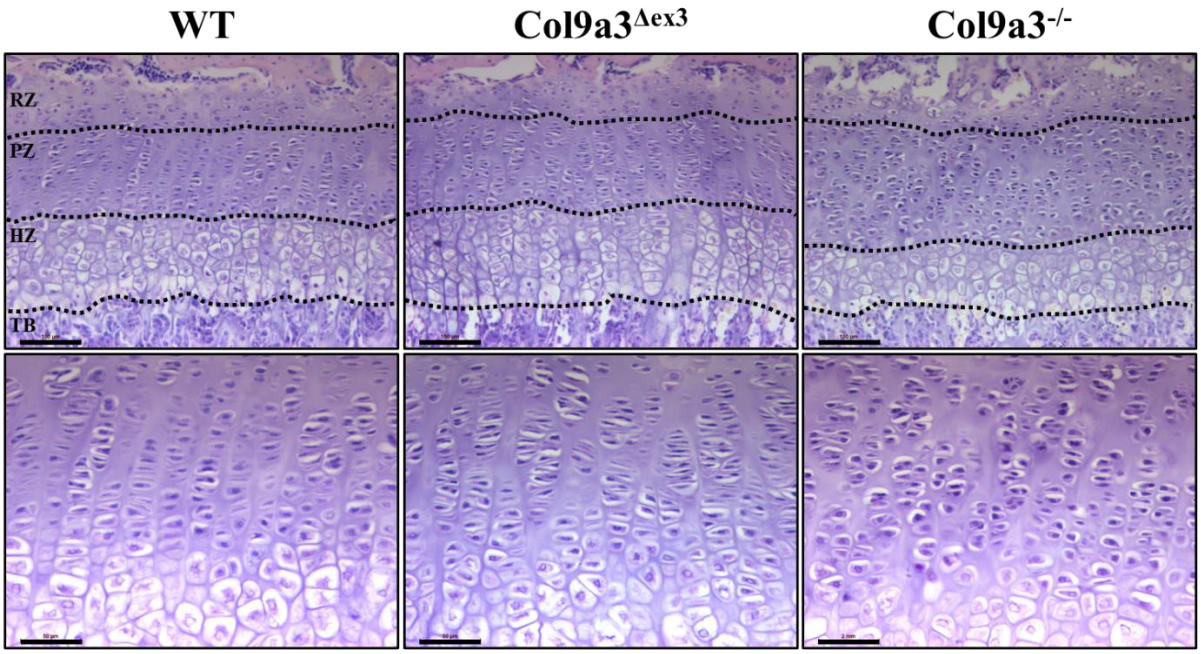

Fig. 5.1 | Tibial growth plate architecture in 3-weeks old mice. H&E staining of tibial growth plates from 3-week old WT, *Col9a3* $^{\Delta ex3}$ and *Col9a3*$^{-/-}$ female mice. Representative images from three mice per genotype, from twelve sections/mouse. RZ= Resting zone; PZ= Proliferative zone; HZ= Hypertrophic zone; TB= Trabecular bone. Upper row panel scale bar =100µm; lower row panel =50µm.

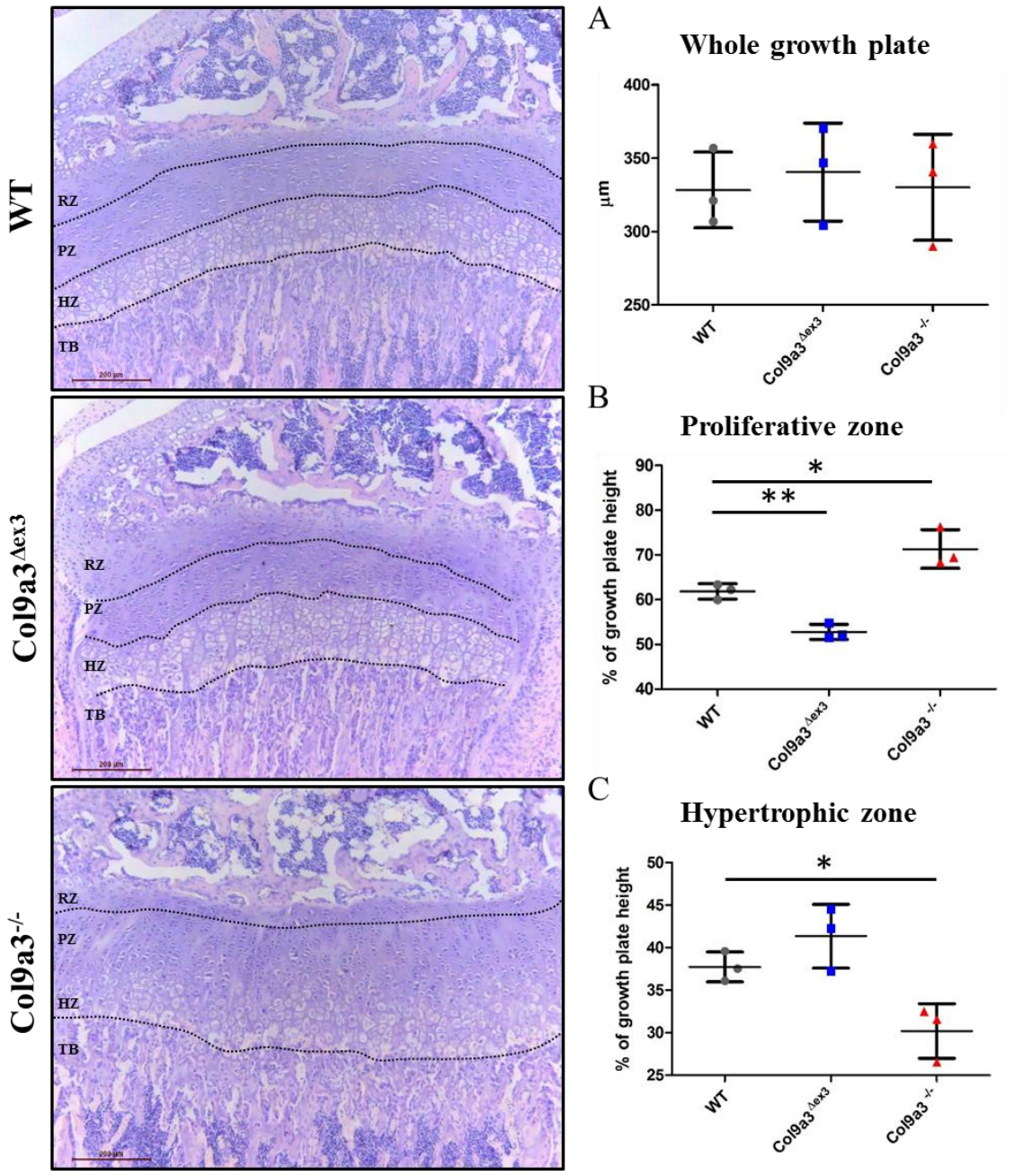

Fig. 5.2 | Tibial growth plate morphometric analysis. Measurements of the different zones of the tibial growth plate at 3-weeks of age (N=3). A. Graph of measurement of whole growth plate height. B. Graph of proliferative zone height expressed as percentage of total growth plate height. C. Graph of hypetrophic zone height expressed as percentage of total growth plate height. Two tailed T-test: *p<0.05, **p<0.01. RZ= Resting zone; PZ= Proliferative zone; HZ= Hypertrophic zone; TB= Trabecular bone.

5.2.2 Ultrastructural analysis of growth plate chondrocytes

A more detailed analysis of chondrocytes morphology in the different zones of growth plate was performed using transmission electron microscopy (TEM). Cartilage tissue was collected from 7-day old tibiae and processed for TEM by researchers at the Electron Microscopy Research Services of Newcastle University.

In the resting zone of *Col9a3*$^{\Delta ex3}$ cartilage, chondrocytes displayed enlargement of their endoplasmic reticulum (ER) possibly caused by low level protein retention. However, some enlargement was also observed in the ER of WT resting chondrocytes (Fig 5.3). *Col9a3*$^{-/-}$ resting chondrocytes were irregular in their morphology and occasionally surrounded by a more dispersed fibril organisation, with regions almost devoid of fibres, indicating a less compact pericellular matrix (Fig. 5.3).

Col9a3$^{\Delta ex3}$ proliferative chondrocytes, as previously stated in the histology analysis, showed an overall organisation similar to WT with some cells having a less defined morphology. In a few examples, chondrons were less compact, showing a loose, spread chondrocyte arrangement (black rectangle in *Col9a3*$^{\Delta ex3}$ Fig. 5.4). In *Col9a3*$^{-/-}$ proliferative zone, the distribution of cells was uneven, with regions devoid of chondrocytes. Chondrocytes were smaller, with an altered morphology, and their arrangement in chondrons was affected (Fig. 5.4). Evidence of ER enlargement was present in *Col9a3*$^{\Delta ex3}$ and *Col9a3*$^{-/-}$ proliferative chondrocytes. A clear pre-hypertrophic region was visible in WT growth plate, but in both mutant mice this defined region was lost. In *Col9a3*$^{\Delta ex3}$ mice cells appeared to progress directly into hypertrophy, whereas *Col9a3*$^{-/-}$ pre-hypertrophic chondrocytes showed an abnormal morphology, more rounded with loss of the normal columnar arrangement (Fig. 5.5).

In *Col9a3*$^{\Delta ex3}$ hypertrophic chondrocytes there was some evidence of enlarged ER with protein retention. In *Col9a3*$^{-/-}$ mice glycogen granules were present in chondrocytes (Fig.5.6). In addition, between the resting and proliferative zone in both mutant mice (but not in the WT) we detected a region lacking all the tissue characteristics typical of growth plate, with no normal chondrocytes and an unusual matrix morphology. The overall characteristic was of a region where severe tissue degeneration occurred, within which necrotic nuclei were detected, along with collagen fibres in an irregular meshwork (Fig. 5.7). This degeneration appeared more severe in the *Col9a3*$^{-/-}$ growth plate.

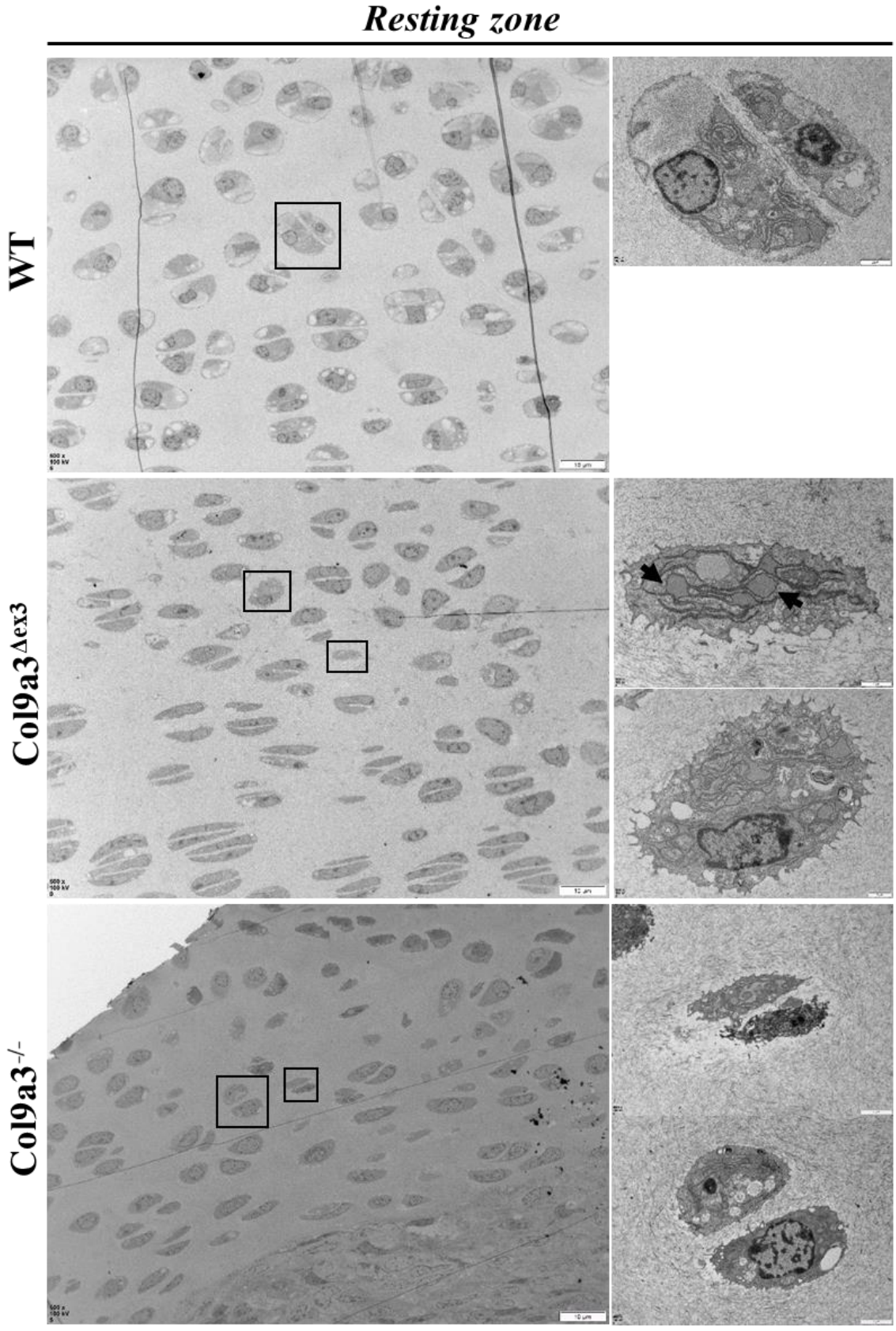

Fig. 5.3 | Ultrastructure of the resting zone in the tibial growth plate.
Electron micrographs of cartilage from 1-week old mutant mice compared to a WT control (N=1). Black arrows indicate ER enlargement. Scale bar = 10μm, higher magnification scale bars = 2 μm.

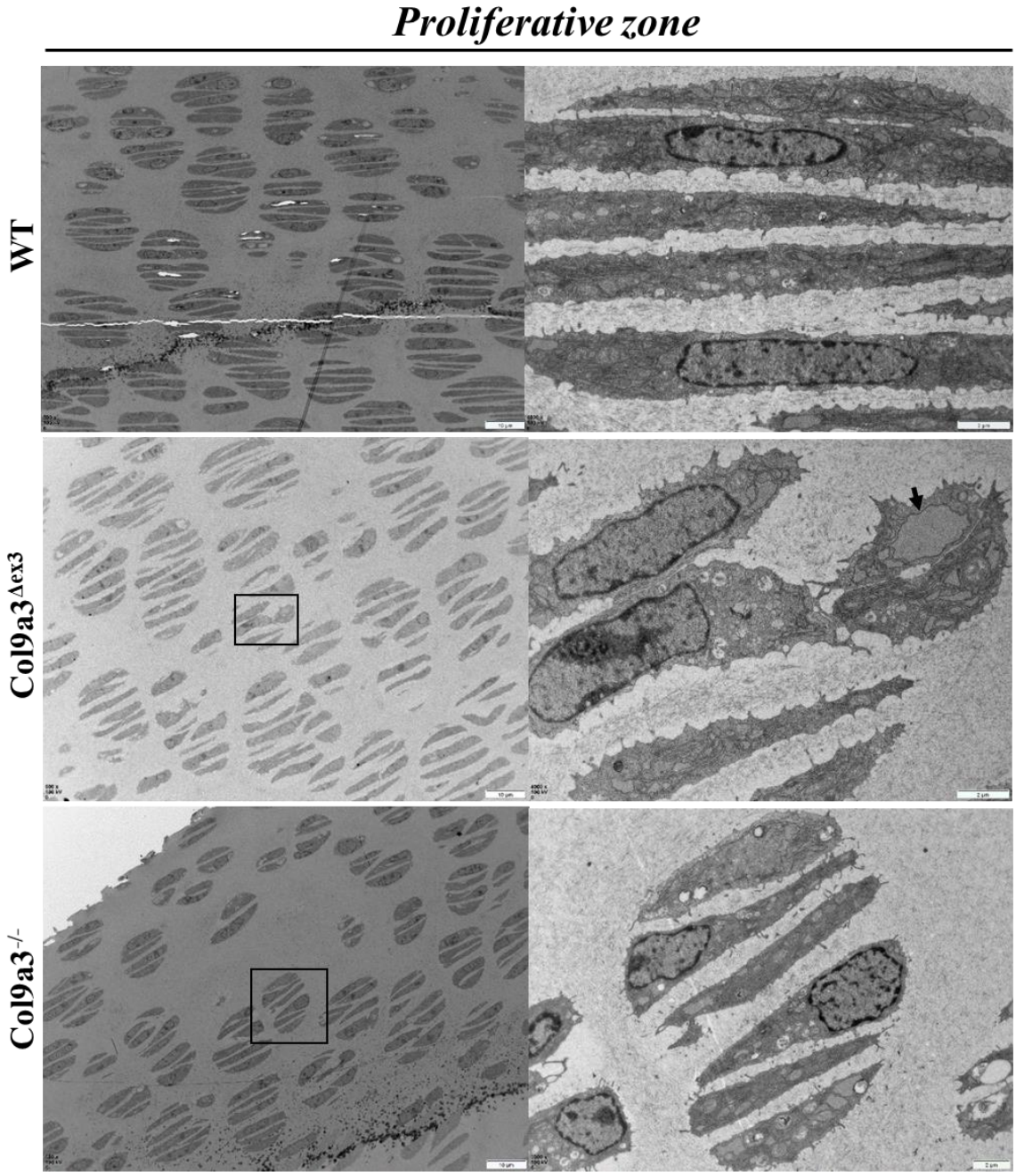

Fig. 5.4 | Ultrastructure of the proliferative zone in the tibial growth plate.
Electron micrographs of cartilage from 1-week old mutant mice compared to a WT control (N=1). Black arrow indicates ER enlargement. Scale bar = 10μm, higher magnification scale bars = 2 μm.

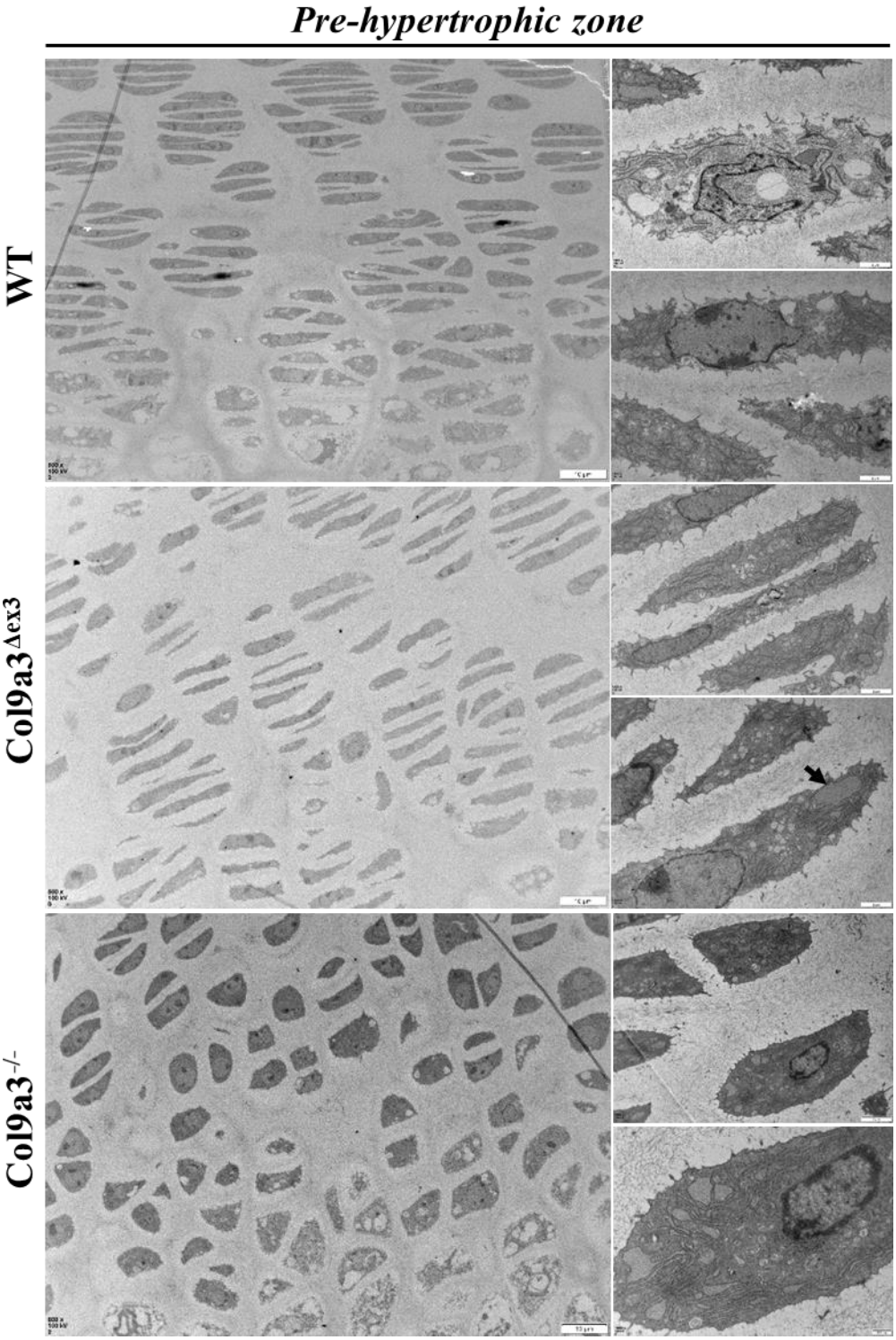

Fig. 5.5 | Ultrastructure of the pre-hypertrophic zone in the tibial growth plate. Electron micrographs of cartilage from 1-week old mutant mice compared to a WT control (N=1). Higher magnification images taken from equivalent regions. Black arrow indicates ER enlargement. Scale bar = 10μm, higher magnification scale bars = 2 μm.

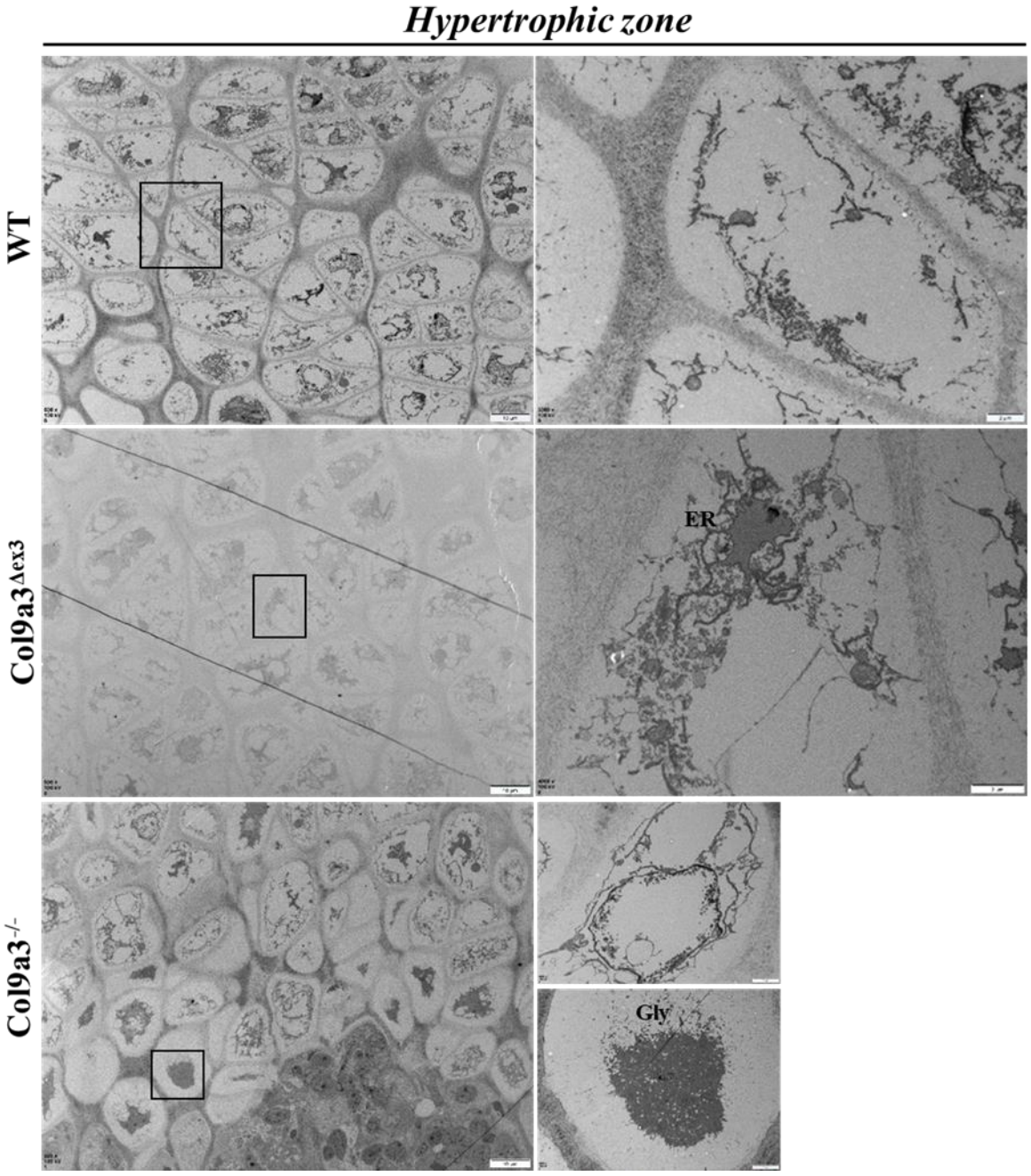

Fig. 5.6 | Ultrastructure of the hypertrophic zone in the tibial growth plate.
Electron micrographs of cartilage from 1-week old mutant mice compared to WT control (N=1). ER= Endoplasmic reticulum; Gly= Glycogen. scale bar = 10μm, higher magnification scale bars = 2 μm.

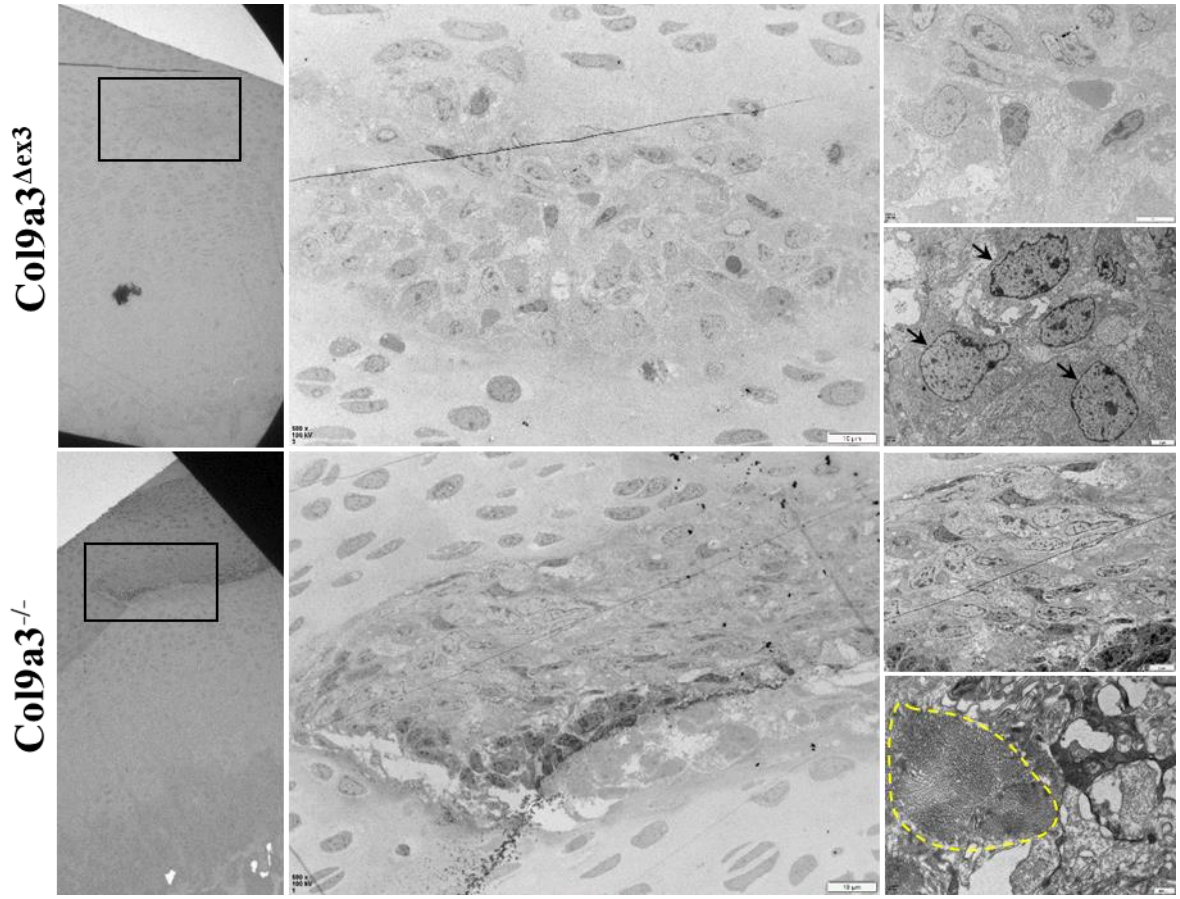

Fig. 5.7 | Alteration of tissue morphology in *Col9a3$^{\Delta ex3}$* and *Col9a3$^{-/-}$* tibial growth plate. TEM images displaying unorganised regions putatively due to tissue degeneration. Note: cells undergoing necrosis (black arrows) and an array of ordered collagen fibrils being engulfed within the mass of degenerated material (yellow dashed line).

5.2.3 Growth plate abnormalities during early development in mutant mice.

TEM findings suggested that a more severe phenotype could be exhibited by the growth plate at earlier post-natal developmental stages. Therefore, further histological investigation on mutant and WT 1-week old tibial epiphysis was needed to confirm the presence of the tissue degeneration observed by TEM.

Unfortunately, because of breeding problems no *Col9a3*$^{\Delta ex3}$ samples were available, at the time of writing, to perform tissue analysis at 1 week, which therefore only compared *Col9a3*$^{-/-}$ mice with their WT littermates. Subsequently the analysis was integrated by adding the tissue sections of 1-week old *Col9a3*$^{\Delta ex3}$ mice. H&E and Toluidine blue stainings were performed on the tibial proximal epiphysis and femoral distal epiphysis growth plates sections. Stainings showed *Col9a3*$^{-/-}$ mice to have a large hypocellular central region, which was absent in WT (Fig. 5.8 C, F, I, N). This hypocellular region was localised along the whole growth plate height. Starting just below the future secondary ossification centre, extending along the resting and proliferative zones and then being engulfed into the hypertrophic zone, it finally protruded into the metaphyseal newly formed trabecular bone, conferring on the hypertrophic zone an unusual V-shaped morphology. The peripheral tibial epiphysis did not show an alteration in chondrocyte density, but only in their distribution. The typical columnar organisation of the proliferative zone was profoundly impaired, and chondrocytes appeared more rounded and randomly arranged, sometimes following the mediolateral axis rather than the proximodistal. Interestingly, no evident broadening of the *Col9a3*$^{-/-}$ tibial condyle was observed at this age. Toluidine blue staining was used as an indication of the proteoglycan content in the growth plate. In none of the samples (N=3) a change in the intensity of toluidine blue staining was noticed, hence no alteration in the proteoglycans abundance or distribution could be observed. However, the possibility of overexposure of sections during a not yet fully optimised staining protocol cannot be excluded. Indication of cell-free areas were also detected in *Col9a3*$^{\Delta ex3}$ tibial sections, mainly localised at proliferating region of the growth plate, although not as severe as in *Col9a3*$^{-/-}$ mice (Fig. 5.8 B, E, H, M). Toluidine staining confirmed no change in the proteoglycan distribution and abundance also in *Col9a3*$^{\Delta ex3}$ tibiae.

The same cartilage defect was observed also in *Col9a3*$^{-/-}$ femurs, where an even more pronounced central region was completely devoid of cells and was surrounded by smaller and round-shaped chondrocytes (Fig. 5.9 C, F, I, N). The femoral hypertrophic zone had reduced

height compared to WT. Hypertrophic chondrocytes were enlarged and their spatial distribution was profoundly disturbed by the partial invasion of the hypocellular region. The presence of a defined circular fold in the tissue section in the middle of the cell-free area, suggested that these morphological changes might have affected the mechanical stability of the tissue, becoming more fragile and looser. More obvious cell-free areas were also recognised in *Col9a3*$^{\Delta ex3}$ femurs compared to tibiae, localised in the central proliferating region of the growth plate and slightly invading the lower hypertrophic zone (5.9 B, E, H, M). Furthermore, we noticed alterations of the secondary ossification centres in both mutant mice (5.10). *Col9a3*$^{-/-}$ mice were found with disrupted secondary ossification centres in femurs (5.10 C, F), due to the cell free areas, and delayed secondary ossification centre in tibia (5.10 I, N) whose chondrocytes appeared smaller and at an earlier stage of differentiation compared to WT (red circles in Fig. 5.10). Interestingly, from *Col9a3*$^{\Delta ex3}$ sections of both tibiae and femurs (Fig.5.10 E, M), we could notice larger chondrocytes showing a hypertrophic phenotype compared to those visualised in WT and *Col9a3*$^{-/-}$ sections. This finding suggested a possibly premature differentiation of chondrocytes and formation of the secondary ossification centre in *Col9a3*$^{\Delta ex3}$ mice compared to WT and *Col9a3*$^{-/-}$ mice.

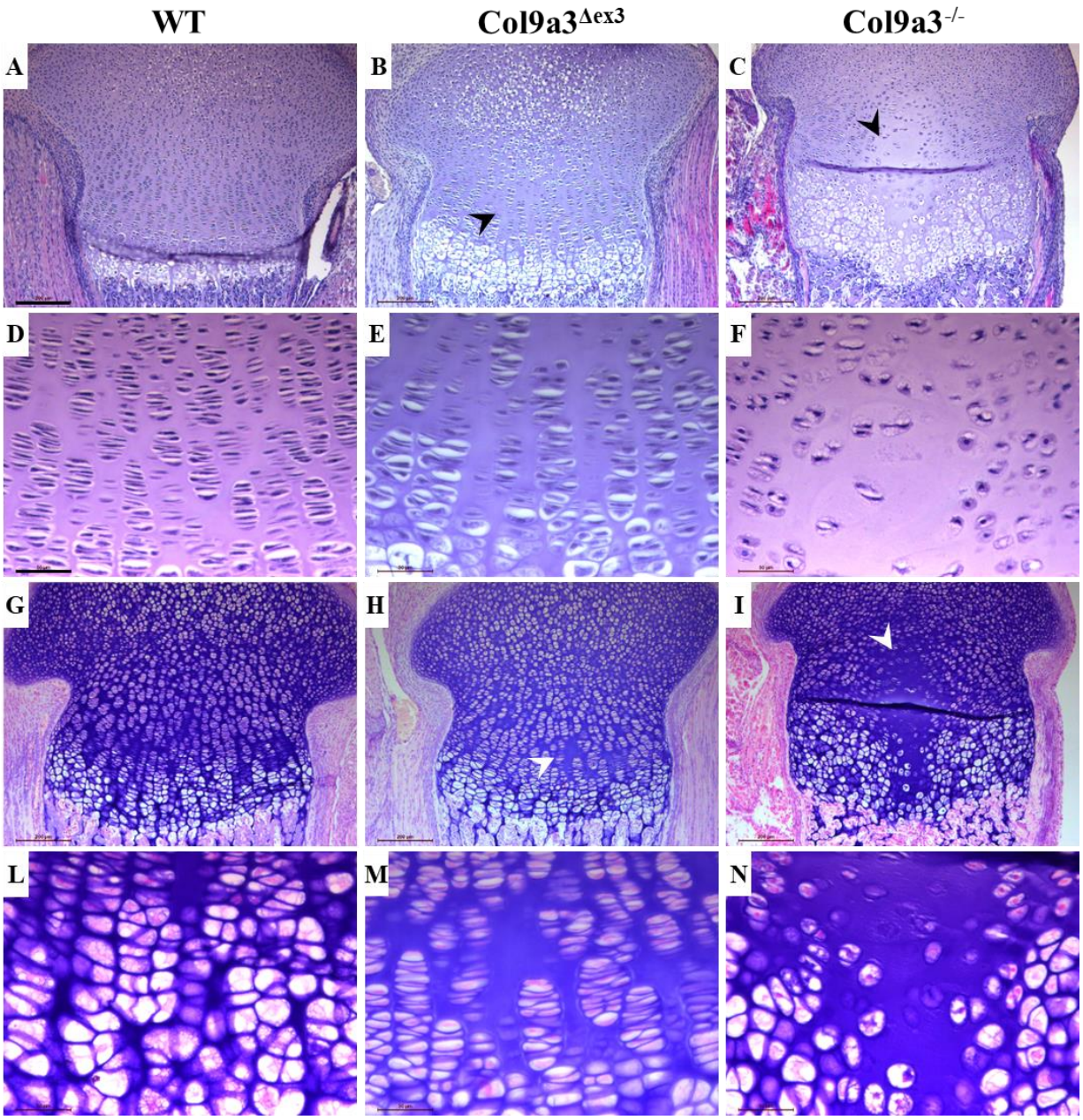

Fig. 5.8 | Analysis of tissue defects in 1-week old tibial proximal epyphisis. H&E (A-F) and Toluidine blue staining (G-N) of 1-week old tibial growth plates from *Col9a3*$^{-/-}$ and WT animals. Hypocellular regions indicated by arrowheads. Representative images of analysis of three mice per genotype. (scale bar = 200μm, Higher magnification scale bars = 50μm).

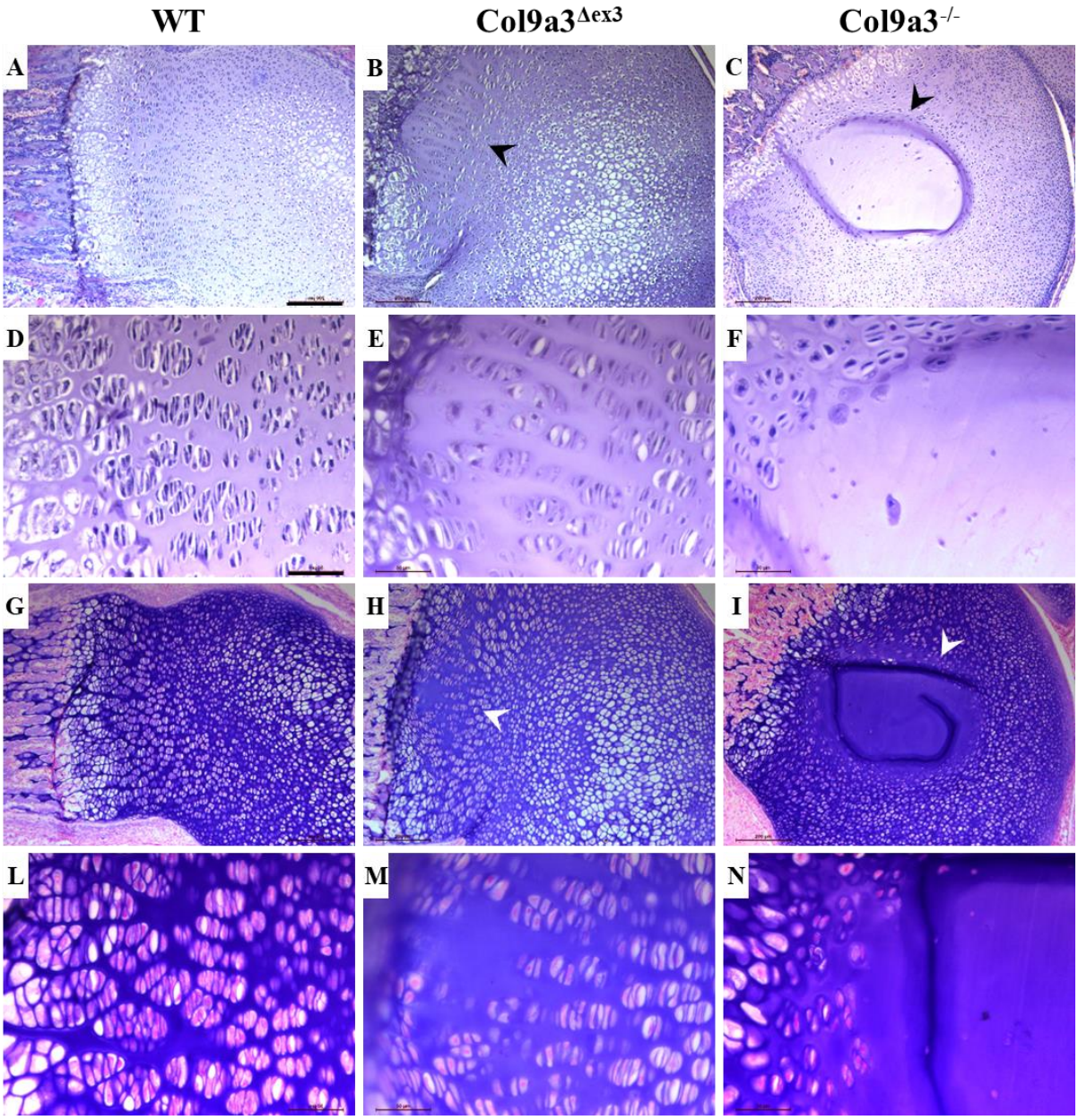

Fig. 5.9 | Analysis of tissue defects in 1-week old femoral distal epiphysis. H&E (A-F) and Toluidine blue staining (G-N) of 1-week old femoral growth plates from *Col9a3*$^{-/-}$ and WT animals. Representative images of analysis of three mice per genotype. Hypocellular regions indicated by arrowheads. (scale bar = 200µm, Higher magnification scale bars = 50µm).

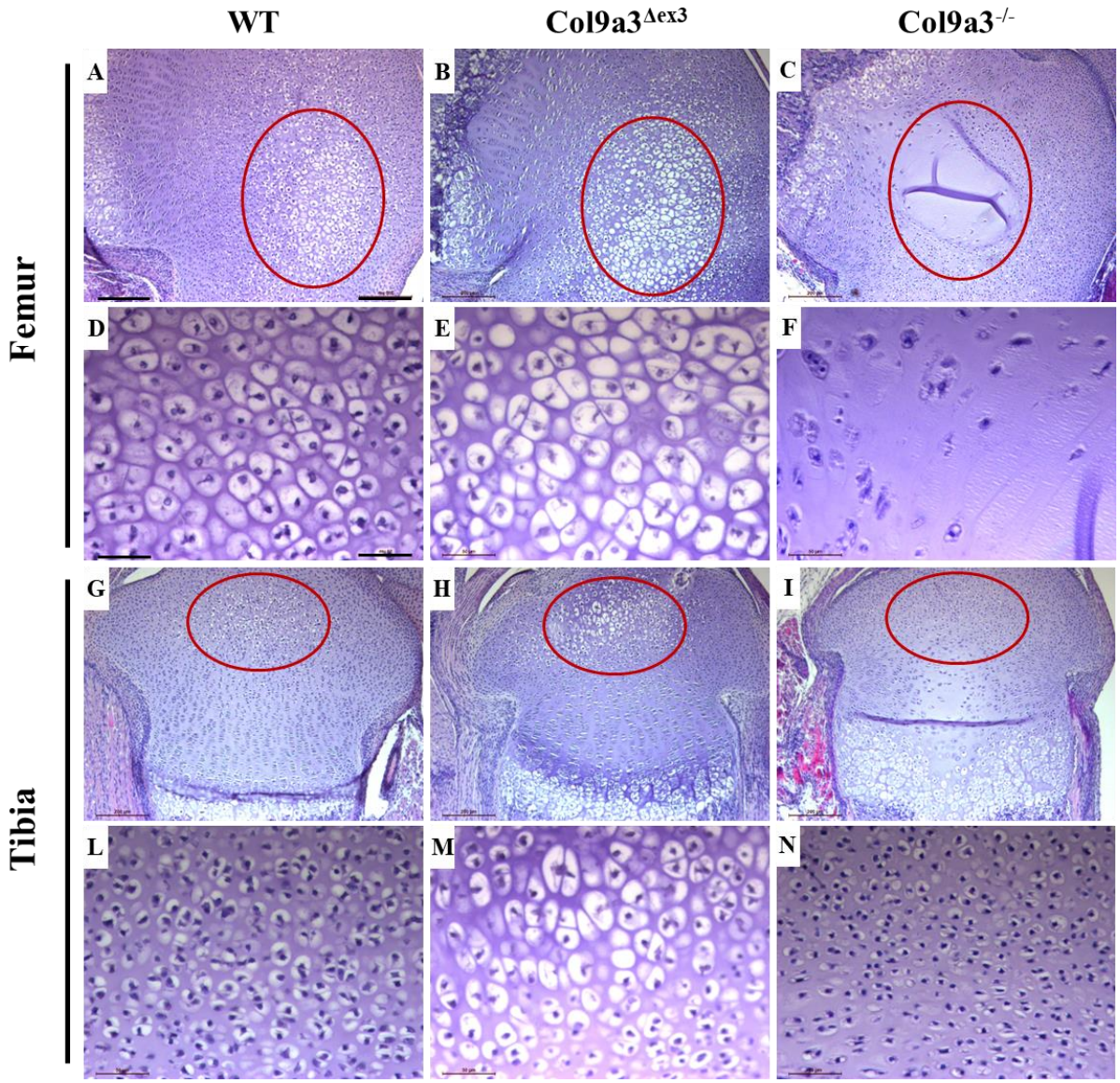

Fig. 5.10 | Secondary ossification centre alterations in *Col9a3$^{\Delta ex3}$* and *Col9a3$^{-/-}$* mice. H&E staining of 1-week old femoral distal epiphysis and tibial proximal epiphysis. Secondary ossification centres indicated by red circles in low magnification pictures. Representative images of analysis of three mice per genotype. (scale bar = 200μm, Higher magnification scale bars = 50μm).

5.2.4 Collagen type IX localisation in tibial growth plate

Collagen type IX localisation in the tibial growth plate was assessed using IHC. Sections of tibiae collected from 3-week old female mice, were probed with a collagen type IX antibody recognising as epitope the NC4 domain of α1(IX) helix (Fig. 5.11). In *Col9a3*$^{\Delta ex3}$ tibial epiphysis, the fluorescence signal corresponding to collagen type IX was weaker than control. In addition, at higher magnification, the signal detected in WT growth plate was predominantly localised in the inter-territorial matrix, surrounding the chondrocytes arranged in columns. Interestingly, *Col9a3*$^{\Delta ex3}$ mice showed collagen type IX to be more localised at the pericellular matrix and reduced in the inter-territorial matrix. In the proliferative zone of *Col9a3*$^{\Delta ex3}$ mice, intracellular staining was observed increased, suggesting a certain level of retention of the 'mutant' protein within the resident proliferative chondrocytes. In *Col9a3*$^{-/-}$ growth plate, the presence of collagen type IX was strongly reduced within the matrix, and the weak staining detected, was mainly exhibited by the irregularly distributed chondrocytes, indicating a possible protein retention, although we cannot exclude the possibility of a staining artefact.

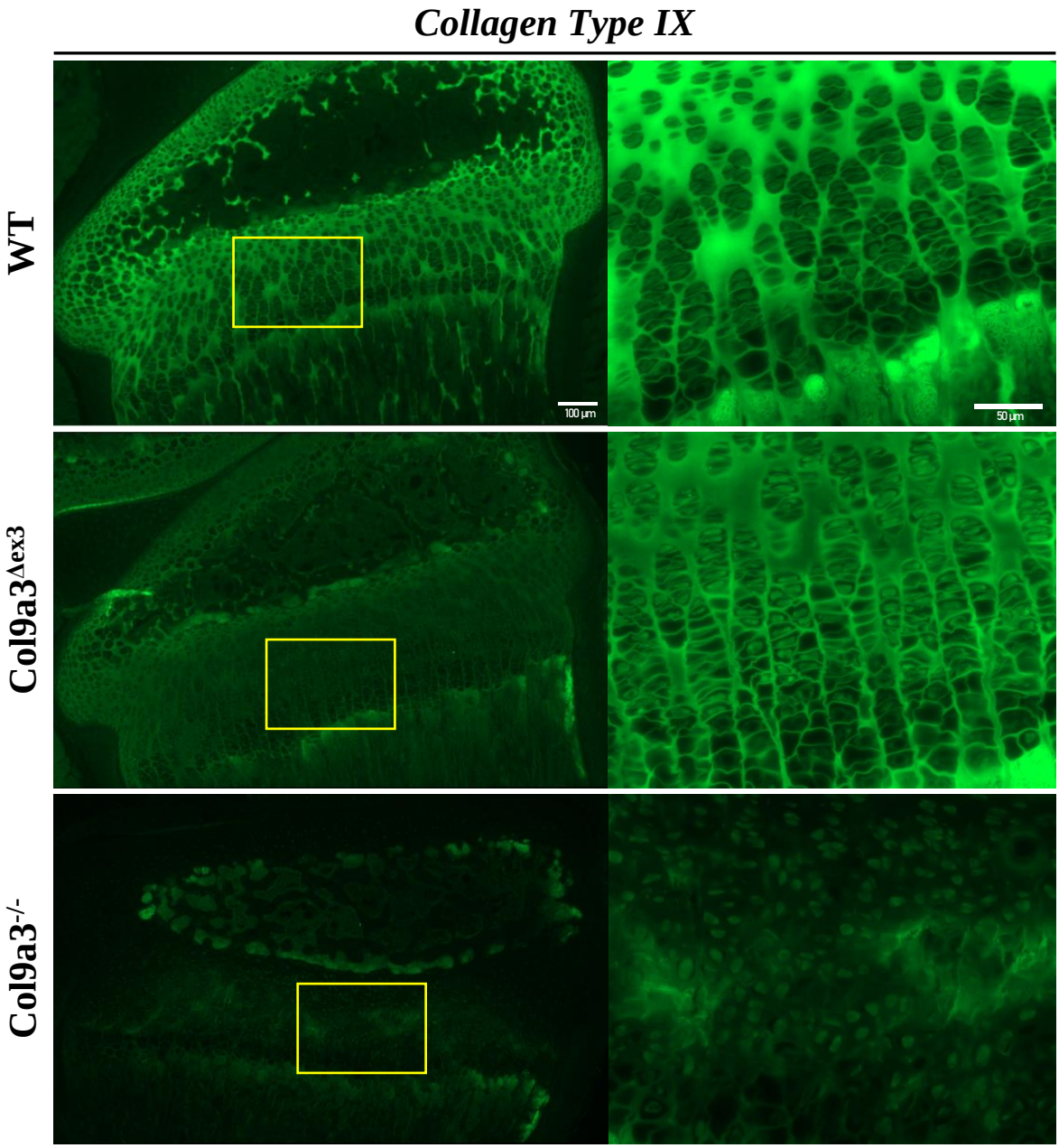

Fig. 5.11 | Collagen type IX abundance in the tibial growth plate of WT and mutant mice. 3-week old tibiae sections (N=3) were probed with an antibody against the α1 chain of collagen type IX. Images were taken at 20X (scale bar = 100µm) and 40X (scale bar = 50µm) magnification and exposure time was set on negative control sections (Appendix C, Fig.C1).

5.2.5 Localisation of Collagen type IX interactors in the ECM.

Col9a3$^{\Delta ex3}$ and *Col9a3*$^{-/-}$ mutations might affect the localisation and retention of other ECM proteins into the matrix. For this reason, the localisation and abundance of other important ECM structural proteins, known to directly interact with collagen type IX, was assessed in 3-week old tibial growth plates (Fig. 5.12).

Matrilin-3 staining did not indicate any relative change in abundance throughout the different zones in both mutant growth plates. Nonetheless, matrilin-3 localisation appeared more pericellular, with some intracellular retention, in *Col9a3*$^{\Delta ex3}$ mice compared to WT animals. Staining for matrilin-3 in *Col9a3*$^{-/-}$ mice was distributed throughout the growth plate and was equally dispersed into the matrix and within proliferating cells. However, the highly altered chondrocyte morphology and organisation and the general impaired growth plate of the *Col9a3*$^{-/-}$ line made the exact localisation difficult to determine.

The intensity of staining for another collagen type IX interactor protein, COMP was only slightly reduced in *Col9a3*$^{\Delta ex3}$ tissue, but not in *Col9a3*$^{-/-}$ growth plates.
When staining for the hypertrophic marker collagen type X was performed, we visualised a more extended fluorescent signal in *Col9a3*$^{\Delta ex3}$ growth plates, indicating a larger hypertrophic zone than in WT controls, confirming our previous growth plate morphometric analysis. Reduced abundance, along with a disorganised staining pattern of collagen type X was observed in the *Col9a3*$^{-/-}$ hypertrophic region.

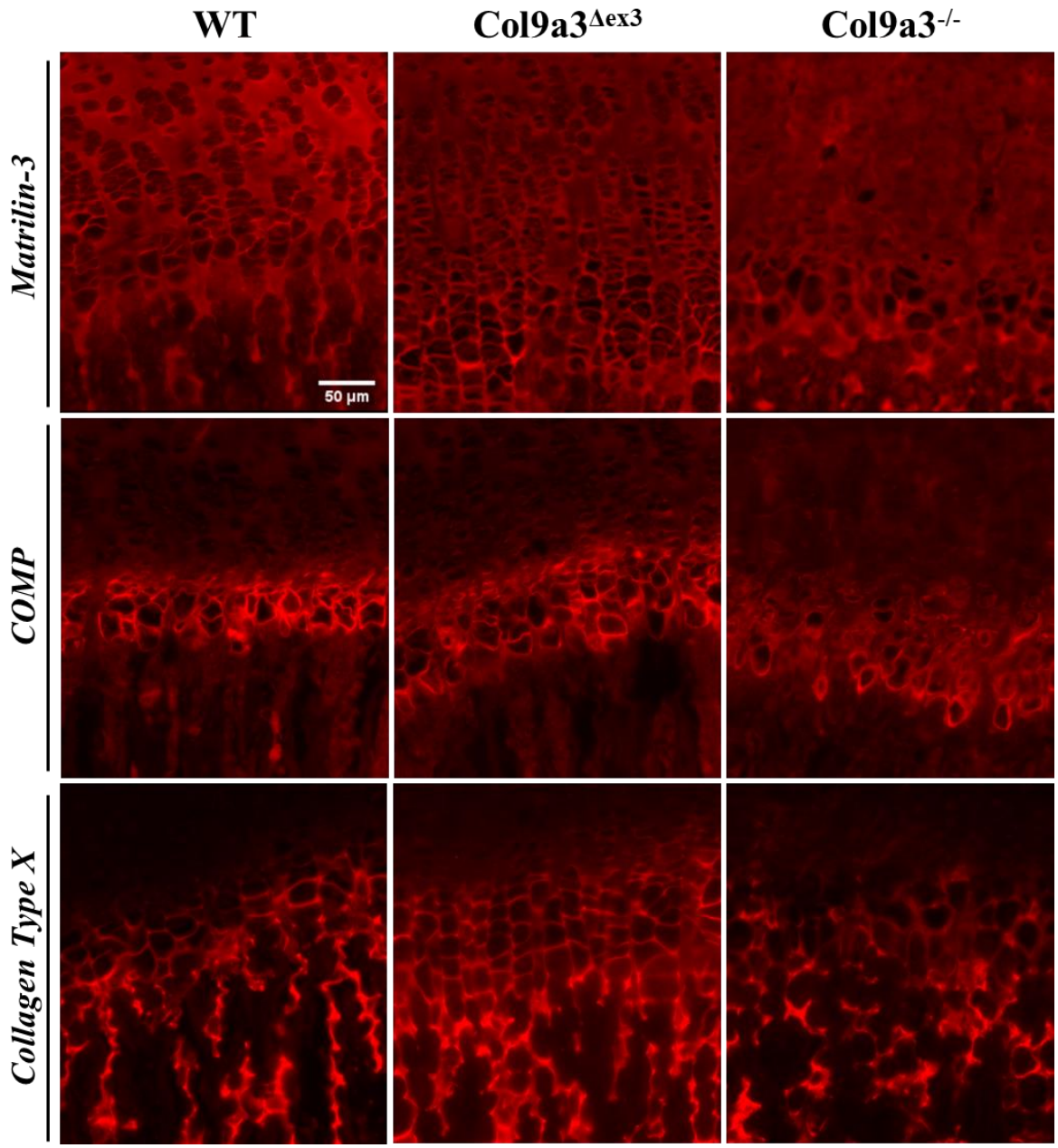

Fig. 5.12 | Localisation of some extracellular matrix proteins in tibial growth plates. Immunofluorescence staining was performed by probing 3-week old tibiae sections (N=3) with antibodies specific for matrilin-3, COMP and collagen type X. Images were taken at 40X (scale bar = 50µm) magnification and exposure time was set on negative control sections (Appendix C, Fig.C1).

5.2.6 Mutated or absent α3(IX) affects chondrocytes proliferation

Proliferation of chondrocytes was analysed in the proliferative zone of the tibial growth plate at 3 weeks of age using a BrdU (5-bromo-2'-deoxyuridine) *in vivo* assay. Bromodeoxyuridine is a synthetic nucleoside that is an analog of thymidine. The assay is commonly used to detect proliferating cells in living tissue by exploiting the capability of BrdU to be incorporated into the newly synthesized DNA of replicating cells (during the S phase of the cell cycle, when DNA is replicated), substituting for thymidine during DNA replication. *Col9a3*$^{\Delta ex3}$, *Col9a3*$^{-/-}$ and WT mice were injected with BrdU solution and their legs harvested two hours post-injection. BrdU positive cells were detected by immunohistochemistry using a specific anti-BrdU antibody and analysis was performed on nine matched sections per mouse (N=3, Fig. 5.13 A) in order to cover the entire growth plate depth. The number of cells undergoing mitosis were expressed relative to the total number of cells present in the proliferative zone.

Our results showed that in WT growth plate, 11.4 % of chondrocytes were in proliferative activity. The number of BrdU positive cells detected in *Col9a3*$^{\Delta ex3}$ and *Col9a3*$^{-/-}$ growth plate proliferative zones were respectively 7.9 % and 6.7 %. Therefore, the proliferation of chondrocytes when compared to wild type littermates was significantly reduced of 31% in *Col9a3*$^{\Delta ex3}$ and 41% in *Col9a3*$^{-/-}$ mice (Fig. 5.13 B-C).

A

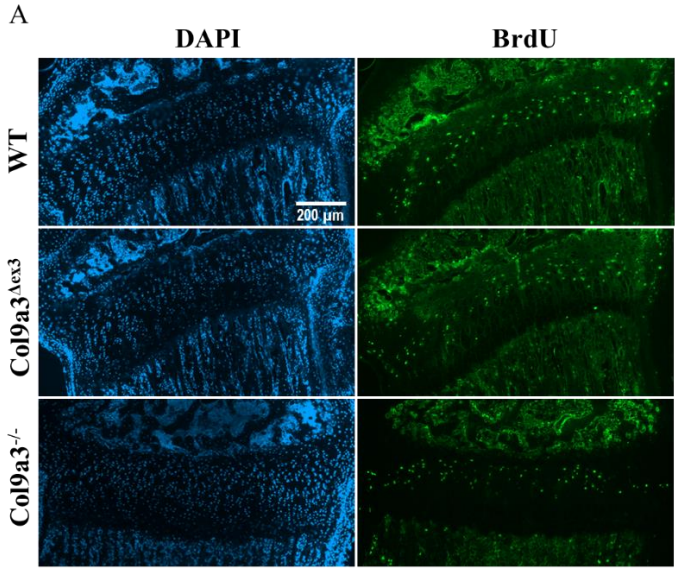

B

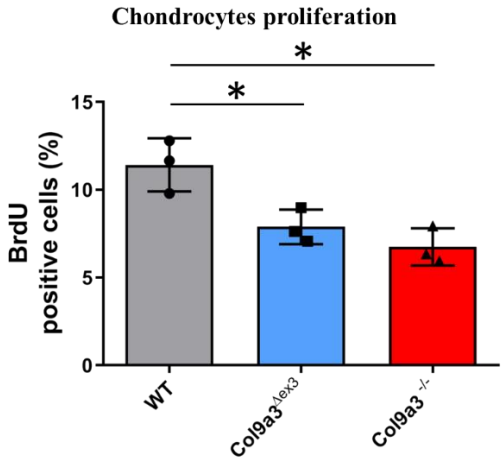

C

Chondrocytes proliferation			
	WT	**Col9a3$^{\Delta ex3}$**	**Col9a3$^{-/-}$**
n. of BrdU positive cells ± SD	113 ± 11	87 ± 9	85 ± 6
n. of DAPI cells ± SD	871 ± 144	1131 ± 125	1229 ± 115
% of BrdU positive cells ± SD	11.4 ±1.5	**7.9±0.9***	**6.7±1.0***

Fig. 5.13 | Proliferation rate of chondrocytes in growth plate proliferative zones of 3-week old WT, *Col9a3$^{\Delta ex3}$* and *Col9a3$^{-/-}$* mice. The level of chondrocytes undergoing mitosis into the proliferative zone of 3-week old tibial growth plates was analysed by BrdU labelling assay in *Col9a3$^{\Delta ex3}$* and *Col9a3$^{-/-}$* female mice and their wild type littermates. A. BrdU-labelled proliferative cells compared to Dapi-stained nuclei of 20X growth plate images (scale bar = 200 µm). B. Graph of BrdU–positive cells expressed as a percentage relative to the total number of cells in the proliferative zone. C. Table with numeric data used to generate "Chondrocytes Proliferation" graph**.** Two tailed T-test: *p < 0.05

5.3 Transcriptomic analysis of *Col9a3$^{\Delta ex3}$* and *Col9a3$^{-/-}$* ribs cartilage.

Transcriptomic analysis was performed to investigate transcriptional changes in homozygous mice for *Col9a3$^{\Delta ex3}$* and *Col9a3$^{-/-}$* mutations compared to their WT littermates. RNA sequencing was conducted using the RNA extracted from chondrocytes of ribs cartilage from 7-day old mice (N=4). After successfully passing the first integrity check (Appendix E, Fig. E.1), RNA was sequenced at Newcastle University Genomics Core Facility and Dr Kathleen Cheung kindly performed the subsequent transcriptomic analysis.

Three females and one male coming from two different litters constituted the WT group of samples; *Col9a3$^{\Delta ex3}$* mice were all male brothers and *Col9a3$^{-/-}$* samples were from two females and two males from two different litters. To explore how the transcriptome compared across all the different samples, we performed a principal component analysis (PCA) (Fig. 5.14). PCA showed distinct clustering of samples according to their genotype confirming that the transcriptome of each genotype was different. To determine the specific gene expression changes contributing to the distinct clustering in the three genotypes, we compared each mutant genotype with the WT gene set using DESeq2 (Love et al. 2014). The result demonstrated statistically significant alterations in expression levels within each group, as visualised by volcano plots (Fig. 5.15). Specifically, the expression of 424 genes resulted significantly upregulated and 271 genes significantly downregulated in *Col9a3$^{\Delta ex3}$* mice compared to WT littermates. The first 15 most significant upregulated and downregulated genes are listed in Table 5.1. Among them was a significant increase in expression of fibroblast growth factor 13 (*Fgf13*) and decreased expression of fibroblast growth factor receptor 3 (*Fgfr3*) in *Col9a3$^{\Delta ex3}$* chondrocytes.

From the comparison of *Col9a3$^{-/-}$* transcriptome profile with WT gene set, 259 genes and 185 genes were respectively upregulated and downregulated in the mutant transcriptome. The first 15 most significant upregulated and downregulated genes are listed in Table 5.1. Some of the genes most significantly upregulated in *Col9a3$^{-/-}$* mice comprised Tensin1 (*Tns1*), Spondin 1(*Spon1*), Versican (*Vcan*) and Cartilage intermediate layer protein (*Cilp*). A significant downregulation of genes such as Thrombospondin type 1 domain containing 4 (*Thsd4*) and Tolloidin like 1 (*Tll1*) was measured in *Col9a3$^{-/-}$* mice. Subsequently we searched for commonalities in the gene expression profiles of the two mutant mice. By comparing the list of differentially expressed genes which exhibited a significant change in *Col9a3$^{\Delta ex3}$* and *Col9a3$^{-/-}$* mice, we identified 75 genes commonly upregulated and 31 genes commonly

downregulated between the two expression profiles (Fig. 5.15). On the lists of genes whose expression changes were found in common in the mutants, we subsequently performed pathway enrichment analysis to identify GO terms using the database for annotation, visualisation and integrated discovery (DAVID) functional annotation tool. When the list of commonly upregulated genes was interrogated, the analysis result displayed significant enriched gene ontology (GO) terms correlating with biological processes involving elastic fibre assembly (*Fbln5*, *Lox*, *Mfap4*, *Tnxb*), extracellular matrix (*Postn*), collagen fibril organisation (*Dpt*, etc..), cell adhesion (*Col6a6*, *Mfap4*, *Spon1*, *Vcan*, *Svep1*), regulation of cell growth (*Igfbp4*) and interestingly embryonic eye morphogenesis (*Fbn2*, *Mfap2*). In contrast, no significant GO terms were obtained using DAVID enrichment analysis out of the significantly downregulated genes shared by the two mutant mice.

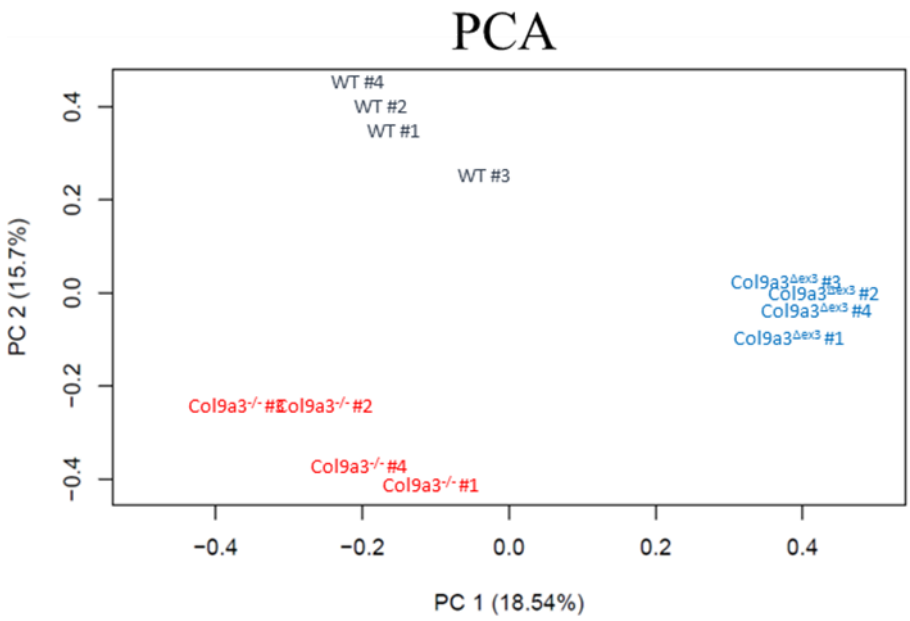

Fig. 5.14 | Principal component analysis of RNA-seq data. Gene expression changes were investigated at 7 days, in costal chondrocytes RNA from *Col9a3*$^{\Delta ex3}$ and *Col9a3*$^{-/-}$ mice versus WT (n=4 per genotype). The PCA was performed using normalised RNA-Seq data and results revealed separation of different biological replicates according to genotype, (WT animals in dark grey; *Col9a3*$^{\Delta ex3}$ in blue; *Col9a3*$^{-/-}$ in red) confirming mutation dependent clustering of RNA-seq profiles.

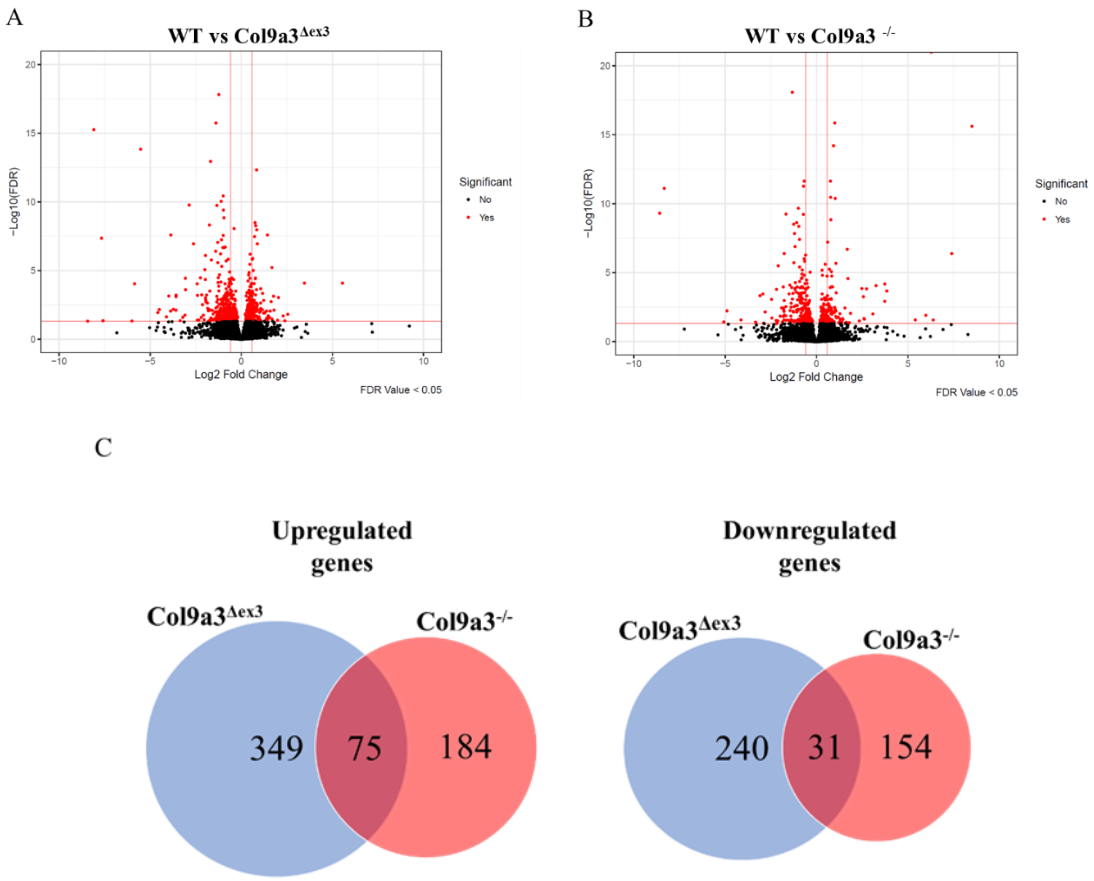

Fig. 5.15 | Outline of significant up- and down-regulated genes (vs. WT) in *Col9a3$^{\Delta ex3}$* and *Col9a3$^{-/-}$* transcriptomes. Volcano plot representation of differential expression analysis of genes in *Col9a3$^{\Delta ex3}$* (A) and *Col9a3$^{-/-}$* (B) mice versus wild-type. The x-axis shows log2fold-changes in expression and the y-axis the log10 of the false discovery rate (FDR) considered significant for values < 0.05. C. Venn diagrams representing the number of genes significantly (padj value < 0.05) up- and down-regulated in *Col9a3$^{\Delta ex3}$* and *Col9a3$^{-/-}$* gene sets compared to WT.

WT vs Col9a3$^{\Delta ex3}$					
Upregulated			Downregulated		
Gene name	**Description**	**Log2 Fold Change**	**Gene name**	**Description**	**Log2 Fold Change**
Eif2s3y	eukaryotic translation initiation factor 2, subunit 3, structural gene Y-linked	6.00	*Flnb*	filamin, beta	-0.84
Fgf13	fibroblast growth factor 13	4.58	*Slc7a2*	solute carrier family 7 (cationic amino acid transporter, y+ system), member 2	-0.75
Muc4	mucin 4	4.50	*Id1*	inhibitor of DNA binding 1	-0.85
Lce1d	late cornified envelope 1D	3.87	*Rapgef4*	Rap guanine nucleotide exchange factor (GEF) 4	-0.73
Pin4	protein (peptidyl-prolyl cis/trans isomerase) NIMA-interacting, 4 (parvulin)	3.73	*Egr3*	early growth response 3	-0.88
Kdm5d	lysine (K)-specific demethylase 5D	3.35	*Tcf4*	transcription factor 4	-0.48
Spata33	spermatogenesis associated 33	3.21	*Arl5b*	ADP-ribosylation factor-like 5B	-0.63
Pde6h	phosphodiesterase 6H, cGMP-specific, cone, gamma	3.09	*Saraf*	store-operated calcium entry-associated regulatory factor	-0.60
Xirp1	xin actin-binding repeat containing 1	3.07	*Fgfr3*	fibroblast growth factor receptor 3	-0.47
Rassf4	Ras association (RalGDS/AF-6) domain family member 4	3.06	*Adssl1*	adenylosuccinate synthetase like 1	-1.68
Ccl21a	chemokine (C-C motif) ligand 21A (serine)	2.86	*Mapk1ip1l*	mitogen-activated protein kinase 1 interacting protein 1-like	-0.66
Mmrn1	multimerin 1	2.62	*Usp36*	ubiquitin specific peptidase 36	-0.43
Lyve1	lymphatic vessel endothelial hyaluronan receptor 1	2.42	*Myo1d*	myosin ID	-0.41
Pkia	protein kinase inhibitor, alpha	2.40	*Tanc1*	tetratricopeptide repeat, ankyrin repeat and coiled-coil containing 1	-0.77
Stab1	stabilin 1	2.34	*Serpine2*	serine (or cysteine) peptidase inhibitor, clade E, member 2	-0.47

WT vs Col9a3$^{-/-}$					
Upregulated			Downregulated		
Gene name	**Description**	**Log2 Fold Change**	**Gene name**	**Description**	**Log2 Fold Change**
Tcfl5	transcription factor-like 5 (basic helix-loop-helix)	0.68	*Chil1*	chitinase-like 1	-1.07
Il11	interleukin 11	0.71	*Eps8l1*	EPS8-like 1	-8.50
Tns1	tensin 1	8.33	*Flnb*	filamin, beta	-0.93
Inhba	inhibin beta-A	1.00	*Rpl13a*	ribosomal protein L13A	-0.76
Alad	aminolevulinate, delta-, dehydratase	1.67	*Prune2*	prune homolog 2	-1.02
Ogfr	opioid growth factor receptor	0.72	*Klhl7*	kelch-like 7	-0.61
Vcan	versican	1.08	*Gcnt1*	glucosaminyl (N-acetyl) transferase 1, core 2	-1.68
Spon1	spondin 1, (f-spondin) extracellular matrix protein	1.25	*Cdc26*	cell division cycle 26	-1.06
Anxa8	annexin A8	0.97	*Adk*	adenosine kinase	-0.47
Plet1	placenta expressed transcript 1	1.20	*Dmwd*	dystrophia myotonica-containing WD repeat motif	-0.71
Sox11	SRY (sex determining region Y)-box 11	0.93	*Rps11*	ribosomal protein S11	-0.30
Gprc5a	G protein-coupled receptor, family C, group 5, member A	1.17	*Rrad*	Ras-related associated with diabetes	-0.81
Slc20a1	solute carrier family 20, member 1	0.68	*Thsd4*	thrombospondin, type I, domain containing 4	-0.58
Mfap2	microfibrillar-associated protein 2	0.65	*Pla2g7*	phospholipase A2, group VII (platelet-activating factor acetylhydrolase, plasma)	-0.84
Cilp	cartilage intermediate layer protein, nucleotide pyrophosphohydrolase	1.24	*Tll1*	tolloid-like	-1.72

Table 5.1 | Significantly up- and down-regulated genes in *Col9a3$^{\Delta ex3}$* and *Col9a3$^{-/-}$* mice.
List of the first 15 most significant up- and down-regulated genes. (Statistical significance padj value < 0.05).

To further investigate putative gene expression programs able to contribute to the mutant mice phenotype, we compared and examined our mice expression profiles using Rank–rank Hypergeometric Overlap (RRHO) and Gene set Enrichment Analysis (GSEA) computational methods.

The RRHO algorithm (Plaisier et al. 2010) was used to check through the two gene lists ranked according to the degree of differential expression exhibited by the two mutant mice, and to measure if the number of overlapping genes was statistically significant. The RRHO analysis output consists of a heatmap showing the overlap trend reflecting the relation between the two expression profiles. The highest intensity points depict the statistically strongest, or the least likely to randomly occur, overlap between the two profiles. The heatmap output of RRHO shows different colours based on the log10-transformed hypergeometric P-values. Therefore, the regions of highly significant overlap are denoted by red coloured high positive intensity areas, those regions where the overlap was lower than expected, are indicated by high negative intensity, purple coloured.

The output map obtained from RRHO comparison of the ranked *Col9a3*$^{\Delta ex3}$ and obtained from WT versus *Col9a3*$^{\Delta ex3}$ and *Col9a3*$^{-/-}$ gene sets, revealed a strong red signal predominantly located at the bottom left quadrant of the map. (Fig. 5.16). This intensity pattern indicated that the highest overlap score was obtained only in the tops of the ranked genes lists. In other words, the strongly significant overlap trend suggested that the two mutant mice have related gene expression programs mostly involving their significant upregulated genes. Whereas not significant overlapping was reported in the downregulated genes of both mice.

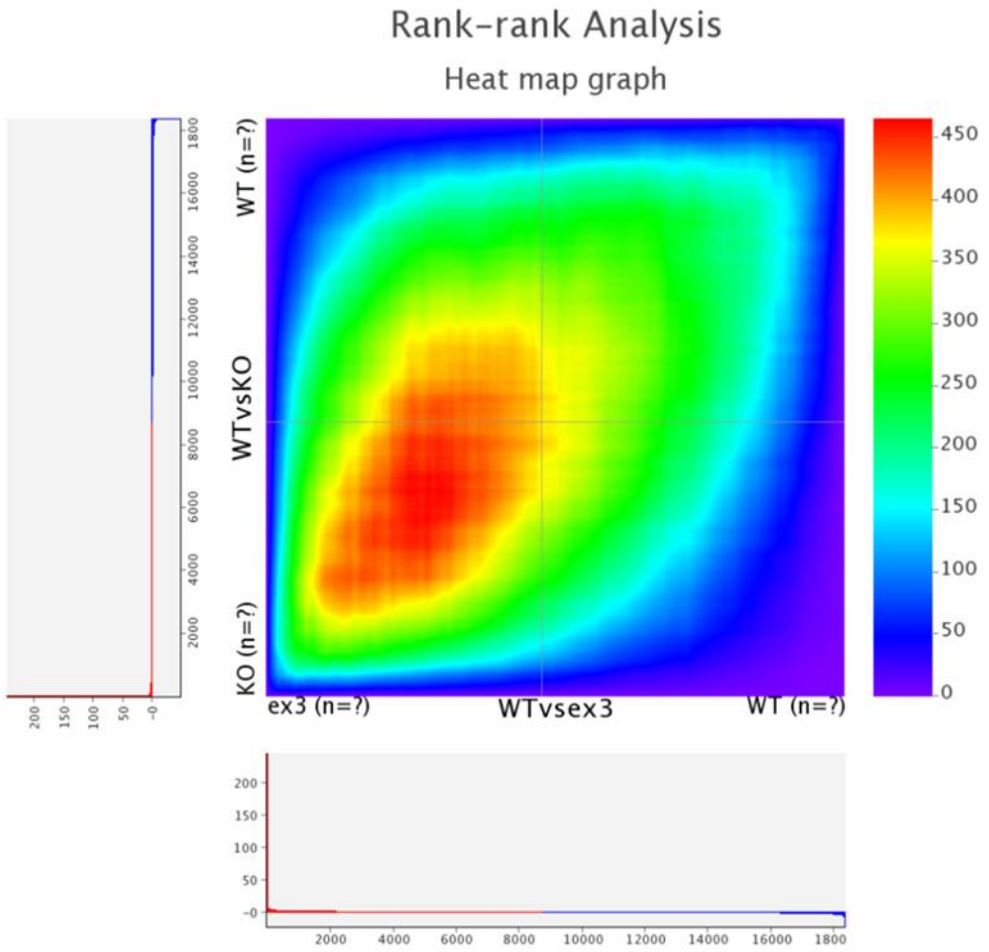

Fig. 5.16 | RRHO heatmap. Heatmap generated by comparing the two ranked lists of transcripts that are differentially expressed in *Col9a3*$^{\Delta ex3}$ and *Col9a3*$^{-/-}$ using the rank-rank hypergeometric overlap (RRHO) algorithm. High intensity signals (red lower corner) indicated that the highest overlap involved the top differentially expressed genes in *Col9a3*$^{\Delta ex3}$ and *Col9a3*$^{-/-}$ chondrocytes. The direction-signed log10-transformed hypergeometric p values are indicated in the associated colour scale.

Along with the RRHO analysis, Gene Set Enrichment Analysis (Mootha et al. 2003, Subramanian et al. 2005) was applied as additional approach to compare different gene sets and to look for statistically enriched or depleted functional related genes in both mutant mice. GSEA significance was determined as a false discovery rate values (FDR) below 0.25. GSEA result showed 102 gene sets to be significantly enriched in *Col9a3*$^{\Delta ex3}$ mice when compared to WT expression profile. Some of the enriched biological processes in *Col9a3*$^{\Delta ex3}$ (Fig. 5.17) comprised : "Cell cycle", "DNA replication", "Collagen formation" (*Adamts14, Col23a1, Col4a2, Col12a1, P4hb, Col5a2, Col5a1, Bmp1, Col4a4, Col1a2, Col10a1, Col4a3, Pcolce, Col14a1, Ppib, Col3a1, Col4a1, Plod1, Col15a1, Col5a3*) and "Extracellular matrix organisation, sharing many genes with "Collagen formation" pathway plus some other additional genes (*Mmp14 , Cma1, Crtap, Elane, Timp1, Pcolce*). Other resulting enriched pathways in *Col9a3*$^{\Delta ex3}$ were "Muscle contraction", "Regulation of apoptosis", "Wnt signalling pathway". In *Col9a3*$^{-/-}$ mice none of the gene sets obtained by GSEA passed the significance threshold for positive enrichment.

Eleven gene pathways were found to be significantly enriched for downregulated genes in *Col9a3*$^{\Delta ex3}$ and these included, "nonsense mediated decay enhanced by the exon junction complex", "signalling by Fgfr mutants" (*Fgfr3, Fgfr2, Fgfr1, Frs2*) and "myogenesis" (*Tcf4, Mef2a, Mef2d, Abl1*). In *Col9a3*$^{\Delta ex3}$ it was worth noticing the downregulation of genes *Gpc6, Gpc1* and *Sdc4*, involved in the "heparin sulphate glycosaminoglycan degradation pathway", whose FDR was 0.26, therefore just above the significance threshold. GSEA report for *Col9a3*$^{-/-}$ displayed significant depletion of 17 gene sets, which involved mainly the metabolism of RNA such as "3'UTR mediated translational regulation", " peptide chain elongation"," nonsense mediated decay enhanced by the exon junction complex", "activation of the mRNA upon binding of the cap binding complex and Eifs and subsequent binding to 43s". Interestingly, only the depletion of two gene sets directly related to ECM, resulted significant from GSEA applied on *Col9a3*$^{-/-}$. They were "extracellular matrix organisation" and "collagen formation" pathways, which showed and shared the downregulation of only *Col9a3* and *Tll1* genes.

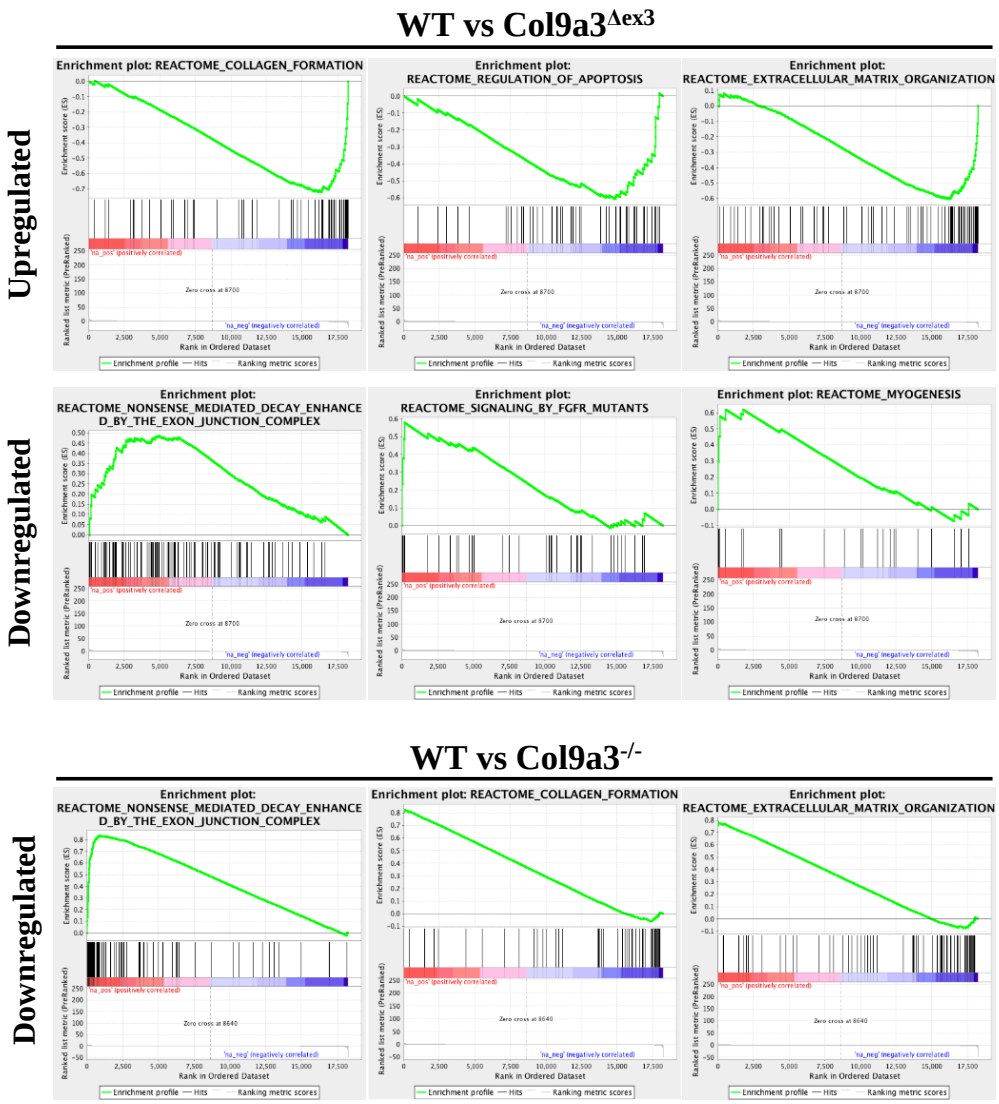

Fig. 5.17 | GSEA enrichment of *Col9a3^{Δex3}* and *Col9a3$^{-/-}$* gene sets in mouse chondrocytes RNA-sequencing data. Plots providing a graphical view of the enrichment scores (ES) of some of the gene sets enriched in response to Col9a3^{Δex3} and Col9a3$^{-/-}$ mutations. The green peak represented in the top portion of the plot shows the running ES for the gene set as the analysis walks down the ranked list. The middle portion of the plot shows where the members of the gene set appear in the ranked list of genes. The bottom portion of the plot shows the value of the ranking metric as you move down the list of ranked genes and it measures a gene's correlation with a phenotype. No plot related to upregulated genes in *Col9a3$^{-/-}$* mice is shown as no gene set was found significantly enriched by GSEA.

5.4 Discussion

In this chapter the role of collagen type IX was explored by assessing the tissue pathology of the growth plate in our two mutant mice. Our investigation was carried out considering the crucial role of the epiphyseal growth plate in linear bone growth and the skeletal findings described in the previous chapter in *Col9a3*$^{\Delta ex3}$ and *Col9a3*$^{-/-}$ mice bones. The aim was to assess whether the putative collagen type IX role in bone formation was fulfilled by affecting cartilage growth plate stability.

When localisation and abundance of collagen type IX was assessed in 3-week old tibial growth plates, *Col9a3*$^{\Delta ex3}$ mice showed a slightly reduced amount of the protein in the extracellular matrix but a more prominent accumulation around the pericellular space and more importantly its retention into chondrocytes. We can speculate a longer protein permanence inside the cell and subsequent delayed trafficking and secretion of it, probably caused by a defect in the correct triple helix formation due to the insertion of a mutated α3 chain into the final protein. The same defect in the triple helix could then prevent or delay the correct integration of the mutated collagen type IX molecule in the inter-territorial ECM, which would explain the accumulation of the protein around the pericellular space as indicated by immunofluorescence localisation. *Col9a3*$^{-/-}$ mice showed very little staining for α1 of collagen type IX, which was predominantly cellular retained. This resulted in the absence of the whole protein into the matrix and therefore into a functional knockout of collagen type IX, as previously demonstrated in *Col9a1*$^{-/-}$ and *Col9a2*$^{-/-}$ mice (Balasubramanian et al. 2019, Dreier et al. 2008, Fassler et al. 1994, Hagg et al. 1997).

We started investigating the consequences of *Col9a3*$^{\Delta ex3}$ and *Col9a3*$^{-/-}$ mutations, by assessing growth plate structure through basic histology using animals at 3-weeks of postnatal development. Microscopy images showed no obvious changes in *Col9a3*$^{\Delta ex3}$ chondrocyte morphology or arrangement; however, an alteration of the relative height of the different zones was measured. On the contrary, tissue analysis showed *Col9a3*$^{-/-}$ mutation to cause a more severe phenotype than *Col9a3*$^{\Delta ex3}$. The *Col9a3*$^{-/-}$ tibial growth plate was severely affected in its organisation, boundaries between the functional distinct zones were confused and chondrocyte morphology and arrangement were severely compromised. We observed alterations in chondrocytes predominantly in their proliferative state, which were visibly smaller, round-shaped and not anymore arranged in the typical columnar distribution. From this finding we could speculate that collagen type IX might have a direct or indirect role in

the process of rotation and cell movement of chondrocytes during columnar arrangement in the proliferative zone. Although to our knowledge no evidence of this has been demonstrated in previous studies. Despite maintaining their morphology, hypertrophic chondrocytes appeared misaligned and less compactly distributed. Based on our observations, by reproducing the growth plate phenotype previously described in *Col9a1*$^{-/-}$ and *Col9a2*$^{-/-}$ mice, we further proved our *Col9a3*$^{-/-}$ mouse to be a functional knockout of collagen type IX.

In a family affected by MED due to a mutation in the α3 chain of collagen type IX, electron micrographs of epiphyseal cartilage biopsies showed lamellar material retained in a dilated rER, organised in a hexagonal array of fibrils. The study authors suggested that this material was an accumulation of aberrant or not fully processed matrix proteins. (Bonnemann et al. 2000). On the contrary, in another study involving MED patients affected by mutations in *COL9A2* gene, articular cartilage biopsies appearance was similar to controls, not showing particular inclusions or variations in fibrils (van Mourik et al. 1998a). These discrepancies could be explained by probable differences in cartilage tissues analysed and their relative tissue- specific gene expression. In our study, TEM was performed on 1-week old tibial growth plates to confirm the findings observed through basic histology and to help visualisation of chondrocyte ultrastructure. A certain degree of ER enlargement was noted in chondrocytes along the different zones of both mutant growth plates. Based on previously described chondrodysplasia mouse models, we could speculate protein retention as the cause for ER enlargement. We speculated whether the dilated ER observed in mutant mice could lead to the activation of ER stress related pathways. However, RNA-seq analysis did not show significant enrichment of the pathways generally associated with ER stress. This could potentially be explained by the fact that RNA-seq was performed on costal chondrocytes and not on growth plate cartilage. The poorly packed chondrocytes observed in the early proliferative zone of both mutant mice, suggests a surrounding matrix with possibly changed mechanical properties. In fact, changes in the structural components of ECM could result in a no longer compact matrix meshwork, with reduced functional support to the encompassed cells. Therefore, the forces that usually help and guide the chondrocytes arrangement into chondrons might be less effective, leading to a loose or even completely impaired chondron structure. Further analysis on cartilage stability to better elucidate any change into the matrix induced by *Col9a3*$^{\Delta ex3}$ and *Col9a3*$^{-/-}$ mutations, will be explored in chapter 6 of this thesis. Despite the morphological abnormalities recognised in *Col9a3*$^{-/-}$ growth plate chondrocytes, the presence of glycogen granules visualised in *Col9a3*$^{-/-}$ hypertrophic chondrocytes indicated

normal physiological functioning of the cells, prior calcification steps. The distribution of glycogen particles indeed increases with the degree of differentiation and maturation of the chondrocytes, reaching the maximum level in hypertrophic chondrocytes. Glycogen in cells provides energy and substrates for protein synthesis. In particular glycolytic breakdown products of glycogen constitutes the necessary substrates for alkaline phosphatase or as source material for the production, or alteration, of cartilage prior to calcification (Daimon 1977).

In addition, TEM images identified an interesting tissue deformity in both 1-week old mutant growth plates, localised just in the central core area between resting and proliferative zone. In this highly disrupted area, the typical morphology of chondrocytes and matrix was lost, instead a confused pattern of poorly defined material was observed. In both mutant animals, the cells in this core region appeared in a state of necrosis, probably indicative of a generalised cell death event within the area. Moreover, in *Col9a3*$^{-/-}$ tissue, an ordered pattern of what appeared an array of collagen fibres was noted to be misplaced and detached from the rest of disordered material, indicating some remnants of a possible ECM. The fact that this acellular core was observed only from the two mutant mice, suggested a mutation related defect, rather than an artefact generated during tissue processing for TEM. However, in order to exclude the possibility of an artefact, we checked tibial growth plates at the same time point (1-week) through basic histology. Both H&E and Toluidine blue staining showed the presence of a region almost devoid of cells in the core region of the growth plate, starting from the resting zone and protruding down to the hypertrophic zone. This tissue defect was severe in *Col9a3*$^{-/-}$ mice, while attenuated in *Col9a3*$^{\Delta ex3}$, similar to the hypocellular region observed by TEM. Interestingly, the cell-free area was observed in both the proximal tibiae and distal femur, with femurs having a more dramatic change in both mutant growth plates. Thus through combined histology and TEM we could conclude, that this hypocellular region formed as consequence of the mutations. Surprisingly, the hypocellularity region was not detected in 3-week old growth plate sections, suggesting mechanisms were responsible for the recovery of the cartilage tissue structure during bone maturation. Similar hypocellular regions were previously described in mutant *Col9a1*$^{-/-}$ and *Col9a2*$^{-/-}$ mice, reinforcing the idea of the lack of collagen type IX causing the generation of these areas. However, interestingly, despite a lack of a significant growth phenotype (at least compared to *Col9a3*$^{-/-}$ or other collagen type IX null mice) also *Col9a3*$^{\Delta ex3}$ mice exhibit the hypocellular region phenomenon. This suggests that the formation of this region might not be a consequence

solely due to the absence of collagen type IX, but perhaps it is sufficient its miss-localisation or altered function to trigger such changes, even though not dramatic as when it is absent. Notably, we noted lack of hypoxic, apoptotic or necrotic gene expression pathways in our costal RNA-seq on *Col9a1*$^{-/-}$ mice. This could be explained by the possibility that ribs are too small to develop such hypocellular regions. Alternatively, considering that RNA-seq is performed on a bulk of cells, it could be possible that the RNA coming from those few remaining cells of that area is lost in the total amount of RNA. Lastly, there is the possibility that a necrotic gene expression signature is not involved in the formation of such regions. Furthermore, delayed or disrupted secondary ossification centres were noticed in *Col9a1*$^{-/-}$ most likely due to the nearby hypocellularity. On the other hand, *Col9a3*$^{\Delta ex3}$ secondary ossification centres showed an early differentiation of chondrocytes into hypertrophic state. This observation was a confirmation on how the different collagen type IX mutations described, elicit different molecular changes reflecting then in the different skeletal phenotype observed in *Col9a3*$^{\Delta ex3}$ and *Col9a3*$^{-/-}$ mice.

Based on our analysis, *Col9a3*$^{\Delta ex3}$ and *Col9a3*$^{-/-}$ mice expressed reduced chondrocyte proliferation rates at 3-weeks of age. This was perhaps to be expected given the highly disrupted growth plate organisation of *Col9a3*$^{-/-}$, but surprising for *Col9a3*$^{\Delta ex3}$ mice, whose growth plate appeared relatively normal. We might hypothesise that the reduced proliferation seen in *Col9a3*$^{-/-}$ mice could contribute to the formation of the hypocellular area, usually predominantly involving the proliferative zone of the growth plate.

For future analysis, assessing apoptosis rates along with proliferation, would provide insights on whether an increase in cell death could account for the generation of the hypocellularity regions, along with the reduced level of cell proliferation. However, previously, apoptosis seemed not to be involved in the generation of cell-free areas in a double deficient mouse model for collagen type IX and COMP (*Col9a1*$^{-/-}$*/COMP*$^{-/-}$) (Blumbach et al. 2008).

Collagen type IX represents an important structural component of ECM, deeply connected with its surrounding protein network. Direct interactions have been shown for collagen type IX through its collagenous and non-collagenous domains with the adapter protein matrilin-3 and to COMP, respectively (Budde et al. 2005, Holden et al. 2001). Notably, no significant expression changes of the genes encoding for matrilin-3 and COMP proteins were observed in the transcriptome of *Col9a3*$^{\Delta ex3}$ or *Col9a3*$^{-/-}$ mice. However, using immunohistochemistry, we assessed the presence and abundance of matrilin-3 and COMP to verify if *Col9a3*$^{\Delta ex3}$ or

Col9a3$^{-/-}$ mutations affected their deposition into the matrix. From our results, we did not detect obvious changes in matrilin-3 abundance in either of the two mutant growth plates. Its distribution though was affected in *Col9a3*$^{\Delta ex3}$ tibiae, which showed pericellular accumulation and potentially some cellular retention of matrilin-3, mainly in the proliferative zone cells. Surprisingly, in *Col9a3*$^{-/-}$ tibial epiphysis, no change in the staining for matrilin-3 was observed, but its distribution was altered although this could be simply due to the impaired growth plate organisation obvious for these animals. In addition, partial cellular retention of matrilin-3 was evident in the *Col9a3*$^{-/-}$ growth plate.

COMP appeared less abundant in *Col9a3*$^{\Delta ex3}$ tibiae, which we could speculate to be due to a probable alteration of its binding site to the mutated collagen type IX, albeit its interaction is known to occur with non-collagenous domains of collagen type IX (Holden et al. 2001). From this, the expectation would have been further reduced staining of COMP in the *Col9a3*$^{-/-}$ mice, however staining in these animals was similar, if not equal, to WT. It is worth noticing that COMP localisation was found unusually prominent in the hypertrophic zone of mice of all genotypes and we believe that this might have occurred because of some antigen-retrieval artefact during the staining protocol. Earlier studies showed that the integration of matrilin-3 and COMP into the matrix was strongly reduced into the cartilage of vertebral bodies and ribs of *Col9a1*$^{-/-}$ mice. A defect in matrilin-3 anchorage to the matrix has also been observed when collagen type IX deficient chondrocytes were cultured (Budde et al. 2005). Subsequently, Blumbach et al. showed that matrilin-3 was absent along with collagen type IX in *Col9a1*$^{-/-}$ tibial epiphysis (Blumbach et al. 2008). Furthermore, the A-domain of matrilin-3 was shown to interact with the COL3 domain of collagen type IX, since this binding was disrupted when collagen type IX contained a mutation leading to a deletion of 12 amino acids (from exon 3) in its COL3 domain (Fresquet et al. 2007).

Collagen type X distribution provided further confirmation of the morphometric analysis result of a more extended hypertrophic zone in *Col9a3*$^{\Delta ex3}$ growth plates compared to WT. However, the reason for an expanded hypertrophic zone in *Col9a3*$^{\Delta ex3}$ growth plates remained unclear. On the contrary, the reduction of collagen type X observed in *Col9a3*$^{-/-}$ hypertrophic regions, was in line with an overall highly disorganised growth plate with likely impaired matrix proteins deposition.

As previously stated, a portion of collagen type IX molecule is covalently attached to the surface of collagen type II fibrils. Moreover, previous observations revealed its role in

modulating the diameter of larger fibrils such as collagen II fibres (Blumbach et al. 2009). Therefore, we found essential the analysis of this other important collagen type IX interactor, collagen type II. However, when this was addressed in this thesis work, staining was unsuccessful. Nonetheless, investigating collagen type II will be one of the priorities in the future follow up of this project.

When we searched for enrichment of genes and gene sets able to explain the alterations or the lack of alterations in our mutant mice phenotypes, we surprisingly observed shared expression profiles between the two mouse lines. Despite showing different phenotypes at the tissue level, the statistically significant overlap pointed out by RRHO analysis of RNA-seq data, indicated relating underlying upregulated gene expression programmes for *Col9a3*$^{\Delta ex3}$ and *Col9a3*$^{-/-}$ mice. It was not a surprise to find pathways associated with collagen fibril organisation, cell adhesion and matrix organisation among the GO terms indicated by DAVID analysis for the communal enriched genes in the mutant mice. On another note, upregulation of gene such as *Fgf13* and downregulation of *Fgfr3* in *Col9a3*$^{\Delta ex3}$ as well as upregulation of *Vcan* and *Cilp* in *Col9a3*$^{-/-}$ drew our attention. These genes and relative gene sets will be the candidate for validation in follow-up experiments leading from this study.

Additionally, it is important to highlight the fact that both *Col9a3*$^{\Delta ex3}$ and *Col9a3*$^{-/-}$ transcriptomes did not show significant expression changes of genes coding for proteins belonging to the collagen type IX interactome (Brachvogel et al. 2013). Same situation was for the other collagen type IX genes.

Col9a3$^{-/-}$ mice, whose phenotype was confirmed to be more severe, showed only *Col9a3* and *Tll1* genes significantly depleted into the extracellular matrix organisation and collagen formation pathways.

Surprisingly, in *Col9a3*$^{\Delta ex3}$ the muscle contraction pathway resulted enriched, whereas *Col9a3*$^{-/-}$ transcriptome had depletion of genes involved in myogenesis. This evidence was unusual considering that our analysis was conducted on chondrocytes transcriptome. On the other hand, the fact that MED has been previously also associated with mild myopathy (Jackson et al. 2010) gives the hint for further investigation on muscle associated genes in these mutant mice to verify if and how muscles could represent a secondary target for collagen type IX mutations.

Furthermore, it was surprising to notice that gene sets such as DNA replication, regulation of apoptosis and Wnt signalling were upregulated only in *Col9a3*$^{\Delta ex3}$, albeit chondrocytes proliferation was reduced in both mutant growth plate.

The nonsense-mediated decay enhanced by the exon junction complex pathway was reduced in both mutant mice, but intriguingly we were unable to detect a *Col9a3* mRNA in *Col9a3*$^{-/-}$ mice.

From the data observed so far, we collected very little evidence of the involvement of ER stress to the skeletal and cartilage phenotype observed into both mutant mice, however its contribution cannot be ruled out from the molecular mechanisms that cause collagen type IX-MED. In addition, taking into account the complex fibrillar network of which collagen type IX is an important constituent, we believe reasonable that *Col9a3*$^{\Delta ex3}$ and *Col9a3*$^{-/-}$ mutations might have altered cartilage stability by affecting the extracellular matrix organisation. This hypothesis will be addressed by the analysis described in the next chapter.

In conclusion, RNA-seq provided important insights about the possible implications of the two collagen type IX mutations we have generated. However, when of interpreting these data, in relation to the histological observations, we should bear in mind the tissue origin of the material analysed. Distinct bone anatomical regions can express different gene expression programmes, resulting in their differential development. We therefore advice a cautious approach when comparing RNA-seq data obtained from costal cartilage, with tissue analysis performed on load-bearing cartilage of long bones.

Summary highlights:

- Collagen type IX mutations affect the skeletal phenotype by altering cartilage stability.
- Severe cartilage tissue phenotype was observed in *Col9a3*$^{-/-}$ mice but not in *Col9a3*$^{\Delta ex3}$.
- Consistent with other collagen type IX functional knockout mice, *Col9a3*$^{-/-}$ mice, and less severely *Col9a3*$^{\Delta ex3}$ mice, exhibited hypocellular regions in early stages of postnatal development, however the specific role of collagen type IX in the generation of this phenotype is not understood.
- Significant reduced chondrocytes proliferation was measured in both mutant mice.
- The cartilage defects observed seemed to be more matrix rather than cellular related, although we cannot exclude that the presence of hypocellular regions might be the cause for delay in bone growth.

Chapter 6.

ECM integrity in Col9a3$^{\Delta ex3}$ and Col9a3$^{-/-}$ mice

6.1 Introduction

The results of Chapter 5 indicated that the skeletal abnormalities detected in *Col9a3*$^{\Delta ex3}$ mice and in particular in *Col9a3*$^{-/-}$ mice might be induced by defects in the ECM stability affecting chondrocyte behaviour. The involvement of collagen type IX in the proper assembly of the fibrillar structure of ECM, and therefore in the complex interplay of its interacting factors, is well recognised. Hence, we hypothesised that the presence of a mutated collagen type IX molecule or its total absence from the ECM might have a negative influence on fibrillar structure assembly. These alterations eventually might change the mechanical properties of the tissue and the right chondrocyte-matrix interactions. In this chapter our aim was to determine whether our mutant mice exhibited an alteration of ECM stability as a result of their *Col9a3* mutations. To assess matrix stability, we applied a multi-technique approach in order to assess various aspects of its integrity. To evaluate the collagen fibrils constituting the ECM we used transmission electron microscopy (TEM). To determine differences in the interaction strength of collagen type IX binding partners, we performed sequential protein extraction from cartilage. In addition, to better elucidate the nanostructure and mechanical properties of the growth plate cartilage, atomic force microscopy (AFM) allowed for simultaneous imaging and stiffness analysis on a nanometer scale of native cartilage samples.

Amongst the clinical findings, patients diagnosed with MED resulting from collagen type IX defects, were reported to have knee joints showing osteochondritis dissecans and early-onset osteoarthritis (OA) (Bonnemann et al. 2000, Lohiniva et al. 2000, Jeong et al. 2014, Muragaki et al. 1996). Moreover, in previous studies it was reported that mice deficient of collagen type IX (*Col9a1*$^{-/-}$) develop early onset OA in their knee and temporomandibular joints (Hu et al. 2006, Fassler et al. 1994, Balasubramanian et al. 2019). These findings suggested a role for collagen type IX in the long-term maintenance of articular cartilage integrity. Therefore, we further assessed the stability of ECM by evaluating articular cartilage integrity to investigate if our mutant mice developed an OA-like phenotype. As a comprehensive approach, we induced an accelerated cartilage degradation by stressing the articular cartilage of mice by performing destabilisation of the medial meniscus (DMM) surgery in young adult mice. In addition, we assessed articular cartilage integrity in aged mice. We focused our attention on the changes at the level of the medial side of the joint, as it has been demonstrated to be the most affected area in *Col9a1*$^{-/-}$ mice (Hu et al. 2006).

6.2 Effect of *Col9a3$^{\Delta ex3}$* and *Col9a3$^{-/-}$* mutations on ECM ultrastructure.

In order to visualise if *Col9a3$^{\Delta ex3}$* and *Col9a3$^{-/-}$* mutations affected ECM fibril structure, images of ECM were obtained by TEM from knee cartilage of 1-week old animals. Within the cartilage growth plate, chondrocytes are surrounded by a thin layer of matrix, the pericellular matrix (PCM). The PCM is usually rich in proteoglycans and characterised by the presence of thinner fibrils. Chondrocytes, and their relative PCM, are then enclosed into the territorial matrix (TM), which contains a network of heterotypic fibrils made of collagen types II, IX and XI. The usual arrangement of chondrocytes into columns together with the PCM and TM form the chondron within the proliferative zone of growth plate. In-between chondrons is the interterritorial matrix (ITM) which contains thick fibrils arranged parallel to each other. When the hypertrophic zone is approached, the separation between different compartments of the ECM is progressively less-well defined, and the PCM, TM and ITM space drastically reduces when chondrocyte enlargement occurs during the transition to hypertrophy.

From TEM images of the PCM and TM, there was no evidence of a difference between WT and *Col9a3$^{\Delta ex3}$* fibrils in the proliferative zones of growth plate sections (Fig. 6.1). However, an indication of thickened collagen fibrils was noted in *Col9a3$^{-/-}$* TM (arrowheads in Fig. 6.1). Progressing towards the pre-hypertrophic and hypertrophic zones, WT and *Col9a3$^{\Delta ex3}$* PCM and TM again displayed a similar pattern of fibrils. On the other hand, in *Col9a3$^{-/-}$* cartilage micrographs, collagen fibrils appeared less dense although their orientation was comparable to WT. From an evaluation of ITM along the same regions of growth plate, a small reduction in the density of fibrils was observed in *Col9a3$^{-/-}$* mice. This difference was more obvious in the hypertrophic ITM (Fig. 6.2). WT fibrils appeared to be oriented on a different plane compared to both mutants in the ITM, which we attributed to the orientation of the cutting plane during tissue sectioning; however, we could observe that fibrils were sparser in the ECM of *Col9a3$^{\Delta ex3}$* line. More remarkable was the variation in *Col9a3$^{-/-}$* cartilage morphology in the hypertrophic zone. The distribution of fibrils was uneven compared to the equivalent area in WT, with many regions characterised by a reduced density of fibrils alternating with areas where the fibrils appeared abnormally compactly clustered (Fig. 6.2).

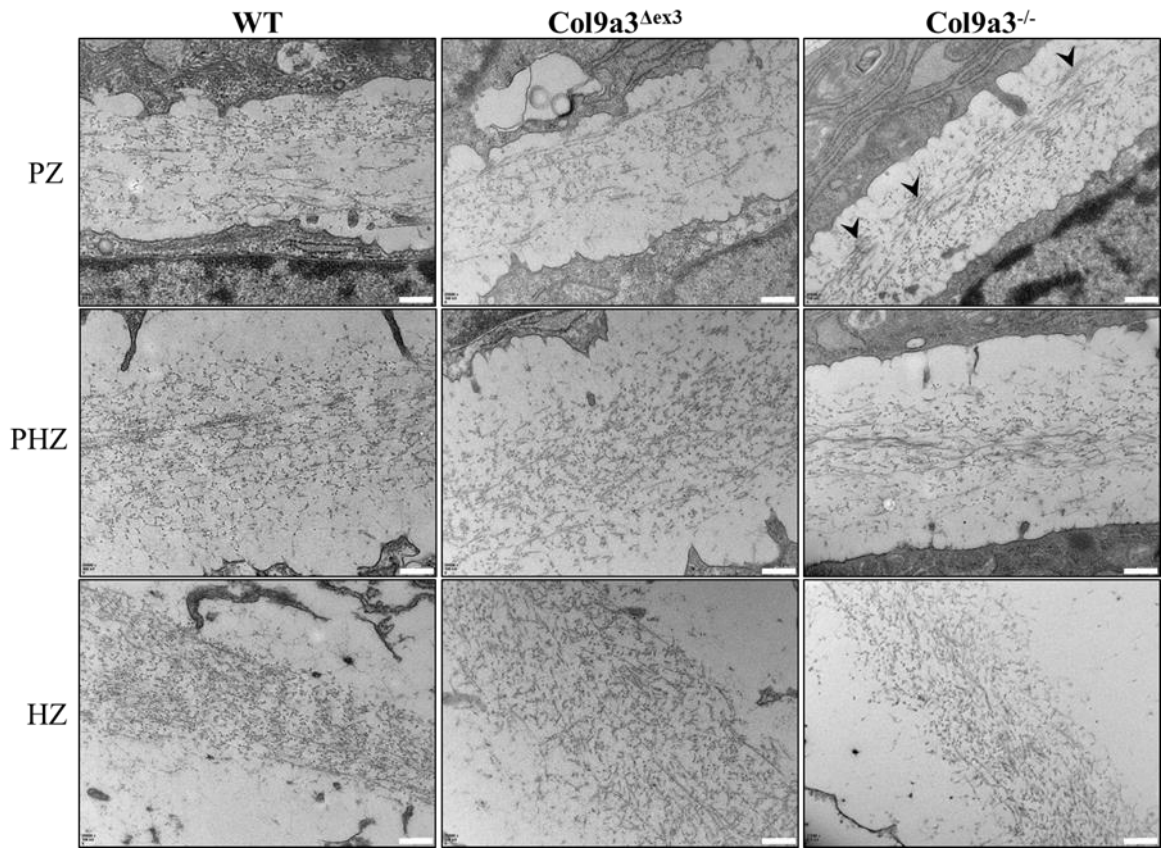

Fig. 6.1 | Electron micrographs of pericellular matrix (PCM) and territorial matrix (TM). Arrowheads indicate thicker fibrils. Scale bar = 400nm; PZ= Proliferative zone; PHZ= Pre-hypertrophic zone; HZ= Hypertrophic zone

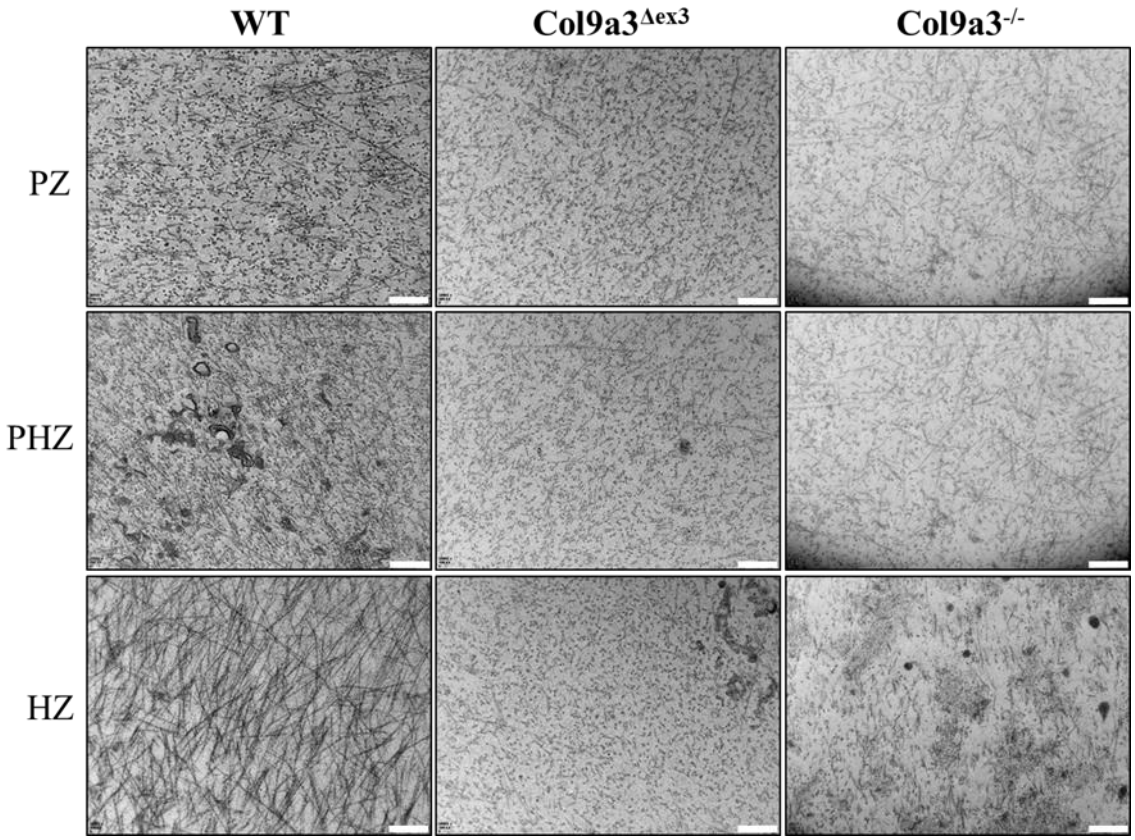

Fig. 6.2 | Electron micrographs of interterritorial extracellular matrix (ITM). Scale bar = 200nm. PZ= Proliferative zone; PHZ= Pre-hypertrophic zone; HZ= Hypertrophic zone

6.3 Effects of *Col9a3*$^{\Delta ex3}$ and *Col9a3*$^{-/-}$ mutations on cartilage protein extractability.

Another approach applied to test ECM stability in our mutant mice involved the analysis of the extractability from the ECM of collagen type IX itself and two other matrix components known to interact directly with it, matrilin-3 and COMP (Budde et al. 2005, Holden et al. 2001). In our hypothesis, the integration of mutated collagen type IX molecules, or its total absence, would affect the incorporation and binding strength of other proteins in the ECM, resulting in changes in their extractability. To test our hypothesis, we collected cartilage from femoral heads of 3-week old mutants and WT mice and from it we sequentially extracted protein using a series of three increasing denaturant properties solutions. We then analysed the cartilage extracts for the presence/absence of collagen type IX, matrilin-3 and COMP proteins by Western blotting.

The analysis of cartilage sequential extractions showed differences in the detection of collagen type IX in mice of different genotypes. Immunoblot for collagen type IX was performed using an antibody recognizing the NC4 domain of the α1 (IX) polypeptide since, as previously mentioned, no specific antibody for α3 (IX) was available. A strong band of around 150 kDa, corresponding to the collagen type IX heterotrimer, was observed in WT controls in all three extractions under reducing conditions. Only in harshest condition (buffer III) was a band corresponding to collagen type IX observed in *Col9a3*$^{\Delta ex3}$ extracts. For *Col9a3*$^{-/-}$, as expected, no band corresponding to collagen type IX was observed. A series of bands whose molecular weight was between ~50 and ~37 kDa was consistently observed especially in mutant extracts from buffer III under reducing condition, however the identity of these proteins remained unclear. The same pattern of extraction was visualised in all the mouse cartilage extracts analysed (Appendix E, Fig. E.2). Analysis of extractability of matrilin-3 revealed a higher quantity of the protein in both reduced and native extracts in buffer I when extracted from *Col9a3*$^{-/-}$ cartilage, although we could not detect a product of 50 kDa, which we considered corresponded to matrilin-3 monomers, under non-reducing conditions (Fig. 6.3 A vs. B). Buffer II non-reduced extracts from *Col9a3*$^{\Delta ex3}$ showed an increase in matrilin-3 quantity compared to WT and *Col9a3*$^{-/-}$. However, the same result was not observed in buffer II extracts of reduced proteins, where the quantity of matrilin-3 monomers extracted was comparable to WT. The extractability of matrilin-3 observed in the final buffer III was equal in WT and *Col9a3*$^{\Delta ex3}$, but decreased in *Col9a3*$^{-/-}$ native and

reduced extracts (Fig. 6.3 A-B). This pattern of extraction was consistent in buffer III extracts under reducing and non-reducing conditions in all the mice analysed (Appendix E, Fig. E.2). A similar extraction profile was noted when we analysed COMP extractability from cartilage. In the mild conditions of buffer I, no difference was noticed in the extraction of the protein from reduced and native extracts of the different genotypes. An increase of COMP extractability in both mutant extracts was noticed when buffer II extracts were resolved under reducing conditions. However, when protein extracted with buffer II was analysed in non-reducing conditions, a greater extractability of COMP was only observed for *Col9a3*$^{-/-}$ cartilage extracts (Fig.6.3B). Immunoblot of proteins extracted in the most stringent extraction buffer III, demonstrated a slightly higher COMP amount in *Col9a3*$^{\Delta ex3}$ compared to WT under both reducing and non-reducing conditions whereas, COMP level were lower in reduced and native *Col9a3*$^{-/-}$ cartilage extracts. This pattern of extractability was not consistent in other mice analysed (Appendix E, Fig. E.2), preventing the possibility of any definitive conclusion regarding COMP stability in the mutant matrix.

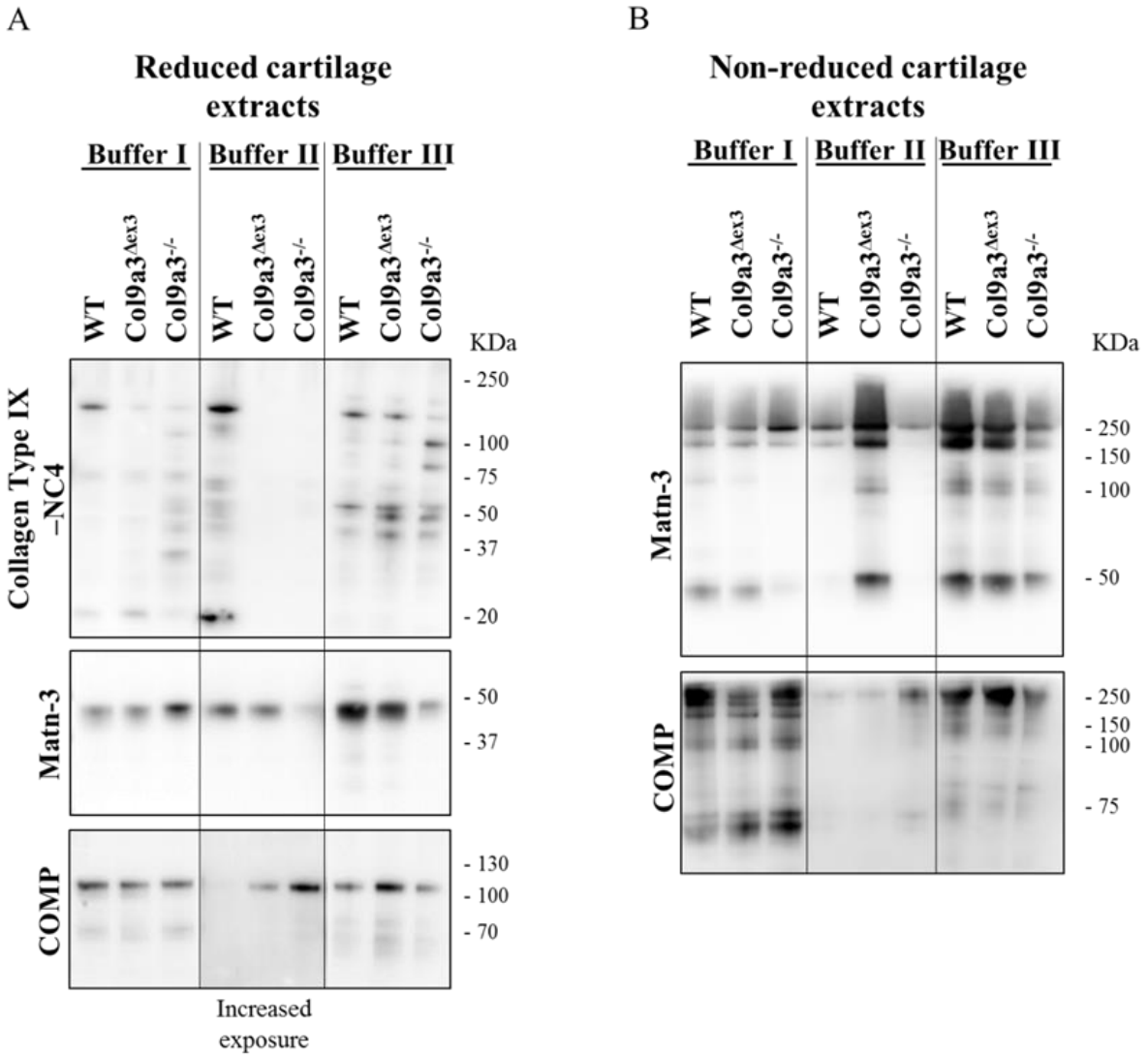

Fig. 6.3 | Genotype dependent differences in the extractability of some ECM proteins. Femoral head cartilage was sequentially extracted from 3-week old WT and mutant *Col9a3*$^{\Delta ex3}$ and *Col9a3*$^{-/-}$ mice using a series of three buffers: Buffer I, II and III. Proteins were separated by SDS-PAGE under reducing (A) and non-reducing (B) conditions and analysed by Western blotting using antibodies specific to the NC4 domain of collagen type IX α1 (Collagen Type IX-NC4), matrilin-3 (Matn-3) and COMP. Images are indicative of the differences detected in protein extraction profiles between mice of the different genotypes; Proteins molecular weight in kilo Daltons (kDa).

6.4 Analysis of *Col9a3$^{\Delta ex3}$* and *Col9a3$^{-/-}$* matrix mechanical stiffness.

Ultrastructural and biochemical properties of the altered ECM structure were assessed using AFM. Limbs from newborn and 6-week old mice of all genotypes, were collected and snap frozen in liquid nitrogen to preserve the cartilage. Samples were sent to the Centre for Applied Tissue Engineering and Regenerative Medicine in Munich, to Dr. Attila Aszodi's laboratory where researcher Bastian Hartmann kindly performed the AFM. Indentation measurements were conducted on the right tibial growth plate in the interterritorial matrix (ITM) of the proliferative zone.

ECM detailed images allowed us to visualise collagen fibrils in a 3 μm^2 area of ITM as shown in Fig. 6.4. No apparent change in fibrils appearance was seen in both mutant newborn cartilage compared to WT. However, at 6 weeks of age, *Col9a3$^{-/-}$* fibrils appeared thinner and less compact compared to fibrils of WT and *Col9a3$^{\Delta ex3}$* ITM images.

Mean values of nano-stiffness measurements from three animals per age and genotype (N=3) showed a bimodal distribution, as previously seen in studies on articular cartilage and for growth plate cartilage. The first peak in stiffness is generally assigned to proteoglycan phase (E1) and the second peak (E2) to the collagen phase (Loparic et al. 2010). In newborn WT mice, indentation measurements within the ITM gave such a bimodal stiffness distribution characterised by a first peak at 25.83 kPa and a second peak at 56.55 kPa. In *Col9a3$^{\Delta ex3}$* newborn mice peak values corresponded to 31.54 kPa and 58.70 kPa, for E1 and E2 respectively, showing nanostiffness similar to WT newborns. However, when measurements at 6 weeks of age were compared, *Col9a3$^{\Delta ex3}$* cartilage exhibited a tendency for softening compared to WT, with E1 values of 29.86 kPa vs. 65.35 kPa for the WT, and E2 values of 61.26 kPa vs. 82.24 kPa for the WT (Fig. 6.5). By comparison, *Col9a3$^{-/-}$* mice had a remarkably softer cartilage compared to both WT and *Col9a3$^{\Delta ex3}$* mice. *Col9a3$^{-/-}$* peaks were E1= 12.95 kPa and E2=28.89 kPa in newborn mice, and E1=14.10 kPa and E2=22.28 kPa at 6 weeks of age (Fig. 6.5).

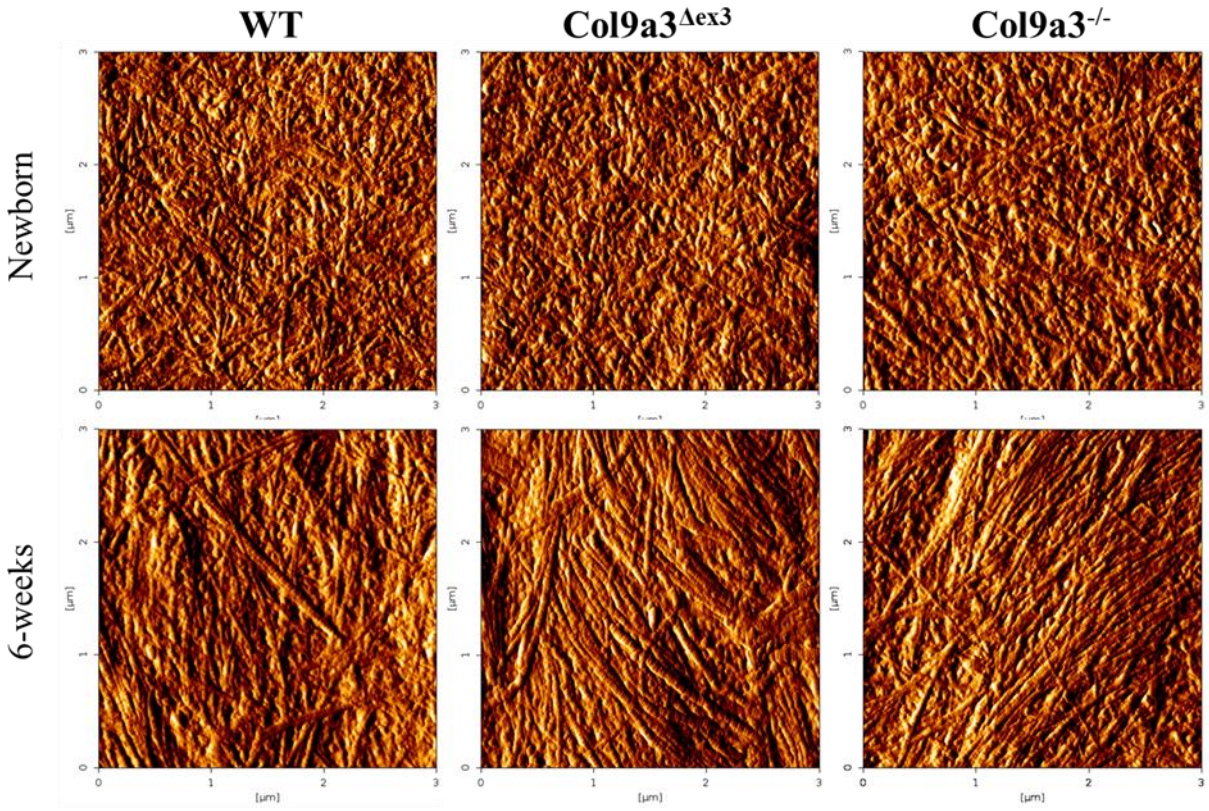

Fig. 6.4 | AFM detailed images of ECM of ITM in the proliferative zone. ITM images of a 3 µm^2 region in the growth plate of newborn and 6-week old WT, *Col9a3*$^{\Delta ex3}$ and *Col9a3*$^{-/-}$ mice. No difference is noted in mutant matrices compared to WT in newborn mice, but thinner fibrils were noted in 6-week old *Col9a3*$^{-/-}$ ECM.

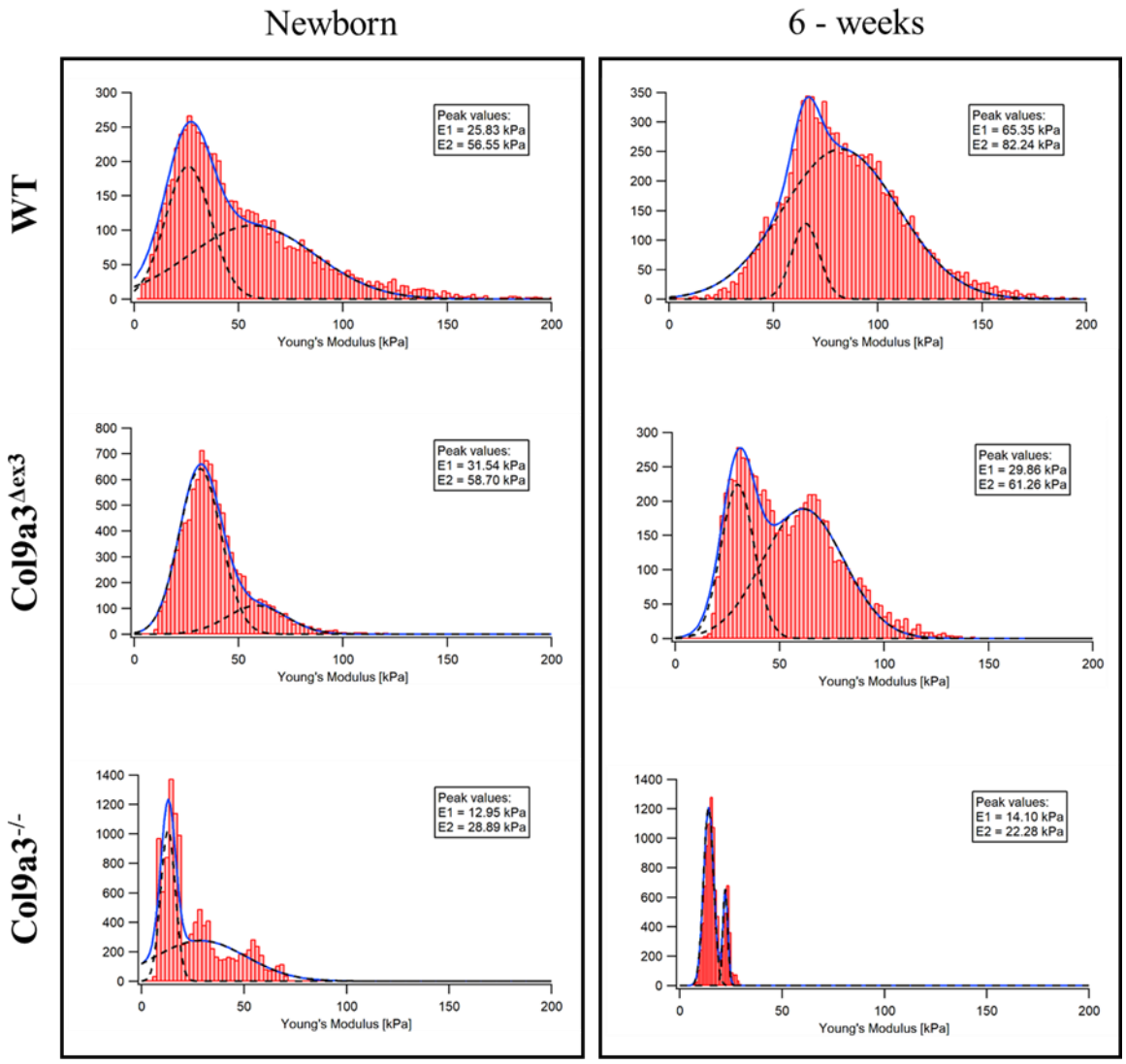

Fig. 6.5 | Distribution of ITM stiffness in the ECM of proliferative zone at different time points. Nanostiffness measurements were performed on newborn and 6-week old WT, *Col9a3*$^{\Delta ex3}$ and *Col9a3*$^{-/-}$ growth plate ITM. Histograms represent mean values of measurements (~10,000) on three slides per mouse and three animals per genotype. Solid line represents the sum of two Gaussian functions, which are represented separately by dashed lines. Calculation of standard deviation was not possible as we did not expect to find just one true value for the Young's modulus since we observed a biological system with all its variations, so the width of the Gaussian distribution did not originate from any uncertainties of the measurement. The standard error would better describe how representing the peak values are with all the values measured. But since in the distributions are so many measurement values (~10000) the standard errors would be overly small compared to the peak value.

6.5 Effect of Col9a3$^{\Delta ex3}$ and Col9a3$^{-/-}$ mutations on articular cartilage stability.

To assess the involvement of mutant collagen type IX in the development of early-onset osteoarthritis (OA), as reported in some MED patients (Jeong et al. 2014, Nakashima et al. 2005, Lohiniva et al. 2000, Holden et al. 1999), we analysed *Col9a3* $^{\Delta ex3}$ knee joints histologically. Additionally, we searched for similar OA-like changes in the knee joints of our mice deficient in collagen type IX as reported previously for *Col9a1*$^{-/-}$ mice (Hu et al. 2006). We applied a double approach for the evaluation of OA changes in the knees of our animals. Our experimental strategy comprised the assessment of OA in mice after inducing a stress in the joint by surgical destabilisation of the medial meniscus (DMM). DMM surgery and post-surgery mice checks were performed by Dr Dimitra Tsompani and Hua Lin. In addition, we assessed for possible changes in the joints of aged mice to evaluate if a potential OA-like phenotype was triggered by naturally occurring ageing. Hua Lin kindly processed the tissue samples for Safranin-O-Fast Green staining.

In the first part of our investigation, we performed DMM to induce OA in 10-week old WT (N= 5), *Col9a3*$^{\Delta ex3}$ (N= 10) and *Col9a3*$^{-/-}$ (N= 9) male animals following the procedure described in section 2.3.13. Eight weeks post-DMM, the mice were sacrificed to collect their right knee joints which had undergone surgery, these were then processed for histological examination and scoring as previously described (Glasson et al. 2010). Two experienced, independent and blinded scorers performed the scoring and data were combined to obtain average values. In this study cartilage degeneration was only scored in the medial femoral condyle (MFC), medial tibial plateau (MTP) (Fig. 6.6) and the severity of OA was indicated by the combination of the two parameters.

At 8 weeks post-surgery, scores relative to the damage of MFC cartilage showed no significant variations amongst the different genotypes (Fig. 6.7 B), whose mean values were 1.58±1.40, 1.71±1.09 and 1.18±1.25 for WT, *Col9a3*$^{\Delta ex3}$ and *Col9a3*$^{-/-}$ respectively. This indicated the presence of very mild lesions especially in WT and *Col9a3*$^{\Delta ex3}$ cartilage, but in *Col9a3*$^{-/-}$ no particular fibrillation of cartilage was apparent and only loss of proteoglycan content was noticed, indicated by partial loss of Safranin-O staining (Fig. 6.7A). Despite being the region where a more severe level of cartilage degeneration was observed, similar cartilage changes were observed in the MTP of *Col9a3*$^{\Delta ex3}$ and WT knees, whose scores were 2.95±2.04 and 2.63±2.20, indicating some loss of surface lamina and slight erosion of the

layer below the surface. In contrast, *Col9a3*$^{-/-}$ cartilage just showed a reduction in proteoglycan staining but overall good condition of the tissue hence the associated score was 1.56±1.7. When we combined MTP and MFC scores, both mutant mice did not show significant alterations in their OA phenotype compared to WT. Therefore, we concluded that *Col9a3*$^{\Delta ex3}$ and *Col9a3*$^{-/-}$ mice exhibited extremely mild OA in their joints, which did not show evidence of increased severity compared to WT. However, the experimental procedure has not been consistent across all the mice. Accidentally, nine of the mice (four *Col9a3*$^{\Delta ex3}$ mice and five *Col9a3*$^{-/-}$ mice) did not have the clips removed after DMM surgery. We believe that this might have had an impact on their movement, consequently in the development of OA in their joints. When we excluded those mice whose clip were left on to verify their effect on the overall damage score (Fig. 6.7C), we noticed indeed that values for both mutants, despite still not significant, shifted towards more severe damage scores. In particular, for *Col9a3*$^{\Delta ex3}$ MFC and MTP, score values of 2.17 ± 0.72 and 3.95± 1.05 indicated vertical cleft and some loss of surface lamina in their articular cartilage. Similar situation, but less severe in *Col9a3*$^{-/-}$ MFC and MTP whose scores were 1.64±1.14 and 2.17 ± 1.87 respectively.

Subsequently, we assessed the susceptibility to degradation of articular cartilage in both mutant mice due to ageing. Two female mice per genotype were kept until the age of 12 months and then their right leg harvested for the same histological treatment used for DMM joints (Fig. 6.8A). The damage score associated to MFC in both mutant mice was equal to 0.56 ± 0.08 and was similar for the WT MFC (0.50±0.0). Similarly, in *Col9a3*$^{\Delta ex3}$ mice the MTP showed only partial loss of proteoglycan with limited tissue fibrillation whose damage score was 0.75 ± 0.35, similar to WT (0.87 ± 0.17). *Col9a3*$^{-/-}$ MTP cartilage appeared almost normal, with only a slight reduction in the proteoglycan content with a 0.25 ± 0.35 damage score. No difference was observed in the combined effect of the MFC and MTP damage in any of the genotypes (Fig.6.8B). Although for the ageing study the small number of animals available did not allow statistical analysis, our histological observation of cartilage damage did not indicate any mutant genotype to be more prone to develop OA during ageing.

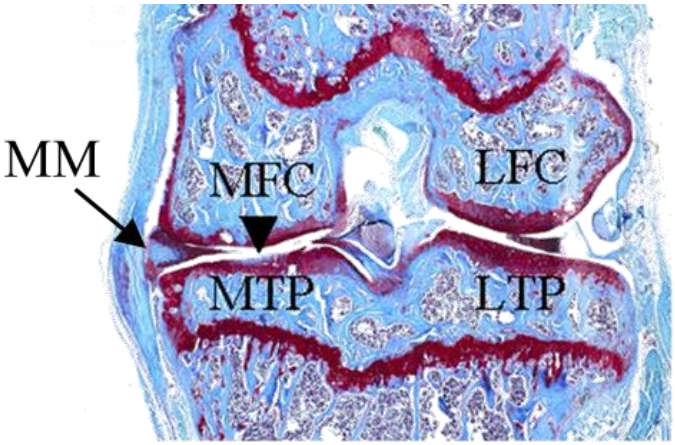

Fig. 6.6 | Mouse knee joint after DMM surgery. Safranin-O staining of posterior view of 8-week old knee joint following DMM procedure. A consistent feature of the DMM model is loss of Safranin-O, fibrillation and cartilage loss on the medial tibial plateau (arrowhead). MFC = medial femoral condyle; LFC = lateral femoral condyle; MTP = medial tibial plateau; LTP = lateral tibial plateau; MM indicates a medially displaced medial meniscus. Adapted from (Glasson et al. 2007)

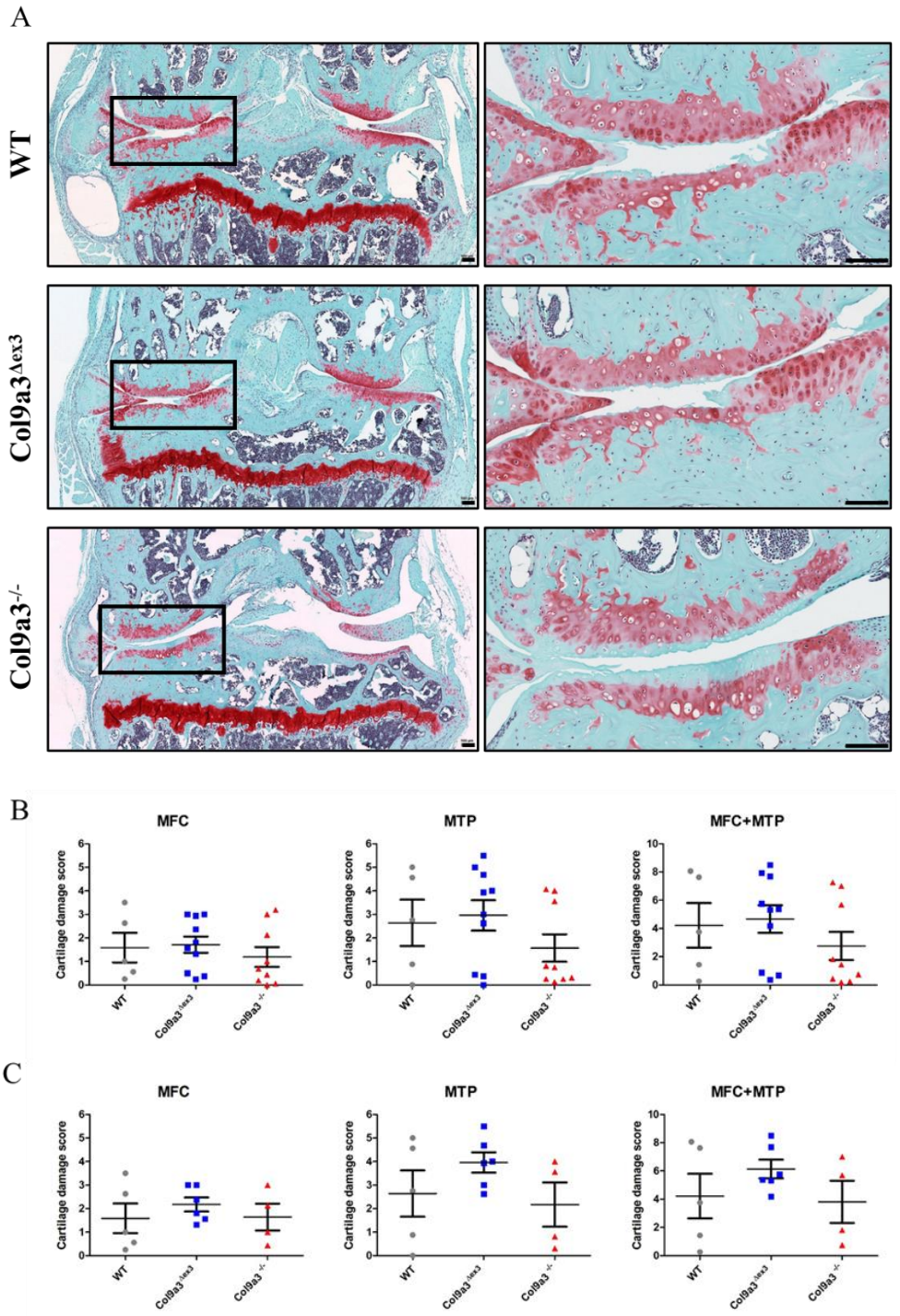

Fig. 6.7 | Accelerated DMM-induced OA in mice. 10-week-old WT (N= 5), *Col9a3*$^{\Delta ex3}$ (N=10) and *Col9a3*$^{-/-}$ (N=9) male mice were subjected to DMM surgery and legs harvested 8 weeks post-surgery and processed for histological staining. A. Representative coronal sections of the knee joint analysed by staining with Safranin O-Fast Green. Highlighted in a rectangle and magnified is the cartilage damage at the MFC and MTP Scale bars =100 µm. B. Graphs showing the results of histological scoring of OA (Glasson et al. 2010) for the three DMM operated groups. C. Graphs showing the same results as B without animals with unremoved clips. Scale bars =100 µm. Scoring was performed by two blind scorers on twenty sections from each mouse. Values are mean ± SD for the medial femoral condyle (MFC), the medial tibial plateau (MTP) and the sum of the medial femoral condyle and the tibial plateau (MFC+MTP) for each genotype group.

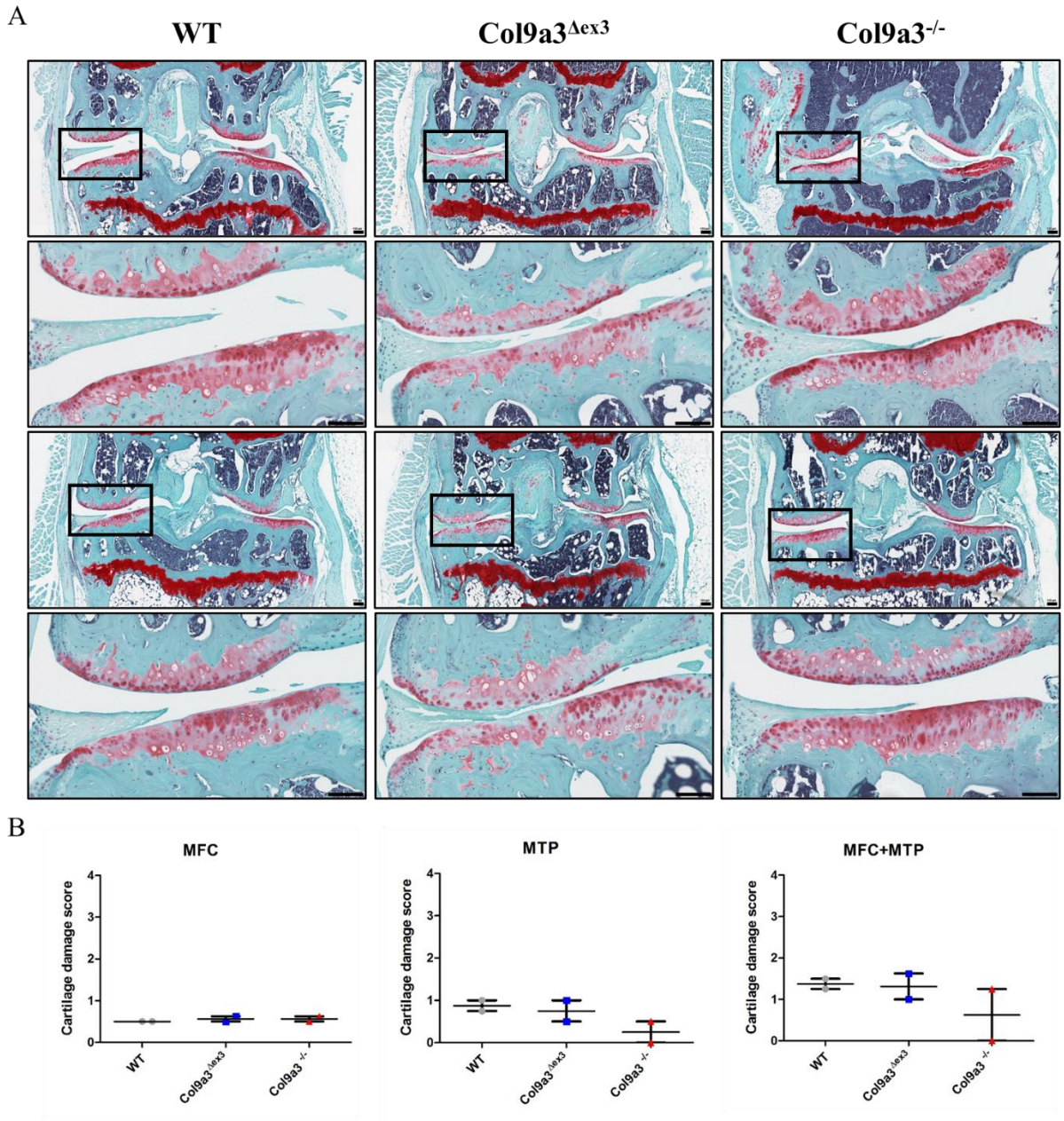

Fig. 6.8 | OA evaluation in aged mice. Legs from 12-month old WT, *Col9a3*$^{\Delta ex3}$ and *Col9a3*$^{-/-}$ female mice (N=2) were harvested and processed for histological staining. A. Representative coronal sections of the knee joint from each mouse, analysed by staining with Safranin O-Fast Green. Highlighted in a rectangle and magnified is the cartilage damage at the MFC and MTP. Scale bars =100 µm. B. Graphs showing the results of histological scoring of OA (Glasson et al. 2010) for the three aged groups. Scoring was performed by two blind scorers on twenty sections from each mouse. Values are mean ± SD for the medial femoral condyle (MFC), the medial tibial plateau (MTP) and the sum of the medial femoral condyle and the tibial plateau (MFC+MTP) for each genotype group. The low number of samples did not allow statistical analysis.

6.6 Discussion

The aim of this chapter was to verify the effect of both collagen type IX mutations on ECM stability. Collagen type IX represents an important element in the ECM thanks to its ability to bind and stabilise other structural proteins. The hypothesis to be tested was therefore the possibility of deleterious changes in the stability of the heterotypic collagen type II/XI/IX fibrils in the mutant ECM as consequence of the two different collagen type IX mutations in our mice. Limited investigation of the cartilage ultrastructure is reported for EDM3 patients due to the lack of patient cartilage biopsies. Most observations predominantly report findings about chondrocyte morphology and speculative evidence of ER enlargement, likely to be due to protein retention (Bonnemann et al. 2000, Spayde et al. 2000). More detailed studies of the ultrastructure of cartilage from collagen type IX deficient mice have indicated that collagen fibril diameter is increased compared to WT or collagen type IX/ COMP double knockout animal fibrils (Blumbach et al. 2009, Budde et al. 2005). From TEM images of our mutant mice growth plates, we could observe mild differences in their cartilage fibrils compared to WT. The alterations were more obvious in null mice, which showed both the TM and ITM with less densely arranged and sporadic unusual clustered fibrils, with an indication of increased thickness in the proliferative TM. On the contrary, *Col9a3*$^{\Delta ex3}$ fibrils were almost identical to WT, with a general less dense population of ITM fibrils.

To assess the strength of incorporation into the ECM of collagen type IX and its direct interactor proteins matrilin-3 and COMP, we evaluated how readily these proteins can be extracted from the matrix of 3-week old animals using three solutions having increasing denaturant properties. This gave an indication of the level of cross-linking of these proteins within the ECM, since it is established that by 3 weeks of age collagen types II, IX and XI are highly cross-linked in mouse cartilage (Mendler et al. 1989). The experiment aim was to find genotype-specific profiles of extraction which gives indication of integration strength, but no actual quantification of protein extracted. Western blot analysis of sequentially extracted femoral head cartilage samples revealed genotype specific differences. Surprisingly, in anti-NC4 α1(IX) immunoblots we were able to detect what we considered, according to its molecular weight, collagen type IX heterotrimer only in WT in all three extraction conditions and in *Col9a3*$^{\Delta ex3}$ extracts only in the final buffer. From the absence of protein detection in *Col9a3*$^{\Delta ex3}$ we can speculate that collagen type IX potentially harbouring a shorter α3 chain is

more tightly integrated within the ECM. Although it seems unlikely that mutated collagen type IX interaction with the surrounding environment can be stronger than WT protein, whose extracts showed collagen type IX band in all buffer conditions. Hence the reason why we did not detect any collagen type IX band in milder extraction conditions in *Col9a3*$^{\Delta ex3}$ samples remains unclear. A possible explanation would be that the collagen type IX harbouring the mutated α3(IX) is less present and very unstably located in the ECM, which might have washed off during extraction steps, and the only protein visible was the one still retained intracellularly, which we could see when cells were lysate by the harsh conditions of buffer III. As anticipated *Col9a3*$^{-/-}$ mice lacked detectable collagen type IX when extracted with any solution.

A reduction of matrilin-3 presence in buffer III *Col9a3*$^{-/-}$ cartilage extracts was consistent and could be due to loss of the protein during the earlier stages of extraction, indicating a possibly weaker integration of the protein within the mutant ECM. Conversely, the COMP extraction profile was more difficult to interpret with results less reproducible. More COMP was extractible from *Col9a3*$^{-/-}$ cartilage and on occasions from *Col9a3*$^{\Delta ex3}$ femoral cartilage. However, in other mice with the same genotype we encountered problems in reproducing a similar extraction profile. The extreme variability in the results obtained, prevented any reasonable conclusion. The findings obtained by μCT related to the bone microstructure pointed out a different status of ossification in *Col9a3*$^{\Delta ex3}$ and *Col9a3*$^{-/-}$ proximal femurs. While *Col9a3*$^{\Delta ex3}$ femoral head was characterised by a fully mature bone with no evidence of lower trabecular bone phenotype, *Col9a3*$^{-/-}$ femoral head was delayed in its ossification. This suggested a possible cause for such a variation observed in the extraction profiles in the femoral head cartilage of different mice.

AFM results showed important changes in the mechanical properties of both mutant matrices. Cartilage ECM has a well-established double composition which confers different mechanical characteristics due to the two main molecule types, proteoglycans and collagen fibrils. Proteoglycans (PG), thanks to their negatively charged glycosaminoglycan (GAG) side chains, create an osmotic balance which leads to the formation of a PG gel able to deform and dissipate the energy under loading conditions. Meanwhile, collagen fibrils, by their extensive covalent cross-linking, form a three dimensional network which confers stability and elasticity to the matrix. Thus, cartilages mechanical propensity to counteract compressive and tensile stresses is provided by the combination of these components. From this concept, it is apparent that the correct ratio between PG, collagen fibrils and water are

required to preserve matrix stability, because changes in this composite network will affect the overall tissue mechanical properties. Using AFM we were able to test these mechanical properties in order to have an indication about changes in the matrix composition. Good evidence of the reliability of our measurements was the reproduction of a bimodal distribution of the nanostiffness, already described in studies where the structural and mechanical properties of the developing murine growth plate and the porcine articular cartilage were assessed by AFM (Prein et al. 2016, Loparic et al. 2010). In these studies, it was shown that nanoscale AFM was able to measure the local matrix nanostiffness by probing the elasticity of separate components, proteoglycan and collagen fibrils. This is reflected into a bimodal Gaussian distribution on the histograms constituted by a lower peak generally indicating the stiffness given by the proteoglycan content and a higher peak as a result of collagen fibril stiffness. In our study, WT newborn samples exhibited elastic moduli ranging in the typical interval reported previously for a young but well-established matrix, with clear peaks showing dense PG and collagen fibrils. In *Col9a3*$^{\Delta ex3}$ matrix the stiffness reported in newborn mice was similar to WT, whereas *Col9a3*$^{-/-}$ mice showed a shift towards lower values, indicating a decrease in nano-stiffness. However, despite being similar to WT during early post-natal stages, *Col9a3*$^{\Delta ex3}$ mice demonstrated a tendency to softening with time in both PG and collagen phases, as shown by 6-week old samples. Likewise, *Col9a3*$^{-/-}$ mice nano-stiffness did not improve with time and their elastic moduli were remarkably shifted towards low values also at 6 weeks of age. We can therefore imply that the absence of collagen type IX severely affects the mechanical properties of the matrix. Similar findings were shown in a study conducted on intervertebral discs of collagen type IX null mice (*Col9a1*$^{-/-}$), where a less dense collagen network was identified by AFM in intervertebral endplates. Nanoindentention AFM measurement indicated a markedly softer ECM in the inner annulus and the articular region of vertebral endplate, consistent with our findings (Kamper et al. 2016). From our TEM analysis, an indication of collagen fibrils thicknening was noticed in *Col9a3*$^{-/-}$ cartilage, observation which was in contrast when *Col9a3*$^{-/-}$ fibrils were imaged from AFM detection. When the cartilage surface of *Col9a3*$^{-/-}$ ITM was visualised through AFM, collagen fibrils appeared thinner compared to WT cartilage surface images. Similar result was given by the observation of collagen fibrils diameter under polarised light after picrosirius red staining. Fibrils diameter was similar to WT in *Col9a3*$^{\Delta ex3}$ but slightly reduced in *Col9a3*$^{-/-}$ as they appeared yellow and green under polarised light (Appendix E, Fig. E.3). In the attempt to elucidate these discrepancies about fibril diameter results, it would be informative to perform a further fibrils diameter measurement on AFM

images of ITM surface. In a previous study, in 1-month old *Col9a1*$^{-/-}$ mice fibril thickening correlated with increased nanostiffness of articular cartilage, which then tended to soften by the age of 12 months (Stolz et al. 2009). Our AFM data on newborn and 6-week old *Col9a3*$^{-/-}$ mice contradicts the findings by Stolz et al. and did not correlate with our TEM observation. Differently from Stolz et al. which performed AFM on articular cartilage of *Col9a1*$^{-/-}$ femoral heads, in our study we analysed tibial growth plate cartilage. This could be accounted for the conflicting results, however further investigation on fibril diameter would contribute to unravel the origin of such discrepancies.

Among the symptoms reported from patients diagnosed with MED caused by collagen type IX mutations, the appearance of early-onset OA was the most commonly mentioned. Moreover, collagen type IX has been frequently associated with OA changes, where its expression is increased in areas of the joint where cartilage defects were present, putatively as an attempt by the diseased cartilage tissue to stabilise and protect the remaining matrix from further destruction (Koelling et al. 2008). Degradation of collagen type IX was also observed in primary stages of OA and rheumatoid arthritis (Diab 1993). In addition, both collagen type IX null mice (*Col9a1*$^{-/-}$ and *Col9a2*$^{-/-}$) were described with early-onset joint degeneration. As consequence *Col9a1*$^{-/-}$ mice present behavioural changes, such as gait changes and impairment during exercise tasks, consistent with anatomic signs of OA and intervertebral disc degeneration (Allen et al. 2009). Findings of OA-like changes in the knee and temporomandibular joints during ageing were described in collagen type IX deficient mice (*Col9a1*$^{-/-}$) (Hu et al. 2006). It was suggested that the proteoglycan depletion and loss of intact collagen II reported in the joints of these mice were caused by an increase of MMP-13 expression due to induction of the discoidin domain receptor-2 (DDR-2). The increased MMP activity generates fragments of collagen type II and fibronectin which by binding to α2β1 and α5β1 respectively, induce more proteinases activity. Also cytokines such as IL-1 further stimulate signalling pathways that induce MMP-13 expression (Li et al. 2007). We therefore decided to perform DMM surgery to induce a damage in the knee joints of our mutant mice which would accelerate the joint cartilage degeneration and progression of OA. The prevalence and clinical manifestation of OA is strongly affected by sex, with men showing higher prevalence of OA than women before the age of fifty (Srikanth et al. 2005). Similarly, also in different strains of mice which develop spontaneous OA, it has long been documented that male mice had a higher incidence of degenerative joint disease than females. Sex hormones play a critical role in the progression of OA in the murine DMM surgical

model, with males having more severe OA than females. This seems to be due to the protective effect exercised by the ovarian-derived hormone on cartilage, whereas male hormones, such as testosterone, have a detrimental effect on the severity of OA (Ma et al. 2007). Therefore, to be able to visualise a more dramatic OA phenotype we chose to perform DMM surgery on male mice. However, when we sought to determine the effect of both of our collagen type IX mutations on the articular cartilage of mice whose joints were stressed by DMM, we could not identify any difference in the damage scores when compared to WT. This observation would mean that the incorporation of a mutant collagen type IX as well as its absence does not affect the articular cartilage stability in this model. A similar observation was obtained when we assessed the tissue damage in articular cartilage of aged mutant mice. Although the very small sample size must be considered, no indication of worsening of articular cartilage was obtained from *Col9a3*$^{\Delta ex3}$ joints and more unexpectedly in *Col9a3*$^{-/-}$ joints. However, our study was greatly underpowered and despite it suggests that *Col9a3*$^{\Delta ex3}$ mice do not reproduce the OA changes observed for EDM3 patients, this cannot be a certain conclusion. Moreover, our observations were in contrast with published evidence that the lack of collagen type IX contributes to OA-like changes in different mouse joints. We focused our attention only on knee joints, maybe missing other sites where possibly the effect of the mutations on cartilage degeneration is more prominent. We also recognise the sample size used in our analysis as a limitation and the possible explanation for the result, therefore increasing the number of animals in each arm of the study is required before a firm conclusion about role of *Col9a3* in OA-like articular cartilage can be drawn.

To summarise, we have explored the effect of *Col9a3*$^{\Delta ex3}$ and *Col9a3*$^{-/-}$ mutations on cartilage stability. *Col9a3*$^{\Delta ex3}$ mutation affects the growth plate cartilage stiffness in late stages of post-natal development, but does not affect fibril appearance, the interactions with matrilin-3 and COMP, nor articular cartilage stability. The absence of collagen type IX has more severe consequences at least at the level of the growth plate cartilage, whose fibrils are less compact and dense. The binding strength of matrilin-3 resulted affected, as it showed to be more soluble in mild extraction conditions, while results obtained regarding COMP stability were inconclusive. The ageing related OA evaluation was inconclusive in both mice. Notably, ageing was evaluated only in females, but indication of sex related differences in the development of OA were noticed for example after DMM surgery, which affects predominantly males. In addition, we questioned if mice should have been kept longer than 12 months or physically challenged by exercise to be able to detect an actual change in their

articular cartilage. Hence we think that implementing our experiment, by increasing the sample size, including male mice and possibly challenging them, will be imperative to fully conclude whether the lack of this fibre plays any role in OA-like disease development in these mice.

Summary highlights

- *Col9a3*$^{\Delta ex3}$ mice presented decreased cartilage nanostiffness in late post-natal development stages, despite retaining the stability of interaction of collagen type IX with matrilin-3 and COMP.
- *Col9a3*$^{-/-}$ mice presented significant decreased cartilage nanostiffness, dispersed collagen fibrils with an indication of mild thickening and possibly weakly integrated matrilin-3 protein in the ECM.
- *Col9a3*$^{\Delta ex3}$ did not phenocopy the OA observed by EDM3 patients.
- *Col9a3*$^{-/-}$ mice did not present an osteoarthritic phenotype in knee joints, contrary to that reported for *Col9a1*$^{-/-}$ and *Col9a2*$^{-/-}$ mice.

Chapter 7.

Discussion

Discussion

Multiple epiphyseal dysplasia (MED) is an autosomal skeletal disorder which when dominant is caused by mutations in structural components of ECM such as COMP, matrilin-3 and the genes coding for the collagen type IX α-helices, *COL9A1*, *COL9A2* and *COL9A3*. Patients belonging to the group of MED cases caused by mutations in the collagen type IX genes are found with the mildest form of symptoms such as irregular epiphysis and early onset OA mainly involving the hip and knee joints. Collagen type IX belongs to the FACIT collagen subfamily and constitutes an important element inside the ECM, as its role in controlling and stabilise the packing of collagen fibrils in the matrix has been suggested, along with its interactions with other collagenous and non-collagenous components within the ECM. Intriguingly, the majority of collagen type IX genes mutations related to MED have been reported to be splice sites mutations in either acceptor or donor splice sites leading consistently to the skip of exon 3 and consequently to the deletion of 12 amino acids in the COL3 domain of the protein. The precise function of the COL3 domain is not understood, but we know that it protrudes together with the NC4 domain into the extracellular space where it reported to have a role in interacting with other ECM components. Because of its persistent association with MED, we believe that the COL3 domain represents a critical region for the pathogenicity of MED caused by collagen type IX mutations, however the pathological mechanism that links its mutations to the onset of MED is still unknown.

The aim of this project was therefore to understand the pathological role of the deletion of exon3 in relation to MED. To do so, our strategy involved the induction in a murine model of the deletion of exon 3 from the *Col9a3* gene to mimic the molecular consequence of splice sites mutations in *COL9A3* (and *COL9A2*) of MED patients, being aware of the high degree of conservation of splicing between human and mouse (Thanaraj et al. 2003). Our aim was to reproduce in the mouse the human MED phenotype to generate a valuable tool for further molecular analysis of the disease mechanism.

Firstly, we described our approach to generate the mutant mice. Using CRISPR/Cas9 gene editing we designed gRNAs targeting the intronic regions flanking the exon 3 of *Col9a3* to induce deletion. We opted for this specific genome editing tool over the more conventional ones for site specific mutagenesis, mainly for its ease of design and use and for being extremely quick and efficient. Moreover, the specificity given by the simple design of the sgRNAs was sufficient to obtain the kind of mutation we were trying to induce, being a simple and short deletion without the need of a DNA template for repair. However, as

consequence of the error prone NHEJ repair mechanism triggered in the cell after Cas9 double-strand cleavage, multiple different alleles carrying the desired deletion were generated. We therefore performed some initial characterisation of the F_0 generation. After screening of all alleles, we selected two deletion mutations to be carried on in established mouse lines. One mutation, which we called *Col9a3*$^{\Delta ex3}$, caused the generation of a shorter *Col9a3* mRNA lacking the 36 nucleotides of exon 3, proving that our strategy was successful in obtaining the desired consequence. From the *Col9a3*$^{\Delta ex3}$ mRNA a shorter α3 (IX) chain is generated, which did not affect the full collagen type IX formation or stability, as suggested by detection of α1 (IX) protein on Western blot analysis. The second mutation, which we termed *Col9a3*$^{-/-}$, impaired *Col9a3* mRNA stability, presumably due to aberrant splicing, and protein formation, resulting in a null mouse for collagen type IX. Aberrant splicing originates from different mechanistic models. It can arise from alterations in core spliceosomal components, leading to global splicing deregulation and resulting in a large number of aberrant products. Similarly, alterations in an accessory splicing factor can lead to deregulation or upregulation of splicing for the limited set of transcripts where the factor is required for accurate splicing. Alternatively, when the genomic mutations are in a critical splicing motif of a single gene, this will change the splicing pattern of just that transcript (Chen and Weiss 2015). We, therefore, consider unlikely that the phenotype we observed in *Col9a3*$^{-/-}$ mice could be caused by aberrant splicing induced stress rather than mutation in *Col9a3* related changes.

By fortuitously obtaining the *Col9a3*$^{-/-}$ mouse, we generated the first knockout mouse for *Col9a3* and importantly we demonstrated that the α3 (IX) chain is indispensable for the formation of collagen type IX heterotrimer, as previously proved for α1 (IX) and α2 (IX) in *Col9a1*$^{-/-}$ and *Col9a2*$^{-/-}$ mice, respectively (Balasubramanian et al. 2019, Fassler et al. 1994, Hagg et al. 1997). Preceding studies on *in vitro* reassociation of the single collagen type IX α-polypeptides, suggested the formation of homotrimeric or heterotrimeric molecules with different stoichiometry (Jaalinoja et al. 2008, Pihlajamaa et al. 1999). However, as mentioned in this thesis work, any sort of compensation of the other two expressed α-helices can be excluded when one of the three is absent *in vivo*. In *Col9a3*$^{-/-}$ mice, despite the mRNAs for α1 (IX) and α2 (IX) chains are normally transcribed (data not shown), we could not detect α1 (IX) polypeptide when a specific antibody was used, and presumably the same result would be given by detection of α2 (IX). The reason for this is beyond the understanding we can reach from our results and investigation. We can presume that α1 (IX)

and α2 (IX) chains might be rapidly degraded or their production might be suppressed at the translational level, when normal collagen folding is not possible in the absence of α3 (IX) chain.

The subsequent characterisation of the two mutant mice was driven by a new double purpose of our study. *Col9a3*$^{\Delta ex3}$ mice were analysed to verify if phenotype commonalities with collagen type IX-MED patients were developed, to define these mice as valuable model for MED. *Col9a3*$^{-/-}$ mouse phenotype was analysed to determine its equivalence to the other collagen type IX functional knockout mice, but also used to verify if phenotype commonalities were shared with Stickler syndrome.

We started the characterisation of the two mutant mouse lines from the analysis of their bone phenotype. *Col9a3*$^{\Delta ex3}$ mice did not show obvious skeletal abnormalities, but presented a low trabecular bone phenotype. On the contrary, *Col9a3*$^{-/-}$ mice showed hip dysplasia, short limbs with widening of tibial epiphysis reproducing the skeletal phenotype shown by other collagen type IX deficient mice, and features of Stickler syndrome patients. Our μCT analysis showed an increased bone volume in femurs and tibia of adult *Col9a3*$^{-/-}$ mice with an unexpected delayed ossification in their proximal femur. However, conflicting bone microstructure observations are reported in literature for mice deficient in collagen type IX, which suggest a variability in the bone phenotype observed probably influenced by different age, anatomical region or mouse background related variation.

In *Col9a3*$^{\Delta ex3}$ mice μCT analysis gave evidence of a reduced trabecular bone phenotype and especially the indication of a "rod-like" structure of the cancellous bone, typical of conditions characterised by bone fragility and osteoporosis (Liu et al. 2010). Low bone mass, osteoporosis and increased incidence of fractures have been observed in several myopathies (Barzegar et al. 2018, van den Berg et al. 2010), neuromuscular disorders characterised by muscle weakness due to dysfunction of muscle fiber. Interestingly, in several skeletal dysplasia phenotypes, myopathy is a recognised neuromuscular complication of the disease. In particular, cases of mild myopathy have been reported for patients diagnosed with MED caused by mutations in *COL9A2* and *COL9A3* genes (Bonnemann et al. 2000, Jackson et al. 2010). No evidence of collagen type IX expression in skeletal muscle have been reported so far (Irwin et al. 1985, Muller-Glauser et al. 1986), however its expression is found in fibrocartilaginous tissue in the enthesis, the attachment site at the tendon to bone interface. Based on this, researchers have considered the possibility of a tendinopathy condition caused

by the expression of a mutant collagen type IX, which might affect the musculoskeletal tissues. A similar myopathy condition analysed in a mouse model for MED resulting from *Comp* mutation (Pirog et al. 2010), helped to further explain this hypothesis. The enthesis site is responsible for transmitting the forces between the tendon and muscle fibers, so an altered structure of the tendon junction might disturb the mechanical forces transmitted to the muscle and therefore alter the ability of those tissues to remodel following stress. The bone is a dynamic tissue which is able to remodel in response to the mechanical load, such as an increase in loading, results in increased bone formation and decreased resorption whilst unloading of the bone has an opposite effect. Bone mineral density correlates directly with the mechanical forces applied by muscle strength, so that a reduced muscle tension on bone and consequent loss of muscular strength negatively affect the bone density. Taking into account these considerations, our finding of low trabecular and osteoporotic-like bone phenotype in *Col9a3*$^{\Delta ex3}$ mice could indicate a possible consequence of a form of muscle weakness in these mice, which would perfectly be in line with the myopathy reported for some colIX-MED patients. A follow-up study aiming at analyse the skeletal muscle and tendons will certainly add to the understanding of *Col9a3*$^{\Delta ex3}$ low trabecular bone phenotype and whether these mice represent a valid model for the study of MED related myopathy. In addition, in the current study we did not undertake any analysis of bone deposition and resorption. An investigation on common bone turn over markers in both mutant mice, is advised as it will help understand if and how the mutations affect bone development and/or homeostasis.

Subsequently, we explored the growth plate phenotype of the mice, by assessing its organisation, chondrocyte proliferation, and the presence and localisation of collagen type IX protein plus two of its binding partners, matrilin-3 and COMP. We investigated the growth plate of our mutant mice at similar time points already assessed previously in other mouse models of MED, to be able to better interpret our results in relation to the other MED models findings. *Col9a3*$^{\Delta ex3}$ growth plate was not severely affected by the mutation in terms of morphology and chondrocytes appearance, although the relative height of the zones, was different from WT and more importantly they presented a significant reduction of chondrocyte proliferation. An indication of partial collagen type IX retention within chondrocytes was noted, but probably was not sufficient to trigger an ER stress response at least according to our transcriptome analysis. Conversely, *Col9a3*$^{-/-}$ growth plates were severely affected in terms of organisation, chondrocyte morphology and proliferation,

reporting some indication of enlarged ER by TEM. Interestingly similar changes of chondrocytes, appearing misaligned and misshapen were also detected in other mouse models of PSACH-MED harbouring mutations in matrilin-3 (moderate MED: Matn3 V194D) ((Leighton et al. 2007) and COMP (mild PSACH: Comp T585M and severe PSACH: Comp DelD469) (Pirog-Garcia et al. 2007, Suleman et al. 2012) as well as in *Col9a1*$^{-/-}$ and *Col9a2*$^{-/-}$ mice (Balasubramanian et al. 2019, Fassler et al. 1994). These mouse models despite having different mutations resulting in different molecular changes responsible for the disease, presented some commonalities. All of them had short stature, misaligned and abnormal chondrocytes shape, decreased chondrocyte proliferation and some of them also had increased and spatially dysregulated apoptosis in the cartilage growth plate. In these previous studies it was hypothesised such changes in chondrocytes proliferation and apoptosis to be the cause of disrupted linear bone growth identifying these features as common disease signatures of these disorders. If this hypothesis can be applied to explain the short stature phenotype of *Col9a3*$^{-/-}$ mice, the same reasoning does not explain the absence of reduced bone growth in *Col9a3*$^{\Delta ex3}$ mice in light of the significant reduction of proliferation in their growth plate. This finding is the first evidence of reduced proliferation which does not affect bone growth, opening the question whether other mechanisms could compensate the detrimental effect of *Col9a3*$^{\Delta ex3}$ mutation on long bone growth or may signify that the reduce stature is not a direct consequence of it but of the interplay of several other factors with it. A phenotype similar to collagen type IX deficient mice was also observed in mice with a cartilage-specific deletion of β1-integrin gene. Integrins mediate cell-matrix interactions and for this reason it is considered the insufficient adhesion of β1-null chondrocytes to be the cause of the change in the cellular morphology and alignment. Collagen type IX has unique cell adhesion properties thanks to its interaction with the cartilage integrins α1β1 and α2β1 (Kapyla et al. 2004) and the importance of this interaction is also demonstrated by the changes of β1 localisation and intensity in *Col9a1*$^{-/-}$ mice (Dreier et al. 2008). We can think that even in our mice the absence of collagen type IX induces structural changes in the ECM which then have consequences on the signalling pathways based on integrins function, which affect chondrocytes morphology, division and survival.

ER stress response has been considered another disease signature of some PSACH-MED, thanks to the study of knock-in models for the disease. A knock-in mouse model for mild PSACH, carrying the T585M mutation in COMP, developed a mid UPR stress without retention of the mutant protein in the ER, while the mutation V194D in matrilin-3 caused

retention of the mutant protein in the ER with subsequent UPR response. A different mutation in COMP DelD469 causing severe PSACH was found to induce a novel cell stress response, independent from the conventional UPR (Leighton et al. 2007, Pirog-Garcia et al. 2007, Suleman et al. 2012). The indication of ER enlargement in both collagen type IX mutant mice might suggest a molecular pathology similar to these mice, where we can speculate that the folding of a proper collagen type IX heterotrimer cannot be fulfilled because of either the absence of α3(IX) or the presence of a mutated α3(IX) chain. The consequence would be longer retention of the mutated collagen type IX molecules and delay of their secretion and insertion in *Col9a3$^{\Delta ex3}$* ECM, probably explaining the pericellular localisation detected by immunostaining. Conversely, we suggest the retention and subsequent targeting for degradation of the other two (α1(IX) and α2(IX)) helices in *Col9a3$^{-/-}$* ER, to be the reason for the ER enlargement and the lack of immunostaining signal observed. However, from our preliminary transcriptomic analysis did not emerge the activation in our mutant mice of specific ER stress pathways. For example, when we looked for expression changes of specific genes belonging to the ER stress and UPR associated genes such as Grp94, Grp78/BiP, Erp72/Pdia4, Calnexin, Calreticulin, CHOP, eIF2α, eIF2αP, none of them passed the threshold for significance in their relative expression in both mutant mice. In *Col9a3$^{\Delta ex3}$* mice the genes Rgs5, Cdh5 which were associated to oxidative stress pathway in a previous study (Suleman et al. 2012), were significantly upregulated. Other genes such as *Cilp* involved in cell proliferation, and *Srxn1* and *Meox* involved in NF-κB signalling (Suleman et al. 2012), were also significantly changed in *Col9a3$^{\Delta ex3}$*. Another significantly upregulated gene in *Col9a3$^{\Delta ex3}$* was *Smad2*, coding for a protein that mediates the signal of the transforming growth factor (TGF)-beta, and thus regulates multiple cellular processes, such as cell proliferation, apoptosis, and differentiation (Eppert et al. 1996). Upregulated genes in *Col9a3$^{-/-}$* included *Cilp, Kera, Srxn1, Sox11, Agtr2*, involved in cell survival and proliferation (Suleman et al. 2012). These observations pointed out that a more in-depth analysis of specific genes pertaining specific stress pathways, other than the classical UPR is needed to create a more comprehensive understanding of the consequences at the molecular level of these two mutations in collagen type IX.

On another note, from RNAseq data we could notice the upregulation of the genes *Lox (Lysyl oxidase), Loxl1(Lysyl oxidase-like 1) and Loxl2 (Lysyl oxidase-like 1)* in both mutant mice (data not shown). These are members of the lysyl oxidase family of genes which encode enzymes oxidizing the side chain of peptidyl lysine permitting the covalent crosslinking of

collagen and elastin chains. This finding reminded of the involvement of *LOXL3* mutations in the onset of Stickler syndrome (Chan et al. 2019). Moreover, biallelic mutations in *COL9A1*, *COL9A2*, and *COL9A3* cause autosomal recessive Stickler syndrome. In this respect, previously described collagen type IX null mice were found with reduced auditory function, reproducing the hearing defects reported by patients affected by Stickler syndrome (Balasubramanian et al. 2019)(Asamura et al. 2005, Suzuki et al. 2005), which in addition to the other skeletal defects described, they represent good models of the disease. Notably the assessment of hearing impairment in our mutant mice was not addressed, but these findings suggest that it would be interesting to investigate the effect of *Col9a3*$^{\Delta ex3}$ and *Col9a3*$^{-/-}$ mutations also in the inner ear.

As mentioned, no collagen type IX was present in *Col9a3*$^{-/-}$ growth plate, as expected, but surprisingly, matrilin-3 and COMP did not appear to be less abundant. This is in contrast with what reported previously in *Col9a1*$^{-/-}$ mice which showed an overall loss of matrilin-3 and re-distribution of COMP in their growth plate (Blumbach et al. 2008). This observation made us question the reliability of the antibodies used, in particular for matrili-3 and in this regard, performing a positive control staining, which was not included initially, would be useful to ascertain the antibody specificity.

The most striking observation was the presence of a hypocellular region, a nearly cell-free area in the centre of young developing tibial and femurs growth plate, in both mutant mice, but less severe in *Col9a3*$^{\Delta ex3}$. The hypocellular region was accompanied with a widening of the epiphysis, which was consistent with the findings reported previously in *Col9a1*$^{-/-}$ and *Col9a2* $^{-/-}$ mice (Balasubramanian et al. 2019, Blumbach et al. 2008, Dreier et al. 2008). TEM also provided the first indication of this cell-free areas in both mutant mice, which we were able to confirm by histology. However, it has to be kept in mind that the observation through TEM came from analysis of only one mouse per genotype, which represents a risk of overinterpretation of results. Especially if we cannot exclude that those areas might also be a sectioning artefact or a cut through the edge of their secondary ossification centres. However, the histological findings and the absence of such area in TEM of WT growth plate make us consider the TEM observations reliable. Notably, mice carrying a targeted deletion of oxygen sensitive transcription factor HIF-1α presented acellular regions in the growth plate cartilage (Schipani et al. 2001) similar to those detected here in *Col9a3*$^{-/-}$ and those of the other collagen type IX null mice. HIF-1α transcription factor is one of the major regulators of the hypoxic response (Semenza 1999) and is required by chondrocytes during normal embryonic

development, as the central regions of the growth plate become hypoxic and as a result cells express HIF-1α which mediates their survival in such condition. The hypothesis provided previously regarding the origin of such regions was considering that cartilage is an avascular tissue, and it is supplied with nutrients and oxygen only by diffusion. Therefore, the widening of the bones of collagen type IX null mice increases the diffusion distance, possibly leading to an undersupply with nutrients and/or hypoxia within the central region, despite no increase in cellular apoptosis was detected as possible explanation for such reduced cell density (Blumbach et al. 2008). On the contrary, considering that cell-free areas were found in both *Col9a3*$^{\Delta ex3}$ and *Col9a3*$^{-/-}$ growth plates, but not widening of epiphysis was noticed in the mice carrying the exon 3 deletion, and taking into account the reduced proliferation detected in both mutant mice, we can speculate the lower cell density to be due to reduced cell division rather than a cell death induced by impaired diffusion of nutrients. Therefore we think that the analysis of cellular apoptosis in both mutant growth plates, which is lacking in this thesis work, will add to the understanding of the origin of these hypocellular areas. In addition, the localisation of other important ECM components and related collagen type IX interactors, could give new insights on the complex ECM network and how it affects important signalling pathways involved in cell viability. This could help understand if such a region is a consequence or the cause of the skeletal phenotype.

From gene expression analysis, we could not detect possible compensatory effects of collagen type IX related proteins in *Col9a3*$^{\Delta ex3}$ and *Col9a3*$^{-/-}$ mice. Nonetheless, the observation of the upregulation of *Fgf13* gene and downregulation of *Fgfr3* in *Col9a3*$^{\Delta ex3}$ suggested variations in the FGF growth factors signalling pathway, one of the major systems for cellular communication throughout development, life, and disease. More than eighteen different FGF ligands transmit extracellular signals through interaction with four receptor tyrosine kinases, FGFR1–4, which exert different physiological functions due to the differences in their temporal and spatial distribution of expression (Johnson and Williams 1993). FGFR3 is expressed in different tissues, but its major physiological function seems to be the regulation of cartilage growth. In this regard, evidence showed FGFR3 to be a physiological negative regulator of skeletal growth, which restricts the length of long bones via inhibition of chondrocyte proliferation. *Fgfr3* null mice have long bone overgrowth due to expanded zones of epiphyseal growth plate cartilage, caused by increased chondrocyte proliferation (Colvin et al. 1996). Gain of function mutations in *FGFR3*, resulting in its overactivation, are at the base of the most common genetic form of human dwarfism,

achondroplasia (Shiang et al. 1994). Moreover, the process of chondrocyte transition from proliferation to hypertrophy depends on the intricate cross-talk between the Ihh and PTHrP signalling pathways, and FGFR3 is known to mediate the downregulation of this pathway and inhibition of Ihh/PTHrP signalling due to aberrant activation of *FGFR3* contributes to disrupted chondrocyte differentiation. *Col9a3*$^{\Delta ex3}$ mice presented enlarged hypertrophic zone, but their chondrocytes proliferation was reduced, therefore we could deduce that such enlargement is probably due to a decrease of the number of chondrocytes exiting the hypertrophic zone, rather than an increase of new proliferative chondrocytes entering it. For instance, Fgf2, which is a ligand for Fgfr3, has been reported to inhibit chondrocytes terminal differentiation (Kato and Iwamoto 1990). In addition, the early differentiation status detected in *Col9a3*$^{\Delta ex3}$ secondary ossification centres, offers ground for speculation about changes in Ihh and PTHrP cross-talk, possibly due to a reduction of the inhibitory effect of FGFR3 on the Ihh/PTHrP pathway. The link between collagen type IX and Ihh/PTHrP signalling was already reported in a study showing that during the embryonic development of the spine in collagen type IX null mice (*Col9a1*$^{-/-}$) an imbalance in the Ihh-PTHrP signaling pathway leads to an accelerated hypertrophic differentiation. Researchers concluded that the changes of collagen fibril interactions and the matrix structure of collagen type IX null mice are the cause of a disturbance of signal molecule diffusion or presentation, creating for example an imbalanced Ihh–PTHrP feedback loop (Kamper et al. 2017). This finding would correlate with our observation of an earlier differentiation state of chondrocytes in the secondary ossification centre found in young *Col9a3*$^{\Delta ex3}$ growth plates. Although in the study it was hypothesised that the accelerated hypertrophic differentiation may result in a higher bone mineral density in the vertebral bodies of newborn *Col9a1*$^{-/-}$ mice and, give rise to the early onset of disc degeneration previously reported in these mice (Kamper et al. 2016). This would be in contrast with the lower trabecular bone phenotype found in tibia and femur of *Col9a3*$^{\Delta ex3}$mice, despite we are considering different tissues at different stages of development.

Studies to unravel the role of *FGF13* in the development of the skeletal muscle have shown that it plays a negative regulatory role in the process of myogenic differentiation (Lu et al. 2015). The upregulation of the *Fgf13* gene then might be the indication of an alteration of the correct skeletal muscle development in *Col9a3*$^{\Delta ex3}$ mice, leading to a possibly weaker and underdeveloped muscle in these mice, recalling the above considerations about myopathy and low trabecular bone phenotype. Furthermore, RNAseq data in *Col9a3*$^{\Delta ex3}$ cartilage showed

reduced expression of other two genes coding for important receptors involved in FGF signalling, *Fgfr1* and *Fgfr2* (data not shown). In mice, targeted ablation of *Fgfr2* impairs postnatal long bone growth, suggesting that *Fgfr2* acts as a positive regulator of endochondral bone formation at the growth plate (Eswarakumar et al. 2002, Yu et al. 2003). In contrast, activating mutations in *FGFR1* cause osteoglophonic dysplasia, another short-limbed skeletal dysplasia in humans, raising the possibility that FGFR1 acts as a negative regulator of skeletal growth (White et al. 2005). Recent studies have also demonstrated that mice conditionally deleted for FGFR1 in osteo-chondro-progenitor cells display an increased hypertrophic zone size, probably due to a decrease in the rate of cartilage resorption and ossification (Jacob et al. 2006). This would further contribute to the explanation of an enlarged hypertrophic zone in *Col9a3*$^{\Delta ex3}$ growth plate.

Despite these findings, the fact that RNAseq was performed on isolated rib chondrocytes, rather than on cartilage of load-bearing anatomical regions, such as the knee, could be considered a limitation of our analysis. A histological analysis to verify if the ribs cartilage follows the same tissue pathology recognised in the growth plate, was not addressed during this work. Indeed, it is very probable that our analysis did not define the expression changes of genes and pathways that are a consequence of the mutations in a site-specific manner.

When we assessed the ECM stability in our mutant mice we started from the hypothesis that the expression in *Col9a3*$^{\Delta ex3}$ mice of a collagen type IX molecule carrying a mutation in the COL3 domain, as well as the absence of the entire molecule in *Col9a3*$^{-/-}$, would affect the stability of other direct interactors of collagen type IX present in the ECM of these mutant mice. In particular we investigated changes in the extractability of matrilin-3 and COMP, along with collagen type IX, as indication of alterations to their anchoring or associations and of the overall functional properties of the tissue. However, when we verified this hypothesis analysing the sequential extraction protein profiles of our mutant mice cartilage extracts, only in *Col9a3*$^{-/-}$ mice we noticed differences in the extractability of only matrilin-3. This confirmed the impact on cartilage stability of the absence of collagen type IX protein. Our analysis did not add information on the consequences of the insertion of collagen type IX with a mutant COL3 domain on matriln-3 and COMP anchoring, which we could not detect through this analytical method. Conversely, the same method resulted efficient when was used previously for similar purposes in other mouse models of PSACH-MED. In this study, the cartilage protein extraction profile of the previously generated targeted mouse models of PSACH-MED with mutations in matrilin-3 (*Matn3* V194D) (Leighton et al. 2007) and

COMP (*Comp* T585M and *Comp* DelD469) (Pirog-Garcia et al. 2007, Suleman et al. 2012) was investigated. Their Western blot analysis of sequentially extracted knee cartilage revealed genotype-specific differences in the extraction of a number of proteins that are all known to interact with each other. Among these, they were able to demonstrate that collagen type IX was more easily extractable from Comp DelD469 and Comp T585M cartilage, suggesting that it may be less tightly integrated into the ECM of these animals, implying an effect on overall integrity of their cartilage. In the same study they detected increased extractability of matrilin-3 and COMP, with some variability of extraction in different conditions and of their molecular forms, giving insights on protein processing and detrimental molecular mechanisms which might be responsible for the disease. Demonstrating indeed that the mutation of matrilin3 or COMP can induce changes to the extractability of other cartilage proteins, confirmed a close functional relationship between matrilin-3 and COMP and FACIT collagens, in particular collagen type IX, in the chondrocyte pericellular matrix and that disruptions to this network might be a key disease trigger in cartilage degradation (Bell et al. 2013). The conclusions obtained in that study were the result of an integrated approach involving also analysis of protein from isolated chondrocytes and semi-quantitative proteomic analysis, which defines our investigation incomplete and suggests that a similar approach could help elucidate the results obtained by sequential extraction.

Consistently with the results obtained by sequential protein extraction and proteomic analysis, the visualization by electron microscopy of the cartilage from the same three mouse models has previously demonstrated changes in the morphology of the ECM (Leighton et al. 2007, Pirog-Garcia et al. 2007, Suleman et al. 2012). In particular, the collagen fibrils were more clearly visible, suggesting that lower levels of fibril surface-associated proteins were decorating individual collagen fibrils.

When we assessed the matrix stability of *Col9a3*$^{\Delta ex3}$ mice, such trait was not observed, as we did not detect any striking difference in the collagen fibrils, the protein extraction profile of matrilin-3 and COMP, or any worsening of OA-like cartilage damage due to DMM or ageing. Despite this, taking into account all the weak points of our methods, we cannot fully conclude that *Col9a3*$^{\Delta ex3}$ joints do not replicate the early onset OA trait often diagnosed in MED patients. Likewise, *Col9a3*$^{-/-}$ mice displayed less abnormalities than expected, in terms of collagen fibril appearance. We did not observe on TEM more exposed collagen fibrils, but they appeared sparser and sometimes aggregated. The indication of fibrils thickening, in line

with previously reported evidence of collagen type IX role in limiting fibrils diameter, which then tends to increase in its absence (Blumbach et al. 2009), was not supported by AFM observations, implying the risk of overinterpretation of TEM findings only based on n=1 biological replicate. An OA-like phenotype is well recognised in the joints of other functional collagen type IX knockouts, with *Col9a1*$^{-/-}$ knee joints developing OA changes already at 3 months of age, which then become severe by 12 months of age. Surprisingly, in *Col9a3*$^{-/-}$ knee joints we could not detect a similar OA phenotype in either DMM stressed 18-week old or in unchallenged aged 12-month old knee joints. However, our analysis was limited to only one tissue joint, and is probably missing changes in cartilage damage in other joints. In addition, no real conclusions about the ageing effect on development of OA could come from an underpower study, as no power analysis was performed to identify the correct number of animals needed to reach a significant result. AFM indentation test revealed reduced nanostiffness in both mutants, which was particularly pronounced in *Col9a3*$^{-/-}$. This result demonstrated that the mutation of collagen type IX and more importantly its absence, has a severe effect on the mechanical properties of the cartilage tissue, probably realised by affecting the distribution and interaction of other matrix components as well as collagen type II fibril diameter. It remains unclear why DMM, ageing or sequential protein extraction showed little effect while the mechanical stiffness of the *Col9a3*$^{-/-}$cartilage was profoundly affected by the mutation.

To conclude, we have generated and described the first mouse model for MED caused by splice sites mutations in *Col9a3* gene. These mice, despite genetically reproducing the patients' mutations molecular result, present very little phenotypic abnormalities which partially, but not completely, mimic patients' phenotype, at least based on our current analysis. Considering that collagen type IX mutations cause a very mild form of MED in humans, we questioned if using mice to replicate such disease is the appropriate approach to undertake. The phenotype expressed by collagen type IX null mice further confirmed the importance of this protein for the stability of cartilage. In addition, their phenotype resembles some features of patients null for collagen type IX who experience Stickler syndrome. This suggested that a mutant collagen type IX protein retains many of the functions of the wild-type protein within the ECM, explaining the limited phenotype observed in the *Col9a3*$^{\Delta ex3}$ mice. Both these mice represented novel tools to gain insights on collagen type IX structure and function, however we were unable to sufficiently expand our understanding of MED mechanism caused by collagen type IX mutations.

Appendix

Appendix A: Buffers

0.5 % Acid alcohol:
0.5% v/v Hydrochloric acid in 70% ethanol

Tris-Acetate-EDTA Buffer (TAE):

0.04M Tris (pH8), 5.7% (v/v) glacial acetic acid and 0.001M Methylenediaminetetraacetic acid (EDTA)

Loading Buffer:

(Tris 0.125M (pH 6.8), 10% (v/v) glycerol and 0.001% (w/v) bromophenol blue)

Tris buffered saline -Tween (TBS-T):

150mM NaCl, 10mM Tris Base pH7.4, 0.1% (v/v) Tween-20)

5X Laemmli sample buffer:

0.1M Tris-HCl, pH 6.8, 0.35M SDS, 20% (v/v) glycerol, 0.01% bromophenol blue and 10% (v/v) β-mercaptoethanol

Towbin transfer buffer:

25mM Tris Base, 192mM Glycine, 20% Methanol

Toluidine blue:

0.04% (w/v) Toluidine Blue, 0.1M sodium acetate buffer pH 3.75

5X 0.1M Borate Buffer (pH 8.5):

30.0g Boric acid, 13.5 ml 10M NaOH, dH_20 to 1liter of volume

Appendix B: PCR Programs

Table. B.1 | PCR program for generation of sgRNA mRNA.

Step	Temperature	Time	n° of cycles
Initial denaturation	98 ˚C	30 seconds	1
Denaturation	98 ˚C	7 seconds	25
Primer annealing	50-72 ˚C	15 seconds	
Elongation	72 ˚C	50 seconds	
Final elongation	72 ˚C	2 minutes	1
Hold	10 ˚C	∞	1

Table. B.2 | PCR program for mice genotyping and cDNA amplification.

Step		Temperature	Time	n° of cycles
Initial denaturation		98 ˚C	30 seconds	1
Denaturation		98 ˚C	5 seconds	35
Primer annealing	mCOL9a3 F/R	69 ˚C	5 seconds	
	mcDNA-COL9a3 F/R	61 ˚C		
Elongation		72 ˚C	10 seconds	
Final elongation		72 ˚C	5 minutes	1

Appendix C: Antibodies

Table. C.1 | List of primary antibodies.

Primary Antibody Name	Company	Code	Raised in	Dilution
Collagen type IX	Professor Frank Zaucke, University of Cologne	N/A	Guinea-pig	IHC 1:500 WB 1:1000
Matrilin-3	R&D Systems	AF3357	Goat polyclonal	IHC 1:500
Comp	GeneTex	GTX14515	Rabbit	IHC 1:100
Collagen type X	Professor Ray Boot-Handford, University of Manchester	N/A	Rabbit	IHC 1:500
Aggrecan	Professor Tim Hardingham, University of Manchester	N/A	Rabbit monoclonal	IHC 1:500
BrdU	Abcam	Ab6326	Rat monoclonal	IHC 1:100

Table. C.2 | List of secondary antibodies.

Secondary Antibody Name	Company	Code	Raised in	Dilution
Anti-guinea pig IgG H+L (AlexaFluor® 488)	Thermo Fisher Scientific	A11073	Goat	1:200
Anti-goat IgG H+L (AlexaFluor® 594)	Thermo Fisher Scientific	A11080	Rabbit	1:200
Anti-rabbit IgG H+L (AlexaFluor® 594)	Thermo Fisher Scientific	A11037	Goat	1:200
Anti-rat IgG H+L (AlexaFluor® 488)	Thermo Fisher Scientific	A21208	Donkey	1:200

Fig. C1 | Immunofluorescence secondary antibody controls (no primary antibody).

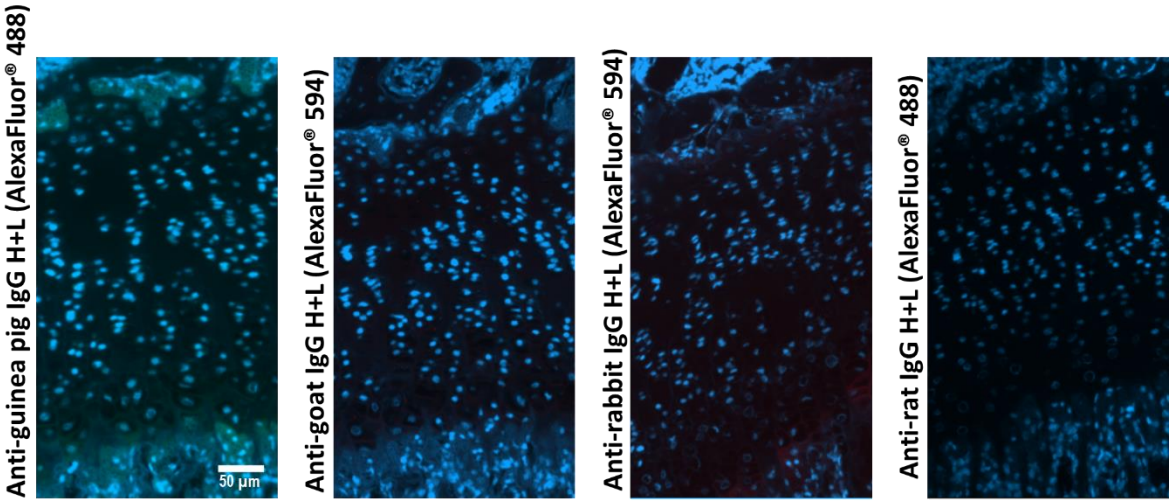

Appendix D: Tissue processing programme

Table. D.1 | Tissue processing programme.

Step	Solution	Time
1.	70 % Ethanol	6 hours
2.	90 % Ethanol	45 minutes
3.	95 % Ethanol	45 minutes
4.	100 % Ethanol	45 minutes
5.	100 % Ethanol	45 minutes
6.	100 % Ethanol	45 minutes
7.	Xylene	30 minutes
8.	Xylene	30 minutes
9.	Xylene	30 minutes
10.	Paraffin wax	1 hour
11.	Paraffin wax	1 hour

Appendix E: Supplementary material

RNA quality determination for RNA sequencing

Before proceeding with RNA sequencing and generating reliable gene expression profiles, the quality of the RNA provided by each sample was verified by analysis using an Agilent Technologies 2100 Bioanalyzer. This analysis provides an RNA integrity number (RIN) value indicative of RNA quality (and the degree of degradation). Samples with RIN > 8 were recommended for following RNA sequencing.

The electropherograms and gel images provided by the Bioanalyzer showed that all samples and controls were of good quality. One peak corresponding to the marker and other two peaks, of 18S and 28S RNA, were detected for all samples, and no other peaks (indicative of RNA degradation) were observed. All RINs assigned were then higher than 9 and all samples passed the quality control check and were subsequently processed for sequencing.

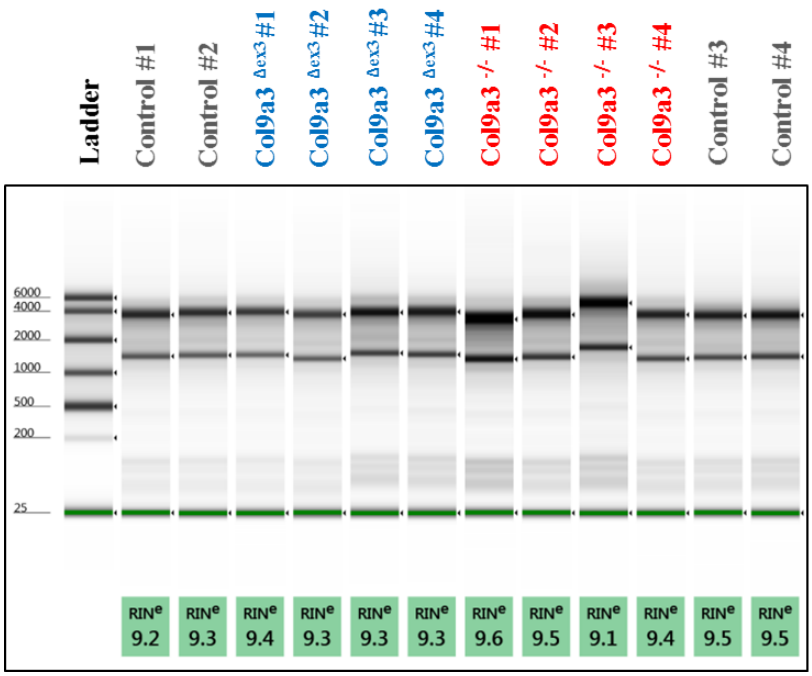

Fig. E.1 | Results of RNA integrity analysis from ribs chondrocytes.
RNA samples (n=4 per genotype) quality was checked before sequencing. Two bands denoting the 18S and 28S ribosomal subunits were detected on the Agilent 2100 Bioanalyzer gel images in all RNA samples and no other bands corresponding to degraded RNA were observed. All samples RINs were above 8 and passed quality control. All samples were therefore used for RNA sequencing.

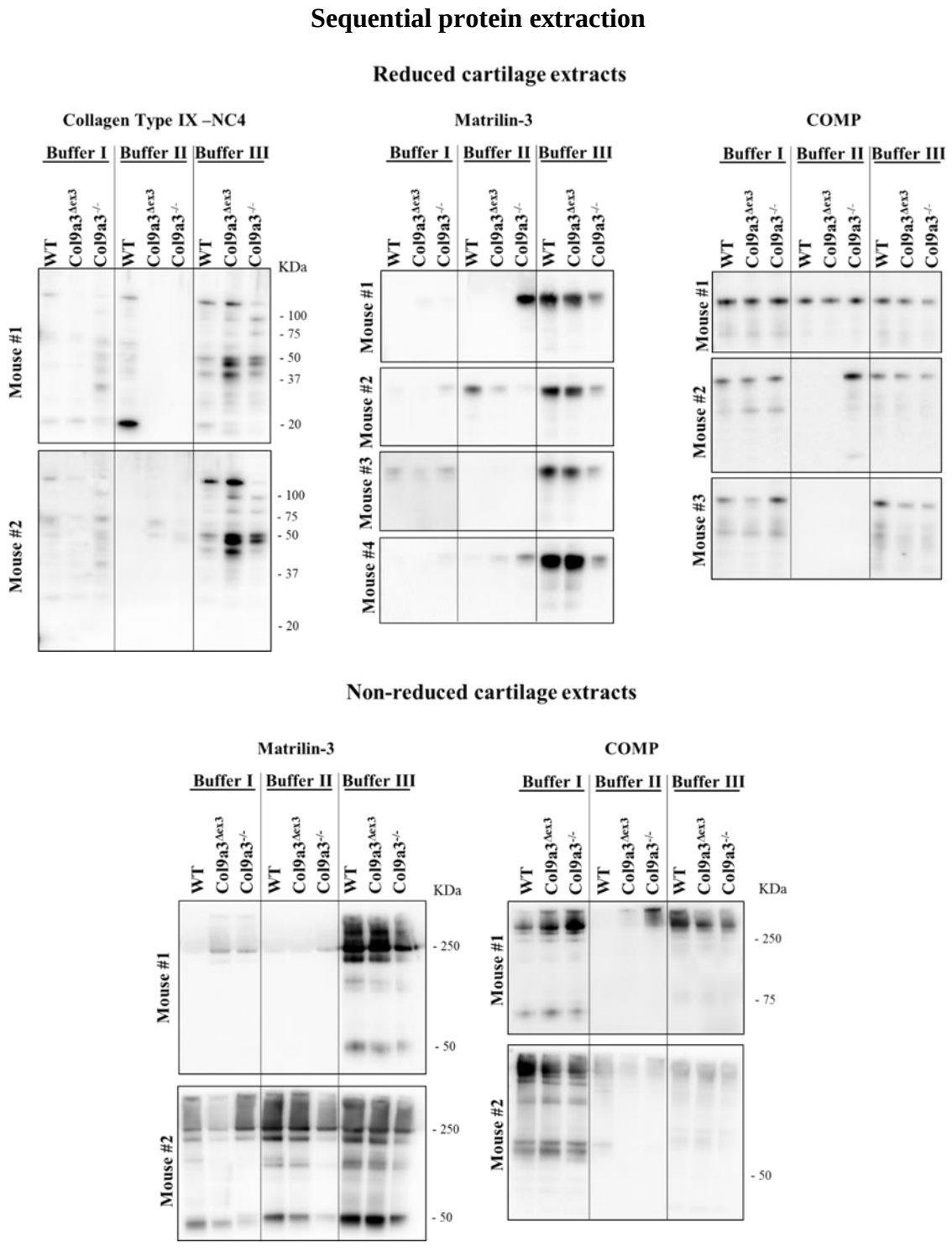

Fig. E.2 | Extractability of some ECM proteins in other mice. Femoral head cartilage was sequentially extracted from 3-week old WT and mutant *Col9a3*$^{\Delta ex3}$ and *Col9a3*$^{-/-}$ mice using a series of three buffers: Buffer I, II and III. Proteins were separated by SDS-PAGE under reducing and non-reducing conditions and analysed by Western blotting using antibodies specific to the NC4 domain of α1(IX) (Collagen Type IX-NC4), Matrilin-3 (Matn-3) and COMP denotes differences detected in protein extraction profiles between mice of different genotypes; Each blot represents one biological replicate for each genotype. Proteins molecular weight in kilo Daltons (kDa).

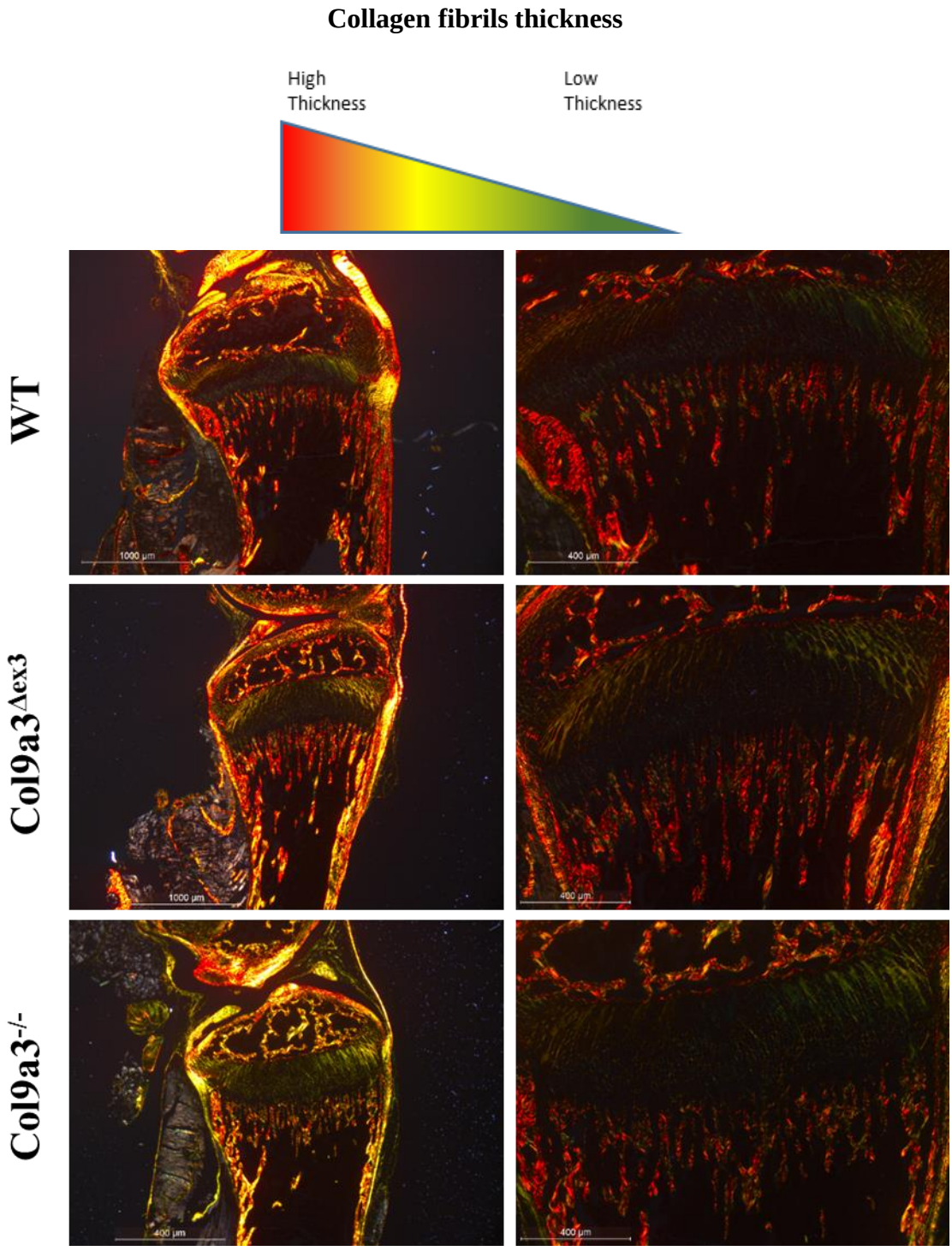

Fig. E.3 | Collagen fibrils thickness. Under polarised light collagen fibrils stained with picrosirius red appear red, orange yellow or green depending on the thickness of the fibril, decreasing in thickness from red to green. Fibrils diameter is similar to WT in *Col9a3*$^{\Delta ex3}$ but slightly reduced in *Col9a3*$^{-/-}$ after picrosirius staining on 3-week old mice tibiae.

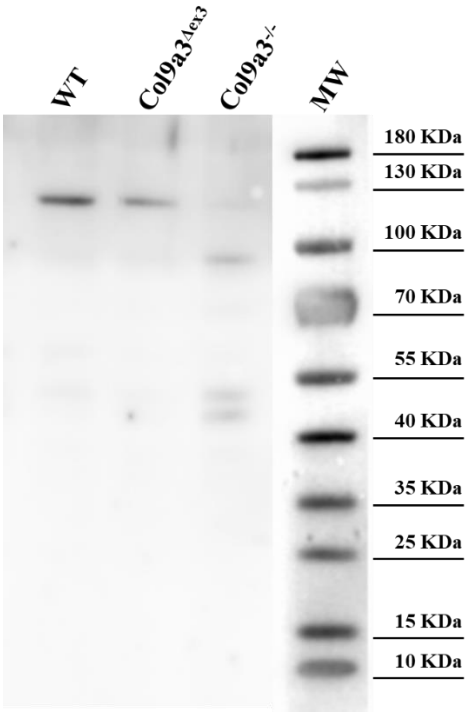

Fig. E4 | Western blot of cartilage protein probed with antibody against α1 (IX). Image showing full blot of results section 3.7 Fig. 3.9. MW= molecular weight. Blot repeated four times using four different biological replicates and no indication of lower protein amount was noticed in *Col9a3*$^{\Delta ex3}$, however no loading control was performed.

Bibliography

ABEDIN M AND KING N. 2010. Diverse evolutionary paths to cell adhesion. Trends in cell biology 20: 734-742.

ALLEN KD, GRIFFIN TM, RODRIGUIZ RM, WETSEL WC, KRAUS VB, HUEBNER JL, BOYD LM AND SETTON LA. 2009. Decreased physical function and increased pain sensitivity in mice deficient for type IX collagen. Arthritis Rheum 60: 2684-2693.

ANDERS C, NIEWOEHNER O, DUERST A AND JINEK M. 2014. Structural basis of PAM-dependent target DNA recognition by the Cas9 endonuclease. Nature 513: 569-573.

ANGEL P, IMAGAWA M, CHIU R, STEIN B, IMBRA RJ, RAHMSDORF HJ, JONAT C, HERRLICH P AND KARIN M. 1987. Phorbol ester-inducible genes contain a common cis element recognized by a TPA-modulated trans-acting factor. Cell 49: 729-739.

ANGLANI F, PICCI L, CAMPORESE C AND ZACCHELLO F. 1990. Heteroduplex formation in polymerase chain reaction. Am J Hum Genet 47: 169-170.

ANNUNEN S ET AL. 1999. An allele of COL9A2 associated with intervertebral disc disease. Science 285: 409-412.

ANSORGE HL, MENG X, ZHANG G, VEIT G, SUN M, KLEMENT JF, BEASON DP, SOSLOWSKY LJ, KOCH M AND BIRK DE. 2009a. Type XIV Collagen Regulates Fibrillogenesis: PREMATURE COLLAGEN FIBRIL GROWTH AND TISSUE DYSFUNCTION IN NULL MICE. J Biol Chem 284: 8427-8438.

ANSORGE HL, MENG XM, ZHANG GY, VEIT G, SUN M, KLEMENT JF, BEASON DP, SOSLOWSKY LJ, KOCH M AND BIRK DE. 2009b. Type XIV Collagen Regulates Fibrillogenesis PREMATURE COLLAGEN FIBRIL GROWTH AND TISSUE DYSFUNCTION IN NULL MICE. Journal of Biological Chemistry 284: 8427-8438.

ASAMURA K, ABE S, FUKUOKA H, NAKAMURA Y AND USAMI S. 2005. Mutation analysis of COL9A3, a gene highly expressed in the cochlea, in hearing loss patients. Auris Nasus Larynx 32: 113-117.

BAKER KE AND PARKER R. 2004. Nonsense-mediated mRNA decay: terminating erroneous gene expression. Curr Opin Cell Biol 16: 293-299.

BAKER S, BOOTH C, FILLMAN C, SHAPIRO M, BLAIR MP, HYLAND JC AND ALA-KOKKO L. 2011. A Loss of Function Mutation in the COL9A2 Gene Cause Autosomal Recessive Stickler Syndrome. American Journal of Medical Genetics Part A 155a: 1668-1672.

BALASUBRAMANIAN K ET AL. 2017. MED resulting from recessively inherited mutations in the gene encoding calcium-activated nucleotidase CANT1. Am J Med Genet A 173: 2415-2421.

BALASUBRAMANIAN K ET AL. 2019. The alpha2 chain of type IX collagen is essential for type IX collagen biosynthesis. Am J Med Genet A 179: 1672-1677.

BALLOCK RT AND O'KEEFE RJ. 2003. Physiology and pathophysiology of the growth plate. Birth Defects Res C Embryo Today 69: 123-143.

BARZEGAR M, NIKNAM E, HABIBI P, SHIVA S AND TAHMASEBI S. 2018. Bone Mineral Density and Bone Metabolism in Patients with Duchenne Muscular Dystrophy. Iran J Child Neurol 12: 77-83.

BELL PA, WAGENER R, ZAUCKE F, KOCH M, SELLEY J, WARWOOD S, KNIGHT D, BOOT-HANDFORD RP, THORNTON DJ AND BRIGGS MD. 2013. Analysis of

the cartilage proteome from three different mouse models of genetic skeletal diseases reveals common and discrete disease signatures. Biol Open 2: 802-811.
BELLUOCCIO D, SCHENKER T, BAICI A AND TRUEB B. 1998. Characterization of human matrilin-3 (MATN3). Genomics 53: 391-394.
BERESHEIM AC, PFEIFFER SK, GRYNPAS MD AND ALBLAS A. 2018. Sex-specific patterns in cortical and trabecular bone microstructure in the Kirsten Skeletal Collection, South Africa. Am J Hum Biol 30: e23108.
BLASCHKE UK, EIKENBERRY EF, HULMES DJ, GALLA HJ AND BRUCKNER P. 2000. Collagen XI nucleates self-assembly and limits lateral growth of cartilage fibrils. J Biol Chem 275: 10370-10378.
BLUMBACH K, BASTIAANSEN-JENNISKENS YM, DEGROOT J, PAULSSON M, VAN OSCH GJ AND ZAUCKE F. 2009. Combined role of type IX collagen and cartilage oligomeric matrix protein in cartilage matrix assembly: cartilage oligomeric matrix protein counteracts type IX collagen-induced limitation of cartilage collagen fibril growth in mouse chondrocyte cultures. Arthritis Rheum 60: 3676-3685.
BLUMBACH K, NIEHOFF A, PAULSSON M AND ZAUCKE F. 2008. Ablation of collagen IX and COMP disrupts epiphyseal cartilage architecture. Matrix Biol 27: 306-318.
BOGDANOVE AJ AND VOYTAS DF. 2011. TAL effectors: customizable proteins for DNA targeting. Science 333: 1843-1846.
BONNANS C, CHOU J AND WERB Z. 2014. Remodelling the extracellular matrix in development and disease. Nat Rev Mol Cell Biol 15: 786-801.
BONNEMANN CG, COX GF, SHAPIRO F, WU JJ, FEENER CA, THOMPSON TG, ANTHONY DC, EYRE DR, DARRAS BT AND KUNKEL LM. 2000. A mutation in the alpha 3 chain of type IX collagen causes autosomal dominant multiple epiphyseal dysplasia with mild myopathy. Proc Natl Acad Sci U S A 97: 1212-1217.
BRACHVOGEL B, ZAUCKE F, DAVE K, NORRIS EL, STERMANN J, DAYAKLI M, KOCH M, GORMAN JJ, BATEMAN JF AND WILSON R. 2013. Comparative proteomic analysis of normal and collagen IX null mouse cartilage reveals altered extracellular matrix composition and novel components of the collagen IX interactome. J Biol Chem 288: 13481-13492.
BRIGGS MD, BELL P AND PIRÓG KA 2017. Pseudoachondroplasia and Multiple Epiphyseal Dysplasia: Molecular Genetics, Disease Mechanisms and Therapeutic Targets. In*:* GRÄSSEL, S AND ASZÓDI, A (Eds.) Cartilage: Volume 2: Pathophysiology, Cham: Springer International Publishing, p. 135-153.
BRIGGS MD, BELL PA AND PIROG KA. 2015. The utility of mouse models to provide information regarding the pathomolecular mechanisms in human genetic skeletal diseases: The emerging role of endoplasmic reticulum stress (Review). Int J Mol Med 35: 1483-1492.
BRIGGS MD, BROCK J, RAMSDEN SC AND BELL PA. 2014. Genotype to phenotype correlations in cartilage oligomeric matrix protein associated chondrodysplasias. Eur J Hum Genet 22: 1278-1282.
BRIGGS MD AND CHAPMAN KL. 2002. Pseudoachondroplasia and multiple epiphyseal dysplasia: mutation review, molecular interactions, and genotype to phenotype correlations. Hum Mutat 19: 465-478.
BRIGGS MD ET AL. 1995. Pseudoachondroplasia and multiple epiphyseal dysplasia due to mutations in the cartilage oligomeric matrix protein gene. Nat Genet 10: 330-336.
BRIGGS MD, WRIGHT MJ AND MORTIER GR 1993-2019. Multiple Epiphyseal Dysplasia, Autosomal Dominant. In*:* ADAM, MP, ARDINGER, HH, PAGON, RA,

WALLACE, SE, BEAN, LJH, STEPHENS, K AND AMEMIYA, A (Eds.) GeneReviews((R)), Seattle (WA).
BROGNA S AND WEN J. 2009. Nonsense-mediated mRNA decay (NMD) mechanisms. Nat Struct Mol Biol 16: 107-113.
BUDDE B, BLUMBACH K, YLOSTALO J, ZAUCKE F, EHLEN HW, WAGENER R, ALA-KOKKO L, PAULSSON M, BRUCKNER P AND GRASSEL S. 2005. Altered integration of matrilin-3 into cartilage extracellular matrix in the absence of collagen IX. Mol Cell Biol 25: 10465-10478.
BURDAN F ET AL. 2009. Morphology and physiology of the epiphyseal growth plate. Folia Histochem Cytobiol 47: 5-16.
CAMPER L, HELLMAN U AND LUNDGREN-AKERLUND E. 1998. Isolation, cloning, and sequence analysis of the integrin subunit alpha10, a beta1-associated collagen binding integrin expressed on chondrocytes. J Biol Chem 273: 20383-20389.
CAPECCHI MR. 2005. Gene targeting in mice: functional analysis of the mammalian genome for the twenty-first century. Nat Rev Genet 6: 507-512.
CARBERY ID, JI D, HARRINGTON A, BROWN V, WEINSTEIN EJ, LIAW L AND CUI X. 2010. Targeted genome modification in mice using zinc-finger nucleases. Genetics 186: 451-459.
CARTEGNI L, CHEW SL AND KRAINER AR. 2002. Listening to silence and understanding nonsense: exonic mutations that affect splicing. Nat Rev Genet 3: 285-298.
CHAN TK, ALKAABI MK, ELBARKY AM AND EL-HATTAB AW. 2019. LOXL3 novel mutation causing a rare form of autosomal recessive Stickler syndrome. Clin Genet 95: 325-328.
CHEN FH, HERNDON ME, PATEL N, HECHT JT, TUAN RS AND LAWLER J. 2007. Interaction of cartilage oligomeric matrix protein/thrombospondin 5 with aggrecan. J Biol Chem 282: 24591-24598.
CHEN FH, THOMAS AO, HECHT JT, GOLDRING MB AND LAWLER J. 2005. Cartilage oligomeric matrix protein/thrombospondin 5 supports chondrocyte attachment through interaction with integrins. J Biol Chem 280: 32655-32661.
CHEN J AND WEISS WA. 2015. Alternative splicing in cancer: implications for biology and therapy. Oncogene 34: 1-14.
CHO SW, KIM S, KIM JM AND KIM JS. 2013. Targeted genome engineering in human cells with the Cas9 RNA-guided endonuclease. Nat Biotechnol 31: 230-232.
CHRISTIAN M, CERMAK T, DOYLE EL, SCHMIDT C, ZHANG F, HUMMEL A, BOGDANOVE AJ AND VOYTAS DF. 2010. Targeting DNA double-strand breaks with TAL effector nucleases. Genetics 186: 757-761.
CHUNG HJ AND UITTO J. 2010. Type VII collagen: the anchoring fibril protein at fault in dystrophic epidermolysis bullosa. Dermatol Clin 28: 93-105.
COLE HA, YUASA M, HAWLEY G, CATES JM, NYMAN JS AND SCHOENECKER JG. 2013. Differential development of the distal and proximal femoral epiphysis and physis in mice. Bone 52: 337-346.
COLVIN JS, BOHNE BA, HARDING GW, MCEWEN DG AND ORNITZ DM. 1996. Skeletal overgrowth and deafness in mice lacking fibroblast growth factor receptor 3. Nat Genet 12: 390-397.
CONG L ET AL. 2013. Multiplex genome engineering using CRISPR/Cas systems. Science 339: 819-823.
CONTI E AND IZAURRALDE E. 2005. Nonsense-mediated mRNA decay: molecular insights and mechanistic variations across species. Curr Opin Cell Biol 17: 316-325.

COTTERILL SL, JACKSON GC, LEIGHTON MP, WAGENER R, MAKITIE O, COLE WG AND BRIGGS MD. 2005. Multiple epiphyseal dysplasia mutations in MATN3 cause misfolding of the A-domain and prevent secretion of mutant matrilin-3. Hum Mutat 26: 557-565.

CSERJESI P, BROWN D, LIGON KL, LYONS GE, COPELAND NG, GILBERT DJ, JENKINS NA AND OLSON EN. 1995. Scleraxis: a basic helix-loop-helix protein that prefigures skeletal formation during mouse embryogenesis. Development 121: 1099-1110.

CUI X, JI D, FISHER DA, WU Y, BRINER DM AND WEINSTEIN EJ. 2011. Targeted integration in rat and mouse embryos with zinc-finger nucleases. Nat Biotechnol 29: 64-67.

CZARNY-RATAJCZAK M ET AL. 2001. A mutation in COL9A1 causes multiple epiphyseal dysplasia: further evidence for locus heterogeneity. Am J Hum Genet 69: 969-980.

DAIMON T. 1977. The presence and distribution of glycogen particles in chondrogenic cells of the tibiotarsal anlage of developing chick embryos. Calcif Tissue Res 23: 45-51.

DAVIS AJ AND CHEN DJ. 2013. DNA double strand break repair via non-homologous end-joining. Transl Cancer Res 2: 130-143.

DEAK F, WAGENER R, KISS I AND PAULSSON M. 1999. The matrilins: a novel family of oligomeric extracellular matrix proteins. Matrix Biol 18: 55-64.

DECKER RS, KOYAMA E AND PACIFICI M. 2015. Articular Cartilage: Structural and Developmental Intricacies and Questions. Curr Osteoporos Rep 13: 407-414.

DEERE M, SANFORD T, FERGUSON HL, DANIELS K AND HECHT JT. 1998. Identification of twelve mutations in cartilage oligomeric matrix protein (COMP) in patients with pseudoachondroplasia. Am J Med Genet 80: 510-513.

DESMET FO, HAMROUN D, LALANDE M, COLLOD-BEROUD G, CLAUSTRES M AND BEROUD C. 2009. Human Splicing Finder: an online bioinformatics tool to predict splicing signals. Nucleic Acids Research 37.

DI CESARE PE, CARLSON CS, STOLLERMAN ES, CHEN FS, LESLIE M AND PERRIS R. 1997. Expression of cartilage oligomeric matrix protein by human synovium. FEBS Lett 412: 249-252.

DI CESARE PE, CHEN FS, MOERGELIN M, CARLSON CS, LESLIE MP, PERRIS R AND FANG C. 2002. Matrix-matrix interaction of cartilage oligomeric matrix protein and fibronectin. Matrix Biol 21: 461-470.

DIAB M. 1993. The role of type IX collagen in osteoarthritis and rheumatoid arthritis. Orthop Rev 22: 165-170.

DOUGLAS SP, JENKINS JM AND KADLER KE. 1998. Collagen IX: evidence for a structural association between NC4 domains in cartilage and a novel cleavage site in the alpha 1(IX) chain. Matrix Biol 16: 497-505.

DREIER R, OPOLKA A, GRIFKA J, BRUCKNER P AND GRASSEL S. 2008. Collagen IX-deficiency seriously compromises growth cartilage development in mice. Matrix Biol 27: 319-329.

EGGLI PS, HERRMANN W, HUNZIKER EB AND SCHENK RK. 1985. Matrix compartments in the growth plate of the proximal tibia of rats. Anat Rec 211: 246-257.

EIKENBERRY E. F. MM, BÜRGIN R., WINTERHALTER K. H., BRUCKNER P. 1992. Articular Cartilage and Osteoarthritis. New York.

ENGEL J AND PROCKOP DJ. 1991. The zipper-like folding of collagen triple helices and the effects of mutations that disrupt the zipper. Annu Rev Biophys Biophys Chem 20: 137-152.

EPPERT K ET AL. 1996. MADR2 maps to 18q21 and encodes a TGFbeta-regulated MAD-related protein that is functionally mutated in colorectal carcinoma. Cell 86: 543-552.
ERKELENZ S, MUELLER WF, EVANS MS, BUSCH A, SCHONEWEIS K, HERTEL KJ AND SCHAAL H. 2013. Position-dependent splicing activation and repression by SR and hnRNP proteins rely on common mechanisms. RNA 19: 96-102.
ESWARAKUMAR VP, MONSONEGO-ORNAN E, PINES M, ANTONOPOULOU I, MORRISS-KAY GM AND LONAI P. 2002. The IIIc alternative of Fgfr2 is a positive regulator of bone formation. Development 129: 3783-3793.
EWELS P, MAGNUSSON M, LUNDIN S AND KALLER M. 2016. MultiQC: summarize analysis results for multiple tools and samples in a single report. Bioinformatics 32: 3047-3048.
EYRE D. 2002. Collagen of articular cartilage. Arthritis Res 4: 30-35.
EYRE DR. 1991. The collagens of articular cartilage. Semin Arthritis Rheum 21: 2-11.
EYRE DR, PIETKA T, WEIS MA AND WU JJ. 2004. Covalent cross-linking of the NC1 domain of collagen type IX to collagen type II in cartilage. J Biol Chem 279: 2568-2574.
FAIRBANK T. 1947. Dysplasia epiphysialis multiplex. Br J Surg 34: 225-232.
FALETRA F, D'ADAMO AP, BRUNO I, ATHANASAKIS E, BISKUP S, ESPOSITO L AND GASPARINI P. 2014. Autosomal recessive Stickler syndrome due to a loss of function mutation in the COL9A3 gene. Am J Med Genet A 164A: 42-47.
FANG C, CARLSON CS, LESLIE MP, TULLI H, STOLERMAN E, PERRIS R, NI L AND DI CESARE PE. 2000. Molecular cloning, sequencing, and tissue and developmental expression of mouse cartilage oligomeric matrix protein (COMP). J Orthop Res 18: 593-603.
FASSLER R, SCHNEGELSBERG PN, DAUSMAN J, SHINYA T, MURAGAKI Y, MCCARTHY MT, OLSEN BR AND JAENISCH R. 1994. Mice lacking alpha 1 (IX) collagen develop noninflammatory degenerative joint disease. Proc Natl Acad Sci U S A 91: 5070-5074.
FAUSTINO NA AND COOPER TA. 2003. Pre-mRNA splicing and human disease. Genes Dev 17: 419-437.
FENG Y, EGAN B AND WANG J. 2016. Genetic Factors in Intervertebral Disc Degeneration. Genes Dis 3: 178-185.
FLECKNELL P. 2002. Replacement, reduction and refinement. ALTEX 19: 73-78.
FOLDAGER CB, TOH WS, GOMOLL AH, OLSEN BR AND SPECTOR M. 2014. Distribution of Basement Membrane Molecules, Laminin and Collagen Type IV, in Normal and Degenerated Cartilage Tissues. Cartilage 5: 123-132.
FORLINO A ET AL. 2005. A diastrophic dysplasia sulfate transporter (SLC26A2) mutant mouse: morphological and biochemical characterization of the resulting chondrodysplasia phenotype. Hum Mol Genet 14: 859-871.
FRESQUET M, JACKSON GC, LOUGHLIN J AND BRIGGS MD. 2008. Novel mutations in exon 2 of MATN3 affect residues within the alpha-helices of the A-domain and can result in the intracellular retention of mutant matrilin-3. Hum Mutat 29: 330.
FRESQUET M, JOWITT TA, YLOSTALO J, COFFEY P, MEADOWS RS, ALA-KOKKO L, THORNTON DJ AND BRIGGS MD. 2007. Structural and functional characterization of recombinant matrilin-3 A-domain and implications for human genetic bone diseases. J Biol Chem 282: 34634-34643.
FU Y, FODEN JA, KHAYTER C, MAEDER ML, REYON D, JOUNG JK AND SANDER JD. 2013. High-frequency off-target mutagenesis induced by CRISPR-Cas nucleases in human cells. Nat Biotechnol 31: 822-826.

GANNON JM, WALKER G, FISCHER M, CARPENTER R, THOMPSON RC, JR. AND OEGEMA TR, JR. 1991. Localization of type X collagen in canine growth plate and adult canine articular cartilage. J Orthop Res 9: 485-494.
GAROFALO S, METSARANTA M, ELLARD J, SMITH C, HORTON W, VUORIO E AND DE CROMBRUGGHE B. 1993. Assembly of cartilage collagen fibrils is disrupted by overexpression of normal type II collagen in transgenic mice. Proc Natl Acad Sci U S A 90: 3825-3829.
GEBAUER JM, KOBBE B, PAULSSON M AND WAGENER R. 2016. Structure, evolution and expression of collagen XXVIII: Lessons from the zebrafish. Matrix Biol 49: 106-119.
GELSE K, POSCHL E AND AIGNER T. 2003. Collagens--structure, function, and biosynthesis. Adv Drug Deliv Rev 55: 1531-1546.
GENTILI C AND CANCEDDA R. 2009. Cartilage and bone extracellular matrix. Current pharmaceutical design 15: 1334-1348.
GILBERT S 2000. Developmental Biology. 6th edition.: Sunderland (MA): Sinauer Associates.
GLASSON SS, BLANCHET TJ AND MORRIS EA. 2007. The surgical destabilization of the medial meniscus (DMM) model of osteoarthritis in the 129/SvEv mouse. Osteoarthritis Cartilage 15: 1061-1069.
GLASSON SS, CHAMBERS MG, VAN DEN BERG WB AND LITTLE CB. 2010. The OARSI histopathology initiative - recommendations for histological assessments of osteoarthritis in the mouse. Osteoarthritis Cartilage 18 Suppl 3: S17-23.
GORDON MK AND HAHN RA. 2010. Collagens. Cell Tissue Res 339: 247-257.
GREGERSEN PA AND SAVARIRAYAN R 1993-2019. Type II Collagen Disorders Overview. In*:* ADAM, MP, ARDINGER, HH, PAGON, RA, WALLACE, SE, BEAN, LJH, STEPHENS, K AND AMEMIYA, A (Eds.) GeneReviews((R)), Seattle (WA).
GUPTA RM AND MUSUNURU K. 2014. Expanding the genetic editing tool kit: ZFNs, TALENs, and CRISPR-Cas9. J Clin Invest 124: 4154-4161.
HAGG R, HEDBOM E, MOLLERS U, ASZODI A, FASSLER R AND BRUCKNER P. 1997. Absence of the alpha1(IX) chain leads to a functional knock-out of the entire collagen IX protein in mice. J Biol Chem 272: 20650-20654.
HANSON-KAHN A, LI B, COHN DH, NICKERSON DA, BAMSHAD MJ, UNIVERSITY OF WASHINGTON CENTER FOR MENDELIAN G AND HUDGINS L. 2018. Autosomal recessive Stickler syndrome resulting from a COL9A3 mutation. Am J Med Genet A 176: 2887-2891.
HECHT JT, HAYES E, HAYNES R AND COLE WG. 2005. COMP mutations, chondrocyte function and cartilage matrix. Matrix Biol 23: 525-533.
HEDBOM E, ANTONSSON P, HJERPE A, AESCHLIMANN D, PAULSSON M, ROSA-PIMENTEL E, SOMMARIN Y, WENDEL M, OLDBERG A AND HEINEGARD D. 1992. Cartilage matrix proteins. An acidic oligomeric protein (COMP) detected only in cartilage. J Biol Chem 267: 6132-6136.
HEDBOM E AND HEINEGARD D. 1993. Binding of fibromodulin and decorin to separate sites on fibrillar collagens. J Biol Chem 268: 27307-27312.
HEIKKINEN A, TU H AND PIHLAJANIEMI T. 2012. Collagen XIII: a type II transmembrane protein with relevance to musculoskeletal tissues, microvessels and inflammation. Int J Biochem Cell Biol 44: 714-717.
HJORTEN R ET AL. 2007. Type XXVII collagen at the transition of cartilage to bone during skeletogenesis. Bone 41: 535-542.

HOLDEN P, CANTY EG, MORTIER GR, ZABEL B, SPRANGER J, CARR A, GRANT ME, LOUGHLIN JA AND BRIGGS MD. 1999. Identification of novel pro-alpha2(IX) collagen gene mutations in two families with distinctive oligo-epiphyseal forms of multiple epiphyseal dysplasia. Am J Hum Genet 65: 31-38.
HOLDEN P, MEADOWS RS, CHAPMAN KL, GRANT ME, KADLER KE AND BRIGGS MD. 2001. Cartilage oligomeric matrix protein interacts with type IX collagen, and disruptions to these interactions identify a pathogenetic mechanism in a bone dysplasia family. J Biol Chem 276: 6046-6055.
HSU PD, LANDER ES AND ZHANG F. 2014. Development and applications of CRISPR-Cas9 for genome engineering. Cell 157: 1262-1278.
HSU PD ET AL. 2013. DNA targeting specificity of RNA-guided Cas9 nucleases. Nat Biotechnol 31: 827-832.
HU K ET AL. 2006. Pathogenesis of osteoarthritis-like changes in the joints of mice deficient in type IX collagen. Arthritis Rheum 54: 2891-2900.
HUBER S, WINTERHALTER KH AND VAUGHAN L. 1988. Isolation and sequence analysis of the glycosaminoglycan attachment site of type IX collagen. J Biol Chem 263: 752-756.
HUG N, LONGMAN D AND CACERES JF. 2016. Mechanism and regulation of the nonsense-mediated decay pathway. Nucleic Acids Res 44: 1483-1495.
HULMES D 2008. Collagen diversity, synthesis and assembly. Collagen: structure and mechanics, New York: Springer.
HULMES DJ. 2002. Building collagen molecules, fibrils, and suprafibrillar structures. J Struct Biol 137: 2-10.
HULMES DJ, JESIOR JC, MILLER A, BERTHET-COLOMINAS C AND WOLFF C. 1981. Electron microscopy shows periodic structure in collagen fibril cross sections. Proc Natl Acad Sci U S A 78: 3567-3571.
IRWIN MH, SILVERS SH AND MAYNE R. 1985. Monoclonal antibody against chicken type IX collagen: preparation, characterization, and recognition of the intact form of type IX collagen secreted by chondrocytes. The Journal of cell biology 101: 814-823.
ITTNER LM AND GOTZ J. 2007. Pronuclear injection for the production of transgenic mice. Nat Protoc 2: 1206-1215.
IZU Y, SUN M, ZWOLANEK D, VEIT G, WILLIAMS V, CHA B, JEPSEN KJ, KOCH M AND BIRK DE. 2011. Type XII collagen regulates osteoblast polarity and communication during bone formation. The Journal of cell biology 193: 1115-1130.
J.H. WAARSING JSD, A.G.H. EDERVEEN, H. WEINANS. 2004. Trabecular thickness increases due to bone loss in aging, OVX and tibolone-treated rats.
JAALINOJA J, YLOSTALO J, BECKETT W, HULMES DJ AND ALA-KOKKO L. 2008. Trimerization of collagen IX alpha-chains does not require the presence of the COL1 and NC1 domains. Biochem J 409: 545-554.
JACKSON GC, MARCUS-SOEKARMAN D, STOLTE-DIJKSTRA I, VERRIPS A, TAYLOR JA AND BRIGGS MD. 2010. Type IX collagen gene mutations can result in multiple epiphyseal dysplasia that is associated with osteochondritis dissecans and a mild myopathy. Am J Med Genet A 152A: 863-869.
JACOB AL, SMITH C, PARTANEN J AND ORNITZ DM. 2006. Fibroblast growth factor receptor 1 signaling in the osteo-chondrogenic cell lineage regulates sequential steps of osteoblast maturation. Dev Biol 296: 315-328.
JEONG C, LEE JY, KIM J, CHAE H, PARK HI, KIM M, KIM OH, KIM P, LEE YK AND JUNG J. 2014. Novel COL9A3 mutation in a family diagnosed with multiple epiphyseal dysplasia: a case report. BMC Musculoskelet Disord 15: 371.

JILKA RL. 2013. The relevance of mouse models for investigating age-related bone loss in humans. J Gerontol A Biol Sci Med Sci 68: 1209-1217.
JINEK M, CHYLINSKI K, FONFARA I, HAUER M, DOUDNA JA AND CHARPENTIER E. 2012. A programmable dual-RNA-guided DNA endonuclease in adaptive bacterial immunity. Science 337: 816-821.
JOHNSON DE AND WILLIAMS LT. 1993. Structural and functional diversity in the FGF receptor multigene family. Adv Cancer Res 60: 1-41.
JUDEX S, GARMAN R, SQUIRE M, DONAHUE LR AND RUBIN C. 2004. Genetically based influences on the site-specific regulation of trabecular and cortical bone morphology. J Bone Miner Res 19: 600-606.
KALES SN, LINOS A, CHATZIS C, SAI Y, HALLA M, NASIOULAS G AND CHRISTIANI DC. 2004. The role of collagen IX tryptophan polymorphisms in symptomatic intervertebral disc disease in Southern European patients. Spine (Phila Pa 1976) 29: 1266-1270.
KAMPER M, HAMANN N, PREIN C, CLAUSEN-SCHAUMANN H, FARKAS Z, ASZODI A, NIEHOFF A, PAULSSON M AND ZAUCKE F. 2016. Early changes in morphology, bone mineral density and matrix composition of vertebrae lead to disc degeneration in aged collagen IX -/- mice. Matrix Biol 49: 132-143.
KAMPER M, PAULSSON M AND ZAUCKE F. 2017. Absence of collagen IX accelerates hypertrophic differentiation in the embryonic mouse spine through a disturbance of the Ihh-PTHrP feedback loop. Cell Tissue Res 367: 359-367.
KAPYLA J ET AL. 2004. The fibril-associated collagen IX provides a novel mechanism for cell adhesion to cartilaginous matrix. J Biol Chem 279: 51677-51687.
KATO Y AND IWAMOTO M. 1990. Fibroblast growth factor is an inhibitor of chondrocyte terminal differentiation. J Biol Chem 265: 5903-5909.
KAWAGUCHI Y, KANAMORI M, ISHIHARA H, OHMORI K, MATSUI H AND KIMURA T. 2002. The association of lumbar disc disease with vitamin-D receptor gene polymorphism. J Bone Joint Surg Am 84: 2022-2028.
KAWAGUCHI Y, OSADA R, KANAMORI M, ISHIHARA H, OHMORI K, MATSUI H AND KIMURA T. 1999. Association between an aggrecan gene polymorphism and lumbar disc degeneration. Spine (Phila Pa 1976) 24: 2456-2460.
KHOSHNOODI J, CARTAILLER JP, ALVARES K, VEIS A AND HUDSON BG. 2006. Molecular recognition in the assembly of collagens: terminal noncollagenous domains are key recognition modules in the formation of triple helical protomers. J Biol Chem 281: 38117-38121.
KIM HJ AND KIRSCH T. 2008. Collagen/annexin V interactions regulate chondrocyte mineralization. J Biol Chem 283: 10310-10317.
KIMURA T, NAKATA K, TSUMAKI N, MIYAMOTO S, MATSUI Y, EBARA S AND OCHI T. 1996. Progressive degeneration of articular cartilage and intervertebral discs. An experimental study in transgenic mice bearing a type IX collagen mutation. Int Orthop 20: 177-181.
KLATT AR, NITSCHE DP, KOBBE B, MORGELIN M, PAULSSON M AND WAGENER R. 2000. Molecular structure and tissue distribution of matrilin-3, a filament-forming extracellular matrix protein expressed during skeletal development. J Biol Chem 275: 3999-4006.
KLATT AR, PAULSSON M AND WAGENER R. 2002. Expression of matrilins during maturation of mouse skeletal tissues. Matrix Biol 21: 289-296.
KO Y, KOBBE B, NICOLAE C, MIOSGE N, PAULSSON M, WAGENER R AND ASZODI A. 2004. Matrilin-3 is dispensable for mouse skeletal growth and development. Mol Cell Biol 24: 1691-1699.

KOELLING S, KRUEGEL J, KLINGER M, SCHULTZ W AND MIOSGE N. 2008. Collagen IX in weight-bearing areas of human articular cartilage in late stages of osteoarthritis. Arch Orthop Trauma Surg 128: 1453-1459.
KOMORI T. 2010. Regulation of bone development and extracellular matrix protein genes by RUNX2. Cell Tissue Res 339: 189-195.
KOOL J AND BERNS A. 2009. High-throughput insertional mutagenesis screens in mice to identify oncogenic networks. Nat Rev Cancer 9: 389-399.
KOSHER RA, KULYK WM AND GAY SW. 1986. Collagen gene expression during limb cartilage differentiation. The Journal of cell biology 102: 1151-1156.
KOZHEMYAKINA E, ZHANG M, IONESCU A, AYTURK UM, ONO N, KOBAYASHI A, KRONENBERG H, WARMAN ML AND LASSAR AB. 2015. Identification of a Prg4-expressing articular cartilage progenitor cell population in mice. Arthritis Rheumatol 67: 1261-1273.
KWAN AP, CUMMINGS CE, CHAPMAN JA AND GRANT ME. 1991. Macromolecular organization of chicken type X collagen in vitro. The Journal of cell biology 114: 597-604.
LAMPE AK, FLANIGAN KM, BUSHBY KM AND HICKS D 1993-2020. Collagen Type VI-Related Disorders. In*:* ADAM, MP, ARDINGER, HH, PAGON, RA, WALLACE, SE, BEAN, LJH, STEPHENS, K AND AMEMIYA, A (Eds.) GeneReviews((R)), Seattle (WA).
LATVANLEHTO A ET AL. 2010. Muscle-derived collagen XIII regulates maturation of the skeletal neuromuscular junction. J Neurosci 30: 12230-12241.
LEIGHTON MP ET AL. 2007. Decreased chondrocyte proliferation and dysregulated apoptosis in the cartilage growth plate are key features of a murine model of epiphyseal dysplasia caused by a matn3 mutation. Hum Mol Genet 16: 1728-1741.
LEJEUNE F, LI X AND MAQUAT LE. 2003. Nonsense-mediated mRNA decay in mammalian cells involves decapping, deadenylating, and exonucleolytic activities. Mol Cell 12: 675-687.
LEWIS BP, GREEN RE AND BRENNER SE. 2003. Evidence for the widespread coupling of alternative splicing and nonsense-mediated mRNA decay in humans. Proc Natl Acad Sci U S A 100: 189-192.
LI W, TENG F, LI T AND ZHOU Q. 2013. Simultaneous generation and germline transmission of multiple gene mutations in rat using CRISPR-Cas systems. Nat Biotechnol 31: 684-686.
LI Y, XU L AND OLSEN BR. 2007. Lessons from genetic forms of osteoarthritis for the pathogenesis of the disease. Osteoarthritis Cartilage 15: 1101-1105.
LIBERFARB RM ET AL. 2003. The Stickler syndrome: genotype/phenotype correlation in 10 families with Stickler syndrome resulting from seven mutations in the type II collagen gene locus COL2A1. Genet Med 5: 21-27.
LIEBER MR. 2008. The mechanism of human nonhomologous DNA end joining. J Biol Chem 283: 1-5.
LIU XS ET AL. 2010. Individual trabeculae segmentation (ITS)-based morphological analysis of high-resolution peripheral quantitative computed tomography images detects abnormal trabecular plate and rod microarchitecture in premenopausal women with idiopathic osteoporosis. J Bone Miner Res 25: 1496-1505.
LOHINIVA J, PAASSILTA P, SEPPANEN U, VIERIMAA O, KIVIRIKKO S AND ALA-KOKKO L. 2000. Splicing mutations in the COL3 domain of collagen IX cause multiple epiphyseal dysplasia. Am J Med Genet 90: 216-222.
LOPARIC M, WIRZ D, DANIELS AU, RAITERI R, VANLANDINGHAM MR, GUEX G, MARTIN I, AEBI U AND STOLZ M. 2010. Micro- and nanomechanical analysis of

articular cartilage by indentation-type atomic force microscopy: validation with a gel-microfiber composite. Biophys J 98: 2731-2740.
LOVE MI, HUBER W AND ANDERS S. 2014. Moderated estimation of fold change and dispersion for RNA-seq data with DESeq2. Genome Biol 15: 550.
LU H, SHI X, WU G, ZHU J, SONG C, ZHANG Q AND YANG G. 2015. FGF13 regulates proliferation and differentiation of skeletal muscle by down-regulating Spry1. Cell Prolif 48: 550-560.
MA HL, BLANCHET TJ, PELUSO D, HOPKINS B, MORRIS EA AND GLASSON SS. 2007. Osteoarthritis severity is sex dependent in a surgical mouse model. Osteoarthritis Cartilage 15: 695-700.
MACDONALD HM, NISHIYAMA KK, KANG J, HANLEY DA AND BOYD SK. 2011. Age-related patterns of trabecular and cortical bone loss differ between sexes and skeletal sites: a population-based HR-pQCT study. J Bone Miner Res 26: 50-62.
MADDOX BK ET AL. 1997. The fate of cartilage oligomeric matrix protein is determined by the cell type in the case of a novel mutation in pseudoachondroplasia. J Biol Chem 272: 30993-30997.
MAEDA K, NAKASHIMA E, HORIKOSHI T, MABUCHI A AND IKEGAWA S. 2005. Mutation in the von Willebrand factor-A domain is not a prerequisite for the MATN3 mutation in multiple epiphyseal dysplasia. Am J Med Genet A 136: 285-286.
MAJAVA M ET AL. 2007. A report on 10 new patients with heterozygous mutations in the COL11A1 gene and a review of genotype-phenotype correlations in type XI collagenopathies. American Journal of Medical Genetics Part A 143a: 258-264.
MANN HH, OZBEK S, ENGEL J, PAULSSON M AND WAGENER R. 2004. Interactions between the cartilage oligomeric matrix protein and matrilins. Implications for matrix assembly and the pathogenesis of chondrodysplasias. J Biol Chem 279: 25294-25298.
MAROTEAUX P, STANESCU R, STANESCU V AND FONTAINE G. 1980. The mild form of pseudoachondroplasia. Identity of the morphological and biochemical alterations of growth cartilage with those of typical pseudoachondroplasia. Eur J Pediatr 133: 227-231.
MATLIN AJ, CLARK F AND SMITH CW. 2005. Understanding alternative splicing: towards a cellular code. Nat Rev Mol Cell Biol 6: 386-398.
MCGLINCY NJ AND SMITH CW. 2008. Alternative splicing resulting in nonsense-mediated mRNA decay: what is the meaning of nonsense? Trends Biochem Sci 33: 385-393.
MENDLER M, EICH-BENDER SG, VAUGHAN L, WINTERHALTER KH AND BRUCKNER P. 1989. Cartilage contains mixed fibrils of collagen types II, IX, and XI. The Journal of cell biology 108: 191-197.
MERRITT TM, BICK R, POINDEXTER BJ, ALCORN JL AND HECHT JT. 2007. Unique matrix structure in the rough endoplasmic reticulum cisternae of pseudoachondroplasia chondrocytes. Am J Pathol 170: 293-300.
MIENALTOWSKI MJ AND BIRK DE. 2014a. Structure, physiology, and biochemistry of collagens. Adv Exp Med Biol 802: 5-29.
MIENALTOWSKI MJ AND BIRK DE 2014b. Structure, Physiology, and Biochemistry of Collagens. In*:* HALPER, J (Ed.) Progress in Heritable Soft Connective Tissue Diseases, Dordrecht: Springer Netherlands, p. 5-29.
MOJICA FJM, DIEZ-VILLASENOR C, GARCIA-MARTINEZ J AND ALMENDROS C. 2009. Short motif sequences determine the targets of the prokaryotic CRISPR defence system. Microbiology (Reading) 155: 733-740.

MONTAGUE TG, CRUZ JM, GAGNON JA, CHURCH GM AND VALEN E. 2014. CHOPCHOP: a CRISPR/Cas9 and TALEN web tool for genome editing. Nucleic Acids Res 42: W401-407.
MONTES M, SANFORD BL, COMISKEY DF AND CHANDLER DS. 2019. RNA Splicing and Disease: Animal Models to Therapies. Trends Genet 35: 68-87.
MOOTHA VK ET AL. 2003. PGC-1alpha-responsive genes involved in oxidative phosphorylation are coordinately downregulated in human diabetes. Nat Genet 34: 267-273.
MORTIER GR, CHAPMAN K, LEROY JL AND BRIGGS MD. 2001. Clinical and radiographic features of multiple epiphyseal dysplasia not linked to the COMP or type IX collagen genes. Eur J Hum Genet 9: 606-612.
MORTIER GR ET AL. 2019. Nosology and classification of genetic skeletal disorders: 2019 revision. Am J Med Genet A 179: 2393-2419.
MUHLRAD D AND PARKER R. 1994. Premature translational termination triggers mRNA decapping. Nature 370: 578-581.
MULLER-GLAUSER W, HUMBEL B, GLATT M, STRAULI P, WINTERHALTER KH AND BRUCKNER P. 1986. On the role of type IX collagen in the extracellular matrix of cartilage: type IX collagen is localized to intersections of collagen fibrils. The Journal of cell biology 102: 1931-1939.
MURAGAKI Y, MARIMAN EC, VAN BEERSUM SE, PERALA M, VAN MOURIK JB, WARMAN ML, OLSEN BR AND HAMEL BC. 1996. A mutation in the gene encoding the alpha 2 chain of the fibril-associated collagen IX, COL9A2, causes multiple epiphyseal dysplasia (EDM2). Nat Genet 12: 103-105.
NAKASHIMA E, KITOH H, MAEDA K, HAGA N, KOSAKI R, MABUCHI A, NISHIMURA G, OHASHI H AND IKEGAWA S. 2005. Novel COL9A3 mutation in a family with multiple epiphyseal dysplasia. Am J Med Genet A 132A: 181-184.
NAKATA K, ONO K, MIYAZAKI J, OLSEN BR, MURAGAKI Y, ADACHI E, YAMAMURA K AND KIMURA T. 1993. Osteoarthritis associated with mild chondrodysplasia in transgenic mice expressing alpha 1(IX) collagen chains with a central deletion. Proc Natl Acad Sci U S A 90: 2870-2874.
NEWTON G, WEREMOWICZ S, MORTON CC, COPELAND NG, GILBERT DJ, JENKINS NA AND LAWLER J. 1994. Characterization of human and mouse cartilage oligomeric matrix protein. Genomics 24: 435-439.
NICOLAE C, KO YP, MIOSGE N, NIEHOFF A, STUDER D, ENGGIST L, HUNZIKER EB, PAULSSON M, WAGENER R AND ASZODI A. 2007. Abnormal collagen fibrils in cartilage of matrilin-1/matrilin-3-deficient mice. J Biol Chem 282: 22163-22175.
NIKOPOULOS K, SCHRAUWEN I, SIMON M, COLLIN RWJ, VECKENEER M, KEYMOLEN K, VAN CAMP G, CREMERS FPM AND VAN DEN BORN LI. 2011. Autosomal Recessive Stickler Syndrome in Two Families Is Caused by Mutations in the COL9A1 Gene. Invest Ophth Vis Sci 52: 4774-4779.
NISHIMASU H, RAN FA, HSU PD, KONERMANN S, SHEHATA SI, DOHMAE N, ISHITANI R, ZHANG F AND NUREKI O. 2014. Crystal structure of Cas9 in complex with guide RNA and target DNA. Cell 156: 935-949.
NISHIMURA I, MURAGAKI Y AND OLSEN BR. 1989. Tissue-specific forms of type IX collagen-proteoglycan arise from the use of two widely separated promoters. J Biol Chem 264: 20033-20041.
NIU Y ET AL. 2014. Generation of gene-modified cynomolgus monkey via Cas9/RNA-mediated gene targeting in one-cell embryos. Cell 156: 836-843.

NIXON TRW, ALEXANDER P, RICHARDS A, MCNINCH A, BEARCROFT PWP, COBBEN J AND SNEAD MP. 2019. Homozygous Type IX collagen variants (COL9A1, COL9A2, and COL9A3) causing recessive Stickler syndrome-Expanding the phenotype. Am J Med Genet A 179: 1498-1506.
NIZON M ET AL. 2012. Further delineation of CANT1 phenotypic spectrum and demonstration of its role in proteoglycan synthesis. Hum Mutat 33: 1261-1266.
NUNDLALL S, RAJPAR MH, BELL PA, CLOWES C, ZEEFF LA, GARDNER B, THORNTON DJ, BOOT-HANDFORD RP AND BRIGGS MD. 2010. An unfolded protein response is the initial cellular response to the expression of mutant matrilin-3 in a mouse model of multiple epiphyseal dysplasia. Cell Stress Chaperones 15: 835-849.
OEHLMANN R, SUMMERVILLE GP, YEH G, WEAVER EJ, JIMENEZ SA AND KNOWLTON RG. 1994. Genetic linkage mapping of multiple epiphyseal dysplasia to the pericentromeric region of chromosome 19. Am J Hum Genet 54: 3-10.
OH B, HWANG S, MCLAUGHLIN J, SOLTER D AND KNOWLES BB. 2000. Timely translation during the mouse oocyte-to-embryo transition. Development 127: 3795-3803.
OLSEN BR. 1997. Collagen IX. Int J Biochem Cell Biol 29: 555-558.
OPOLKA A, RATZINGER S, SCHUBERT T, SPIEGEL HU, GRIFKA J, BRUCKNER P, PROBST A AND GRASSEL S. 2007. Collagen IX is indispensable for timely maturation of cartilage during fracture repair in mice. Matrix Biol 26: 85-95.
OTTEN C, WAGENER R, PAULSSON M AND ZAUCKE F. 2005. Matrilin-3 mutations that cause chondrodysplasias interfere with protein trafficking while a mutation associated with hand osteoarthritis does not. J Med Genet 42: 774-779.
PAASSILTA P, LOHINIVA J, ANNUNEN S, BONAVENTURE J, LE MERRER M, PAI L AND ALA-KOKKO L. 1999. COL9A3: A third locus for multiple epiphyseal dysplasia. Am J Hum Genet 64: 1036-1044.
PAASSILTA P ET AL. 2001. Identification of a novel common genetic risk factor for lumbar disk disease. JAMA 285: 1843-1849.
PARSONS P, GILBERT SJ, VAUGHAN-THOMAS A, SORRELL DA, NOTMAN R, BISHOP M, HAYES AJ, MASON DJ AND DUANCE VC. 2011. Type IX collagen interacts with fibronectin providing an important molecular bridge in articular cartilage. J Biol Chem 286: 34986-34997.
PATRO R, DUGGAL G, LOVE MI, IRIZARRY RA AND KINGSFORD C. 2017. Salmon provides fast and bias-aware quantification of transcript expression. Nat Methods 14: 417-+.
PERCIVAL CJ AND RICHTSMEIER JT. 2013. Angiogenesis and intramembranous osteogenesis. Dev Dyn 242: 909-922.
PIHLAJAMAA T ET AL. 2004. Characterization of recombinant amino-terminal NC4 domain of human collagen IX: interaction with glycosaminoglycans and cartilage oligomeric matrix protein. J Biol Chem 279: 24265-24273.
PIHLAJAMAA T, PERALA M, VUORISTO MM, NOKELAINEN M, BODO M, SCHULTHESS T, VUORIO E, TIMPL R, ENGEL J AND ALA-KOKKO L. 1999. Characterization of recombinant human type IX collagen. Association of alpha chains into homotrimeric and heterotrimeric molecules. J Biol Chem 274: 22464-22468.
PIHLAJAMAA T, PROCKOP DJ, FABER J, WINTERPACHT A, ZABEL B, GIEDION A, WIESBAUER P, SPRANGER J AND ALA-KOKKO L. 1998. Heterozygous glycine substitution in the COL11A2 gene in the original patient with the Weissenbacher-Zweymuller syndrome demonstrates its identity with heterozygous OSMED (nonocular Stickler syndrome). American Journal of Medical Genetics 80: 115-120.

PIROG-GARCIA KA, MEADOWS RS, KNOWLES L, HEINEGARD D, THORNTON DJ, KADLER KE, BOOT-HANDFORD RP AND BRIGGS MD. 2007. Reduced cell proliferation and increased apoptosis are significant pathological mechanisms in a murine model of mild pseudoachondroplasia resulting from a mutation in the C-terminal domain of COMP. Hum Mol Genet 16: 2072-2088.
PIROG KA, JAKA O, KATAKURA Y, MEADOWS RS, KADLER KE, BOOT-HANDFORD RP AND BRIGGS MD. 2010. A mouse model offers novel insights into the myopathy and tendinopathy often associated with pseudoachondroplasia and multiple epiphyseal dysplasia. Hum Mol Genet 19: 52-64.
PLAISIER SB, TASCHEREAU R, WONG JA AND GRAEBER TG. 2010. Rank-rank hypergeometric overlap: identification of statistically significant overlap between gene-expression signatures. Nucleic Acids Res 38: e169.
PLUIJM SM, VAN ESSEN HW, BRAVENBOER N, UITTERLINDEN AG, SMIT JH, POLS HA AND LIPS P. 2004. Collagen type I alpha1 Sp1 polymorphism, osteoporosis, and intervertebral disc degeneration in older men and women. Ann Rheum Dis 63: 71-77.
POOLE CA. 1997. Articular cartilage chondrons: form, function and failure. J Anat 191 (Pt 1): 1-13.
POOLE CA, AYAD S AND GILBERT RT. 1992. Chondrons from articular cartilage. V. Immunohistochemical evaluation of type VI collagen organisation in isolated chondrons by light, confocal and electron microscopy. J Cell Sci 103 (Pt 4): 1101-1110.
POSEY KL, HANKENSON K, VEERISETTY AC, BORNSTEIN P, LAWLER J AND HECHT JT. 2008a. Skeletal abnormalities in mice lacking extracellular matrix proteins, thrombospondin-1, thrombospondin-3, thrombospondin-5, and type IX collagen. Am J Pathol 172: 1664-1674.
POSEY KL, VEERISETTY AC, LIU P, WANG HR, POINDEXTER BJ, BICK R, ALCORN JL AND HECHT JT. 2009. An inducible cartilage oligomeric matrix protein mouse model recapitulates human pseudoachondroplasia phenotype. Am J Pathol 175: 1555-1563.
POSEY KL, YANG Y, VEERISETTY AC, SHARAN SK AND HECHT JT. 2008b. Model systems for studying skeletal dysplasias caused by TSP-5/COMP mutations. Cell Mol Life Sci 65: 687-699.
PREIN C, WARMBOLD N, FARKAS Z, SCHIEKER M, ASZODI A AND CLAUSEN-SCHAUMANN H. 2016. Structural and mechanical properties of the proliferative zone of the developing murine growth plate cartilage assessed by atomic force microscopy. Matrix Biol 50: 1-15.
QIU S, ADEMA CM AND LANE T. 2005. A computational study of off-target effects of RNA interference. Nucleic Acids Res 33: 1834-1847.
RAJPAR MH ET AL. 2009. Targeted induction of endoplasmic reticulum stress induces cartilage pathology. PLoS Genet 5: e1000691.
RAN FA ET AL. 2013a. Double nicking by RNA-guided CRISPR Cas9 for enhanced genome editing specificity. Cell 154: 1380-1389.
RAN FA, HSU PD, WRIGHT J, AGARWALA V, SCOTT DA AND ZHANG F. 2013b. Genome engineering using the CRISPR-Cas9 system. Nature Protocols 8: 2281-2308.
RAPPSILBER J, RYDER U, LAMOND AI AND MANN M. 2002. Large-scale proteomic analysis of the human spliceosome. Genome Res 12: 1231-1245.
RAUCH F. 2005. Bone growth in length and width: the Yin and Yang of bone stability. J Musculoskelet Neuronal Interact 5: 194-201.

REHN M AND PIHLAJANIEMI T. 1994. Alpha 1(XVIII), a collagen chain with frequent interruptions in the collagenous sequence, a distinct tissue distribution, and homology with type XV collagen. Proc Natl Acad Sci U S A 91: 4234-4238.
RISSO D, NGAI J, SPEED TP AND DUDOIT S. 2014. Normalization of RNA-seq data using factor analysis of control genes or samples. Nat Biotechnol 32: 896-902.
ROSENBERG K, OLSSON H, MORGELIN M AND HEINEGARD D. 1998. Cartilage oligomeric matrix protein shows high affinity zinc-dependent interaction with triple helical collagen. Journal of Biological Chemistry 273: 20397-20403.
ROZARIO T AND DESIMONE DW. 2010. The extracellular matrix in development and morphogenesis: a dynamic view. Dev Biol 341: 126-140.
SANDYA S, ACHAN MA AND SUDHAKARAN PR. 2007. Parallel changes in fibronectin and alpha5beta1 integrin in articular cartilage in type II collagen-induced arthritis. Indian J Biochem Biophys 44: 14-18.
SCHIPANI E, RYAN HE, DIDRICKSON S, KOBAYASHI T, KNIGHT M AND JOHNSON RS. 2001. Hypoxia in cartilage: HIF-1alpha is essential for chondrocyte growth arrest and survival. Genes Dev 15: 2865-2876.
SCHMID TM AND LINSENMAYER TF. 1990. Immunoelectron Microscopy of Type-X Collagen - Supramolecular Forms within Embryonic Chick Cartilage. Developmental Biology 138: 53-62.
SCHMITZ M, NIEHOFF A, MIOSGE N, SMYTH N, PAULSSON M AND ZAUCKE F. 2008. Transgenic mice expressing D469Delta mutated cartilage oligomeric matrix protein (COMP) show growth plate abnormalities and sternal malformations. Matrix Biol 27: 67-85.
SCHRAUWEN I, SOMMEN M, CLAES C, PINNER J, FLAHERTY M, COLLINS F AND VAN CAMP G. 2014. Broadening the phenotype of LRP2 mutations: a new mutation in LRP2 causes a predominantly ocular phenotype suggestive of Stickler syndrome. Clin Genet 86: 282-286.
SEGAT D, FRIE C, NITSCHE PD, KLATT AR, PIECHA D, KORPOS E, DEAK F, WAGENER R, PAULSSON M AND SMYTH N. 2000. Expression of matrilin-1, -2 and -3 in developing mouse limbs and heart. Matrix Biol 19: 649-655.
SEKI S ET AL. 2005. A functional SNP in CILP, encoding cartilage intermediate layer protein, is associated with susceptibility to lumbar disc disease. Nat Genet 37: 607-612.
SEKI S ET AL. 2006. Association study of COL9A2 with lumbar disc disease in the Japanese population. J Hum Genet 51: 1063-1067.
SEMENZA GL. 1999. Regulation of mammalian O2 homeostasis by hypoxia-inducible factor 1. Annu Rev Cell Dev Biol 15: 551-578.
SHAHI M, PEYMANI A AND SAHMANI M. 2017. Regulation of Bone Metabolism. Rep Biochem Mol Biol 5: 73-82.
SHAW LM AND OLSEN BR. 1991. FACIT collagens: diverse molecular bridges in extracellular matrices. Trends Biochem Sci 16: 191-194.
SHEN G AND DARENDELILER MA. 2005. The adaptive remodeling of condylar cartilage--a transition from chondrogenesis to osteogenesis. Journal of dental research 84: 691-699.
SHIANG R, THOMPSON LM, ZHU YZ, CHURCH DM, FIELDER TJ, BOCIAN M, WINOKUR ST AND WASMUTH JJ. 1994. Mutations in the transmembrane domain of FGFR3 cause the most common genetic form of dwarfism, achondroplasia. Cell 78: 335-342.
SMITH J ET AL. 2006. A combinatorial approach to create artificial homing endonucleases cleaving chosen sequences. Nucleic Acids Res 34: e149.

SMITHIES O, GREGG RG, BOGGS SS, KORALEWSKI MA AND KUCHERLAPATI RS. 1985. Insertion of DNA sequences into the human chromosomal beta-globin locus by homologous recombination. Nature 317: 230-234.
SOLOVIEVA S, KOUHIA S, LEINO-ARJAS P, ALA-KOKKO L, LUOMA K, RAININKO R, SAARELA J AND RIIHIMAKI H. 2004. Interleukin 1 polymorphisms and intervertebral disc degeneration. Epidemiology 15: 626-633.
SOLOVIEVA S, LOHINIVA J, LEINO-ARJAS P, RAININKO R, LUOMA K, ALA-KOKKO L AND RIIHIMAKI H. 2006. Intervertebral disc degeneration in relation to the COL9A3 and the IL-1ss gene polymorphisms. Eur Spine J 15: 613-619.
SOPHIA FOX AJ, BEDI A AND RODEO SA. 2009. The basic science of articular cartilage: structure, composition, and function. Sports Health 1: 461-468.
SOSIC D, BRAND-SABERI B, SCHMIDT C, CHRIST B AND OLSON EN. 1997. Regulation of paraxis expression and somite formation by ectoderm- and neural tube-derived signals. Dev Biol 185: 229-243.
SPAYDE EC, JOSHI AP, WILCOX WR, BRIGGS M, COHN DH AND OLSEN BR. 2000. Exon skipping mutation in the COL9A2 gene in a family with multiple epiphyseal dysplasia. Matrix Biol 19: 121-128.
SRIKANTH VK, FRYER JL, ZHAI G, WINZENBERG TM, HOSMER D AND JONES G. 2005. A meta-analysis of sex differences prevalence, incidence and severity of osteoarthritis. Osteoarthritis Cartilage 13: 769-781.
STERNBERG SH, REDDING S, JINEK M, GREENE EC AND DOUDNA JA. 2014. DNA interrogation by the CRISPR RNA-guided endonuclease Cas9. Nature 507: 62-67.
STICKLER GB, BELAU PG, FARRELL FJ, JONES JD, PUGH DG, STEINBERG AG AND WARD LE. 1965. Hereditary Progressive Arthro-Ophthalmopathy. Mayo Clin Proc 40: 433-455.
STODDARD BL. 2011. Homing endonucleases: from microbial genetic invaders to reagents for targeted DNA modification. Structure 19: 7-15.
STOLZ M ET AL. 2009. Early detection of aging cartilage and osteoarthritis in mice and patient samples using atomic force microscopy. Nat Nanotechnol 4: 186-192.
SUBRAMANIAN A ET AL. 2005. Gene set enrichment analysis: a knowledge-based approach for interpreting genome-wide expression profiles. Proc Natl Acad Sci U S A 102: 15545-15550.
SULEMAN F, GUALENI B, GREGSON HJ, LEIGHTON MP, PIROG KA, EDWARDS S, HOLDEN P, BOOT-HANDFORD RP AND BRIGGS MD. 2012. A novel form of chondrocyte stress is triggered by a COMP mutation causing pseudoachondroplasia. Hum Mutat 33: 218-231.
SUZUKI N, ASAMURA K, KIKUCHI Y, TAKUMI Y, ABE S, IMAMURA Y, HAYASHI T, ASZODI A, FASSLER R AND USAMI S. 2005. Type IX collagen knock-out mouse shows progressive hearing loss. Neurosci Res 51: 293-298.
SVENSSON L, ASZODI A, HEINEGARD D, HUNZIKER EB, REINHOLT FP, FASSLER R AND OLDBERG A. 2002. Cartilage oligomeric matrix protein-deficient mice have normal skeletal development. Mol Cell Biol 22: 4366-4371.
TAKAHASHI I, ONODERA K, BAE JW, MITANI H AND SASANO Y. 2005. Age-related changes in the expression of gelatinase and tissue inhibitor of metalloproteinase genes in mandibular condylar, growth plate, and articular cartilage in rats. Journal of molecular histology 36: 355-366.
TAKAHASHI M, HARO H, WAKABAYASHI Y, KAWA-UCHI T, KOMORI H AND SHINOMIYA K. 2001. The association of degeneration of the intervertebral disc with 5a/6a polymorphism in the promoter of the human matrix metalloproteinase-3 gene. J Bone Joint Surg Br 83: 491-495.

THANARAJ TA, CLARK F AND MUILU J. 2003. Conservation of human alternative splice events in mouse. Nucleic Acids Res 31: 2544-2552.
THOMAS KR AND CAPECCHI MR. 1987. Site-directed mutagenesis by gene targeting in mouse embryo-derived stem cells. Cell 51: 503-512.
THUR J, ROSENBERG K, NITSCHE DP, PIHLAJAMAA T, ALA-KOKKO L, HEINEGARD D, PAULSSON M AND MAURER P. 2001. Mutations in cartilage oligomeric matrix protein causing pseudoachondroplasia and multiple epiphyseal dysplasia affect binding of calcium and collagen I, II, and IX. J Biol Chem 276: 6083-6092.
TIBBITT MW AND ANSETH KS. 2009. Hydrogels as extracellular matrix mimics for 3D cell culture. Biotechnol Bioeng 103: 655-663.
TILLGREN V, ONNERFJORD P, HAGLUND L AND HEINEGARD D. 2009. The tyrosine sulfate-rich domains of the LRR proteins fibromodulin and osteoadherin bind motifs of basic clusters in a variety of heparin-binding proteins, including bioactive factors. J Biol Chem 284: 28543-28553.
UNGER S, BONAFE L AND SUPERTI-FURGA A. 2008. Multiple epiphyseal dysplasia: clinical and radiographic features, differential diagnosis and molecular basis. Best Pract Res Clin Rheumatol 22: 19-32.
URNOV FD, MILLER JC, LEE YL, BEAUSEJOUR CM, ROCK JM, AUGUSTUS S, JAMIESON AC, PORTEUS MH, GREGORY PD AND HOLMES MC. 2005. Highly efficient endogenous human gene correction using designed zinc-finger nucleases. Nature 435: 646-651.
URNOV FD, REBAR EJ, HOLMES MC, ZHANG HS AND GREGORY PD. 2010. Genome editing with engineered zinc finger nucleases. Nat Rev Genet 11: 636-646.
VAN CAMP G ET AL. 2006. A new autosomal recessive form of Stickler syndrome is caused by a mutation in the COL9A1 gene. Am J Hum Genet 79: 449-457.
VAN DEN BERG LE, ZANDBERGEN AA, VAN CAPELLE CI, DE VRIES JM, HOP WC, VAN DEN HOUT JM, REUSER AJ, ZILLIKENS MC AND VAN DER PLOEG AT. 2010. Low bone mass in Pompe disease: muscular strength as a predictor of bone mineral density. Bone 47: 643-649.
VAN DER WEYDEN L, WEI L, LUO J, YANG X, BIRK DE, ADAMS DJ, BRADLEY A AND CHEN Q. 2006. Functional knockout of the matrilin-3 gene causes premature chondrocyte maturation to hypertrophy and increases bone mineral density and osteoarthritis. Am J Pathol 169: 515-527.
VAN MOURIK JB, BUMA P AND WILCOX WR. 1998a. Electron microscopical study in multiple epiphyseal dysplasia type II. Ultrastruct Pathol 22: 249-251.
VAN MOURIK JB, HAMEL BC AND MARIMAN EC. 1998b. A large family with multiple epiphyseal dysplasia linked to COL9A2 gene. Am J Med Genet 77: 234-240.
WANG CJ, IIDA K, EGUSA H, HOKUGO A, JEWETT A AND NISHIMURA I. 2008. Trabecular bone deterioration in col9a1+/- mice associated with enlarged osteoclasts adhered to collagen IX-deficient bone. J Bone Miner Res 23: 837-849.
WANG H, YANG H, SHIVALILA CS, DAWLATY MM, CHENG AW, ZHANG F AND JAENISCH R. 2013. One-step generation of mice carrying mutations in multiple genes by CRISPR/Cas-mediated genome engineering. Cell 153: 910-918.
WANG L ET AL. 2014a. CARM1 methylates chromatin remodeling factor BAF155 to enhance tumor progression and metastasis. Cancer Cell 25: 21-36.
WANG T, WEI JJ, SABATINI DM AND LANDER ES. 2014b. Genetic screens in human cells using the CRISPR-Cas9 system. Science 343: 80-84.
WEFERS B, MEYER M, ORTIZ O, HRABE DE ANGELIS M, HANSEN J, WURST W AND KUHN R. 2013. Direct production of mouse disease models by embryo

microinjection of TALENs and oligodeoxynucleotides. Proc Natl Acad Sci U S A 110: 3782-3787.
WHITE KE ET AL. 2005. Mutations that cause osteoglophonic dysplasia define novel roles for FGFR1 in bone elongation. Am J Hum Genet 76: 361-367.
WIBERG C, KLATT AR, WAGENER R, PAULSSON M, BATEMAN JF, HEINEGARD D AND MORGELIN M. 2003. Complexes of matrilin-1 and biglycan or decorin connect collagen VI microfibrils to both collagen II and aggrecan. Journal of Biological Chemistry 278: 37698-37704.
WINTERBOTTOM N, TONDRAVI MM, HARRINGTON TL, KLIER FG, VERTEL BM AND GOETINCK PF. 1992. Cartilage Matrix Protein Is a Component of the Collagen Fibril of Cartilage. Dev Dynam 193: 266-276.
WU H, WANG S, CHEN W, ZHAN X, XIAO Z, JIANG H AND WEI Q. 2018. Collagen IX gene polymorphisms and lumbar disc degeneration: a systematic review and meta-analysis. J Orthop Surg Res 13: 47.
WU JJ AND EYRE DR. 1998. Matrilin-3 forms disulfide-linked oligomers with matrilin-1 in bovine epiphyseal cartilage. J Biol Chem 273: 17433-17438.
WU JJ, WEIS MA, KIM LS AND EYRE DR. 2010. Type III collagen, a fibril network modifier in articular cartilage. J Biol Chem 285: 18537-18544.
YU K, XU J, LIU Z, SOSIC D, SHAO J, OLSON EN, TOWLER DA AND ORNITZ DM. 2003. Conditional inactivation of FGF receptor 2 reveals an essential role for FGF signaling in the regulation of osteoblast function and bone growth. Development 130: 3063-3074.
ZAUCKE F, DINSER R, MAURER P AND PAULSSON M. 2001. Cartilage oligomeric matrix protein (COMP) and collagen IX are sensitive markers for the differentiation state of articular primary chondrocytes. Biochem J 358: 17-24.
ZHANG GY, YOUNG BB AND BIRK DE. 2003. Differential expression of type XII collagen in developing chicken metatarsal tendons. J Anat 202: 411-420.
ZHANG L, HU J AND ATHANASIOU KA. 2009. The role of tissue engineering in articular cartilage repair and regeneration. Crit Rev Biomed Eng 37: 1-57.